ICUS REPORT 2011 - 03

INTERNATIONAL CENTER FOR
URBAN SAFETY ENGINEERING

INSTITUTE OF INDUSTRIAL SCIENCE
THE UNIVERSITY OF TOKYO

4th JOINT STUDENT SEMINAR ON CIVIL INFRASTRUCTURES
August 1-2, 2011

Edited by

**Dr. Hyunmyung Kim, Dr. Akiyuki Kawasaki, ,
Dr. Kyung-Ho Park , Dr. Thirayoot Limanond
and Dr. Kunnawee Kanipong**

ICUS, IIS, The University of Tokyo, Japan

ISBN 4-903661-52-0

Serial Number 57

4th Joint Student Seminar on Civil Infrastructures

1-2 August 2011
Bangkok, Thailand

Co-Organized by

School of Engineering and Technology,
Asian Institute of Technology (AIT), Thailand

International Center for Urban Safety Engineering (ICUS)
Institute of Industrial Science
The University of Tokyo, Japan

Myongji University, Korea
and

Chonnam National University

Edited by

Dr. Hyunmyung Kim, Dr. Akiyuki Kawasaki, ,
Dr. Kyung-Ho Park , Dr. Thirayoot Limanond
and Dr. Kunnawee Kanipong

Organization Teams

Prof. Worsak Kanok-Nukulchai (AIT, Thailand)
Dr. Pennung Warnitchai (AIT, Thailand)
Dr. Kyung-Ho Park (AIT, Thailand)
Dr. Kunnawee Kanipong (AIT, Thailand)
Dr. Thirayoot Limanond (AIT, Thailand)
Dr. Masahiko Nagai (AIT, Thailand)
Dr. Mukand Singh Babel (AIT, Thailand)
Dr. Pakawat Sancharoen (SIIT, Thailand)
Dr. Withit Pansuk (Chulalongkorn U, Thailand)

Prof. Kimiro Meguro (UT, Japan)
Prof. Haruo Sawada (UT, Japan)
Dr. Akiyuki Kawasaki (UT, Japan)
Dr. Shinji Tanaka (UT, Japan)
Dr. Wataru Takeuchi (JSPS, Thailand/UT, Japan)

Dr. Hyunmyung Kim (Myongji U, Korea)
Prof. Yongtaek Lim (Chonnam National U, Korea)
Prof. Hee-Jung Kang (Konkuk U, Korea)

4^{th} JOINT STUDENT SEMINAR ON CIVIL INFRASTRUCTURES

August 2011

PREFACE

In this era of rapid globalization, having an international sense and broad human resource network is essential. In particular, building up a good relationship with various communities during young school days will be of advantage in the future. To give such an opportunity to students from Asian countries, we held the 1^{st}, 2^{nd} 3^{rd} and joint student seminar in July 2008, July 2009 and July 2010, respectively, and following this success the "4^{th} Joint Student Seminar on Civil Infrastructures" was held on 1-2^{th} August, 2011.

The objectives of this seminar are:

1) to experience the international seminar,
2) to improve the presentation skill,
3) to share the research information and friendships.

The number of participants was 65, consisting of 2 faculties and 63 students from Chonnam National University, Sirindhorn International Institute of Technology, Thammasat University, Chulanongkorn University, The University of Tokyo and Asian Institute of Technology.

On the first day, we had a presentation session, having 2 faculties' lectures and 16 students' presentation. The topics covered wide range areas of civil engineering and every student did their best in his/her presentation. During the seminar, students and faculties had lively exchange of views beyond their specialty, culture and nationality. At the end of the seminar, excellent presentation awards were given to the following 4 students.

1. Mr. Sathita Taothong from Thailand
2. Mr. Michael Coo from Thailand
3. Mr. Soti Rajendra from Japan
4. Ms. Sho Oh from Japan

On the second day, we had a field visit to the PRUKSA PRECAST Company Limited (a Precast concrete factory); visit Ayutthaya (Wat Chai Wattanaram Temple, Wat Phrasrisanphet, Wat Mahathat, Wat Rat Burana and Ayutthaya Floating Market)

The seminar was quite successful and fruitful: this seminar gave not only knowledge and information but also a lot of other stimuli to the students. We hope to continue to hold this kind of interchange activities in the coming years.

Finally, we would like to express our sincere gratitude for those who kindly supported and contributed to the success of this seminar.

HYUNMYUNG KIM, AKIYUKI KAWASAKI,
KYUNG-HO PARK, THIRAYOOT LIMANOND
AND KUNNAWEE KANIPONG

Table of Contents

Registration

Opening ceremony (Prof. Worsak)

Dr. Akiyuki Kawasaki

Prof. Kimiro Meguro

Dr. Kunnawee Kanipong

Mr. Viet-Dung Tran

Mr. Tian Jiang

Ms. Aris Mahasiripan

Mr. Soti Rajendra

Mr. Kullachai Tantayopin

Mr. Makinodan Kohei

Mr. Sudniran Phetcharat

Ms. Juhye Kim

Mr. Michael Coo

Mr. Tachibana Kazuki

Ms. Sathita Taothong

Mr. Nakao Yushi

Mr. Prasong Permsuwan

Ms. Sho Oh

Md. Reaz Akter Mullick

Mr. Nakai Hiroyuki

Closing ceremony (Mr. Masahiko Nagai)

Excellent Presentation from Japan

Excellent Presentation from Thai

Presentation Precast concrete factory


Presentation Precast concrete factory


Presentation Precast concrete factory

Seminar: Group Photo at AIT CC (Morning)

Seminar: Group Photo at AIT CC (Afternoon)

Field Trip: Group Photo at PRUKSA PRECAST Company Limited

Field Trip: Group Photo at Ayutthaya

Invited Lectures

GREEN HIGHWAYS FOR ENVIRONMENTAL AND ECONOMICAL SUSTAINABLE DEVELOPMENT

Kunnawee Kanitpong
School of Engineering & Technology, Asian Institute of Technology,
P.O. Box 4, Klong Luang, Pathumthani 12120, Thailand
kanitpon@ait.ac.th


Water, Ecosystems, Agriculture
Built Environment
We tends to care more about "Green" and "Sustainability"
Energy and Environment
Materials and Toxics


Green Highway Characteristics
Provides net increase in environmental functions and values of the watershed
Goes beyond minimum standards set forth by environmental laws and regulations
Identifies and protects important historical and cultural landmarks
Maps all resources in the area in order to identify, avoid, and protect critical resource areas
Uses innovative, natural methods to reduce imperviousness, and cleanse all runoff within the project area
Maximizes use of existing transportation infrastructure, provides multi-modal transportation opportunities, and promotes ride-sharing / public transportation
Uses recycled materials to eliminate waste and reduce the energy required to build the highway
Links regional transportation plans with local landuse through partnerships
Controls populations of invasive species, and promotes the growth of native species
Incorporates post project monitoring to ensure environmental results
Protects the hydrology of wetlands and streams channels through restoration of natural drainage paths
Results in a suite of targeted environmental outcomes based upon local environmental needs
Reduces disruptions to ecological processes by promoting wildlife corridors and passages in areas identified through wildlife conservation plans
Encourages smart growth by integrating and guiding future growth and capacity building with ecological constraints
Source: Green Highways Partnership

Source: Green Highways Partnership

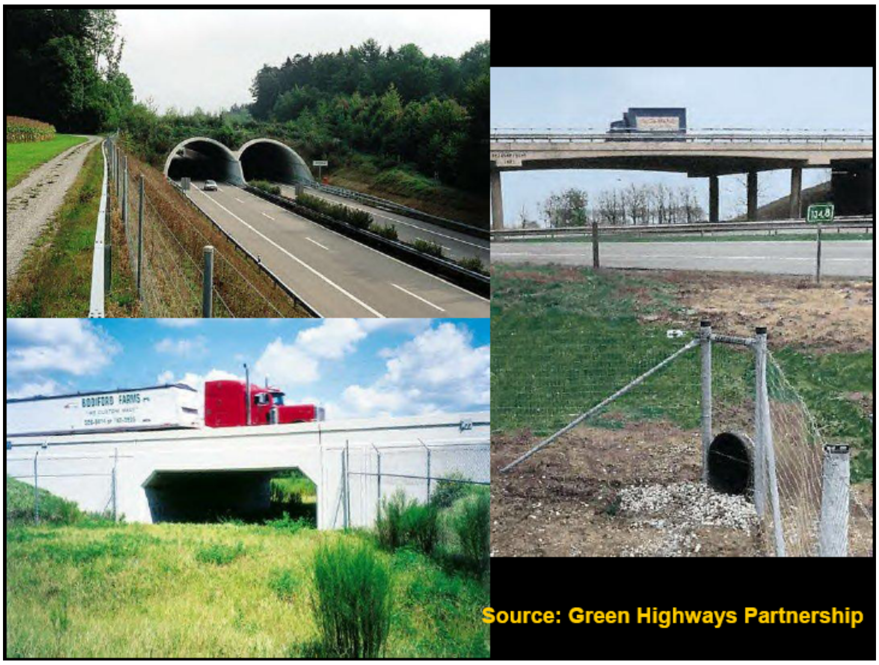
Source: Green Highways Partnership

Sustainable Pavement and Green Road

Environmental Consumption in Building Roads

- We use lots of raw material
  - In pavements: Agg, Asphalt, Cement
  - 2000 Co2 by sources—transportation 30%
  - Energy use –transportation

Demand for Quality Materials

- **Long life material design**
  - Crushes and angular aggregate
  - Manufactured sands
- **High friction demand**
  - Improve texture – decrease wear
- **High quality mixes**
  - Selective aggregate size
- **Management and treatment of runoff, Leachate control**
- **Use of industrial by-products**
  - Coal combustion products
  - Slag
  - Foundary sand
- **Use of waste and by-product**
  - Crumb rubber

Sustainability: System for use

- Concrete pavement
- WMA (Warm Mix Asphalt)
- Porous Asphalt
- Cool pavement

"Green roads" a rating system designed to distinguish performance sustainable new or redesigned/rehab roads

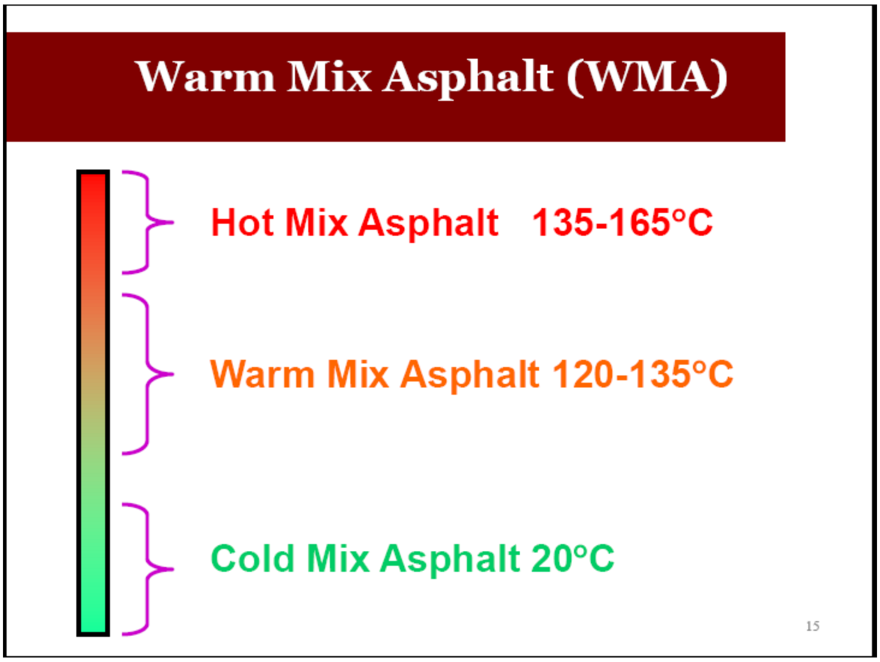

Warm Mix Asphalt (WMA)
Hot Mix Asphalt 135-165°C
Warm Mix Asphalt 120-135°C
Cold Mix Asphalt 20°C
15

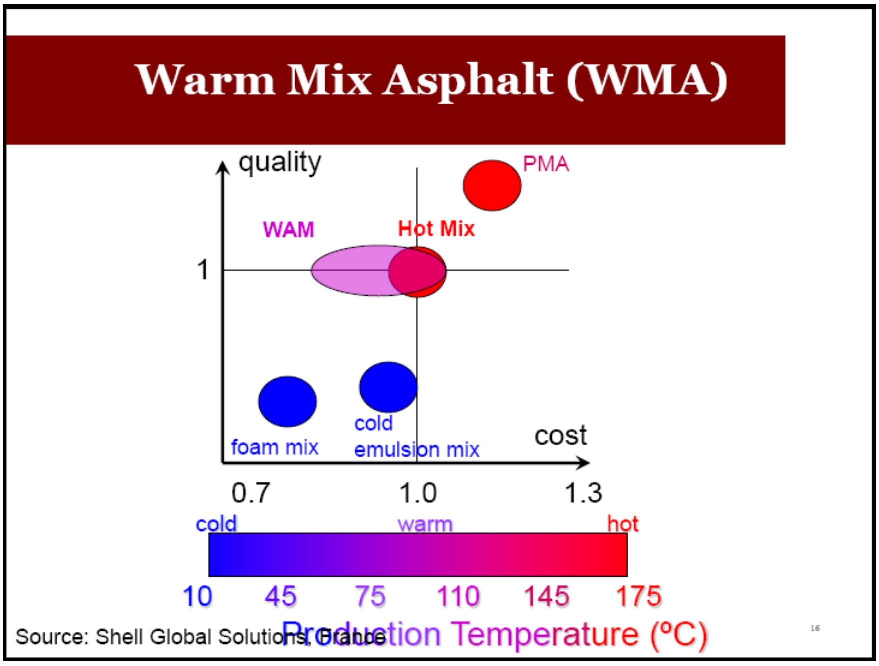

Warm Mix Asphalt (WMA)
quality
PMA
WAM
Hot Mix
1
foam mix
cold
emulsion mix
cost
0.7
1.0
1.3
cold
warm
hot
10
45
75
110
145
175
Production Temperature (ºC)
Source: Shell Global Solutions, France
16

Introduction - WMA

- Warm Mix Asphalt (WMA) is a technology widely used to reduce production and compaction temperatures
- Benefits of temperature reduction (Hurley and Prowell, 2005 and NAPA 2002)
  - Save energy to heat asphalt
  - Less production of fumes, emissions, and odors
  - Less oxidative hardening

17

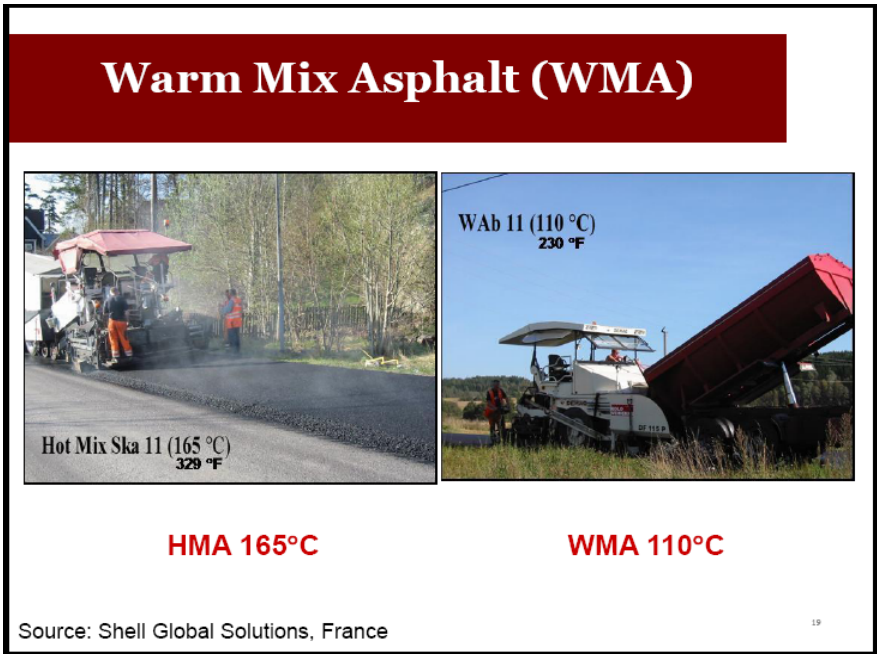
Warm Mix Asphalt (WMA)
Hot Mix Ska 11 (165 °C)
329 °F
WAb 11 (110 °C)
230 °F
HMA 165°C
WMA 110°C
Source: Shell Global Solutions, France
19

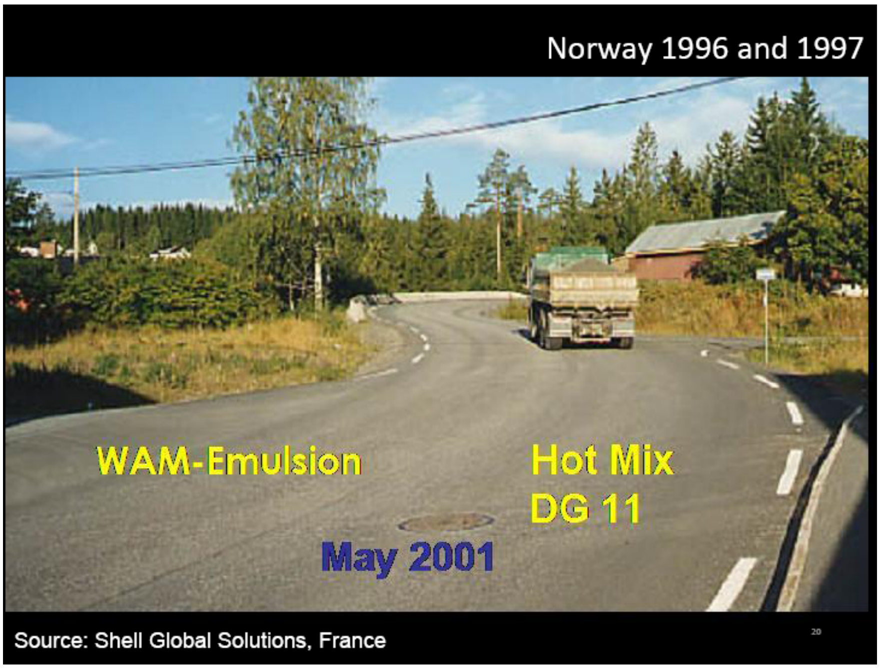
Norway 1996 and 1997
WAM-Emulsion
Hot Mix
DG 11
May 2001
Source: Shell Global Solutions, France
20

Porous Asphalt

- Terminology
  - Open-graded mix
  - OGFC
  - Permeable friction mix/asphalt
  - Porous asphalt – extension of OGFC but incorporating drainage. Air voids exceeding 20% and voids are interconnected.

Porous Mix Characteristics

- Coarse aggregates constitute more than 85% of mix composition
- Porosity or air voids exceeding 20%
- A very permeable material

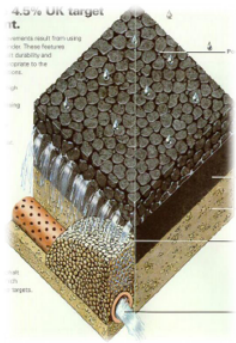

Advantages

Ability to eliminate ponding water

- Improve skid resistance
- Eliminates splash and spray
- Diminishes hydroplaning potential
- Reduces glare
- Lowers traffic noise

IMPROVE TRAFFIC SAFTY

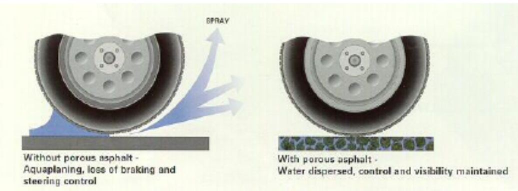


PHOTO: LARRY GAVAN, VIRGINIA DEPT. OF CONSERVATION & RECREATION

Noise Barriers

Do not provide total shelter
Upper floors of high rise apartments not protected

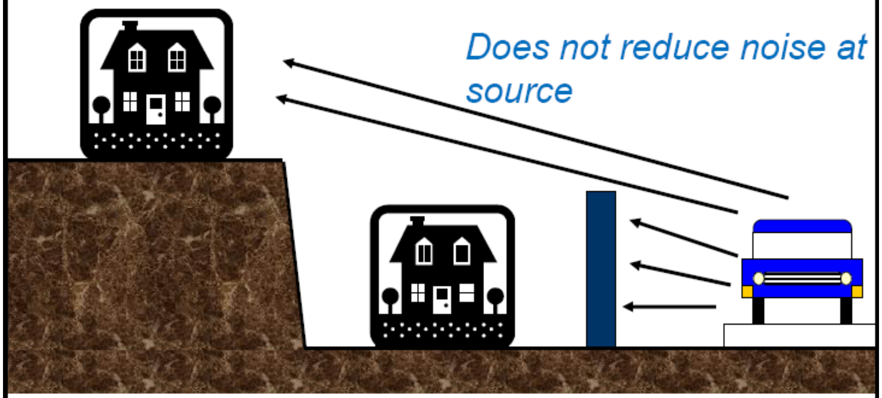

Courtesy of The Asphalt Pavement Alliance - Asphalt: The Quiet Pavement

Disadvantages

- Easily clogged. Difficult to unclog especially pavements in the tropics
- Traffic overcompaction leads to permeability loss
- Bitumen hardens/aged rapidly
- Short design life
- High cost, more than 50% costlier (but compensated by reduction in traffic accident/fatalities)
- Easily disintegrates due to ravelling

Cool Pavement

- The term currently refers to paving materials that reflect more solar energy, enhance water evaporation, or have been otherwise modified to remain cooler than conventional pavements.

Benefits and Costs

- *Reduced stormwater runoff and improved water quality*
- *Lower tire noise*
- *Enhanced safety:*
- *Better nighttime visibility*
- *Improved local comfort*

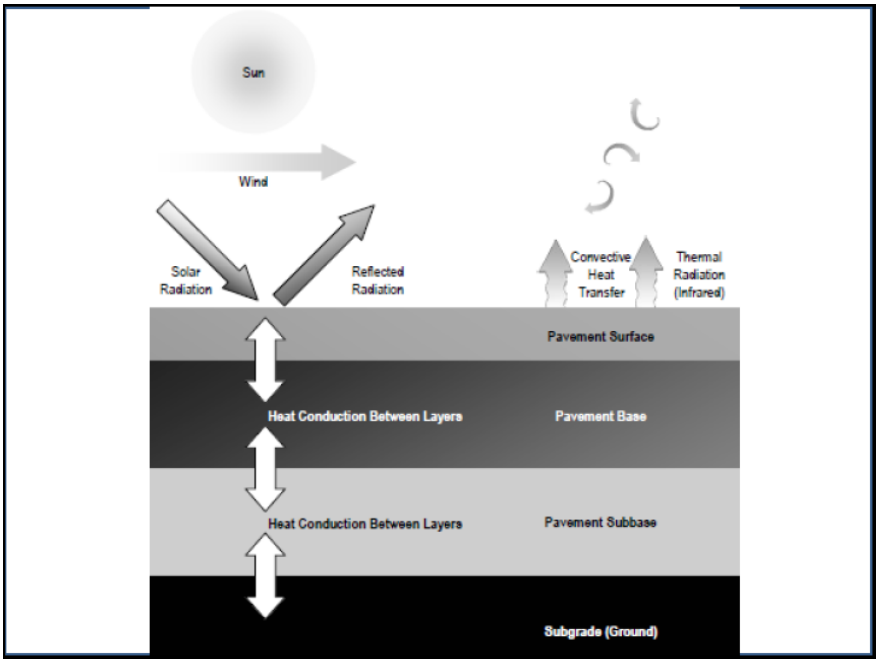

Asphalt Pavement: Energy and Recycling

- Asphalt pavements require about 20% less energy to produce and construct than other pavements.
- Faster construct and rehabilitate → opened to traffic quicker→ no need to wait for material to cure
- Can be recycle

- Other materials are recycled into asphalt pavements such as rubber from used tires, blast furnace slag, glass

Source: http://pavegreen.com

Asphalt Pavement: Performance

- **Asphalt is Perpetual Pavement**

  Perpetual Pavement is constructed so that distress occurs in the top layer only.

- **Rubblization for sustainability**

When concrete pavements reach end of life, it is left in place, "rubblized" (fractured), and used as base for Perpetual pavement.

- **Smooth asphalt road gives vehicle tires good contact with the road**

  OGFC allows rainwater to drain through the surface layer and off to the sides, reducing the amount of splash and spray kicked up by vehicles

Source: http://pavegreen.com

Asphalt Pavement: Performance

- **Noise Reduction**
  - Quiet asphalt pavement technologies include open-graded surfaces, fine-graded surfaces, and two-layer open-graded pavements.
  - Noise reductions of 3 to 10 dB(a).
  - Reducing noise by 3 dB(a) is the same as doubling the distance from the road to the listener, or reducing traffic volume by 50 percent

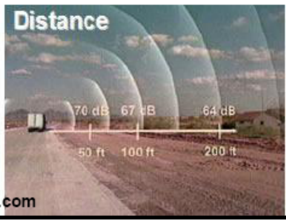

Source: http://pavegreen.com

Asphalt Pavement: Performance

- **Smoothness and conservation**
  - Driving on smoother surfaces can reduce fuel consumption of 4.5-5%.
  - When trucks are driven on rough surfaces, the tires bounce and deliver heavy, punishing impacts to the pavement. Some experts estimate that a 25 percent increase in smoothness can result in a 9 to 10 percent increase in the life of pavements.

Source: http://pavegreen.com

Asphalt Pavement: Water Quality

- **Porous Asphalt Pavement**
  - Permeable surface can turn runoff into infiltration; restore the hydrology of a site, or even improve it; improve water quality; and eliminate the need for detention basins.
- **Asphalt pavements do not leach**

  - Studies show that asphalt pavements and stockpiles of reclaimed asphalt pavement do not leach.

Source: http://pavegreen.com

Asphalt Pavement: Clean Air and Cool Cities

- Emissions from asphalt plants, including greenhouse gases, are very low and well-controlled.
- Cool Cities
  - Porous asphalt pavements have been shown to lower nighttime surface temperatures as compared to impervious pavements.
  - It can retain, radiate, and/or release heat.
- Traffic relief
  - Asphalt's speed of construction allows planners and managers a way to fix congestion hot spots and bottlenecks, quickly and cost-effectively → consume less fuel and produce less greenhouse gases.

Source: http://pavegreen.com

Concrete Pavement

- Environmental Impact of Concrete
  - The world's yearly cement production of 1.6 billion ton's accounts for about 7% of the global loading of carbon dioxide into the atmosphere. (Metha, P.K., 1999)
  - "Producing a ton of Portland cement requires about 4GJ energy and Portland cement clinker manufactures releases approximately 1 ton of carbon dioxide into atmosphere (Metha, P.K., 2001)

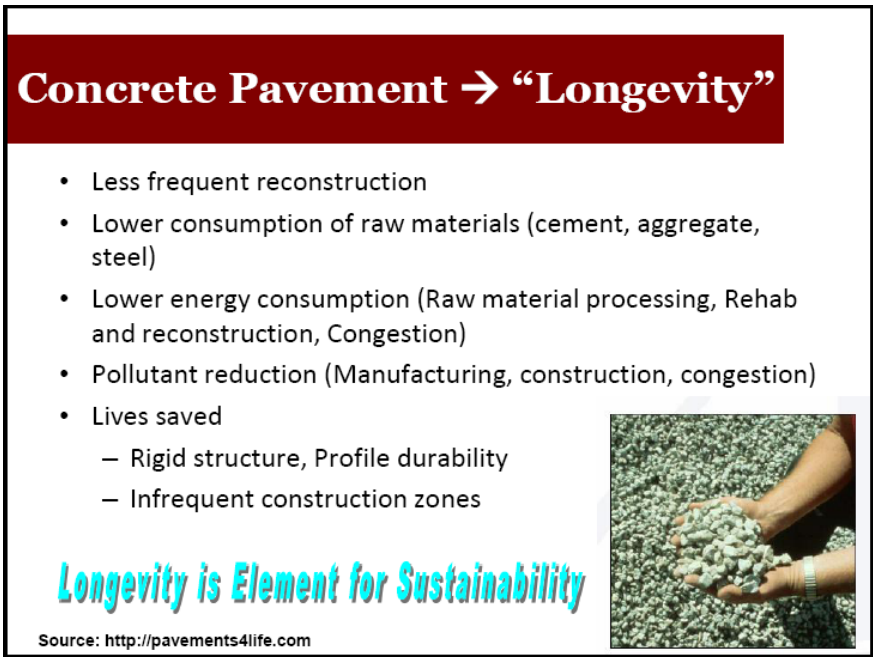
Concrete Pavement → "Longevity"
• Less frequent reconstruction
• Lower consumption of raw materials (cement, aggregate, steel)
• Lower energy consumption (Raw material processing, Rehab and reconstruction, Congestion)
• Pollutant reduction (Manufacturing, construction, congestion)
• Lives saved
– Rigid structure, Profile durability
– Infrequent construction zones
Longevity is Element for Sustainability
Source: http://pavements4life.com

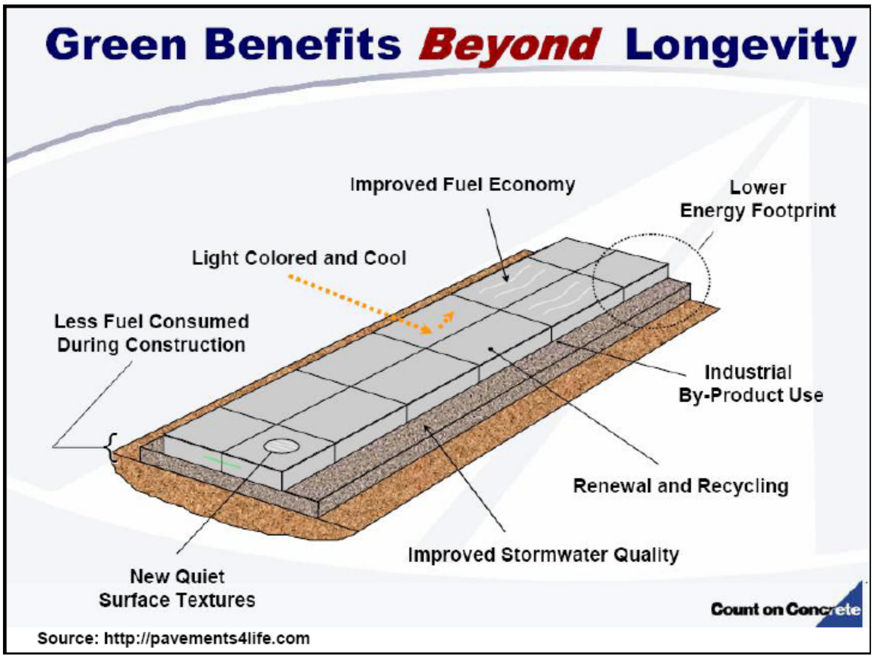
Green Benefits Beyond Longevity
Improved Fuel Economy
Lower Energy Footprint
Light Colored and Cool
Less Fuel Consumed During Construction
Industrial By-Product Use
Renewal and Recycling
Improved Stormwater Quality
New Quiet Surface Textures
Count on Concrete
Source: http://pavements4life.com

Concrete Pavement: Improved Fuel Economy

- Rigid surface → less deflection →low rolling resistance → reduce fuel consumption
- Significant fuel consumption reductions for trucks on concrete pavement (0.8-6.9%)
- Hugh environment and cost saving..

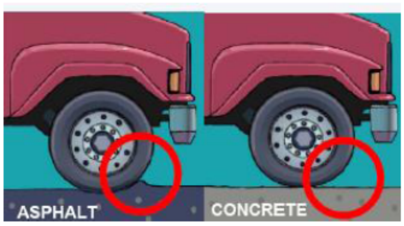

Source: http://pavements4life.com

Concrete Pavement: Fuel Savings and Emission Reduction

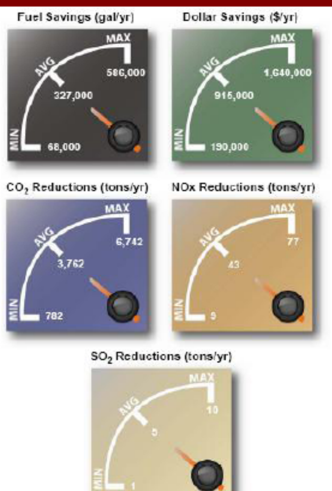

Economical Impact

Environmental Impact

Based on traffic volume of 82,000 vehicles per day with 12% trucks, truck fuel mileage of 5.5 miles/gallon, and a local fuel price of $2.80/gallon

Source: http://pavements4life.com

Concrete Pavement: Low Fuel Consumption during Construction

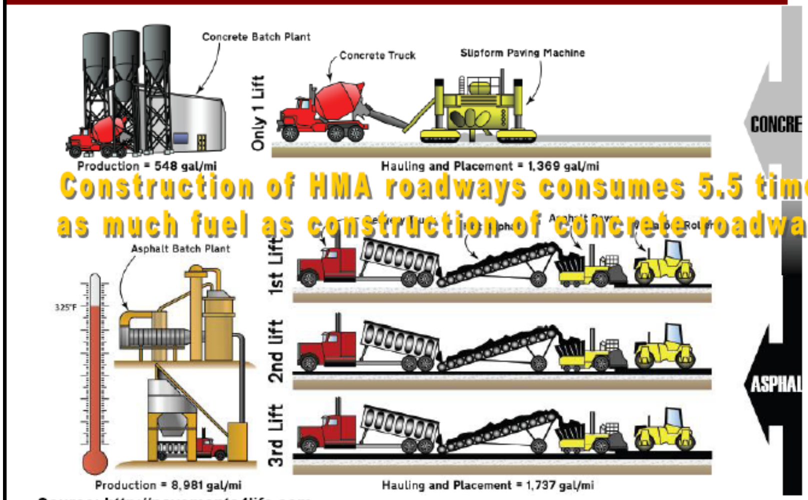

Source: http://pavements4life.com

Concrete Pavement: Use of Industrial By-Products

- Concrete is a huge consumer of industrial by-products.
- Reduces disposal, lowers cement intensity (with its CO2) and improves both performance and longevity
- Fly ash, Slag aggregate, Kiln dusts

Source: http://pavements4life.com

Concrete Pavement: Recycling and Reuse

- Concrete 100% recyclable-in new concrete, subbases and granular fill (even on site operations)

Source: http://pavements4life.com

Concrete Pavement: Light Colored and Cool

- Enhanced nighttime visibility:
  - Improved pedestrian and vehicle safety
  - Reduced lighting and energy requirement
- Urban Heat Island Mitigation:
  - -Urban areas up to 9ºF warmer due to UHI
  - -Lower city temperatures
  - -Lower cooling costs
  - -Reduce smog formation

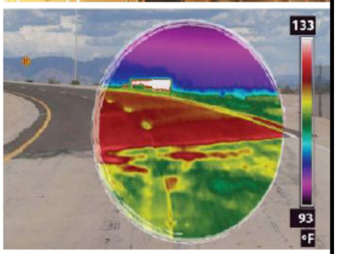

Source: http://pavements4life.com

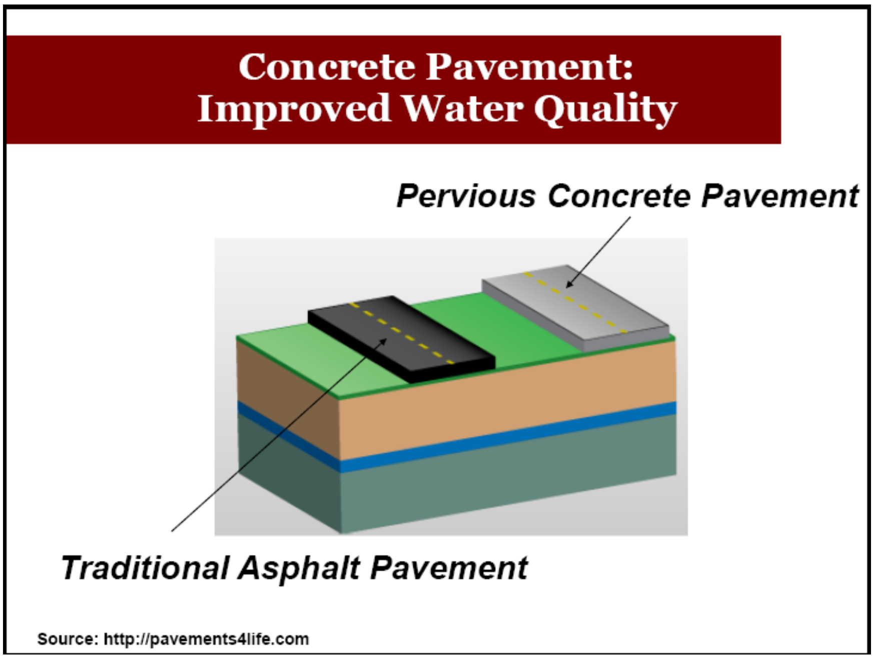
Concrete Pavement:
Improved Water Quality
Pervious Concrete Pavement
Traditional Asphalt Pavement
Source: http://pavements4life.com

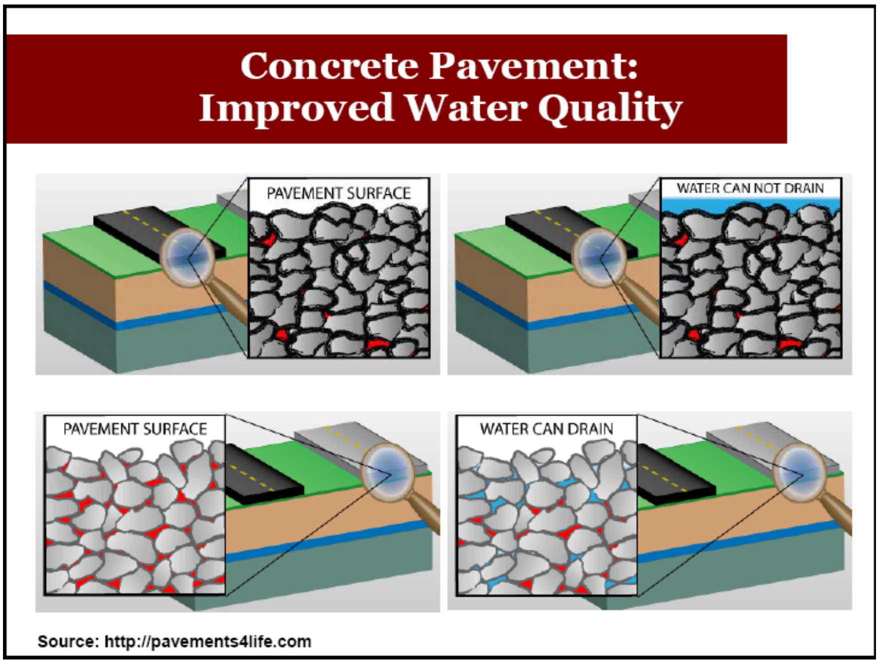
Concrete Pavement:
Improved Water Quality
PAVEMENT SURFACE
WATER CAN NOT DRAIN
PAVEMENT SURFACE
WATER CAN DRAIN
Source: http://pavements4life.com

Concrete Pavement: Improved Water Quality

After raining, where does water goes?

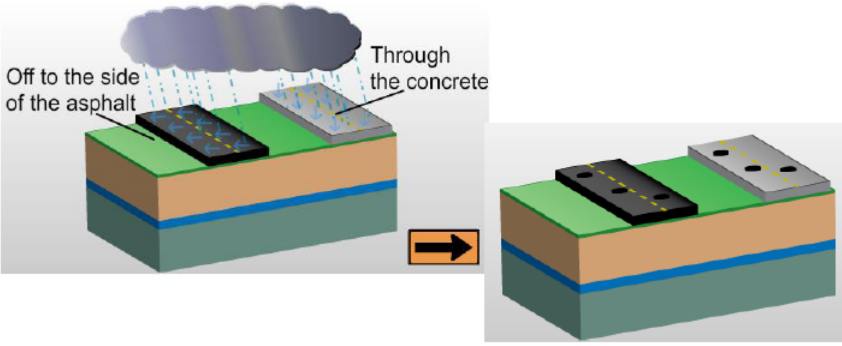

After sometime, vehicle oil will retain on surface

Source: http://pavements4life.com

Concrete Pavement: Improved Water Quality

After raining, where will oil go?

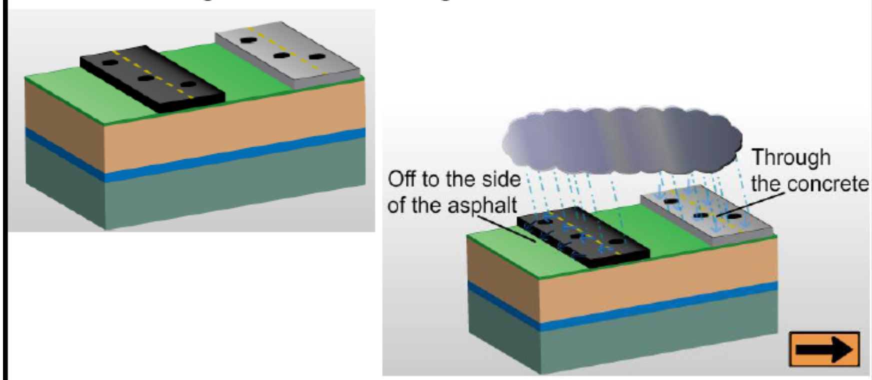

Source: http://pavements4life.com

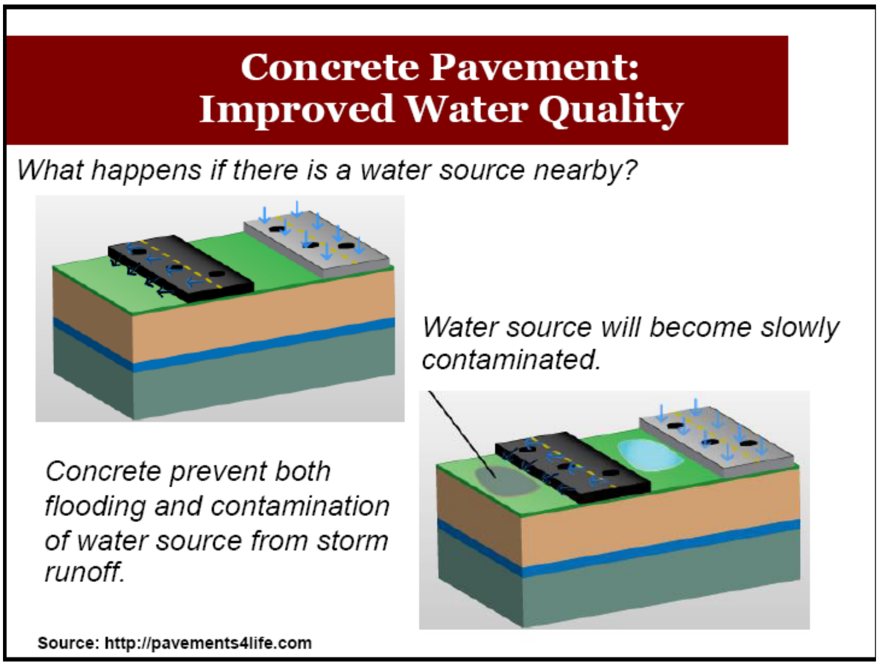
Concrete Pavement:
Improved Water Quality
What happens if there is a water source nearby?
Water source will become slowly contaminated.
Concrete prevent both flooding and contamination of water source from storm runoff.
Source: http://pavements4life.com

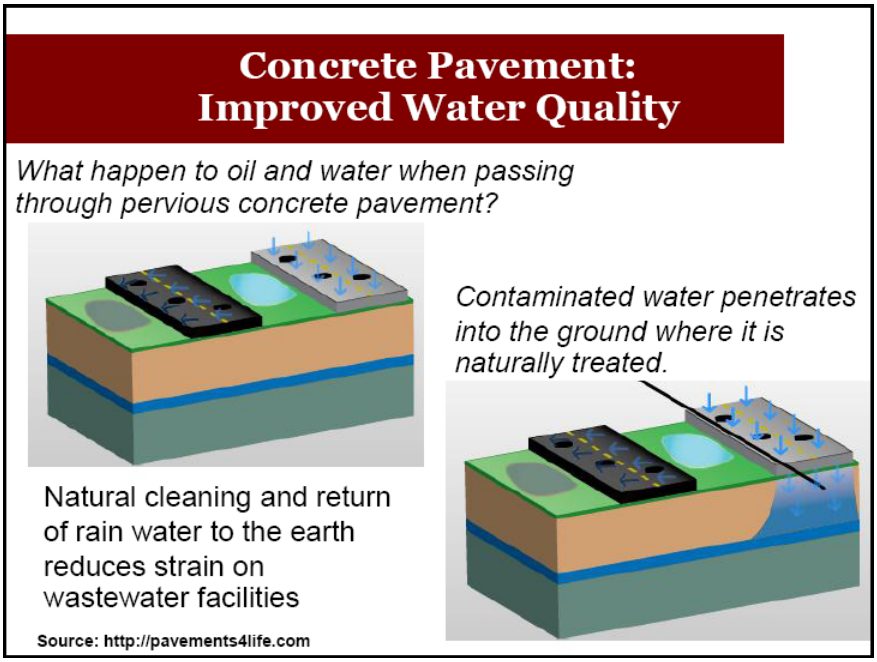
Concrete Pavement:
Improved Water Quality
What happen to oil and water when passing through pervious concrete pavement?
Contaminated water penetrates into the ground where it is naturally treated.
Natural cleaning and return of rain water to the earth reduces strain on wastewater facilities
Source: http://pavements4life.com

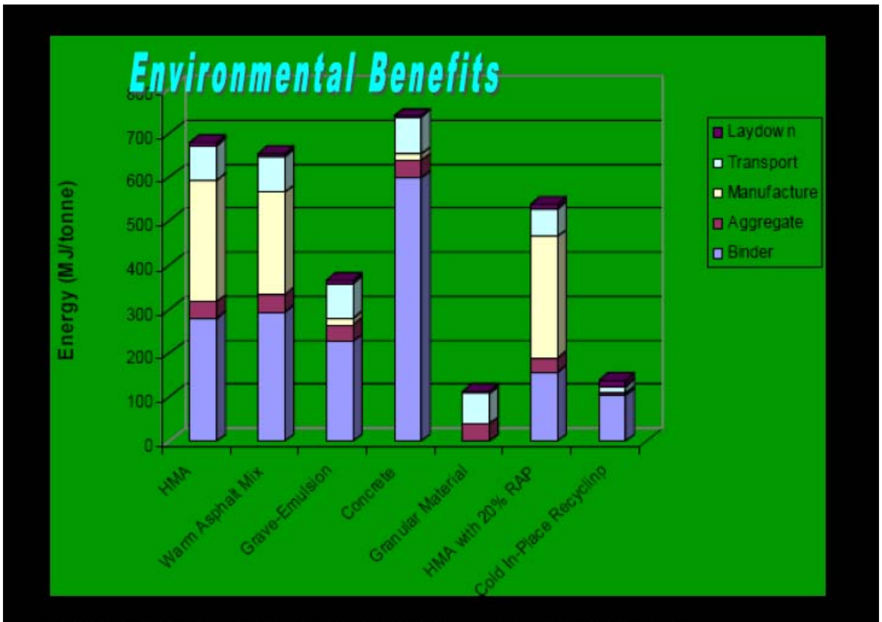

Source: *Road Rehabilitation Energy Reduction Guide for Canadian Road Builders, Natural Resources Canada, 2005, p. 16*

Treatment	Energy Consumption (MJ/t)	Energy Consumption (MJ/m²)	Percentage Decrease from HMA (%)
Hot Mix Asphalt	680	82	-
Warm Mix Asphalt	654	78	5
Recycled Asphalt Shingle Hot Mix	535	64	12
In-Place Recycling	139	31	62
Micro Surfacing	496	9	89
High Performance Chip Seal	667	12	85

Source: *Road Rehabilitation Energy Reduction Guide for Canadian Road Builders, Natural Resources Canada, 2005, p. 16*

Summary

- Asphalt and Concrete pavement can be both environmentally sensitive and economically sustainable roadways.
- Many technologies have been used to produce sustainable products
  - Save Energy
  - Reduce Emission
  - Urban Heat Island Mitigation
  - Recyclable and Reuse
  - Noise Reduction
  - Improve Safety

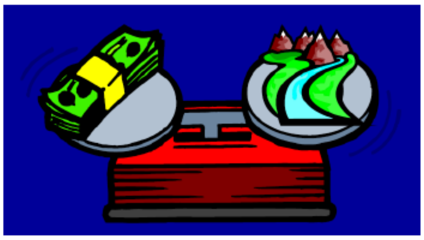

THANK YOU

Student Presentations

3D NUMERICAL SIMULATION OF STACKED TWIN-TUNNEL

Viet-Dung Tran[1]
[1] School of Engineering & Technology, Asian Institute of Technology,
P.O. Box 4, Klong Luang, Pathumthani 12120, Thailand
vietdungtran0324@gmail.com

ABSTRACT

In tunneling construction, one of the most important issues is the prediction of the tunneling-induced ground movement. In this paper, a 3D simplified numerical simulation is conducted with two key parameters: the partial released stress ratio α_{dec} and the length of the unlined zone L_{dec}. The effects of model parameter α_{dec} are investigated. The tunneling-induced ground movement from simulated result are analyzed in longitudinal and transverse directions and compared with the measured data obtained from the settlement makers of Bangkok Blue Line subway project. The results of the numerical simulation may be used for the prediction of tunneling-induced ground movements in the planned South Blue Line Extension subway project.

***Keywords**: tunneling-induced ground movements, numerical simulation, stacked twin-tunnel, Bangkok subway tunnel*

1. INTRODUCTION

The first phrase of Bangkok Blue Line Subway project has been completed and opened to public in 2004. Due to the thick soft clay layer, Earth Pressure Balance Shield (EPB) was used to maintain control of the excavation face in order to prevent the settlement. The tunneling-induced ground movement can be reduced by applying the balance horizontal pressure compare with Earth pressure. However, control settlement does not stop as the face. In most case, the secondary settlement (after the shield has passed) is more significantly than the settlement experienced as the machine mines past a point. This secondary settlement depends on different aspects, such as the over-cut of the shield, the lining properties, the effective of the grouting, the time delay to install the support system. Tunneling-induced ground movement in soft clay is the most important issue to underground construction in urban area. The surface and subsurface ground movements are significant caused damage to the foundations of existing structures. To ensure the safety of the underground constructions and adjacent building when excavated the tunnel, prediction of the extension and the magnitude of tunneling-induced ground movement need to be made.

Numbers of researches have been done to analyze the tunneling-induced ground movement. Generally, these researches can be divided into

3 methods: empirical, analytical and numerical methods. Empirical method assumes the distribution of ground movement with some coefficients. These coefficients are determined through fitting field or centrifuge observations (Peck 1969, O'Reilly & New 1982). Meanwhile, analytical method focuses on the boundary conditions around the opening during the tunnel construction process. The surface and lateral ground movement can be defined base on the assumption of uniform radial displacement (Sagaseta 1987, Verruijt & Booker 1996) or oval-shaped radial displacement (Loganathan & Poulos 1998, Park 2004, 2005) pattern around the tunnel.

To overcome the limitations of empirical and analytical method, in recent years, numerical simulation becomes much more common to consider the excavation in urban area (Leca 1996, Dasari et al. 1996, Stallebrass et al. 1996, Cheng et al. 2008). However, numerical modeling often deals with a lot of complex aspects, for example non-linear behavior of soil, magnitude of face pressure, installation of defining support, soil-structure interaction (soil-tunnel, soil-pile). In order to simplify these aspects, the combination with the gap due to over-cut of the shield machine lead to the assumption of stress reduction factor. Various authors have suggested various values of stress reduction factor. Panet (1973) suggested a 33% for the stress reduction factor. Meanwhile, Muir Wood (1975) recommended 50% for this value according to his closed-form solution. Negro (1988) found the stress reduction factor by combining the radial displacements and a full range of diagrams in a variety of geometric and geotechnical. Kim et al. (2006) introduced a reliable method to determine the value of stress reduction factor for different soil strengths, tunnel depth and in-situ stress ratios. Panet & Guenot (1982) used the stress release factor λ to simulate for the 3D problem. The method consists of excavation of the core elements and application of a gradual release of boundary stresses to simulate the tunnel advance. The in-situ stresses along the excavated boundary are gradually reduced to a certain percentage of the original stresses to simulate the installation of a linning at a certain distance from the face. Mrouh & Sharouh (2008) introduced a 3D simplified model technique to simulate the excavation of a single tunnel. The model bases on convergence-confinement concept, in which the out-balance forces caused by tunnel excavation are released partially at different construction stages.

This study considers the tunneling-induced ground movement of vertical stacked twin-tunnel. The 3D numerical simulation is conducted using 2 keys parameter: partial released stress ratio α_{dec} and the length of the unlined zone L_{dec}. The case history is chosen from the first phase of Bangkok Blue Line Subway project (Zone 4T from Lumphini to Bon Kai). The surface settlements are analyzed in terms of surface settlement at tunnel face (w_a), in the unlined zone (w_b) and due to complete released stress (w_c). The simulated result is compared with the measured data.

2. BANGKOK BLUE LINE SUBWAY PROJECT

The first phase of the Bangkok Blue Line Subway project has 20 kilometers of twin-tunnel which is subdivided into 2 main tunnel sections, namely, the North Tunnel Section and the South Tunnel Section (Figure 1). The tunneling construction was done mostly in soft ground, using EPB shield. Each of twin tunnels is 6.3 m in outer diameter and 5.7 m in inner diameters. In some areas, the twin-tunnel were stacked over each other in order to avoid pile foundations of existing fly-over bridges along the route. The lower tunnel (Southbound) was excavated first and then the upper tunnel (Northbound) was excavated. The Northbound was located in the stiff clay layer, but in some sections where the tunnel was very shallow, the tunnel crown was located within the soft clay layer. The Southbound mostly was excavated within the sand layer.

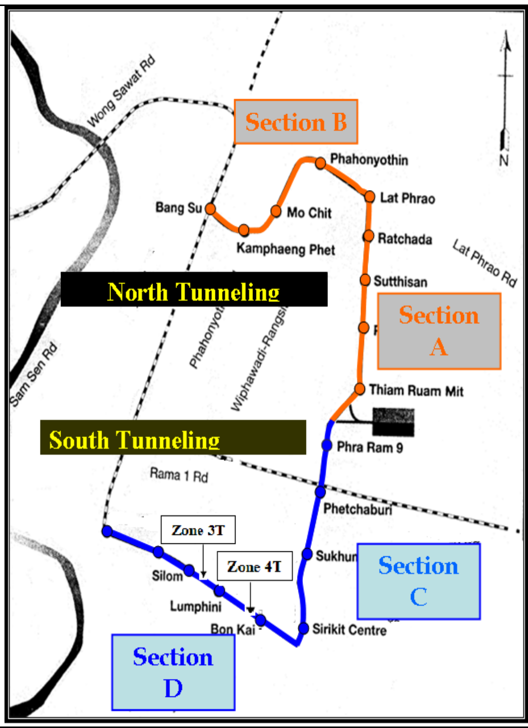

Figure 1: MRT Bangkok Blue Line

During the underground construction, the surface settlement makers were used to measure the maximum surface settlement at the centerline during excavation. These makers were installed approximately 50 m interval along the tunnel alignment. Moreover, in some chosen location, a line of surface settlement makers were installed to monitor the ground settlement in transverse direction. The reading was taken overtime covering a period before the shield approaching and after the shield passing.

3. NUMERICAL SIMULATION

3.1 Modeling mesh

The analysis described in this paper was performed using finite different element program FLAC^{3D}. Figure 2 shows the typical modeling mesh adopted from the program. The tunnel axis is along the Y-axis, which is called the longitudinal direction, X-direction is the transverse direction and Z-direction is the depth direction. The geometry model for numerical simulation is designed with the length of 100 m long in the longitudinal direction, 80 m wide in the transverse direction and 40 m depth in the vertical direction.

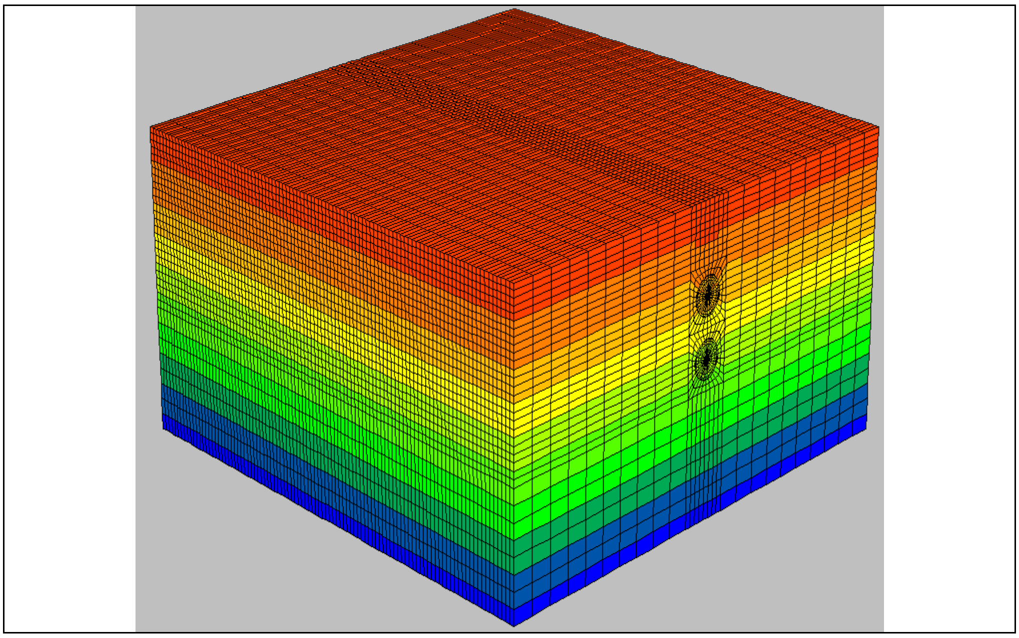

Figure 2: 3D modeling meshes

The left and right boundaries are hinged to prevent the movement in the horizontal direction, but are free to allow the movement in the vertical direction. The width of left through right boundaries is widely set to avoid the boundary effect to the perimeter of the tunnel. The bottom boundary is set in to the stiffest soil material and is fixed against vertical movements.

3.2 Material models and parameters

The constitute law used for the soil elements is elasto-plastic associated Mohr-Coulomb model. Figure 3 shows the typical soil profile and value of soil properties simulating in FLAC^{3D}. The values of soil properties are considered based on the soil test results of South Contract in Bangkok Blue Line Subway project. Bulk modulus (K) and shear modulus (G) are related to Young modulus (E) and Poisson's ratio (ν), by following equations:

$$K = \frac{E}{3(1-2\nu)}$$

(1)

$$G = \frac{E}{2(1+\nu)}$$

(2)

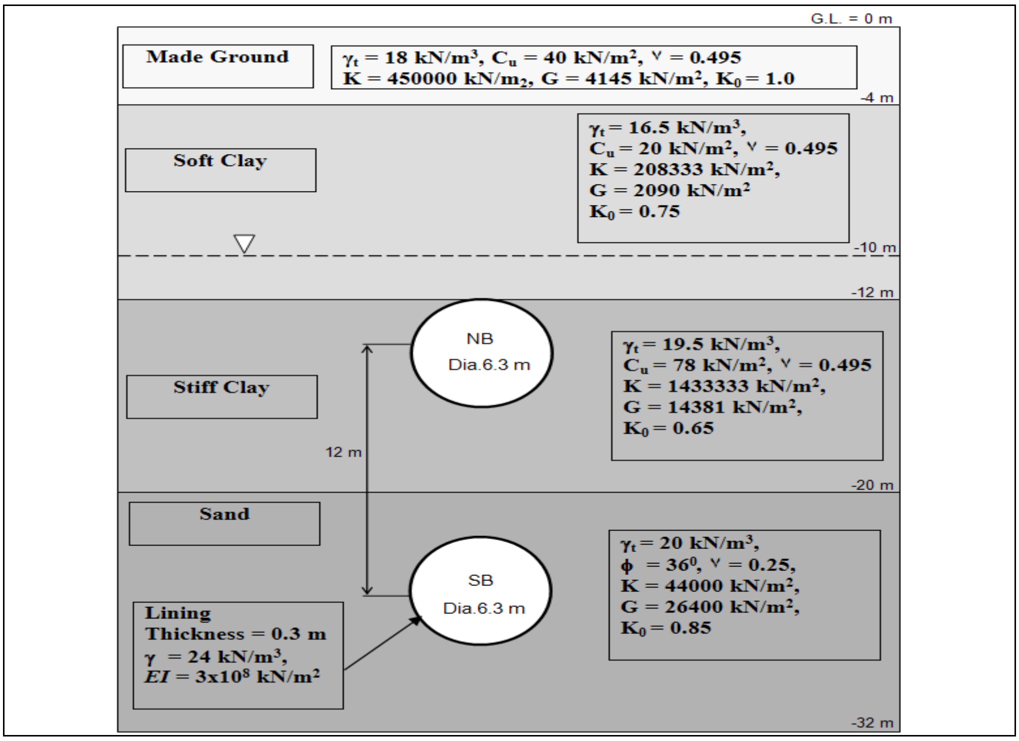

Figure 3: Soil properties

The water table located at 10 m depth below the ground surface. The lining and grouting were modeled by using shell element. The lining had 0.3 m of thickness. The properties of the lining are also shown as in Figure 3.

3.3 Tunnel advancement simulation procedure

The simulation procedure, based on force controlled approach, is considered in this study using two main parameters: the partial stress release α_{dec} and the length of unlined zone L_{dec}. The value of α_{dec} is varied to investigate the effects of this parameter on the tunnel-induced ground movement. While the value of L_{dec} is equal to the shield diameter (1D = 6 m). The step by step procedure in the simulation of excavation and shield advance can be summarized:

In the first step of excavation, (a) remove the ring of soil element equal to 7 m ahead of the shield (6 m for the length of the shield and the length of unlined zone (L_{dec}) and 1 m for the supported zone (L_{lin}) where the lining will be installed), (b) release stress around the tunnel, (c) install lining 1 m at the end of the excavated, (d) grout the removed area and measure the displacement at the tunnel boundary and at the surface, (e) back fill material and apply face pressure to prepare for the next excavation.

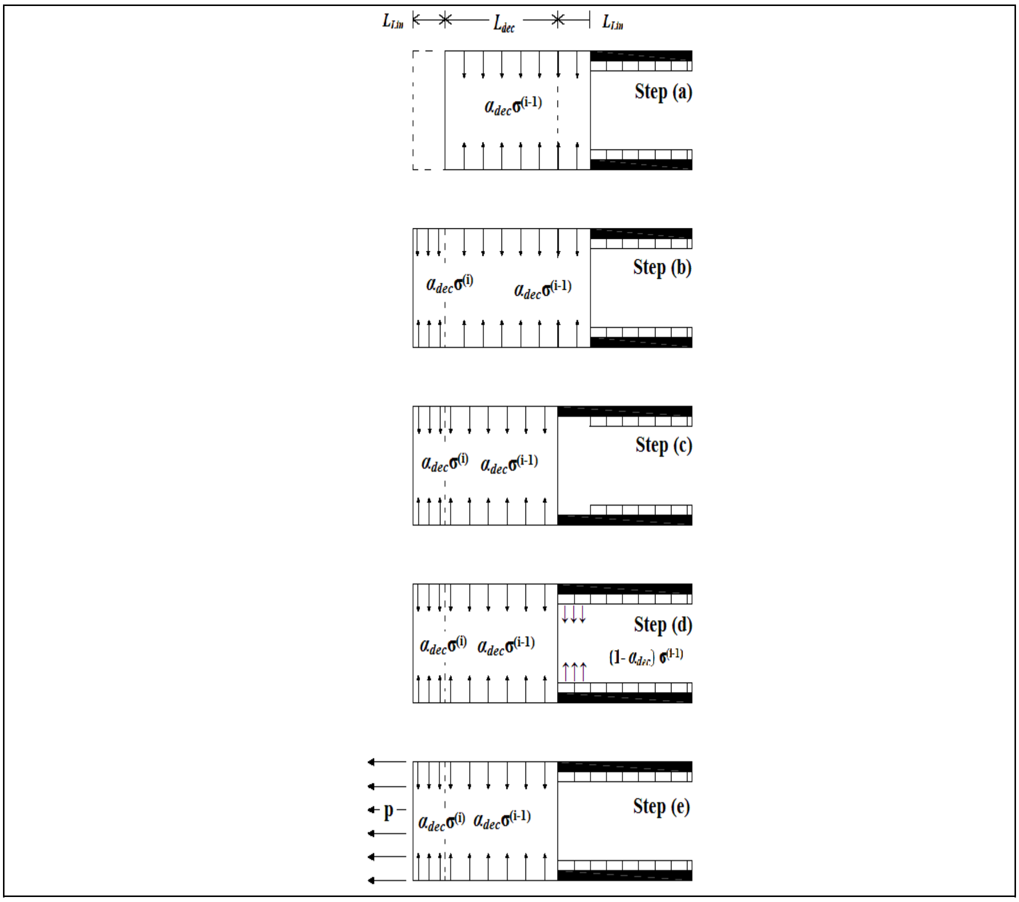

Figure.4: Step for tunnel advance

Figure 4 shows the steps for tunnel advance: (a) remove the ring of soil element ahead of the tunnel face, (b) release the stress using α_{dec}, (c) activate the lining element in removed area with the length of L_{lin}, (d) grout the removed area, release completed stress and take the measurement of ground movement, (e) apply the pressure at the tunnel face. Then repeat from (a) to (e).

3.4 Simulation results

Figure 5 shows the numerical results of surface settlement for a single and twin tunnel (SB&NB), using α_{dec} = 0.2, 0.4 and 0.6, together with the measured one. L_{dec} = 6 m is used. In single tunnel, the surface settlement start to occur -24 m (= -6D) before the shield reaching and continue to 42 m (= 7D) after the shield. The value of surface settlement at tunnel face (w_a), in the unlined zone (w_b) and due to complete released stress (w_c) is considered and compared with the maximum surface settlement (w_{max}). From the ratio of (w_a/w_{max}), (w_b/w_{max}) and (w_c/w_{max}), it can be seen that the surface settlement mostly occurred at the tunnel face (35 ~ 39 % of maximum surface settlement) and in the complete released stress zone (39 ~ 42 %). In stacked twin-tunnel, the surface settlement already occurred before the Northbound excavated. The value of this addition surface settlement is equal to the maximum surface settlement occurred when the excavation of the Southbound tunnel is finished. This is also the main reason that the surface settlement in the Northbound mostly occurred at the tunnel face. The ratio of (w_a/w_{max}) shows that 73 ~ 90% of maximum surface settlement occurred before the shield reaching and at the tunnel face.

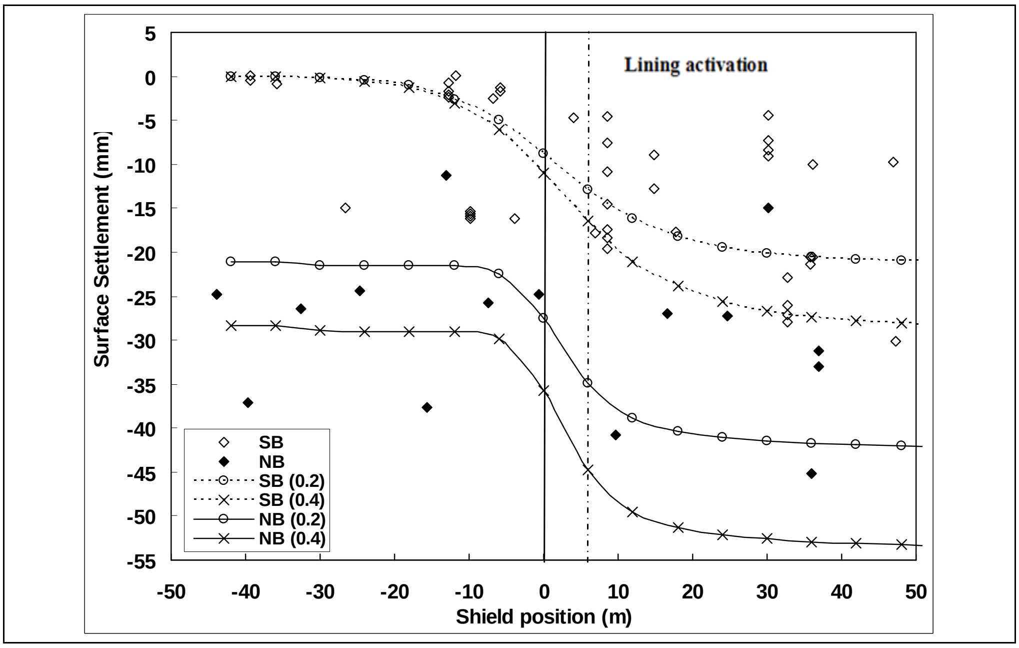

Figure 5: Simulated results in longitudinal direction (SB&NB)

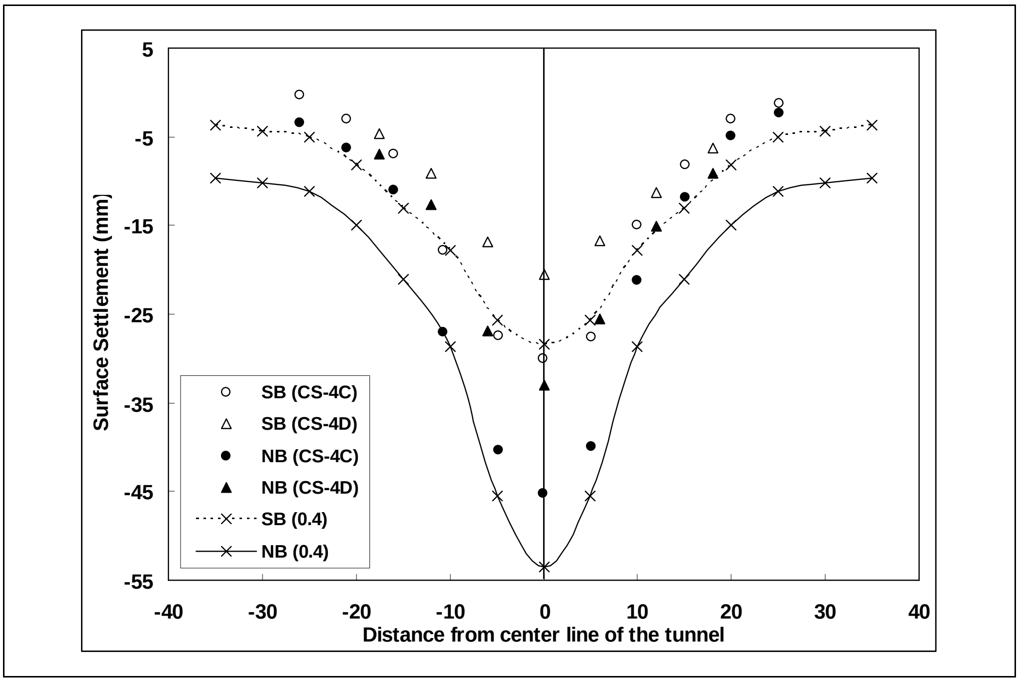

Figure 6: Simulated results in transverse direction (SB&NB)

Table 1: Comparison for parameters of Peck formula

	i/D	V_s/V_{exc} (%)
SB	1.63 ~ 1.72	1.66 ~ 2.35
NB	1.27 ~ 1.49	2.59 ~ 3.86
Mroueh &Shahrour (2008)	1.17	0.26
Attewell (1977)	1.25	1 ~ 5
O'Reilly & New (1982)	0.68 ~ 1.22	0.5 ~ 3
Oteo & Sagaseta (1982)	0.77 ~ 1.43	

The comparison of the surface settlement in transverse direction between the simulated results and the measured data is shown in Figure 6. As same as the measured data, the settlement trough is narrow and symmetric. The maximum surface settlement occurred in the center line of the tunnel's alignment. The values of the parameters of Peck formula (Peck, 1969) are compared with the values suggested in previous researches, as shown in Table 1.

4. CONCLUSION

Numerical simulation of vertically stacked twin-tunnel in the Blue Line Subway project has been performed. The simulated results are compared with the measured data obtain from the settlement maker of Zone 4T in Bangkok Blue Line Subway project. Similar with the measured data, the simulated surface settlement in longitudinal mainly occurred before the shield reaching and after the shield passing. The settlement trough is narrow and symmetric. The simulated results show that the model parameter α_{dec} highly affects the maximum surface settlement. As α_{dec} increases, the maximum surface settlement increases. The measured surface settlements can be ranged within α_{dec} = 0.2 ~ 0.6. The results of the numerical simulation may be used for the prediction of tunnelling-induced ground movements in the planned South Blue Line Extension subway project.

REFERENCES

Attwell, P.B. (1977). *Ground movements caused by tunneling in soil*. 1st Conference on Large Ground Movements and Structures, Pentech Press, London, pp 812-948.

Cheng, C.Y., Dasari, G.R., Chow, Y.K., Lueng, C.F. (2008). *Finite element analysis of tunnel-soil-pile interaction using displacement controlled model*. Tunnelling and Underground Space Technology, 22, 450-466.

Dasari, G.R. (1996). *Modelling the variation of soil stiffness during sequential construction*. PhD dissertation, University of Cambridge.

Kim, H.J., Eisenstein, Z., Chae, B.G., Jeong, C.H. (2006). *Estimates of stress reduction factors for the tunnel design*. Tunneling Underground Space Technology, Vol 21, pp 1-6.

Leca, E. (1996). *Modelling and prediction for bored tunnels*. Proceedings of International Symposium on Geotechnical Aspects of Underground Construction in Soft Ground, Balkema, London, pp 27–42.

Longanathan, N., Poulos, H.G. (1998). *Analytical prediction for tunnelling induced ground movement in clay*. Journal of Geotechnical and Geoenvironmental Engineering, Vol. 124 No. 9, pp 846-856.

Mroueh, H., Shahrour, I. (2008). *A simplified 3D model for tunnel construction using tunnel boring machines*. Tunnelling and Underground Space Technology, Vol. 23, pp 38-45.

Muir Wood, A.M. (1975). *The circular tunnel in elastic ground*. Geotechnique, Vol.25 No.1, pp 115-125.

Negro, A.Jr. (1988). *Design of shallow tunnels in soft ground*. Ph.D. Thesis, Department of civil engineering, University of Alberta.

O'Reilly, M.P., New, B.M. (1982). *Settlements above tunnels in the United Kingdom – their magnitude and prediction*. Proceedings of the International Conference Tunnelling '82, Institution of Mining and Metallurgy, London, pp 55-64.

Oteo, C.S., Sagaseta, C. (1982). *Prediction of settlements due to underground openings*. International Symposium on Numerical Methods in Geomechanics, Zurich, 13-17 September, pp 654-659.

Panet, H. (1973). *La stabilite des ouvrages souterrauns-soutenement et revetement*. Rapport de recgercge, 28, Paris: Laboratoires des Ponts et Chaussees.

Panet, M., Guenot, A. (1982). *Analysis of convergence behind the face of a tunnel*. Tunneling 82. The Institution of Mining and Metallurgy, pp 197-204.

Park, K.H. (2005). *Analytical solution for tunnelling-induced ground movement in clays*. Tunnelling and Underground Space Technology, Vol. 20 No. 3, pp 249-261.

Park, K.H., (2004). *Elastic solution for tunnelling-induced ground movement in clays*. International Journal of Geomechanics ASCE, Vol. 4 No. 4, pp 310-318.

Peck, R.B. (1969). *Deep excavations and tunnelling in soft ground*. Proceedings of 7th International Conference on Soil Mechanics and Foundation Engineering, Mexico City, State-of-the-Art volume, pp 225-290.

Sagaseta, C. (1987). *Analytical of undrained soil deformations due to ground loss*. Geotechnique, Vol. 37 No. 3, pp 301-320.

Stallebrass, S.E., Grant, R.J., Taylor, R.N. (1996). *A finite element study of ground movements measured in centrifuge model tests of tunnels*. Proceedings of International Symposium on Geotechnical Aspects of Underground Construction in Soft Ground, Balkema, London, pp 595-600.

Verruijt, A., Booker, J.R. (1996). *Surface settlements due to deformation of a tunnel in an elastic half plane*. Geotechnique, Vol. 46 No.4, pp 753-756.

A FRAMEWORK OF OPTIMAL SENSOR PLACEMENT IN HIGHWAY TRAFFIC OPERATIONS

Tian Jiang[1], Marc Miska[2], Kuwahara Masao[3], Shinji Tanaka[4] and Takashi Oguchi[5]
[1] PhD student, School of Eng., The University of Tokyo, Japan
xiaodark@iis.u-tokyo.ac.jp
[2] Research Associate (Program Director), Smart Transport Research Centre, Queensland University of Technology, Australia
[3] Professor, Graduate School of Information Sciences, Tohoku University, Japan
[4] Lecturer, ICUS, IIS, The University of Tokyo, Japan
[5] Professor, IIS, The University of Tokyo, Japan

ABSTRACT

While research focuses on using available traffic data sources to improve traffic models and operation systems, less work is devoted answering the question of how and where to collect traffic data, so that control systems can perform in an optimal, and cost-efficient manner. In this paper, we present a framework to assess traffic detection systems, by introducing the level of detection as value to allow for an objective comparison of multiple detector placement scenarios. In contrast to existing studies, proposing new or alternative detector locations based on errors of travel time or traffic state estimators, our approach is solely based on network parameters, detection technology, and traffic demand, which allows the usage of the framework for network operations, as well as planning purposes. By translating traffic operation goals into data demand functions, and detector capabilities, combined with their location, into data supply functions, it is possible to optimize detector locations with well know tools from operations research. The latter one is important, since it allows for including additional boundary conditions, such as costs.

Keywords*: detection, optimization, highway*

1. INTRODUCTION

To ensure the mobility of our cities, dynamic traffic management became essential to operate existing road networks in the most efficient way. Models estimate traffic conditions, predict traffic states in the short and long-term, and provide traveler information to keep the traffic flow as fluid as possible. Those models are fed with real-time traffic data, collected from the roadside or transmitted from probe vehicles in the network, and their performance depends strongly on where the data were collected, and of which quality the traffic data are.

Given the importance of the traffic data collection, the detector placement problem is a relatively less explored research topic in transportation. Relevant research includes the work done in transportation planning for obtaining accurate origin-destination trip matrices (Yang et al, 1998) and several simulation-based studies identifying the relationship between detector location and travel characteristics on arterial roads (Sisiopiku et al, 1994; Thomas, 1999; Oh et al, 2003). One real-world traffic data study on the detector placement problem for freeways (Edara et al, 2008), found that accurate travel time estimates varied by location and traffic conditions, and that evenly spaced detectors did not necessarily provided better results.

Common in those studies is that they result in case specific, non-transferable optimizations. The real-world study developed a method, including GPS data collection and mathematical tools, to effectively determine preferable detector locations for the objective to minimize the travel time estimate error. However, no hint was given what effect the new detector locations would have on incident detection, or how they could serve for additional purposes such as feeding ramp metering algorithms. The underlying problem is that these studies optimize the input for a specific algorithm, instead of actually identifying the information gained from the traffic detection.

In contrast to those existing studies, our approach aims to identify that knowledge and to optimize it for various combinations of algorithms. Further, the framework is solely based on network parameters, detection technology, and traffic demand, which allow the usage of the framework for network operations, as well as planning purposes. To achieve this, we translate traffic operation goals into data demand functions, and detector locations and capabilities into data supply functions. Then it is possible to optimize detector locations with well-known tools from operations research. This becomes important when considering additional boundary conditions, such as costs, which for a highway detection scheme is often the limiting factor.

2. DATA SUPPLY FUNCTION

In a first step, we have translated detector capabilities and positions into data supply functions. For this, we looked at a possible speed profile of a link with an active bottleneck as shown in Figure 1.

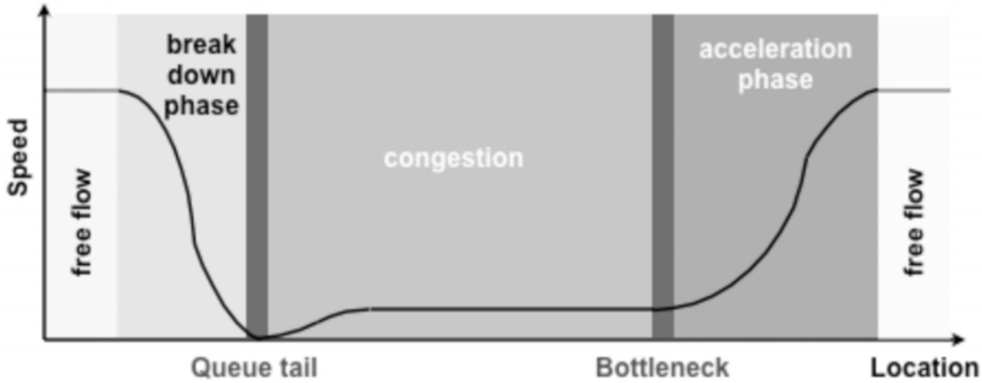

Figure 1: Speed profile with categorization of traffic state on a link with active bottleneck

In free-flow condition, a detector placed anywhere on the link, will give a good indication of the average speed on the link. The same can be said for a completely congested link. When however, the link is only partly congested, the knowledge gained from just one detector is limited. Placed in the free-flow or congested zone, the validity of the measurement is restricted to the homogeneous zone, and if placed in either the breakdown or acceleration zone, the information gathered is valid only on the spot. Based on these assumptions, we can develop a data supply function that indicates the gained knowledge based on the traffic state and the detector position as follows:

$$\varphi_{i,v} = \begin{cases} \varphi_{n-1,v}, \quad s_{n-1,0} < x < s_{n-1,1} \\ \dfrac{\varphi_{n-1,v} - 1}{s_{n-1,1} - s_{n,0}} x + \dfrac{s_{n-1,1} - s_{n,0}\varphi_{n-1,v}}{s_{n-1,1} - s_{n,0}}, \quad s_{n-1,1} < x < s_{n,0} \\ 1, \quad s_{n,0} < x < s_{n,1} \\ \dfrac{\varphi_{n+1,v} - 1}{s_{n+1,0} - s_{n,1}} x + \dfrac{s_{n+1,0} - s_{n,1}\varphi_{n+1,v}}{s_{n+1,0} - s_{n,1}}, \quad s_{n,1} < x < s_{n+1,0} \\ \varphi_{n+1,v}, \quad s_{n+1,0} < x < s_{n+1,1} \end{cases} \tag{1}$$

where :

$\varphi_{i,v}$: speed data supply by detector i

$\varphi_{n-1,v}$: speed data supply at neighbor upstream free - flow or congestion area n - 1

$\varphi_{n+1,v}$: speed data supply at neighbor downstream free - flow or congestion area n + 1

$s_{n,0}$: transition point from break down or acceleration phase to free - flow or congestion phase

$s_{n,1}$: transition point from free - flow or congestion phase to break down or acceleration phase

$$\varphi_{n-1,v} = 1 - \frac{|v_n - v_{n-1}|}{v_{n-1}}$$

v_n : speed in free - flow or congestion area n

$$\varphi_{n+1,v} = 1 - \frac{|v_n - v_{n+1}|}{v_{n+1}}$$

We assume that each detector has a “valid range” and the speed collected by the corresponding detector can be used to depict the speed condition in the “valid range”. A valid range consists of five zones: the homogeneous zone where the detector placed, two neighbor homogeneous zones (one is in upstream and the other one is in the downstream), two transition zones (break down or acceleration). The supply function can compute the detection accuracy in valid range and calculate values of accuracy for these five zones. Detection accuracy is assumed to be 100% in the homogeneous area where the corresponding detector is placed. In the two neighbor homogeneous zones, the accuracy is calculated by speed difference between the real speed and detection speed, which means when the detector speed is used to depict the speed in its neighbor areas, the more difference between the real speed and detection speed, the less detection accuracy obtained. Based on the detection accuracy in three homogeneous zones, data accuracy in transition zones could be calculated by linear functions to ensure smooth connection between two homogeneous zones. To illustrate the behavior of the function, Figure 2 shows the knowledge function for speed along the link.

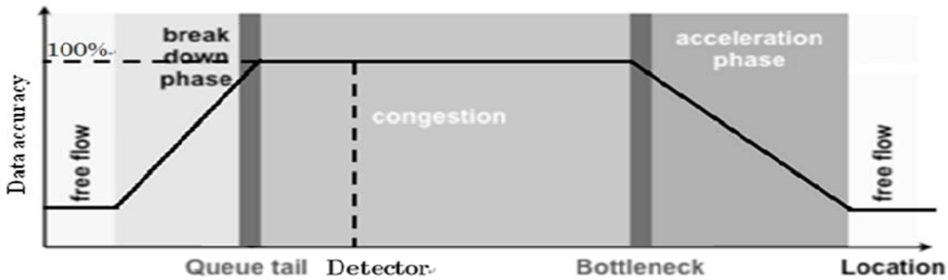

Figure 2: Speed data supply along the link when one detector is placed in congestion area

To test these assumptions, we have modeled MEX C1 Route of the Tokyo Metropolitan Expressway (MEX) in the microscopic simulator VISSIM (see Figure 3).

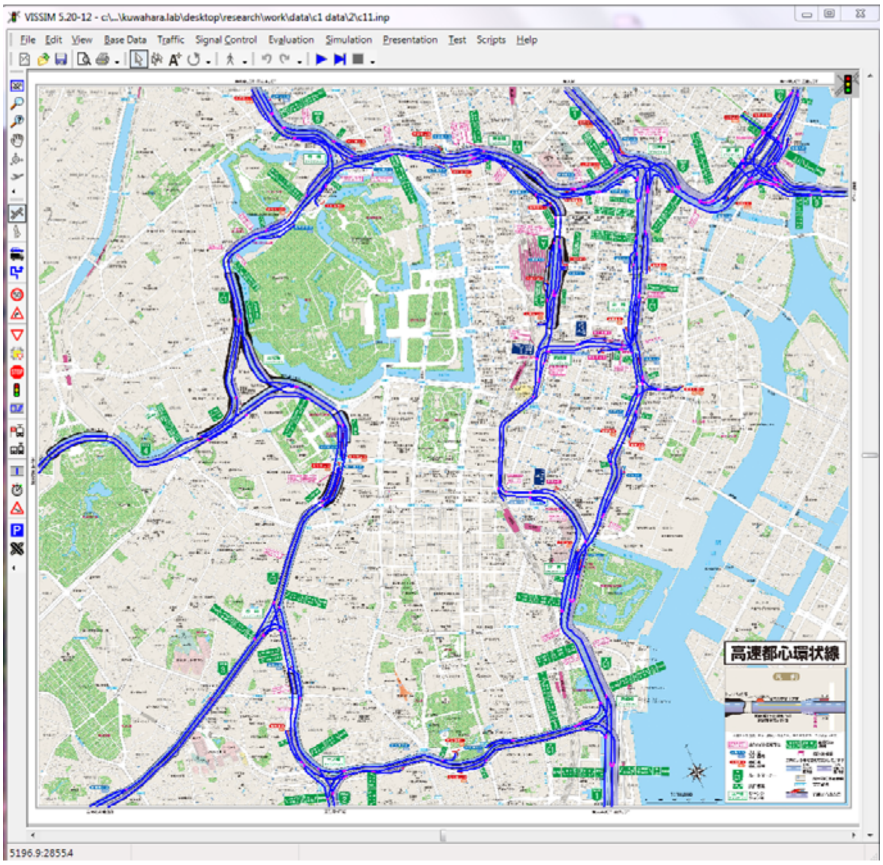

Figure 3: MEX C1 Route network in the Vissim simulation

By Running Dynamic Traffic Assignment (DTA) models in Vissim, we can simulate traffic conditions in MEX. Based on the simulated speed information, dynamic bottleneck activities and queue lengths can be monitored in detail. Most vehicles using MEX have onboard devices for electronic toll collection (ETC). With access to this ETC data, we were able to determine the real origin-destination (OD) matrices for 30-minute time intervals for the network. We selected the morning peak from 6am to 9am as study period.

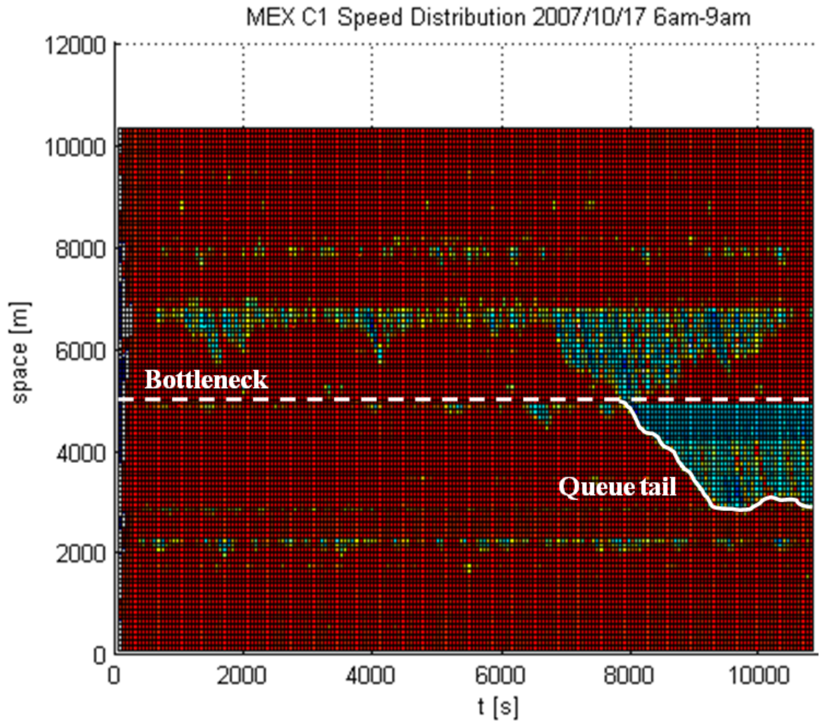

Figure 4: Traffic state of the C1 network in the morning peak

Figure 4 shows the traffic state of a ten-kilometer link with several bottlenecks in a time space diagram.

With this information and our data supply function definition, we were then able to determine the real information gathered by a detector at any given place. Figure 5 shows the example of a detector being placed at 4000 meter. The area around the detector location, and bounded by the white lines, equals the knowledge space over time. At the beginning of the simulation period, since most parts of the link is in free flow condition, the detector can provide accurate speed data up to the end of the link. With the bottleneck active in the downstream, the knowledge area decreases and the detector can only provide the information up to the nearest queue tail. For the last 40 minutes, when the queue is back up to the detector location, the detector starts to collect the speed information in the queue. Since the vehicle speed in the congestion area is fairly constant, the knowledge increases again. To verify the result, we compared the actual traffic measurements on MEX with detectors placed along the link, to check the correlation between the measurements with the expected correlation from the simulated traffic state. The comparison showed, that the prediction of the queue tail, and hence the correlation of the speed measurements was well replicated.

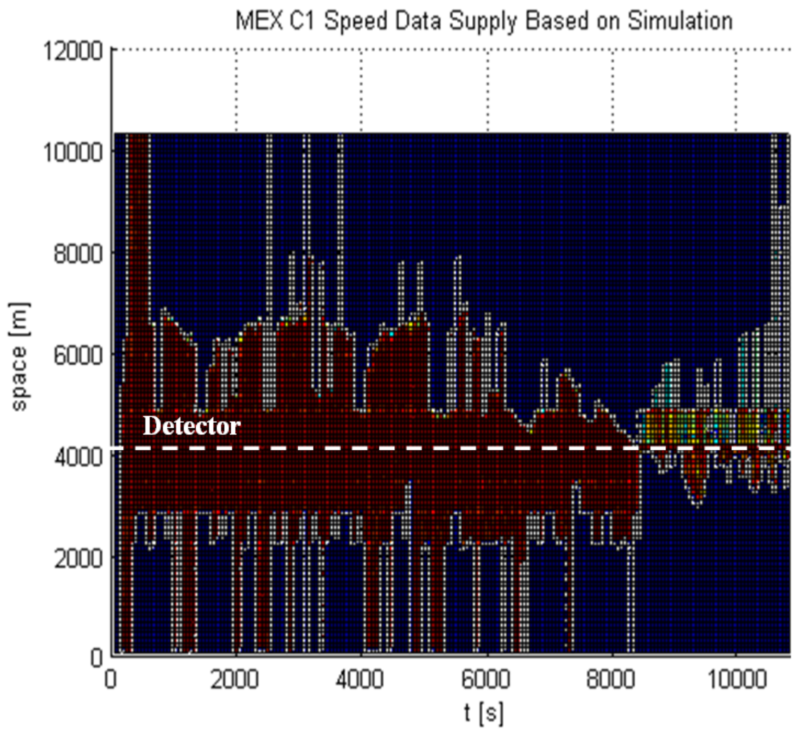

Figure 5: Full knowledge map of the link provided by the detector at location 4000m

Similar to speed data supply, those functions can be found for all measurement values.

3. DATA DEMAND FUNCTIONS

Compared with data supply functions, data demand functions are independent from detector types and locations. Data demand is determined by the way how traffic authorities use the data. Different types of data need be collected in essential spots and even a whole link to support traffic management measures or provide travel information to drivers. According to highway management policies, traffic authorizes decide which traffic management measures are selected to improve their services considering congestion conditions, safety issues and environment impacts. We define a general data demand function as:

$$
\begin{aligned}
&\chi_{\mathrm{i},\delta} = g_{\eta,\rho}(x) \\
&\text{where:} \\
&\chi : \text{traffic data demand [\%]} \\
&\text{x} : \text{position [m]} \\
&\text{i} : \text{link i} \\
&\delta : \text{data type} \\
&\eta : \text{Traffic management measures} \\
&\rho : \text{Management policies}
\end{aligned} \qquad (2)
$$

The data demand functions are static and do not vary with traffic conditions. The data demand function for a link is the maximum over all demands at a certain location. In a very crisp definition this would lead to a demand of either 0 or 1 at position x along the link. However, by introducing weights, based on policies of the road authority, it is possible to emphasize certain demands. We choose several general traffic data applications as examples to introduce how to determine the data demand based on the functions we defined above. Many basic or advanced methodologies have been developed for traffic management measures. Even the same traffic management measure has several algorisms to achieve it, which leads to different data demands. For instance, a lot of practical methodologies are developed to improve accuracy and reliability of travel time prediction. The comparison of data demands for two different methodologies is shown in Figure 6

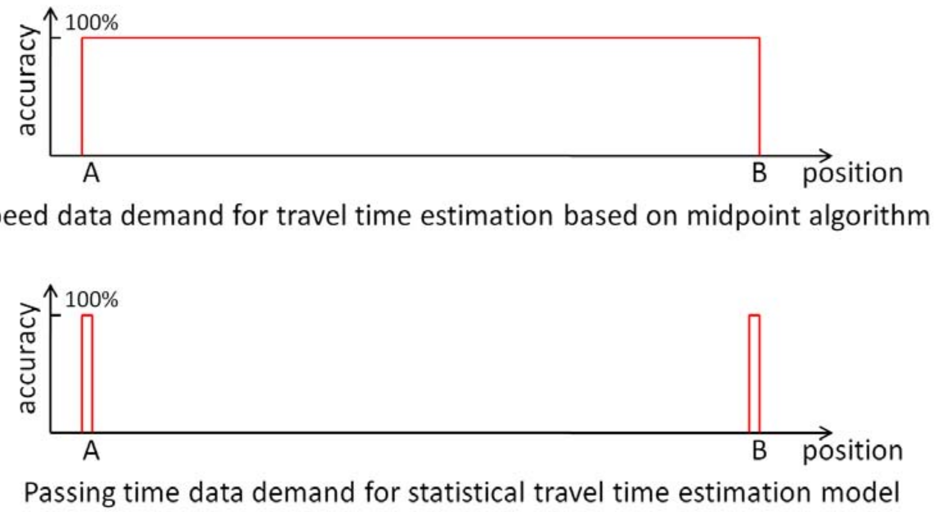

Figure 6: Comparison of data demands for two methodologies of travel time estimation.

Midpoint algorithm is a classical methodology which uses speed collected at the detectors and the spacing between the detectors. The midpoint between two neighbor detectors is used to determine the valid range of the speed data, and theoretically less distance between the detectors more estimation accuracy is obtained (Kristin et al, 2008). Therefore, as shown in the upper part of Figure 8, when travel time from A to B needs to be predicted based on midpoint algorithm, basically all speed information between A and B are required to fully implement the methodology (CHUNG et al, 2004). On the other hand, some statistical travel time estimation models do not needs link speed data but passing time data instead. Based on passing time at location A and B, historical travel time data are recorded to forecast travel time in the next time period. Apparently different methodologies for same management measure needs various types of data at different locations. Therefore the data demands should be carefully determined based on the methodologies selected for highway management measures.

4. EVALUATION AND OPTIMIZATION

A traffic detection scheme is evaluated by comparing the data demand and supply function, introduced as level of detection:

$$\psi_{i,\delta} = \begin{cases} \dfrac{f_{\omega,\tau,\mu}(x,t)}{g_{\eta,\gamma,\rho}(x,t)} & f_{\omega,\tau,\mu}(x,t) < g_{\eta,\gamma,\rho}(x,t) \\ 1 & f_{\omega,\tau,\mu}(x,t) \geq g_{\eta,\gamma,\rho}(x,t) \end{cases}$$

where:

$\psi_{i,\delta}$:level of detection for data type δ on link i (3)

The value indicates the percentage of the data demand that can be supplied by the sensors placed along a link. This value is objective and a good indicator for planning or changing detection installation plans.

To optimize the detection of the road we have to maximize the level of detection by moving sensors in the link or by adding sensors, depending on the budget constraints.

The usual optimization cycle has the following steps:

- Determine potential spot for road way sensor deployment and a minimal unit length for potential spots
- Determine total number of available detector according to the budget constrains
- Generate an initial set of acceptable samples of detector placement randomly
- According to genetic algorism (GA), randomly crossovers among of the samples are implemented and an offspring set is obtained.
- Select samples with high LOD as a new parent set to generate new offspring set.
- Repeat the procedures above to newly generated offspring till a pre-specified number of generations

5. PRELIMINARY CASE STUDY

To test the framework under real world conditions we have chosen C1 Route of Tokyo Metropolitan Expressway (MEX) for case studies, due to the data availability through the International Traffic Database (http://www.trafficdata.info).

C1 Route, located in the center of Tokyo, connects other routes of MEX network such as Route 3 Shibuya Line, Route 4 Shinjuku Line, Route 5 Ikebukuro Line and etc.. The C1 Route carries a huge amount of traffic and is highly congested during the rush hours.

As we introduce in the Data Supply Functions section, traffic state analysis is the key point to determine the speed data supply conditions. We use actual ETC data as inputs of traffic simulation to identify the speed distribution in the study area, and a rush hour sample is shown in Figure 4. As demand for the section firstly we chose travel time estimation for the entire ten kilometer link. By using the optimization methodology we introduced in Evaluation and Optimization Section, the optimal sensor placements are determined with limited number of detector automatically as shown in Figure 7

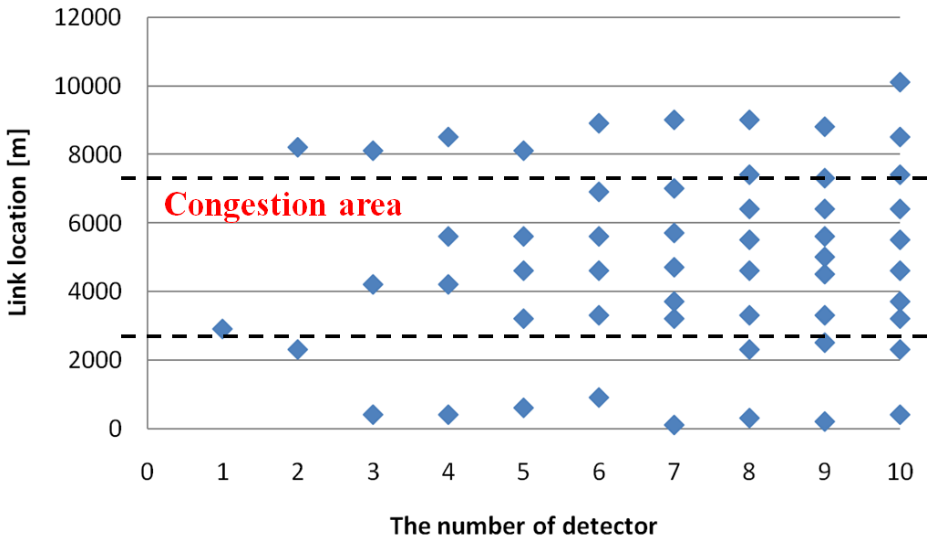

Figure 7: Optimal detector locations of a ten kilometer link on MEX C1 Route for travel time estimation.

According to the traffic state visualized in Figure 4, we can observe the Frequency of detectors placed in a congested area (from 2500m to 7500m) is higher than other parts of the link. To verify the placement results, we compare level of detection (LOD) for optimal placements with LOD for even spacing placements as shown in Figure 8

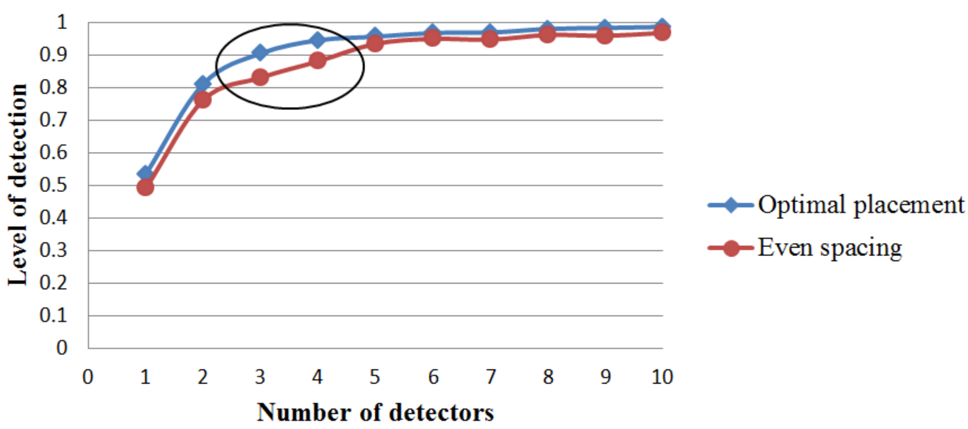

Figure 8: Comparison of optimal placements and even spacing placements

LOD for optimal placements are higher than simply even spacing placements, particularly when the number of detectors are quite few such as the total number of available sensors are 3 or 4.

6. DISCUSSION

In this paper we have introduced the concept of network and link knowledge maps that represent the information that can be gathered from a network by monitoring only. To allow this, we have introduced data supply functions, which determine the coverage area in which they gather reliable information. Combining this information with historical data and incident statistics, leads to a solid basis for detector location optimization. While a link based view seems very straight forward, the complexity increases quickly when extending to network scale, and by adding more requirements and data supply functions. Future work will include the addition of more data supply functions, and the extension of the link based method to a network based methods, which will require link boundary conditions. Further, with commonly accepted methodologies for estimating measured values based on local measurements, we will include knowledge maps that can consider estimated information in the optimization.

REFERENCES

Yang, H., and Zhou, J. *Optimal Traffic Counting Locations for Origin-Destination Matrix Estimation*. Transportation Research Part B, Vol. 32, 1998, pp. 109-126

Sisiopiku, V.P., Rouphail, N.M., and Santiago, *A. Analysis of Correlation Between Arterial Travel Time and Detector Data from Simulation and Field Studies*. Transportation Research Record, No. 1457, 1994, pp. 166-173

Thomas, G. *The Relationship Between Detector Location and Travel Characteristics on Arterial Streets*. Institute of Transportation Engineering Journal, Vol. 169, 1999, pp. 36-42

Oh, S., Ran, B., and Choi, K. *Optimal Detector Location for Estimating Link Travel Speed in Urban Arterial Roads*. In Proceedings of the 82nd Annual Meeting of the Transportation Research Board, Washington DC, 2003

Edara, P., Guo, J., Smith, B. L., McGhee, C., *Optimal placement of point detectors on Virginia's freeways: Case studies of Northern Virginia and Richmond*, Report No. VTRC 08-CR3, Virginia Transportation Research Council, Richmond, 2008

Kristin Tufte, Sirisha Kothuri, Report No: *OTREC-RR-08-02 Assessment and Refinement of Real-Time Travel Time Algorithms for Use in Practice,* Final Report October 2008

Chung, E., Warita, H., Bajwa, S. and Kuwahara, M. (2004). Travel time prediction: issues and benefits. 10th World Conference on Transport Research, (CD), Istanbul, Turkey

STUDY OF ALUMINIUM AND MAGNESIUM ALLOY AS SACRIFICIAL ANODE FOR CORROSION PROTECTION OF STRUCTURAL STEELS BY IMMERSION TEST

Aris MAHASIRIPAN[1], Ekkarut VIYANIT[2*], Wanida PONGSAKSAWAD[2], Benya CHERDHIRUNKORN[2,3], Somnuk TANGTERMSIRIKUL[4,5] and Pakawat SANCHAROEN[5]

[1]Graduate Student, School of Civil Engineering and Technology (CET), Sirindhorn International Institute of Technology, Thammasat University, Pathumthani 12121 Thailand
amrissy@hotmail.com
[2]Researcher, National Metal and Materials Technology Center (MTEC), 114 Thailand Science Park, Pathumthani 12120 Thailand
[3]Researcher, Material Science Major, Department of Physics, Faculty of Science and Technology, Thammasat University, Thailand
[4]Professor, School of Civil Engineering and Technology (CET), Sirindhorn International Institute of Technology, Thammasat University, Thailand
[5]Researcher, Construction and Maintenance Technology Research Center (CONTEC), Sirindhorn International Institute of Technology, Thammasat University, Pathumthani 12121 Thailand

ABSTRACT

In this paper, structural steel, which is hot-rolled steel grade SS400 according to JIS G3101 was determined corrosion rate and corrosion behavior of material by potentiostatic polarization technique. In this test, real seawater and artificial seawater were used as the electrolyte solution. Real seawater was collected from Gulf of Thailand. And artificial seawater was synthesized by dissolving sodium chloride (NaCl) that is comparable in term of Cl^- ion concentration to that of the real seawater. The hot-rolled steel grade SS400 attached with aluminium and magnesium sacrificial anode were determined corrosion rate by immersing in the artificial seawater for a period of 1 month. The results of surface morphology showed that hot-rolled steel grade SS400 attaching with aluminium sacrificial anode has denser surface morphology than specimen attached with magnesium sacrificial anode. So aluminium anode can protect steel corrosion in marine environment better than magnesium anode.

***Keywords**: Corrosion, Cathodic Protection, Sacrificial Anode, Carbon Steel, Marine Environment*

1. INTRODUCTION

Currently, the steels are widely applied to build the many engineering structures such as pipelines and marine structures including ships, submarines and offshore structure. These structures are normally located in the soil and seawater. So they are rapidly deteriorated by corrosion. The corrosion is a major problem affecting safety and serviceability of the structures because it causes reduction of sectional area of the steel members. Consequently, consideration of corrosion control methods are essential for maintain the serviceability of the structures.

The problems of corrosion become a crucial for structural steel in marine environment. Structures should be well maintained for its designed life. Corrosion science, protective engineering and galvanic corrosion are important topics. Cathodic protection is one of the ways to protect structural steel from corrosion which has mainly two categories: impressed current cathodic protection (ICCP) and galvanic anode cathodic protection. ICCP has to applied current for protecting steel that it has apply. Graphite, copper or platinum are used as anode in this systems. In contrast, galvanic anode cathodic protection or sacrificial anode doesn't need applied current to system. Sacrificial anode was used as material for giving electron to protect structural steel which is a cathode by electrochemical method.

Cathodic protection technique is not widely used in Thailand because of its complicating both in design and application. Former steel structures are only constructed in atmospheric. Due to expansion of economic system in the recent years, marine and underground structures such as coated facilities and pipelines made from steels, are extensively constructed in the industrial area. Sacrificial anodes are initially applied to protect corrosion in Thailand. However, it is essential to study the protective behaviour of sacrificial anodes to protect structural steels in Thailand.

Aluminium is popular to be used for making sacrificial anode because of its high current capacity, low cost, long life and light weight. Magnesium anode has highly negative potential and dissolve too rigorously in seawater. But it is useful to protect structure in high electrically resistivity environment. AZ91D magnesium alloy is among the best lightweight structural materials with a relatively high strength to weight ratio. Therefore, magnesium attracts special attention of researchers working in automotive and aircraft industry [1]. This is because magnesium alloy is the most active metal in the galvanic series [2], and a magnesium alloy component is always the active anode if it is in contact with other metals.

Aluminium alloy anode or Al-Zn-Mg alloy is one of sacrificial anode for this experiment which suitable for cathodic protection. It was developed in the recent years. The system is more efficient with respect to the superficial activation of anode (preventing the formation of superficial aluminium oxide film) [3].

2. EXPERIMENTAL

2.1 Materials

2.1.1 Steels

The specimens for this study were hot-rolled steels grade SS400 according to JIS G3101, SM490YA according to JIS G3106 and SMA490A according to JIS G3114. The surface areas of specimen were 20 cm^2 and 40 cm^2.

Specimen for immersion test is SS400 hot-rolled steel which was welded with copper cable by current power of 90 V. Then specimen was coated all surfaces except the top surface by epoxy resin as shown in figure 1.

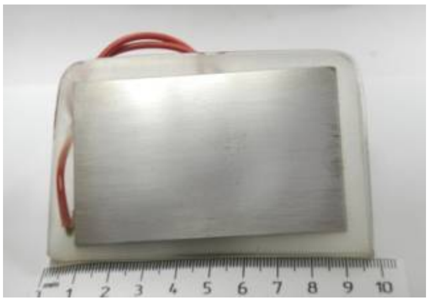

Figure1: Cathode specimen before immersion test

2.1.2 Anode

Two types of sacrificial materials were used as an anode: AZ91D magnesium alloy ingot and aluminium alloy (Al) ingot. All specimens were grinded by emery paper No.80 – 600 before tested corrosion behavior [4]. Specimen for immersion test is AZ91D magnesium anode and aluminium anode in figure 2 which was drilled by screw with copper cable for attaching between cable and specimen then specimen was coated all other surfaces except the top surface by epoxy resin as shown in figure 3.

Aluminium anode	Magnesium anode
	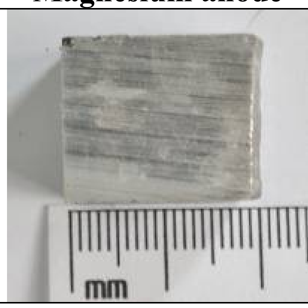

Figure 2: Anode specimen

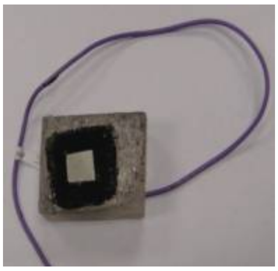

Figure 3: Anode specimen before immersion test

2.2 *Testing*

2.2.1 Spark emission testing

SS400 hot-rolled steel specimen size 150 mm and 150 mm was grinded by emery paper No. 80 before tested chemical compositions by spark emission spectrometer

2.2.2 Microstructure testing

SS400 hot-rolled steel, AZ91D magnesium alloy and aluminium alloy were cut with the gauge diameter and length to the size of 15 × 15 mm. It were grinded by emery paper No. 80 – 4000 and polished by diamond paste 1 – 9 μm. Then it was etched by 6% by volume nitric acid for measuring microstructure at 200X by optical microscope (OM). Specially AZ91D magnesium alloy must measured microstructure and was analyzed its element by Scanning electron microscope (SEM) at 2000X together with Energy dispersion spectrometer (EDS) technique.

2.3 Analysis of the polarization curve

Polarization curve was conducted to determine corrosion rate by electrochemical testing and use potentiostatic technique to measured potential and current density of materials. AZ91D magnesium alloy was chosen because it give electron more than aluminium alloy. In this experiment, AZ91D magnesium alloy, aluminium alloy and SS400 hot-rolled steel were used as working electrode (WE). Saturated calomel electrode (SCE) was used as a reference electrode (RE), and platinum rod (Pt) was used as electric path. Anodic potentiostatic polarization of carbon steel and weathering steel electrode with actual sea water as the solution was achieved using potentiostatic /galvanostat EG&G 273A at a rate of 0.167 mVs^{-1}.

2.4 Solution preparation

Electrolyte solution for this study is real-seawater from Gulf of Thailand which was determined its ion concentration by Ion Chromatography (IC). Real-seawater from 5A has the highest chloride ion concentrative. Then artificial seawater was prepared by dissolve sodium chloride (NaCl) in de-ionized (DI) water to be same chloride concentration as in real-seawater.

2.5 Immersion testing

Hot-rolled steel grade SS400 was used as a cathode, AZ91D magnesium alloy and aluminium alloy were used as a sacrificial anode which were immersed in artificial seawater as shown in figure.4

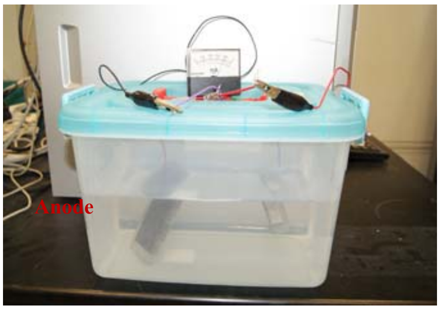

Figure 4: Installation specimen for immersion test

2.6 Surface analysis

2.6.1 Sacrificial anode

After immersion test anode specimen was cleaned by chromium trioxide and phosphoric acid (CrO_3 + H_3PO_4) with 85 degree celcius and 10 minute in G1 standard for cleaning specimen.

2.6.2 Steels

After immersion test specimen was cleaned by 50% hydrochloric acid (HCl) 10 minute and then dry out the moisture. Specimen was studied surface morphology by Scanning Electron Microscope (SEM).

3 RESULTS AND DISCUSSION

3.1 Materials selection and physical properties

Chromium (Cr), nickel (Ni) and silicon (Si) element content can increase corrosion resistance of structural steel in marine environment. Table 1 showed that chemical composition of SS400 hot-rolled steel compare to others steel: SM490A and SM490YA, SM490A has Cr content higher than others. It is the highest corrosion resistance. SS400 have the lowest Cr content makes it is the worst corrosion resistance. So it should install sacrificial anode to protect corrosion and failure in this study.

Table 1: Chemical composition of three types of structural steels.

Material	Chemical composition (wt %)					
	C	Si	Mn	P	S	Cr
JIS G3101	0.14-0.22	≤ 0.30	0.30-0.65	≤ 0.045	≤ 0.050	-
SS400	0.04744	0.17401	1.0398	0.01012	0.00606	0.02572
JIS G3114	≤ 0.20	≤ 0.55	≤ 1.60	≤ 0.035	≤ 0.035	-
SM490A	0.11499	0.39619	0.36757	0.07608	0.00503	0.68137
JIS G3106	≤ 0.20	≤ 0.55	≤ 1.60	≤ 0.035	≤ 0.035	-
SM490YA	0.07025	0.21799	0.35244	0.00887	0.01563	0.03082

Figure 5 showed microstructure of structural steel. SS400 hot-rolled steel has many grain boundaries and has ferrite phase increasing corrosion of SS400 hot-rolled steel.

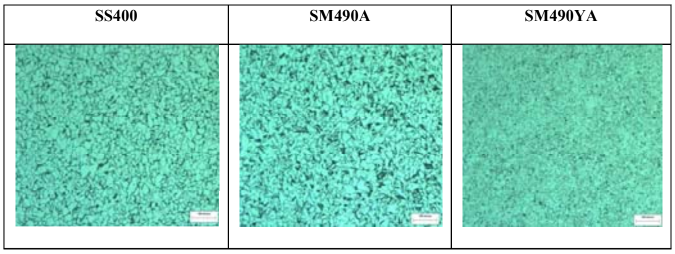

Figure 5: Microstructure of three types of steels by optical microscope 200X

Figure 6 showed that microstructure of sacrificial anode both of Al anode and Mg anode Microstructure of aluminium alloy and magnesium alloy are same that have three phase consists of matter, solid solution (Al and Mg compound or phase alpha) and phase of aluminium element or phase beta. Phase beta (β) and phase alpha (α) are found in microstructure. Alpha phase increases corrosion resistance because it has more mixing compound that has aluminium and magnesium content than others phase. Aluminium alloy has higher corrosion resistance than magnesium alloy because aluminium alloy has higher amount of alpha phase.

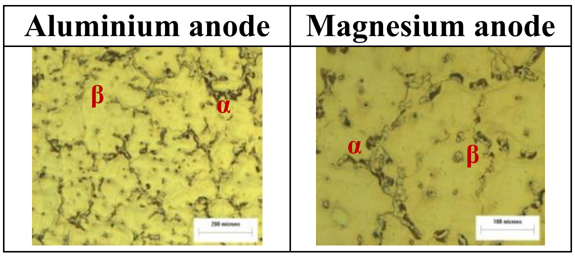

Figure 6: Comparing microstructure between aluminium alloy and magnesium alloy.

3.2 Real-seawater analysis

Table.2 showed the result of anion concentration in real-seawater determined ion by ion chromatography (IC). Rack location of real-seawater has chloride ion, sulfate ion bromide ion and fluoride ion are a lot higher than other locations.

Table 2: Anion concentration in real-seawater from Gulf of Thailand.

Location of real seawater	**Ion concentration (ppm)**			
	Chloride	**Sulfate**	**Bromide**	**Fluoride**
Coastline	18821.87	3041.60	58.21	4.09
In the sea	19231.71	3088.45	59.65	4.06
Middle between coastline and sea	19586.46	3147.58	60.75	4.13

3.3 Corrosion behavior of materials

3.3.1 Steel tested in real-seawater

Polarization curve can describe the current density and potential of materials behavior as shown in figure.7. It was shown in table.3 that polarization curve of SS400 hot-rolled steel which has the highest corrosion current density about 0.77×10^{-6} A/cm^2 and corrosion potential about -0.7092 volts. Analyzed corrosion rate by tafel slope between cathodic polarization curve and anodic polarization curve, was 0.008 mmpy. When chloride concentration is increased in location of seawater can effect to corrosion current density and corrosion potential of polarization curve is increased too. Due to corrosion rate of materials which tested in seawater is increased.

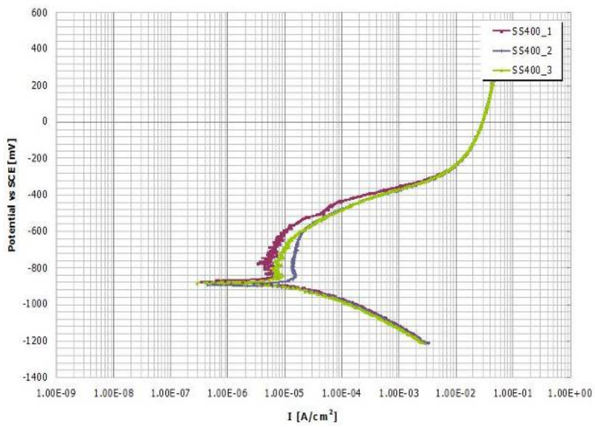

Figure 7: Example of polarization curve of structural steel grade SM490YA hot-rolled steel in real-seawater

Table 3: Corrosion potential and current density of three types of structural steels in real seawater.

Location	Materials	Ecorr (V)	Icorr (A/cm2)	Corrosion Rate (mmpy)
Coastline	SS400	-0.8821	4.62E-06	0.0440
	SM490A	-0.8462	0.05E-06	0.0015
	SM490YA	-0.7005	0.95E-06	0.0099
In the sea	SS400	-0.8799	7.06E-06	0.0736
	SM490A	-0.8672	0.58E-06	0.0060
	SM490YA	-0.7092	0.77E-06	0.0080
Middle between coastline and sea	SS400	-0.8852	6.28E-06	0.0654
	SM490A	-0.6778	0.18E-06	0.0018
	SM490YA	-0.7088	0.19E-06	0.0021

3.3.2 Steel tested in artificial seawater

Polarization curve can describe the current density and potential of materials behavior as shown in figure.8. It was shown in table.4 that polarization curve of SS400 hot-rolled steel which has the highest corrosion current density about 8.18×10^{-5} A/cm^2, corrosion potential about -0.6315 volts and corrosion rate was 0.752 mmpy. So that SS400 hot-rolled steel has to be protected by cathodic protection to extend its service life in marine environment.

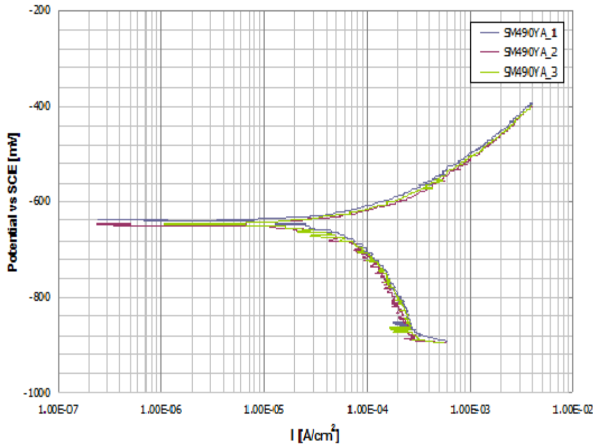

Figure 8: Polarization curve of structural steel grade SM490YA hot-rolled steel in 3.22%NaCl

Table 4: Corrosion potential and current density of three types of structural steels in artificial seawater.

Location	Materials	Ecorr (V)	Icorr (A/cm2)	Corrosion Rate (mmpy)
Coastline	SS400	-0.6367	6.47E-05	0.752
	SM490A	-0.6523	4.64E-05	0.539
	SM490YA	-0.6430	7.38E-05	0.858
In the sea	SS400	-0.6313	8.18E-05	0.951
	SM490A	-0.6439	5.64E-05	0.655
	SM490YA	-0.6275	9.13E-05	1.060
Middle between coastline and sea	SS400	-0.6394	7.03E-05	0.817
	SM490A	-0.6657	4.50E-05	0.523
	SM490YA	-0.6438	7.39E-05	0.859

All results of polarization curve of steel in real-seawater and artificial seawater, corrosion rate are shown in table.3 and table.4. They are shown that steel tested in artificial seawater has corrosion rate more than tested it in real seawater. This is due to lower pH and higher conductivity of artificial seawater as explained later. The results conflict theory that corrosion rate from laboratory should less it than from real seawater. However, can discuss the results cause of pH and conductivity of electrolyte. pH is less which is effected to high corrosion rate and conductivity is more effected to high corrosion rate too.

3.3.3 Anode tested in artificial seawater

- ***Magnesium anode***

Figure 8 showed that polarization curve of AZ91D magnesium alloy which has potential approximate -1400 mV vs SCE and corrosion current density about 1×10^{-7} A/cm^2.

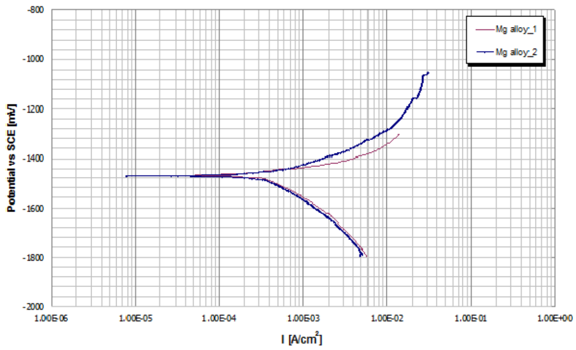

Figure 8: Polarization curve of AZ91D magnesium alloy in 3.22%NaCl artificial seawater.

- ***Aluminium anode***

Figure 9 showed that corrosion potential of aluminium alloy was around -1250 mV and less than that of magnesium alloy because aluminium alloy gives electron less than magnesium alloy.

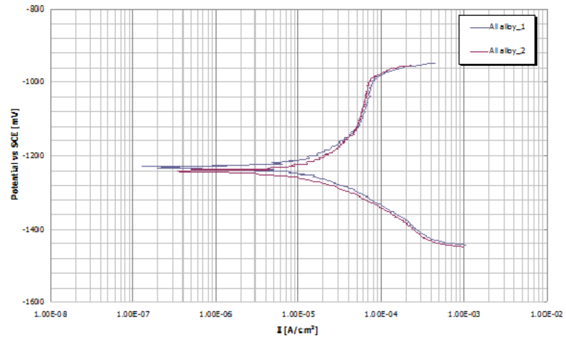

Figure 9: Polarization curve of aluminium alloy in 3.22%NaCl artificial seawater.

When comparing polarization curve between magnesium alloy and aluminium alloy, polarization curve of aluminium alloy has passive film more stable than magnesium alloy. Therefore, aluminium alloy tend to show higher corrosion resistance than magnesium alloy also aluminium alloy has weight loss less than magnesium alloy which is suitable for making sacrificial anode in marine environment.

Table 5: Corrosion potential and current density of three type of aluminium anode and magnesium anode in artificial seawater.

Location	Materials	Ecorr (V)	Icorr (A/cm2)	Corrosion Rate (mmpy)
Middle between coastline and sea	Magnesium anode	-1.4710	1.87E-05	1.64
	Aluminium anode	-1.2264	9.72E-06	1.48

3.4 pH and conductivity of solution

Real-seawater and artificial seawater were analyzed their pH and conductivity by water analyzer. Result showed that real-seawater from three locations have higher pH than artificial seawater tested in laboratory as shown in table.6. So corrosion rate of structural steel in artificial seawater is more than tested in real-seawater because artificial seawater has low pH. But, conductivity of real-seawater solution is lower than artificial seawater. It means that when testing corrosion in artificial seawater gives a higher corrosion rate than tested in real-seawater.

Table 6: Comparing pH and conductivity between real-seawater and artificial seawater

Seawater	Position	pH	Conductivity (mS)
Real-seawater	Shore [3.14%NaCl]	7.30	66.4
	Far [3.17%NaCl]	7.35	68.9
	Rack [3.22%NaCl]	7.38	69.2
Artificial-seawater	Rack [3.22%NaCl]	5.42	72.3

3.5 Immersion testing analysis

In this section, relationship between corrosion current and time of immersion in artificial seawater was explained. As shown in figure.10 steel was attached with Al alloy showed more stable current exchange than specimen attached with Mg alloy from figure.11. The current exchange means that both of anode can reduce corrosion rate of steel, but aluminium anode has lower maintenance cost than magnesium anode.

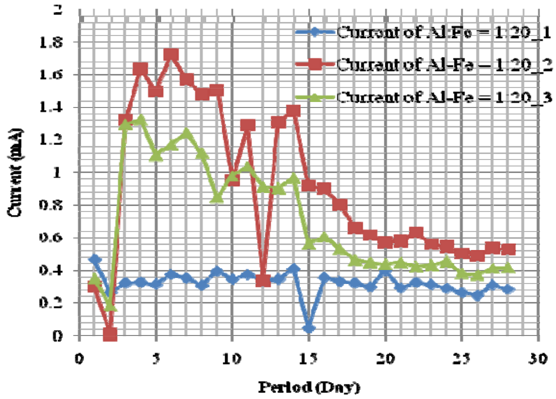

Figure 10: Relationship between day of immersion and current exchange from aluminium anode to protected cathode

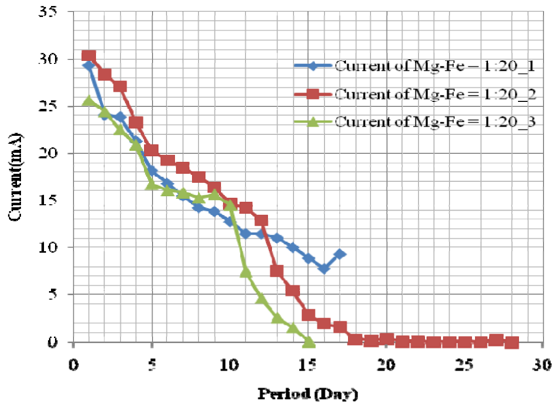

Figure 11: Relationship between day of immersion and current exchange from magnesium anode to protected cathode

3.6 Surface morphology

3.6.1 Sacrificial anode

After immerse steel in artificial seawater is found that magnesium anode was used up, but aluminium anode was remained. Then surface was cleaned by CrO_3 + H_3PO_4 to measure weight loss of anode and surface morphology.

Table 7: Surface morphology of sacrificial anode which is attached by different amount of aluminium anode after immersion test

Surface preparing	Aluminium anode	Magnesium anode
Before cleaning	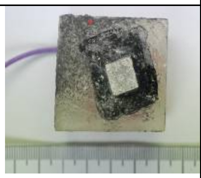	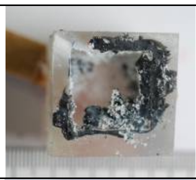
After cleaning	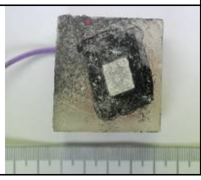	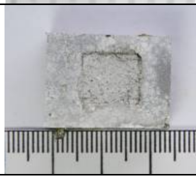

3.6.2 Steels

Figure 12 showed that surface morphology of SS400 hot-rolled steel when has no sacrificial anode to reduce corrosion. Rusting on clearly be observed on the surface.

Table 8 showed the surface morphology of steel when it was protected by aluminium anode at difference anode to cathode ratio. Area ratio between steel to anode as 1:20 is more effective than 1:40 ratio because anode can give more electron to steel.

Figure 12: Surface morphology of SS400 hot-rolled steel without sacrificial anode

Table 8: Surface morphology of SS400 hot-rolled which is attached by different amount of aluminium anode

Surface preparing	Al : Steel = 1 : 20	Al : Steel = 1 : 40
Before cleaning	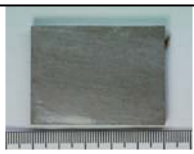	
After cleaning	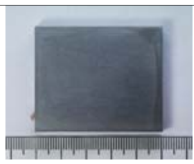	

Table 9 showed that surface morphology of SS400 hot-rolled steel when using magnesium sacrificial anode to protect corrosion. Surface morphology of specimen with magnesium anode was insufficient to protect steel from corrosion. This is due to the fast consuming of magnesium anode in seawater.

Table 9: Surface morphology of SS400 hot-rolled which is attached by different amount of magnesium anode.

Surface preparing	Mg : Steel = 1 : 20	Mg : Steel = 1 : 40
Before cleaning	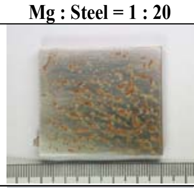	
After cleaning		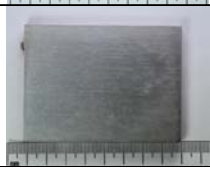

Table 10 showed the result of measured during weight loss. It is obtained by calculate current measured during immersion testing in the duration of 30 days. Weight loss can be calculated by current flow from sacrificial anode to cathode. Equation.1 is used to calculate weight loss

$$W = \frac{I \times t \times M}{n \times F} \quad \text{..........}\textbf{Equation.1}$$

W = Weight loss of steel (g)
I = Current (A)
M = Atomic weight for iron equal to 55.85 g/mol
n = number of exchanging electron, equal to 2
F = Faraday's constant is equal to 96500 coulombs/mol
t = Time (second)

Weight loss from equation.1 is used to calculate corrosion rate by equation.2 for predict service life of sacrificial materials.

$$\text{Corrosion Rate} = \frac{87600W}{DAT} \quad \text{..........}\textbf{Equation.2}$$

W = weight loss from equation.1 (mg)
D = Density of steel (A/cm^2)
A = Surface area of steel (cm^2)
T = Immersed time (s)

Table 10 showed that weight loss and corrosion rate of aluminium anode and magnesium anode. Alumiunium anode is consumed less than magnesium anode. Then aluminium anode can use last longer than magnesium anode to protect corrosion of steel in cathodic protection by use sacrificial anode in marine environment.

Table 10: Weight loss and corrosion rate when using sacrificial anode

Sacrificial anode type	Area ratio between anode and cathode	Weight loss per 30 day (mg)	Corrosion rate (mmPY)
Magnesium alloy	1 : 20	564.05	0.4359
	1 : 40	1713.16	0.6620
Aluminium alloy	1 : 20	12	0.0093
	1 : 40	45	0.1739

4 . CONCLUSION

This study can conclude that structural steel grade SMA490A has corrosion rate less than SS400 hot-rolled steel because it has Cr content higher than others. So it is necessary to improve SS400 hot-rolled steel which can be used as structural steel in marine environment due to its lower cost than others. Cathodic protection was used to protect steel from corrosion. Aluminium anode can be used to protect steel same as magnesium anode but magnesium anode is consumed at the higher rate. Therefore, aluminium alloy is suitable more than magnesium alloy to protect steel corrosion in marine environment.

ACKHOWLEDGEMENTS

The study was supported by Failure Analysis of Metal and Materials Corrosion (FAMC) laboratory, National Metal and Materails Technology Research Center (MTEC) a member of National Science and Technology Development Agency (NSTDA).

REFERENCES

A. Eliezer, E.M. Gutman, E. Abramov and Ya. Unigovski., 2001. *Corrosion fatigue of die-cast and extruded magnesium alloys*, Journal of light metals1, 1(1): 179-186.

G. Song, B. Johannesson, S. Hapugoda and D. StJohn., 2003. *Galvanic corrosion of magnesium alloy AZ91D in contact with an aluminium alloy, steel and zinc*, Corrosion science, 46: 955-977.

M.A. Talavera, J. Juarez-Islas and J. Genesca., 2003. *Electrochemical testing of Al-Zn-Mg sacrificial anodes,* Corrosion science, 46: 955-977.

ASTM G5, 1999, *Standard reference test method for making potentiostatic and potentiodynamic anodic polarization measurement*.

SEISMIC RETROFITTING OF NON-ENGINEERED MASONRY HOUSES USING BAMBOO-BAND MESH

Rajendra SOTI[1], Sathiparn NAVARATNARAJ[2], Muneyoshi NUMADA[3] and Kimiro MEGURO[4]

[1] Graduate Student, Department of Civil Engineering, University of Tokyo, Japan
soti@risk-mg.iis.u-tokyo.ac.jp

[2] Post-Doctoral Research Fellows,
Institute of Industrial Science (IIS), University of Tokyo, Japan
sakthi@risk-mg.iis.u-tokyo.ac.jp

[3] Research Associate
International Center for Urban Safety Engineering (ICUS), IIS, University of Tokyo
numada@iis.u-tokyo.ac.jp

[4] Professor, Director, ICUS, IIS, University of Tokyo, Japan
meguro@iis.u-tokyo.ac.jp

ABSTRACT

The collapse of unreinforced masonry structures, which are widely distributed around the earthquake prone regions of the world, is one of the greatest causes of death in major earthquake events. This paper presents an innovative retrofitting method for masonry structures, which uses bamboo band arranged in a mesh fashion and embedded in a mortar overlay. In order to determine the effectiveness of the proposed retrofitting technique, shake table tests were conducted using retrofitted and non-retrofitted 1/4 scaled masonry houses and each house was subjected to sinusoidal ground motion inputs. Based on the experimental results, the retrofitted specimen exhibited good seismic performance by withstanding a more than twice input energy than non-retrofitted specimen.

Keywords*: unreinforced masonry, bamboo-band mesh, shaking table test*

1. INTRODUCTION

The collapse of the unreinforced masonry building induced by the earthquake events is one of the greatest causes of the human casualties around the world. The failure of unreinforced masonry structures contributes to more than 60 % of the structural damage of masonry structures (Mayorca and Meguro 2004). Around 30 % of the world's population live in adobe construction (Houben & Guillard) and large proportion of the structures are located in earthquake prone regions. Thus, strengthening of unreinforced masonry structure is indispensable need to reduce the casualties significantly.

Till date, several types of retrofitting methods have been developed for unreinforced masonry structures. Retrofitting technique for developing countries should consider not only the effectiveness in terms of seismic performance but also the issues like economic viability, cultural adoptability and material as well as technological availability. Under the aforementioned circumstances, PP-Band Retrofitting Technique is one of the appropriate retrofitting techniques and different aspects of this method have already been researched in Meguro Laboratory, in the Institute of Industrial Science, The University of Tokyo. On the other hand, another strengthening technique, which uses bamboo band meshes as a strengthening system, has been proposed and different aspects are being researched in Meguro laboratory.

Bamboo-band retrofitting technique is simple enough to be understood and applied by layman without any prior expertise. Shake table tests were carried out to understand the dynamic response of masonry buildings, crack propagation, failure mechanism, and overall effectiveness of the newly developed retrofitting technique.

2. EXPERIMENTAL PROGRAM

2.1. Specimen Details

Two models were built in the reduced scale of 1:4 using the un-burnt bricks as a masonry units and cement, lime and sand (1:2.8:8.5) mixture as mortar with c/w ratio of 0.33. Even though the materials used were from Japan, great attention was paid to make the models as true replica of brick masonry building in developing countries in terms of masonry strength. Both models represented a one-story building with roof. As Figure 1 shows, the dimensions of both buildings were 950mm×950mm×720mm with 50mm thick walls and the sizes of door and window in opposite walls were 243mm×485mm and 325mm× 245mm, respectively. The size of the adobe brick used was 75mm×50mm× 35mm. Surface finishing was applied both on retrofitted and non-retrofitted buildings. These two building were identical in terms of geometry, construction materials, mix proportion, construction process and technique and other conditions that may affect the strength of the model house. The cross section of the band used was 8mm×0.75mm and the mesh pitch was 40mm. Surface finishing was applied to both specimens.

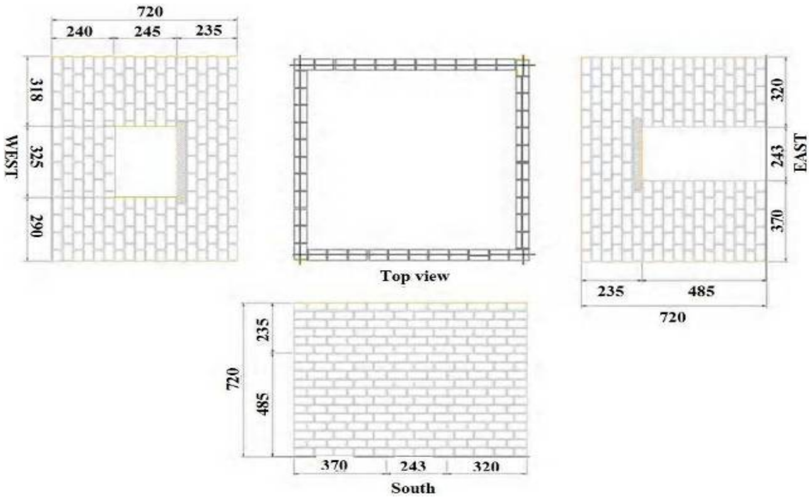

Figure1: Model dimension (mm) (without roof)

2.2. Retrofitting Procedure

Bamboo band mesh was first prepared on a square grid in a way that one band crosses over another band in different layers at subsequent crossing points. This process was quite similar to the basket weaving process. The straw, which was used to ensure hole during model construction, was removed. Straw was placed at approximately 200 mm pitch. In case of existing structures holes can be prepared by drilling through the wall. The prepared mesh was then installed both on outside and inside of the wall and wrapped around the corner of the house. The inside and outside meshes were connected by the Polypropylene strings (PP strings) which were passed through the hole. The overlapping and wrapping of the meshes was also made around the opening and roof. Figure 2 illustrates the overall retrofitting procedure.

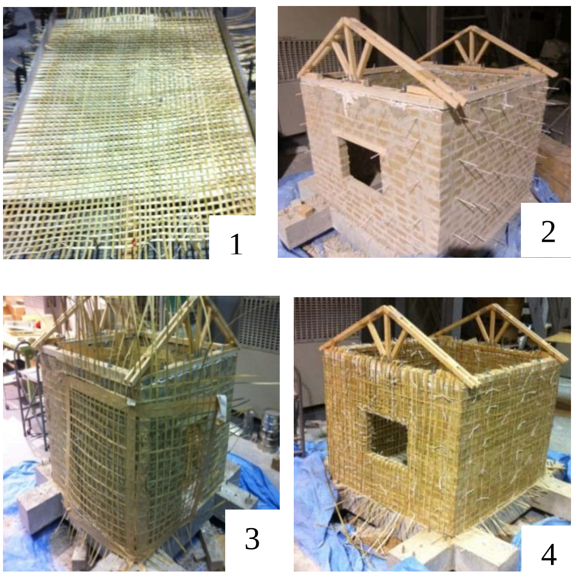

1. Preparing bamboo-band mesh in size
2. Securing holes using the straw during model construction
3. Wrapping the building from inside and outside by the mesh
4. Connecting inner and outer meshes by PP string and overlapping around the opening and roof

Figure 2: Retrofitting procedures

2.3. Instrumentation

The test was carried out in the shaking table facility available in the Institute of Industrial Science, the University of Tokyo. The size of the shaking table is 1.5m X 1.5m. It has six degrees of freedom and operates in frequencies ranges from 0.1 to 50 Hz. It has a maximum displacement capacity of ± 100 mm and the maximum weight of the specimen that can be tested is 2 tons.

2.4. Input motions

Sinusoidal motions of frequencies ranging from 35 Hz to 2 Hz and amplitude ranging from 0.05g to 1.4g were applied to obtain the dynamic response of both retrofitted and non-retrofitted structures. Figure 3 shows the typical shape of the applied sinusoidal wave. The number of cycles was constant for all frequencies. Thus, lower frequency input motion had longer duration.

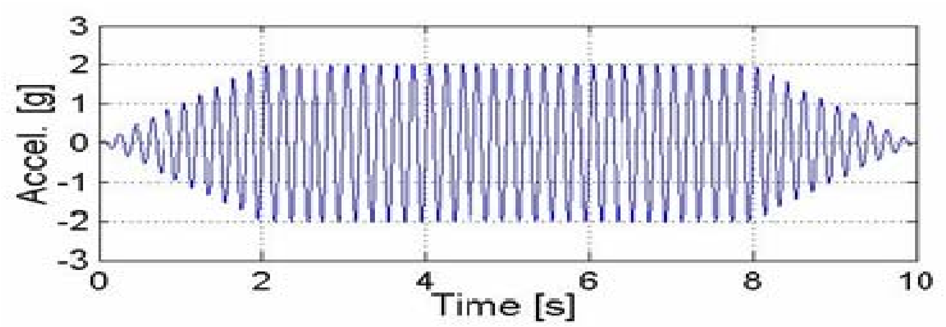

Figure 3: Input Sinusoidal motion

Loading was started with a sweep motion of amplitude 0.05g and frequency ranging from 2 to 50 Hz for identifying the dynamic properties of the models. The sequence of loading is given in Table 1. The numbers in table indicate the run numbers. General trend loading was from higher frequency to low frequency and from lower amplitude to higher amplitude. Higher frequencies motions were skipped towards the end of the runs.

3. CRACK PATTERN AND FAILURE BEHAVIOUR

At the end of each sinusoidal ground motion, inspection of the specimen was carried out. In addition, observed cracks were marked to highlight their locations. The crack formation for both specimens is shown in Figure 4 and Figure 6 after 42nd run of input motion. The initial crack patterns for both specimens were similar. However, these cracks widen in each successive loading in case of non-retrofitted model and new cracks appeared and propagated in the retrofitted model. For non-retrofitted model, no major crack was observed up to run 25. Initial crack was appeared from Run 26. At run 26; minor cracks were observed close to connection between roof and south wall. Run 31 caused crack in point close to connection between roof and south and north wall. Similar cracks were also observed in top of east wall and its adjacent wall. 'X' shaped cracks were observed in south wall

Table 1: Loading sequence

Amplitude (g)	Frequency (Hz)							
	2	5	10	15	20	25	30	35
1.4		50						
1.2	54	49						
1.0		48						
0.8	53	47	43	40	37	34	31	28
0.6	52	45	42	39	36	33	30	27
0.4	51	44	41	38	35	32	29	26
0.2	46	25	24	23	22	21	20	19
0.1	18	17	16	15	14	13	12	11
0.05	10	09	08	07	06	05	04	03
Sweep	01,02							

Loading sequence For both specimens

Loading sequence After non-retrofitted specimen collapsed completely

In run 33, cracks from the corner of the door opening propagated up to the top layer of the wall. Existing cracks appeared from the previous run were propagated up to the bottom of the wall at run 38. Run 40 caused the falling of surface finishing from south wall. Large damages were observed in the run of 43 at which separation between east wall and its adjacent walls was occurred with the significant detachment of surface finishing from the walls. The run 44 caused the total separation of top part of the East-North corner from the specimen. At run 45, all the top part of the north and south wall totally separated from the specimen and roof was totally supported by east and west walls which are perpendicular to the shaking direction. The run 47 led the non-retrofitted building to total collapse (see Figure 5).

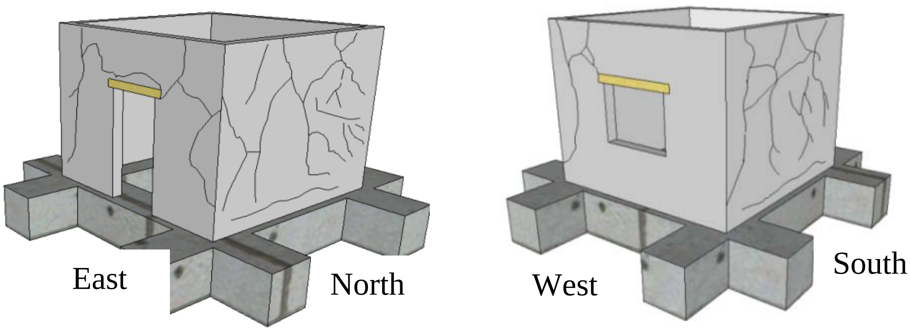

Figure 4: Crack patterns of non-retrofitted building model after run 42

Figure 6: Non-retrofitted building model after run 46 (L) and 47(R)

In case of the retrofitted building model, similar cracks in the case of non-retrofitted building started from top corner of the door opening in the run 27. Run 28 caused the propagation of the existing vertical cracks to the top corner of the door opening. In addition, some vertical and diagonal cracks were also observed around the window opening. The new inclined cracks were appeared in south wall at the run 40.Lots of cracks were observed at run 43. The inclined cracks originated from the corner of the window opening were extended to the top and bottom layer of the wall. 'X' shaped cracks were appeared in north and south wall with few detachment of surface finishing from the specimen. At run 47, most of the existing cracks were extended to the top and bottom layer of the walls. Most of the new cracks were concentrated in the bottom parts of the walls. This run caused the significant detachment of surface finishing from the specimen. Widening of existing cracks with the formation of few new cracks was continued to the run 49. At run 50, most of brick joints were cracked and few brick units fell down from the bottom part of the door opening. There was a large gap in some part of the specimen between the brick units and the mesh was broken at the corner of the wall. At run 52, the building lost the overall integrity and collapsed completely (see Figure 7).

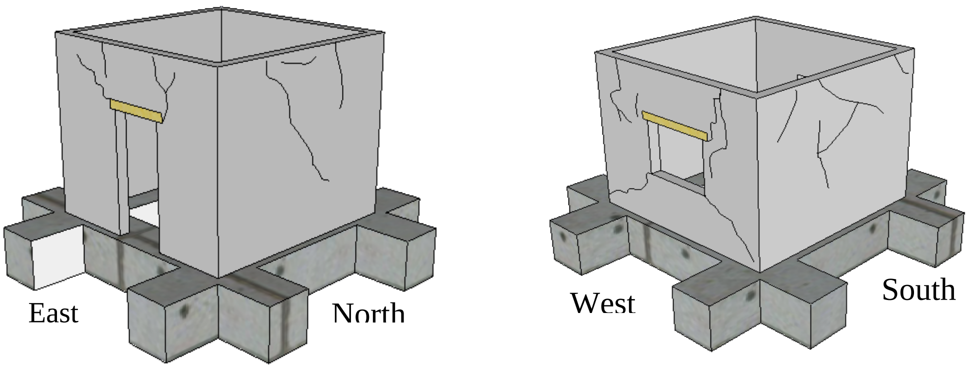

Figure 6: Crack patterns of retrofitting building model after 42 run

Figure 7: Retrofitting building model after 51 run (left) and 52 run (right)

4. PERFORMANCE EVALUATION

The performance of the models was assessed on the damage level of the building at the different level of shaking. The damage level categories are specified on the Table 2. The Japan Meteorological Agency (JMA) seismic intensity scale is a measure used in Japan to indicate the severness of ground motions. JMA seismic intensity is a single number ranging from 0 to 7 and it describes the degree of shaking at a point on the Earth's surface. The JMA intensities were calculated based on the input motions to the structure at different runs. Table 3 shows the performance of model houses with different JMA intensities.

*Table 2**:** Damage categories*

D0: No damage	No damage to structure
D1: Light Structural damage	Hairline cracks in very few walls. The structure resistant capacity has not been reduce noticeably.
D2: Moderate structural damage	Small cracks in masonry walls, falling of plaster block. The structure resistant capacity is partially reduced.
D3: Heavy structural damage	Large and deep cracks in masonry walls. Some bricks are fall down. Failure in connection between two walls is observed.
D4: Partially collapse	Serious failure of walls. Partial structural failure of roofs. The building is in dangerous condition.
D5: Collapse	Total or nearly collapse.

The collapse of the non- retrofitting building is observed at 47^{th} run at JMA 5+. The retrofitted model performed moderate structural damage level at 47^{th} run at which the non-retrofitted model collapsed. Moreover, moderate performance continued to 48th run. The retrofitted building sustained JMA 6- before going to complete collapse.

Figure 8 shows the performance of the model house with respect to the duration of shaking. The non-retrofitted specimen collapsed at a time when a retrofitted performed heavy structural damage. The collapse time was extended to 70 sec for retrofitted specimen than non-retrofitted specimen.

The arias intensity was initially defined by Arias (Arias A., 1970) as

$$I_a = \frac{\pi}{2g}\int_0^t a^2(t)dt \qquad (1)$$

and was called scalar intensity. It is directly quantifiable through the acceleration record a(t), integrating it over the total duration of the shaking. The arias intensity is claimed to be measure of the total seismic energy inputted to the specimen from the ground.

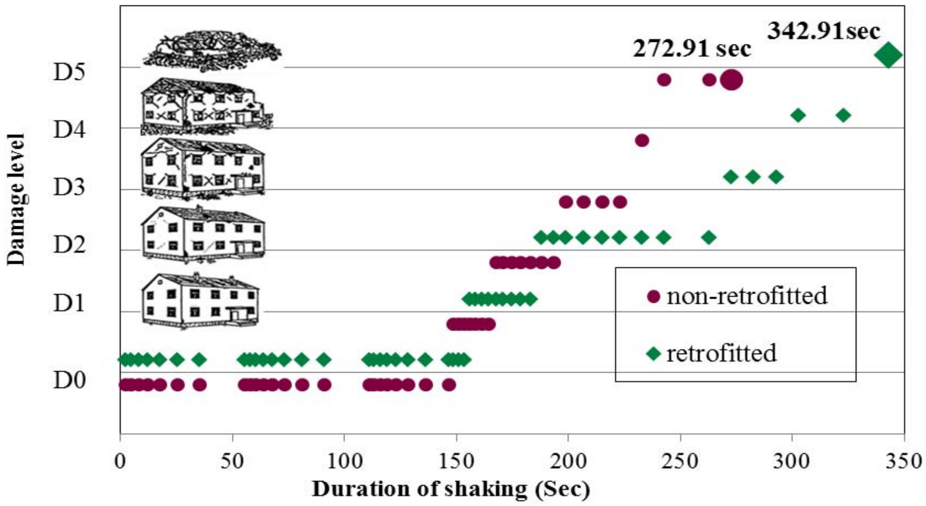

Figure 8: Damage level comparison

Figure 9 shows the performance of the specimen based on arias intensity. From the results, retrofitted model could withstand twice more input energy than non-retrofitted model.

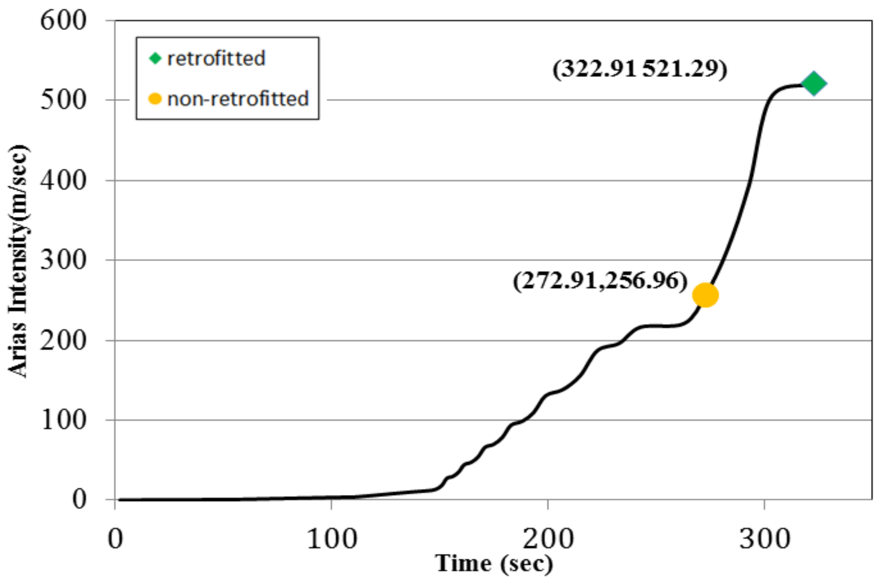

Figure 9: Seismic capacity comparison

CONCLUSIONS

This paper discussed the result of a shaking table test carried out using non-retrofitted and retrofitted hose model by the bamboo band mesh as a strengthening system. The dynamic behavior of models was analyzed and failure behaviors and performances were evaluated. The result showed that the bamboo-band mesh retrofitting technique enhances the seismic resistant capacity of the masonry building model significantly. The retrofitted masonry building could withstand more than twice input energy than non-retrofitted specimen. Bamboo is universally available construction material and its use for retrofitting works not only enhances the seismic resistant capacity of new and existing building but also promote the local business in the vicinity.

REFERENCES

Sathiparan, N.: Experimental study on PP-Band Mesh Seismic Retrofitting for Low Earthquake Resistant Masonry Houses, Ph.D. Dissertation, The University of Tokyo, Japan, 2008.

Meguro, K., Mayorca, P. Guragain R., Sathiparan, N. and Nesheli N.: Shaking Table Experiment of Masonry Buildings and Effectiveness of PP-Band Retrofitting Technique, Seisan-Kenkyu, Vol. 6, pp. 30-33, 2009.

Nazir, S., Sathiparan, N., Numada, M. and Meguro, K.: Experimental Study of Seismic Behavior of Scaled Non-Engineered Masonry structures retrofitted by PP-Band Mesh, Bulletin of Earthquake Resistant Structure Research Center, No. 43, pp. 77-84, March 2009.

Sathiparan, N., Mayorca, P., Meguro, K.: Seismic Study of ¼ Scale Unreinforced Adobe Masonry Models Retrofitted with PP –Band Meshes, Bulletin of Earthquake Resistant Structure Research Center, No. 42, pp. 85-94, March 2009.

Alidad Hahemi and Khalid M. Moslam.: Shake –table Experiment on Reinforced Concrete Structure Containing Masonry Infill Wall, Earthquake Engineering and Structural Dynamics, Vol. 35, pp. 1827-1852, 2006.

Roko Zarnic, Samo Gostic, Adam J.Crewe and Colin A. Taylorm, Shaking Table Tests of 1/4 Reduced Scale Models of Masonry Infilled Reinforced Concrete Frame Buildings, Earthquake Engineering and Structural Dynamics, Vol.30, pp. 819-834, 2001.

Sathiparan, N., Mayorca, P. and Meguro, K.: Experimental Study on Static and Dynamic Behavior of PP-Band Mesh Retrofitted Adobe Masonry Structure.7th International Conference on Urban Earthquake Engineering(7CUEE), March 3-5, Tokyo Institute of Technology, Tokyo, Japan, 2010

SSI EFFECT ON SEISMIC RESPONSE OF HIGH-RISE BUILDING IN JAKARTA, INDONESIA

James FRANK[1], Kullachai TANTAYOPIN*[1]
[1]School of Engineering & Technology, Asian Institute of Technology,
P.O. Box 4, Klong Luang, Pathumthani 12120, Thailand
kullachai@gmail.com

ABSTRACT

High-rise buildings are conventionally analyzed under fixed base assumption without considering soil-structure interaction (SSI) because it provides a conservative design. However, recent studies show that conventional fixed base analysis may underestimate the seismic response and lead to unsafe design. This study deals with the effects of SSI for a typical high-rise building in Jakarta, Indonesia. Nonlinear time history analysis is performed and the inclusion of seismic SSI is modeled through dynamic beam on nonlinear Winkler foundation method. The results show that the peak story shear and moment are reduced when considering SSI, while, in the first floor level, SSI analysis gives a larger response than that of the non-SSI analysis. Therefore, the effects of SSI for the typical example building are not always beneficial and may be detrimental in some part of the building.

Keywords*: soil-structure interaction, high-rise building, nonlinear seismic response*

1. INTRODUCTION

High-rise buildings are conventionally analyzed under fixed base assumption without considering soil-structure interaction (SSI) because it provides a conservative design. However, recent studies show that conventional fixed base analysis may underestimates the seismic response and this may lead to unsafe design.

Mylonakis et al. (2000) investigated the role of SSI on the collapse of 18 piers of the Hanshin expressway during Kobe earthquake and found that the effects of SSI might cause collapse of Hanshin Expressway. Jeremic et al. (2003) studied the influence of SSI on seismic response of an elevated highway bridge (the I-880 viaduct) and found that the SSI can have both beneficial and detrimental effects. Yue and Wang (2009) studied the influences of SSI on the high-rise frame shear wall structure in Fujian province of China. The results show that effects of SSI amplified dynamic response of structure in some stories which indicated that SSI cannot be neglected in analysis.

The previous studies indicate that fixed base analysis on seismic response can lead to unsafe design and the SSI effects shall be investigated for each different site. This study discusses the SSI effects on the seismic response of high-rise building for a typical high-rise building in Jakarta, Indonesia. As Indonesia has been well known with its high seismic activity (Irsyam et al., 2008), the seismic response of the high-rise building in Jakarta is important to be analyzed.

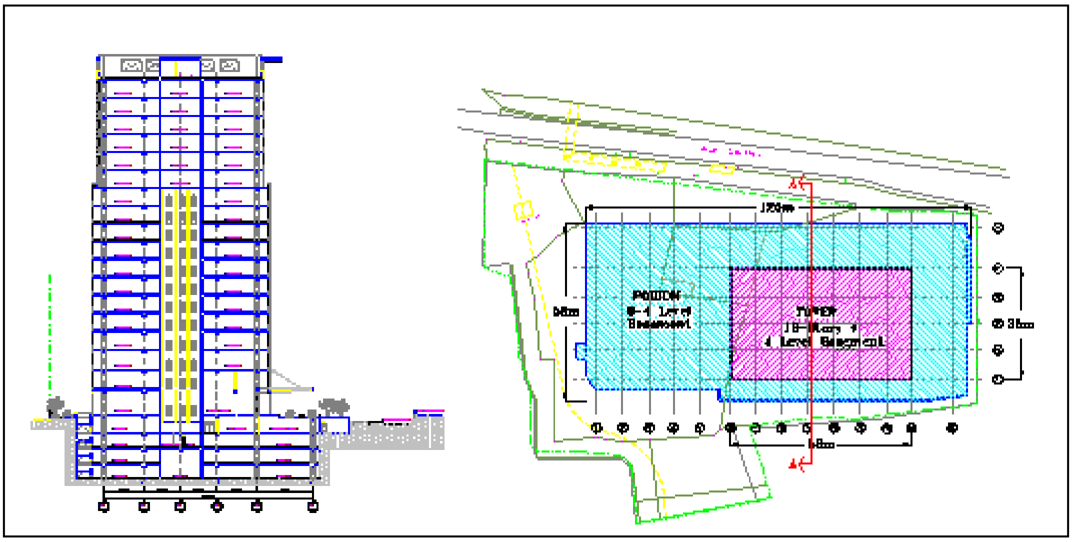

Figure 1: Transversal building cross section and layout of building plan

2. STUDY BUILDING

The selected typical building consists of 18-story floors and 4-level basements with central concrete core wall system. The basements are essentially larger in floor plate area comparing to the tower foot print area as shown in Figure 1. The gravity framing system at the tower is reinforced concrete post-tensioned beam with reinforced concrete slab. The gravity framing system at the ground floor and basement floor is reinforced concrete flat-slab with drop panel at the slab-column connection. The structure configurations are briefly described in Table 1.

Soil investigation and laboratory soil test were conducted to identify the subsoil condition at the site. The subsoil at the site can be divided into 3 major zones. The upper zone is occupied with recent deposits which are low in strength. The old deposits at the middle zone are competent as a bearing layer. The older deposits at the lower zone are also competent but less stiff than the middle zone. The generalized soil profile is presented in Figure 2 including shear wave velocity (Vs) obtained from field downhole seismic test. With the presence of relatively deep basements (4-level), the building is originally designed with raft foundation which is able to sit directly on the middle zone. In order to study the effects of SSI for deep foundation, the building is also designed using pile foundation. Bored pile with the diameter of 800mm and the length of 24m is utilized to support the building. The 2D dynamic analysis is performed in transversal building cross section.

Table 1: Structure model configuration

Level	Vertical element				Horizontal element		
	Core wall thickness		Column size	fc'	Beam section	flat-slab thickness	fc'
	Outer	Inner					
	m	m	m^2	MPa	m^2	m	MPa
B4	0.45	0.25	0.90x0.90	50	-	0.250	32
B2-B3	0.45	0.25	0.90x0.90	50	-	0.175	32
B1	0.45	0.25	0.90x0.90	50	-	0.200	32
L1	0.45	0.25	0.90x0.90	50	0.45x0.65	0.200	32
L2	0.45	0.25	0.90x0.90	50	0.45x0.65	0.150	32
L3-L11	0.45	0.25	0.90x0.90	40	0.45x0.65	0.150	32
L12-L16	0.25	0.25	0.80x0.80	32	0.45x0.65	0.150	32
L17-L18	0.25	0.25	0.75x0.75	32	0.45x0.65	0.150	32

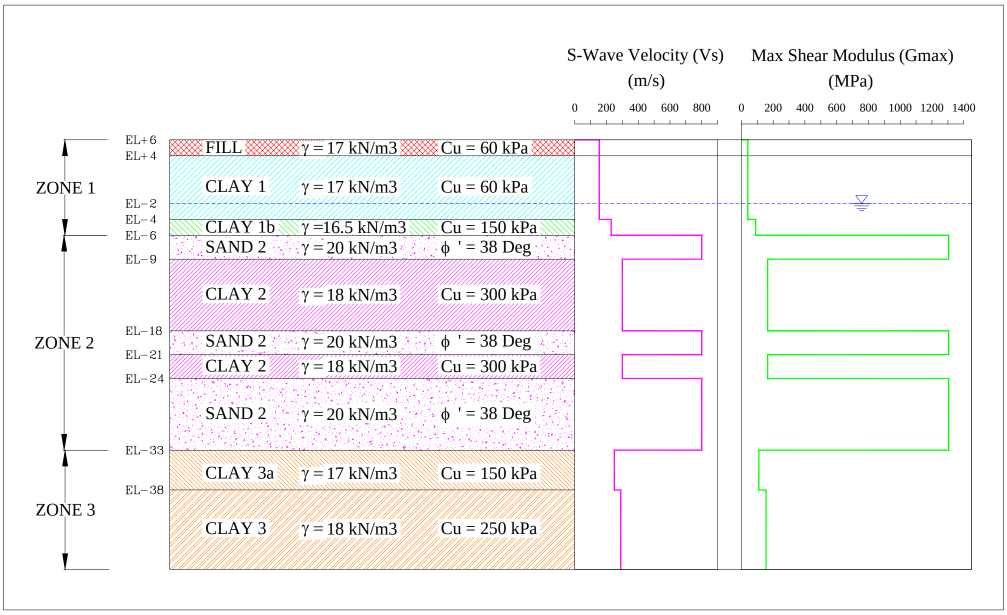

Figure 2: Generalized soil profile

3. NONLINEAR MODEL

The building is expected to exhibit the nonlinear behavior under severe earthquake level. In order to identify the actual response of the building, the behavior of the SSI and structure elements need to be described using nonlinear model.

3.1 SSI Model

The nonlinear SSI is modeled based on the dynamic beam on nonlinear Winkler foundation (BNWF) method suggested by Boulanger et al. (1999) using the lateral load-displacement (p-y) element of the pile. The nonlinear (p-y) element conceptually consists of elastic, plastic and gap component in series. The gap and plastic components represent the near-field component while the elastic component represents the far-field component. Radiation damping is modeled using a dashpot in parallel with elastic component. The nonlinear behavior of the plastic, closure and drag springs is described using the following equations:

$$p = p_{ult} - (p_{ult} - p_0)\left[\frac{cy_{50}}{cy_{50} + \left|y^p - y_0^p\right|}\right]^n \tag{1}$$

$$p^c = 1.8 p_{ult}\left[\frac{y_{50}}{y_{50} + 50(y_0^+ - y^g)} - \frac{y_{50}}{y_{50} - 50(y_0^- - y^g)}\right] \tag{2}$$

$$p^d = C_d p_{ult} - (C_d p_{ult} - p_0^d)\left[\frac{y_{50}}{y_{50} + 2\left|y^g - y_0^g\right|}\right] \tag{3}$$

3.1.1 Pile Foundation

Boulanger (2000) originally implemented the nonlinear SSI model into Open Sees computer program platform for pile foundation case using three types of nonlinear SSI element: nonlinear (p-y); nonlinear (q-z); nonlinear (t-z) to represent the load-displacement behavior of lateral load capacity; bearing at pile tip; skin friction of the pile, respectively. In this study, only the PySimple1Gen command is used to generate nonlinear (p-y) elements along the pile in Open Sees developed by Brandenberg (2004). The influence of two other nonlinear elements is insignificant to the response of the pile.

3.1.2 Raft Foundation

Raychowdhury and Hutchinson (2008) modified the load-displacement relationship of the pile foundation to be applied for shallow foundation case and calibrated the model based on shallow footing test. The nonlinear behavior of SSI for raft foundation is described using three nonlinear SSI elements: nonlinear (p-y); nonlinear (q-z); nonlinear (t-z) which represent the load-displacement behavior of lateral passive earth pressure at footing side; bearing capacity of footing; friction resistance along base of the footing, respectively. The nonlinear (p-y), (q-z), and (t-z) for shallow foundation case are implemented in Open Sees as PySimple2, QzSimple2, and TzSimple2 material models, respectively.

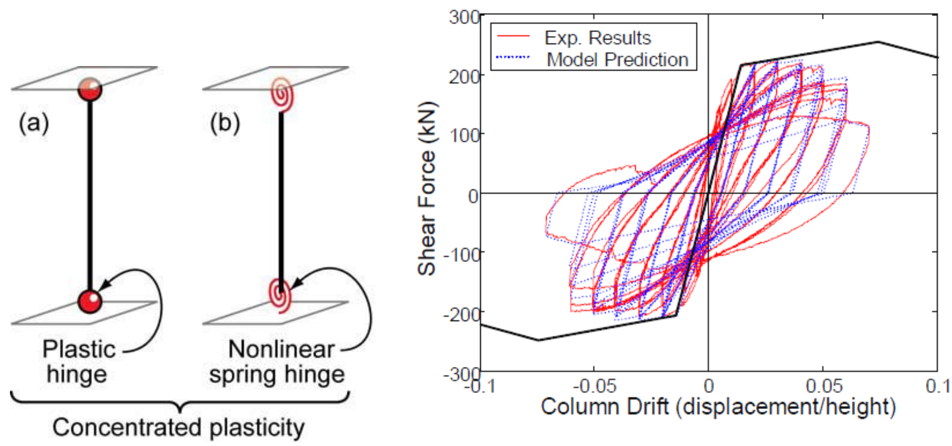

a) Lumped plasticity model
b) cyclic response of lumped plasticity model

Figure 3: a)Lumped plasticity model, b)cyclic response of lumped plasticity model

3.1.3 Structural Element

The nonlinear behavior of the structural element is described using lumped plasticity model which consists of elastic element and concentrated plastic hinge at each end as shown in Figure 3a. Concentrated plastic hinge is modeled using rotational spring where the monotonic backbone curve is calibrated from the experimental reinforced concrete test. Figure 3b shows the cyclic response of the nonlinear structural element using lumped plasticity model. The monotonic backbone curve of the concentrated plastic hinge is described by five parameters: yield moment (My), yield chord rotation (qy), hardening stiffness (Ks), capping rotation (qcap), and post-capping stiffness (Kc). These five parameters are determined based on the modeling parameter by Haselton et al. (2008) as recommended in PEER/ATC-72-1 (2010). The monotonic backbone curve of the concentrated plastic hinge is defined using Clough material model in OpenSees platform.

4. SEISMIC INPUT MOTIONS

The seismic input motions for the building are specified based on Indonesian Seismic Code SNI 03-1726-2003. The code determines the seismic design load based on design basis earthquake (DBE) corresponding to the uniform seismic hazard level of 10% probability of exceedance in 50 years. According to the code, Jakarta city is located in seismic Zone 4 with the peak base rock acceleration of 0.20g. Based on the subsoil condition at the site, the site can be categorized as medium soil site. The nonlinear time history analysis is required to be performed in maximum considered earthquake (MCE) level which is assumed to be 1.5 times the DBE level. The design response spectrum for MCE level is therefore defined for analysis.

Table 2: Selected earthquake ground motions

No.	Earthquake Event	Year	Denotation	M_w	PGA (g)
1	Cape Mendocino	1992	CM-EUR-090	7.0	0.18
2	Hector Mine	1999	HM-H-000	7.1	0.27
3	Imperial Valley	1979	IMP-CH-012	6.5	0.27
4	Loma Prieta	1989	LP-HSP-000	6.9	0.37
5	Superstition Hills	1987	SH-PR-360	6.5	0.30
6	Mentawai Island	2007	MEN-ISL-HNN	7.9	0.13
7	South Sumatra	2007	SO-SUM-HNN	8.4	0.04

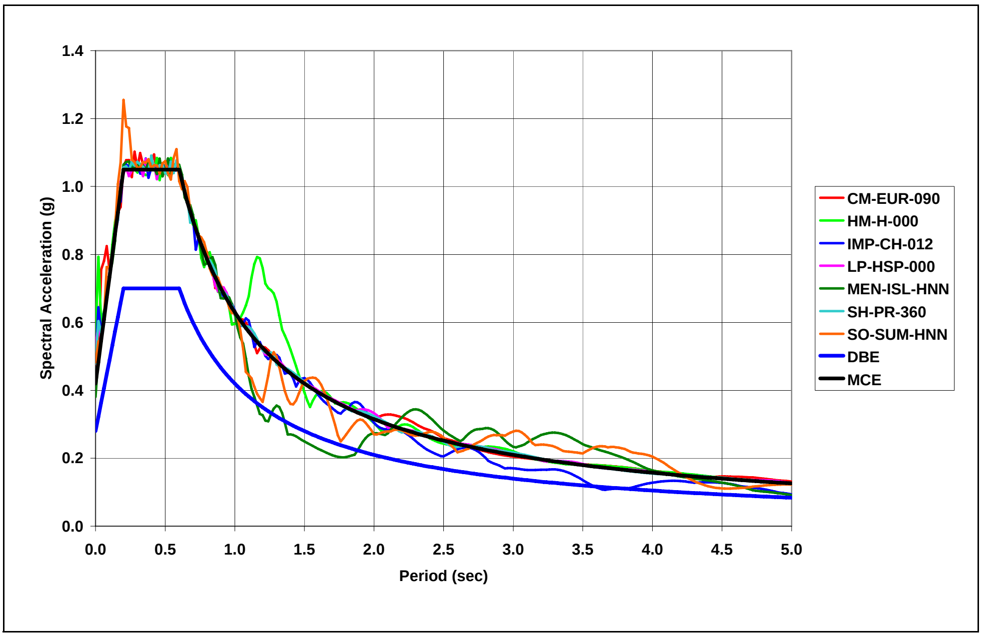

Figure 4: Response spectra of scaled ground motions

Seven earthquake records are used in this analysis to satisfy seismic design code requirement (UBC 1997, EURO8) for average response. Five strong earthquake records from worldwide database and two earthquake records from inside Indonesia area are selected to cover the wide range of earthquake variation as shown in Table 2. The ground motions are scaled to match with the MCE response spectrum by using spectral matching software RspMatch2005 (Hancock et al., 2006) as shown in Figure 4. Free-field site response analysis is then performed using SHAKE91 software (Idriss and Sun, 1991) to provide the seismic input motions along the different depths considered.

5. ANALYSIS RESULTS

In order to identify the effects of SSI on seismic response of the buildings, the nonlinear time history analysis is performed for three foundation cases: fixed (Non-SSI), raft (SSI), and pile (SSI) foundation cases and the analysis models for the three foundation cases are shown in Figure 5.

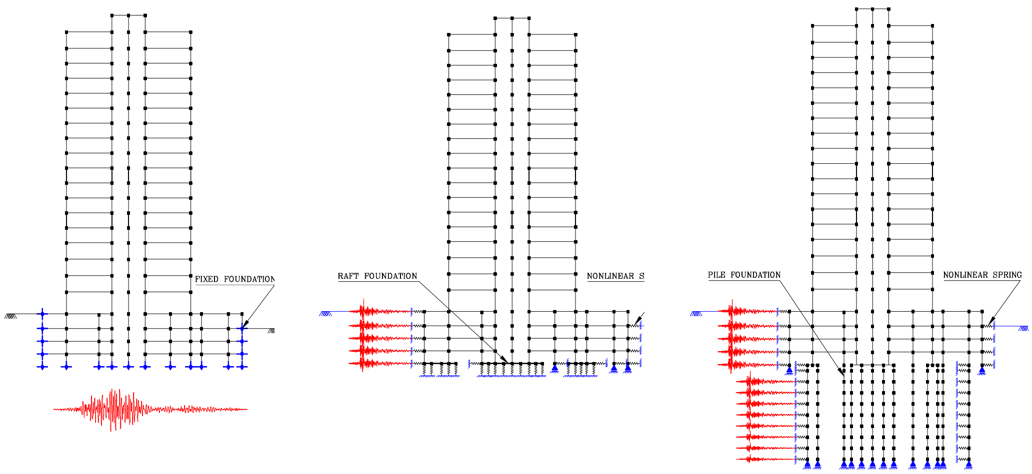

a) Fixed (Non-SSI) b) Raft (SSI) c) pile (SSI)

Figure 5: Fixed, raft and pile foundation models

5.1 Modal Analysis

Table 3 shows the results of natural period for non-SSI and SSI analyses. It is shown that the effects of SSI cause to increase natural periods as shown in Table3. The natural mode shapes of the building essentially have the similar pattern for the three foundation types as shown in Figure 6. A large difference of the natural mode shapes are only found at the basement level for the 3rd mode.

Table 3: Natural periods of building

Foundation Model	Natural Period (sec)		
	Mode 1	**Mode 2**	**Mode 3**
Fixed (Code)	1.632	-	-
Fixed	1.425	0.297	0.130
Pile	2.269	0.372	0.165
Raft	1.835	0.355	0.179

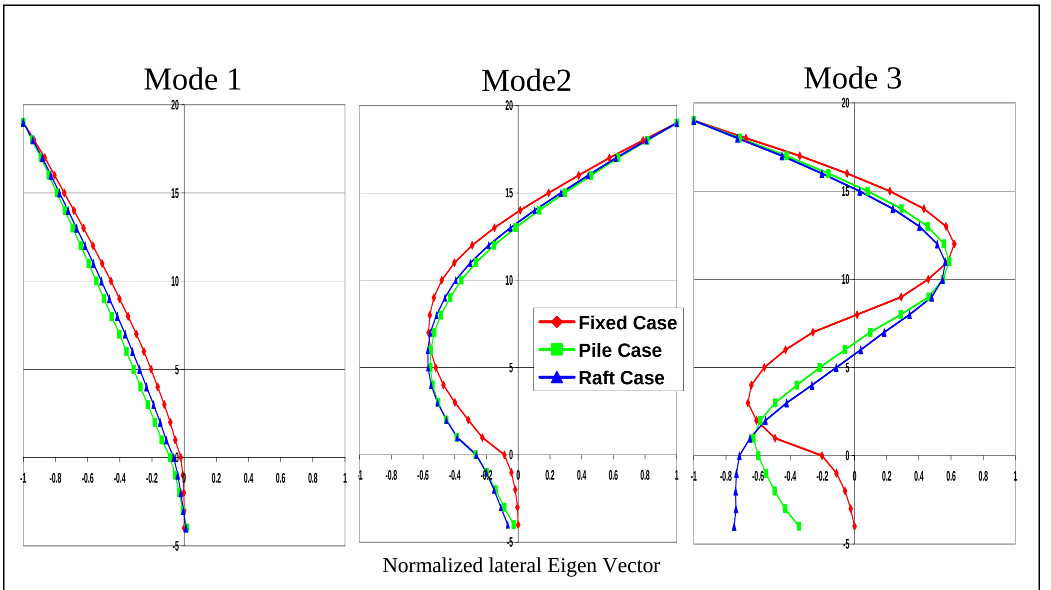

Figure 6: Natural mode shapes of building

5.2 Nonlinear Time History Analysis

The nonlinear time history analysis is performed to obtain the seismic response of the building. The seismic responses of the building are determined in term of force and deformation responses. The force responses are described as shear force and bending moment while the deformation response are described as relative displacement and interstory drift ratio.

5.2.1 Force Response

The average response profiles of shear force and bending moment from the seven earthquake ground motions are summarized in Figure 7. Non-SSI analysis shows the maximum response of shear force and bending moment except for the first floor level where the maximum responses are provided from SSI analysis. The responses of shear and bending moment above the basement level for pile and raft foundation cases are similar while the different responses are only found at the basement level with the larger response resulted from pile foundation case.

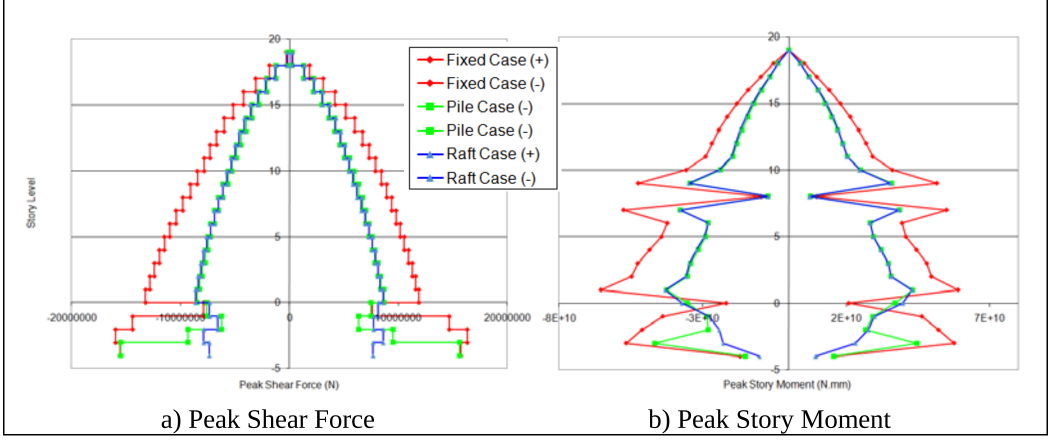

a) Peak Shear Force b) Peak Story Moment

Figure 7: Average response profile of force

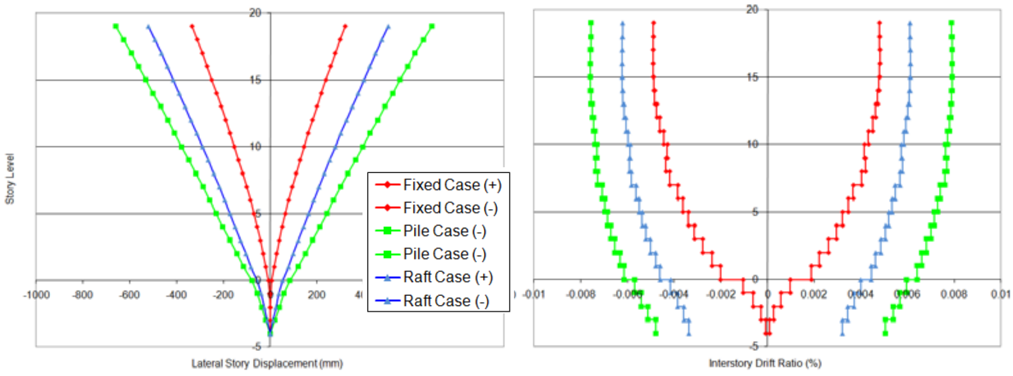

a) Lateral story displacement b) Interstory drift ratio

Figure 8: Average response profile of displacement

5.2.2 Deformation Response

The average response profiles of the peak story relative lateral displacement and the interstory drift ratio from the seven earthquake ground motions are summarized in Figure 8. The maximum relative lateral displacement and interstory drift ratio are provided from pile foundation case while the minimum values are provided from non-SSI case. The effects of SSI increase the deformation response of the building. The maximum relative displacement at the roof level increases about 55% to 100% for raft and pile foundation cases, respectively, compared to fixed foundation case.

6. CONCLUSION

The effects of SSI have been considered for a typical high-rise building in Jakarta, Indonesia. The results show that SSI analysis reduces seismic responses in term of peak story shear and moment. However, at the first floor level, the moment response from the SSI analysis gives a larger response than that of the non-SSI analysis. Therefore, the effects of SSI for this typical building are not always beneficial and may be detrimental in some part of the building.

REFERENCES

Boulanger, R. W., Curras, C. J., Kutter, B. L., Wilson, D. W., and Abghari, A., 1999. Seismic soil-pile-structure interaction experiments and analyses. *Journal of Geotechnical and Geoenvironmental Engineering*, Vol. 125, No. 9, pp.750-759.

Boulanger, R. W., 2000. The PySimple1, QzSimple1, and TzSimple material documentation. Document for the OpenSees platform.

Branderberg, S. J., 2004. PySimple1Gen OpenSees command. Document for OpenSees platform.

FEMA, 2000. Prestandard and commentary for the seismic rehabilitation of buildings. *Report No. FEMA–356*, Federal Emergency Management Agency.

Hancock, J., Lamprey, J. W., Abrahamson, N. A., Bommer, J. J., Markatis, A., McCoy, E., and Mendis, R., 2006. An improved method of matching response spectra of recorde earthquake ground motion using wavelets. *Journal of Earthquake Engineering*, Vol. 10, Special Issue 1, pp. 67-89.

Haselton, C. B., Liel, A. B., Taylor Lange, S., and Deierlein, G. G., 2008. Beam-column element model calibrated for predicting flexural response leading to global collapse of RC frame buildings. *PEER Report 2007/03*, Pacific Earthquake Engineering Research Center, University of California, Berkeley, California.

Idriss, I. M., and Sun, J., 1991. *User's Manual for SHAKE91*. Center for Geotechnical Modeling, Department of Civil and Environmental Engineering, University of California, Davis, CA.

Irsyam, M., Dangkua, D. T., Hendriyawan, Hoedajanto, D., Hutapea, B. M., Kertapati, E. K., Boen, T., and Petersen, M. D., 2008. Proposed seismic hazard maps of Sumatra and Java Island and microzonation study of Jakarta city, Indonesia. *Journal of Earth System Science*, Vol. 117, pp.865-878.

Jeremic, B., Kunnath, S., and Xiong, F., 2004. Influence of soil-foundation-structure interaction on seismic response of the I-880 viaduct. *Journal of Engineering Structure*, Vol.26, Issue 3, pp.391-402.

Mylonakis, G., Gazetas, G., Nikolaou, S., and Michaelides, O., 2000b. The role of soil on the collapse of 18 piers of the hanshin expressway in the Kobe earthquake. *Proceedings of 12th World Conference on Earthquake Engineering*, New Zealand, Paper No. 1074.

PEER, 2007. PEER Column Database. Pacific Earthquake Engineering Research Center, University of California, Berkeley, California.

PEER/ATC-72-1, 2010. Modeling and acceptance criteria for seimic design and analysis of tall buildings. Applied Technology Council, Redwood City, California.

Raychowdhury, P., and Hutchinson, T., 2008. Nonlinear material models for Winkler-based shallow foundation response evaluation. *Proceedings of GeoCongress 2008*, New Orleans, Louisiana, March, pp.686-693.

SNI, 2003. Indonesian Seismic Code for Buildings. SNI 03-1746-2003, Standard National Indonesia, Department of Public Work.

Yue, M., and Wang, Y., 2009. Soil-structure interaction of high-rise building resting on soft soil. *Electronic Journal of Geotechnical Engineering*, Vol.3, Bund. D, pp.1-20

STUDY ON RISKS AND HUMAN EVACUATION PLAN IN KOTO DELTA AREA IN JAPAN, DURING LARGE FLOOD

Kohei MAKINODAN[1], Miho OHARA[2] and Kimiro MEGURO[3]

[1]Master Student, Department of Civil Engineering,
The University of Tokyo, Japan
makinodan@risk-mg.iis.u-tokyo.ac.jp
[2]Assosiate Professor, Interfaculty Initiative in Information Studies
/Institute of Industrial Science,
The University of Tokyo, Japan
[3]Professor, Interfaculty Initiative in Information Studies
/Institute of Industrial Science,
The University of Tokyo, Japan

ABSTRACT

In recent years, it is reported that the Koto Delta Area in Tokyo whose elevation is lower than sea level, has large-scale flood risk. When flood occurs, the municipalities give the evacuation counsel or evacuation order. However people don't evacuate to the area which flood doesn't reach because people don't have the imagination of flood risk. For these reasons, people living in the area which flood reach will be severely damaged. In order to reduce this damage, it is important to study action of emergent evacuation after flood occurs. This paper focuses on detail analysis of flood risk of the whole Koto Delta Area using GIS data of flood, population distribution and building inventory. Then, using the result of analysis, we discussed the appropriate human evacuation plan of the area. Based on the obtained results, we can conclude that if people use only evacuation centers officially designated by local municipalities, about 75% of them can't evacuate successfully. However, if they use existing tall buildings as evacuation centers, they can all evacuate successfully.

***Keywords**: Flood, Risk analysis, Evacuation*

1. INTRODUCTION

East part of the Tokyo Metropolitan area has high risk of large-scale urban flood. Especially, Koto Delta Area whose elevation is lower than sea level is surrounded by rivers and expected to face the severe problems of human evacuation in the future flood disaster. According to the Cabinet Office in Japan, the maximum predicted number of death is approximately 3,500 and that of displaced number of people is approximately 720,000 [1)] in case that drainage pump station, drainage pump vehicle and water gate are unavailable. In this paper, considering whole Koto Delta as a study area, we carried out detail analysis of flood risk of the area using GIS data of flood, population distribution and building inventory.

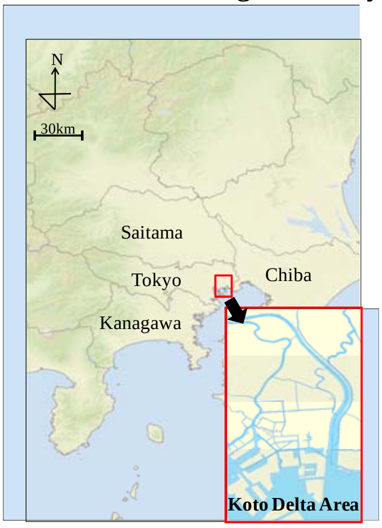

Figure 1: Location of Koto Delta Area

2. IMPACT OF LARGE-SCALE FLOOD ON KOTO DELTA AREA

Detail flood risk analysis of the area was conducted using GIS in a 125m-mesh with flood data from Cabinet Office[2)] and additional information like population distribution and building inventory. This paper discuss on large scale flood impact and problems on evacuation.

2.1 Expected inundation in Koto Delta Area

Figure 2 shows inundated depth and inundated area which comes up 2m of depth in most of the area. In this area, residents can't use lower buildings (below 2 floors) and the number of these buildings is 49,449 among total 114,646 buildings.

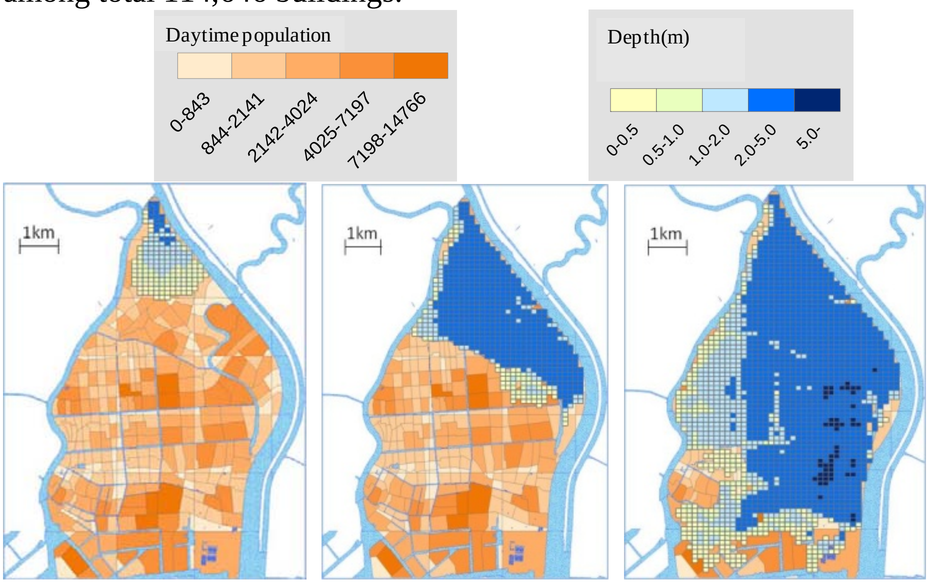

a) 1 hour later b) 6 hours later c) 24 hours later

Figure 2: Alteration of inundated depth

2.2 The area where it is impossible to walk

Figure 3 shows the area where people can't walk after flood occurs estimated by comparing inundated depth to limited depth for walking calculated by equation(1) [3)] in each mesh. It is impossible to walk in most inundated area.

$$h_L = 0.7 \times (1 - u/2.5) \qquad (1)$$

h_L : limited depth for walking (m), u : velocity(m/s)

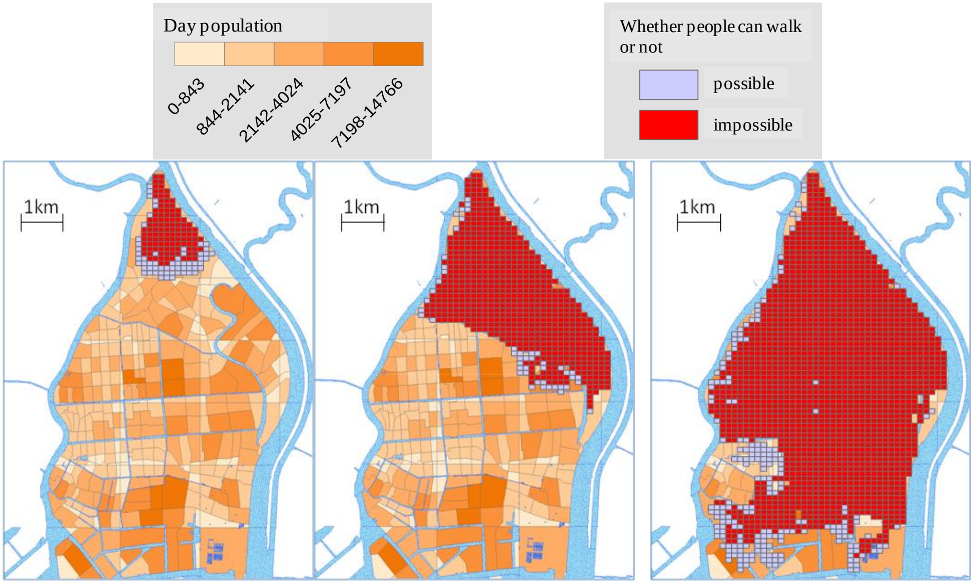

a) 1 hour later b) 6 hours later c) 24 hours later

Figure 3: The area where it is impossible to walk

2.3 The number of damaged wooden houses

The number of damaged wooden houses is also estimated. Table 1 shows the relationship between hydrodynamic pressures and damaged wooden houses. Hydrodynamic forces are defined as multiplication of inundated depth and square velocity. Figure 4 shows the number of wooden houses which fall under different levels described in Table 1. The number of wooden houses which are slightly damaged is 628, the number of damaged wooden houses which have difficulties in living and the number of wooden houses which can be washed out is 283.

Table 1: Relationship between hydrodynamic pressure and damaged wooden houses[4)5)]

Pressure(m^3/s^2)	Damaged wooden houses
Level 1 (0〜under 1.5)	Houses hardly have the potential to be damaged
Level 2 (1.5〜under 2.5)	Wooden houses are damaged somewhat
Level 3 (2.5〜 under 20)	Wooden houses can be damaged, then people can't live in these wooden houses
レベル4 (more than 20)	Wooden houses have the potential to wash out

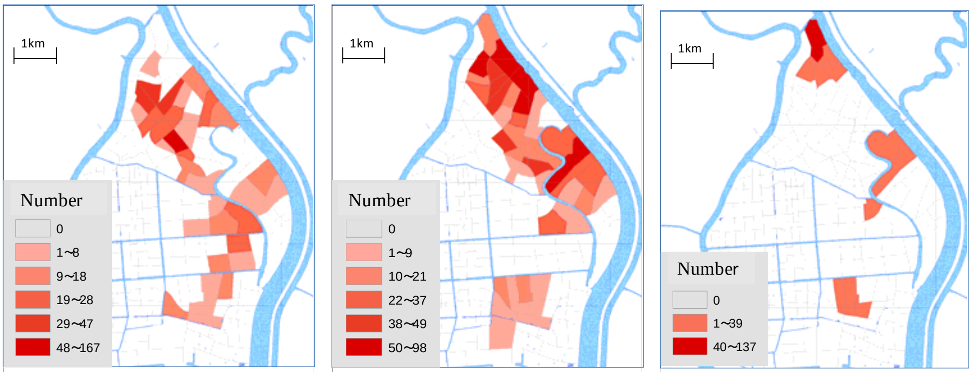

a) Level 2 b) Level 3 c) Level 4

Figure 4: The number of damaged wooden houses

3. STUDY ON APPROPRIATE EVACUATION AT FLOOD DISASTER

In this section, considering the area where flood can reach within 1 hour, we discuss the appropriate human evacuation plan. Considering some places as evacuation center, we compare the capacity in evacuation centers to the number of people who should evacuate at the flood disaster. Based on the obtained result, we discuss how many people can be accommodated in following 3 cases.

(1) In case of using evacuation centers officially designated by local municipalities
(2) In case of using municipal building as evacuation center in addition to case (1)
(3) In case of using other tall building as evacuation center in addition to case (2)

Also, based on location of evacuation centers, required time from each place to evacuation center is estimated in the area where flood can reach within 1 hour.

3.1 Capacity for evacuation

3.1.1 Capacity of evacuation centers officially designated by local municipalities

Figure 5 shows the capacity in evacuation centers officially designated by local municipalities and the number of people who should evacuate there under case (1). The capacity in each evacuation center is defined as the number subtracted the capacity in gym, 1st floor and 2nd floor from capacity in each evacuation center during peacetime which is published in municipalities. The number of people who should evacuate is defined as floor area in each house, which are under area of more than $1.5m^3/s^2$ (hydrodynamic pressure) and more than 2m (inundated depth), divided by floor area per capita in the target area. Table2 shows capacity and the number of people who should evacuate in each evacuation centers. The estimated number of people who should be evacuated to each evacuation center is bigger than the capacity in most evacuation centers. The difference between the number of people who should be evacuated and the capacity is 40 times in one center. Figure 6 shows the number of people who should be evacuated in each district of the town before and after using evacuation centers officially designated by local municipalities. The capacity in evacuation centers is insufficient in most district of the town and there is variation of the number of people who can be accommodated.

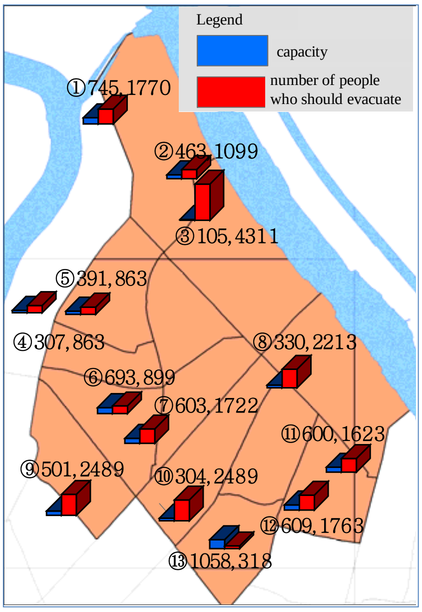

Figure 5: The capacity and the number of people who should evacuate

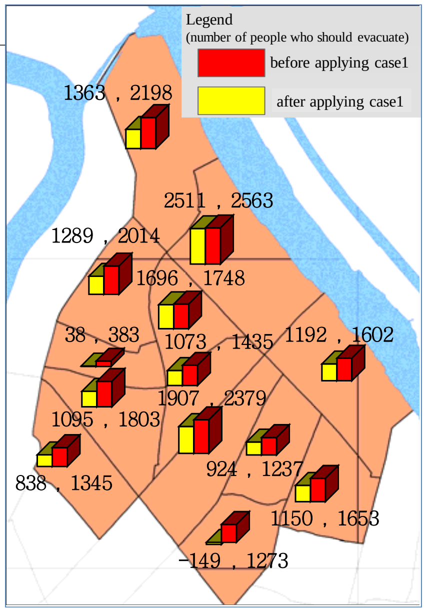

Figure 6: Alteration of the number of people who should evacuate in each area

Table 2: Capacity and the number of people who should evacuate in each evacuation center

Evacuation designated by local municipalities		Capacity	Number of people who should evacuate
①	Kanegafuchi junior high school	745	1,770
②	Sumida elementary school	463	1,099
③	Sumida second elementary school	105	4,311
④	Tsutsumi elementary school	307	863
⑤	Umewaka elementary school	391	863
⑥	Mukoujima junior high school	693	899
⑦	Terajima second elementary school	603	1722
⑧	Yahiro elementary school	330	2,213
⑨	Terajima elementary school	501	2,489
⑩	Terajima third elementary school	304	2,489
⑪	Azuma fifth elementary school	600	1,628
⑫	Azauma second junior high school	609	1,763
⑬	Terajima junior high school	1,058	318

3.1.2 Additional capacity of evacuation using municipal buildings

Figure 7 shows the capacity in municipal buildings in this area such as apartment administered by municipalities. The capacity in each municipal building is calculated based on the floor area of corridors in municipal buildings divided by floor area per capita. The total capacity in the targeted area is 40,409. This number is bigger than the total number of people who should evacuate. However, the distribution of municipal buildings is not even. Many people can't reach local evacuation centers. Therefore, case (2) is insufficient as emergency evacuation centers after flood occurs.

3.1.3 Additional capacity using tall buildings for evacuation

Figure 8 shows the capacity in evacuation centers officially designated by local municipalities, municipal houses and other tall buildings and the number of people who should be evacuated in each district of the town. Existing tall buildings which are non-wooden house and more than 4 stories (for example, apartment, office and educational facility) are considered as additional evacuation centers. The number of people who should be evacuated is bigger than the capacity in most districts of the town. Also, in the area which doesn't have enough capacity of accommodation, if municipalities appropriately guide people to evacuate in the centers next to these areas, all people can be accommodated in safer location

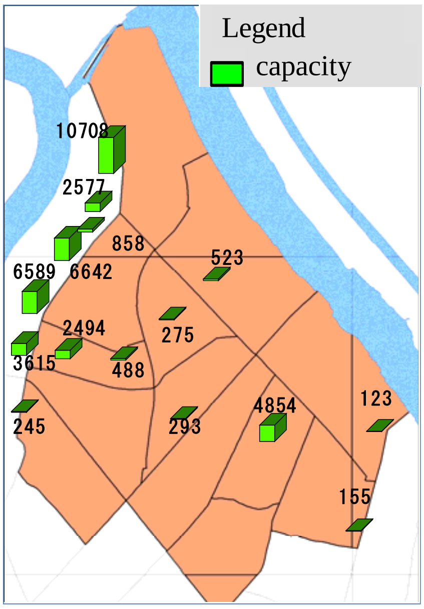

Figure 7: Capacity in case 2

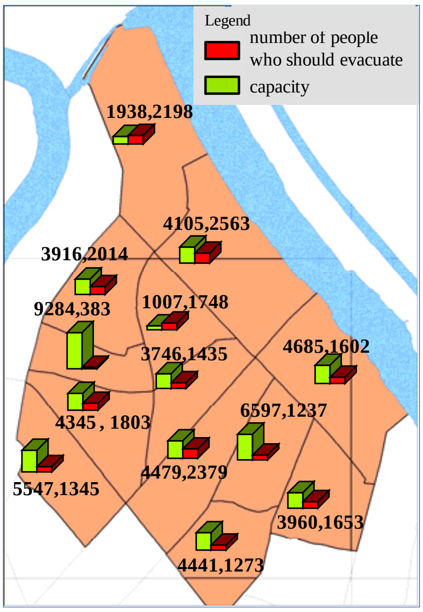

Figure 8: Capacity in case 3

3.2 Required time to evacuation center

In this section, time required for evacuating people to evacuation centers is estimated. We estimated required time from central point of 125m-mesh which is used in GIS to each evacuation centers officially designated by local municipalities in the area which flood reaches within 1 hour. At the beginning, distance from each evacuation center to each central point of 125m-mesh is measured by using GIS. Then required time for evacuation was calculated as distances divided by walking speed, which of adult male is 1.5m/s, adult female is 1.3m/s and elderly people and children is 1.0m/s based on empiric formula of Fruin[6)]. Figure 9 shows the number of meshes per each required times in the area which flood reaches within 1 hour. In most mesh, required time is under 10 minutes. So, the distribution of evacuation centers officially designated by local municipalities is comparatively even.

Figure 10 shows the worst timing that an adult male should start evacuation to evacuation centers officially designated by local municipalities. After this timing, he become impossible to evacuate as flood water depth exceed the limited depth for walking explained in equation (1). Red meshes in this figure show the area that residents don’t have lead time for evacuation before flood starts. Therefore, despite the distribution of evacuation centers is even, some residents don’t have enough time for evacuation.

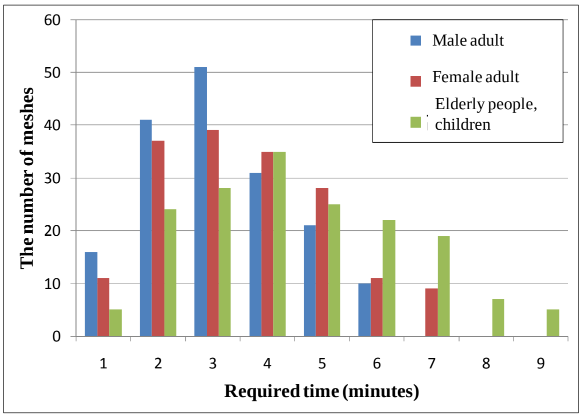

Figure 9: The number of meshes per each required time

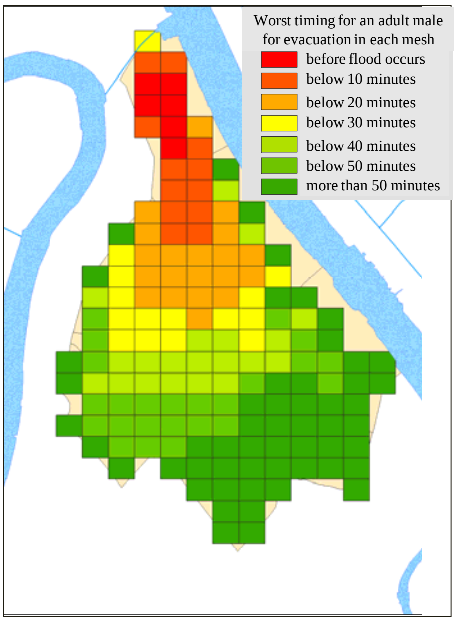

Figure 10: Worst timing for an adult male for evacuation in each mesh

3.3 Proposal of appropriate evacuation plan

In this research, emergency evacuation for residents is discussed. In the view point of capacity and the number of people who should evacuate, we can conclude that if people use only evacuation centers officially designated by local municipalities, about 70% of them can’t be evacuated successfully. However, if they use existing tall buildings as additional evacuation centers, they all can be evacuated successfully. In the view point of location of evacuation centers, although the distribution of evacuation centers officially designated by local municipalities is even, there are many areas where people don't have enough time for evacuation before flood starts. In order to solve this problem, it is important to provide evacuation counsel or evacuation order to residents earlier before flood starts considering the required time for evacuation.

4. CONCLUSIONS

In this research, considering whole Koto Delta as a study area, we carried out detail analysis of flood risk of the area using GIS data of flood, population distribution and building inventory. Then, using the result of analysis, we discussed the appropriate human evacuation plan of the area. Although emergency evacuation for residents after flood is discussed in this research, some problems related to isolated residents in many buildings are remained. From now on, it's important to study appropriate preparedness for evacuation and increase resident's awareness on the flood disaster risk.

REFERENCES

Cabinet Office, Japan, http://www.bousai.go.jp/jishin/chubou/suigai/100402/100402_shiryo_2.pdf, 2010, 4, 39-41.

Bureau of Urban Development Tokyo Metropolitan Government, Survey on Land Use in Tokyo Metropolitan Area.

Kyozo SUGA， Preliminary Study on Feasible Safe Evacuation in Flood Disaster, Annual Journal of Hydraulic Engineering, 1995, 2, 879-882.

Yoshiki KAWATA and Hajime NAKAGAWA, Flood Disaster in the MISUMI RIVER - Flooding and Damages of Houses - , Disaster Prevention Research Institute Annuals, 1984, 4, 179-196.

Satoshi SATO, Fumihiko IMAMURA and Nobuo SHUTO, Numerical Simulation of Flood and Damage to Houses – A Case of the Yoshida River due to Typhoon No.8610 -, Annual Journal of Hydraulic Engineering, 1989, 2, 331-336.

John J. Fruin, PEDESTRIAN - Planning and Design -, Kajima Institute Publishing Company Ltd, 1976

INFLUENCE OF SURFACE COMPLEXITY TO GCPS DISTRIBUTION

Sudniran Phetcharat , Masahiko Nagai and Taravudh Tipdecho
RS & GIS, Asian Institute of Technology, Thailand
sudniran@gmail.com

ABSTRACT

Geometric correction is unavoidable in order to increase precision and eliminate the displacement of positions in the images taken by satellite imaging due to the positioning of the receiver and the curvature of the earth. The geometric correction process of satellite image with no physical sensor parameter provided requires small group of GCPs. The problem is how are GCPs to be distributed so that precision is achieved. Generally GCPs is distributed evenly throughout the surface but that is not appropriate when there are different types of the surfaces because more relief displacement occurs at high level. The polynomial model is one of the most useful tools for geometric correction requiring GCPs to determine the coefficients of the equation for the unknown variables. In this study, conventional 3D polynomial equations 2nd order is employed as the tool to determine GCPs distribution characteristic. The principle of GCPs distribution in this study is based on influences of the complexity of the surfaces. The surfaces are divided into two complexity types consisting of low complexity and high complexity area. Results of the comparative study for GCPs selection based on the principle of evenly distributed and the principles of complexity through the examination of accuracy of RMSE by ICPs at 68 points was 2.11 pixels and 0.96 pixels respectively. This leads to the conclusion that the transformation from object space to image space using polynomial and a set of GCPs along with consideration of the complexity of the surface yields results with higher accuracy than the conventional evenly distributed method. This is because GCPs distribution corresponds with surface complexity. The results of this study reduce the time needed for trial and error in selecting the GCPs' location and can be applied for the different images by assigning a weighting criteria for high and low complexity to 55 and 45 percent respectively.

Keywords*: surface complexity, ground control points, polynomial coefficients function*

1. INTRODUCTION

Aerial photographs or satellite images are the basic data used in the analysis of data in the geographic information system (GIS), remote sensing, or mapping. The image acquisition process derived from the different type of sensors used. Ayoub (2008) revealed that geometrical distortions of current pushbroom satellites such as SPOT, ASTER, Quickbird, and HiRise can be categorized under two main causes: the modeling inaccuracy of the CCD sensor geometry and the jitter of the instrument's platform during image acquisition. Distortion of the image is unavoidable, especially in photogrammetry. Likewise, high resolution satellite images are prone to geometric distortions and to correct these imprecision, geometric corrections is a vital process (Arif, 2006). Major distortions include internal distortion and external distortion. The internal distortion is the distortion within a system that can be adjusted by using the characteristics of a sensor such as lens distortion which is adjusted using co-linearity equation. The external distortion is an outside error from external sensor characteristics such as the curvature of the Earth, change the condition of the atmosphere, reflectance characteristics of light and altitude of the surface in the vicinity. These errors are difficult to control and they directly affect pixel position making them inconsistent with the position on the ground. The characteristics of the ground depths, high, low and unevenness can especially cause distortion in the manner of relief displacement. In some cases the images used in the analysis have no information on physical sensor model subjected to adjustment by other appropriate models. One of the many models used is the polynomial model, a simple and convenient model for analyzing. This model can transform the object coordinates to the image coordinates and convert data from 3 dimensional to 2 dimensional data. This transformation by using ground control points may be obtained from the survey using integrated information from ground survey, photogrammetry or GPS which consists of the coordinates X, Y. and Z. Results of the transformation are the coefficient of polynomial equations. Generally, the polynomial equations order in photogrammetry will not exceed the 3rd order, because it may result in errors rather than accuracy.

2. STUDY AREA AND GCPs AVAILABILITY

The area studied is located in Chiang Mai and Lampoon, Northern provinces of Thailand. The distance from Bangkok to the location is approximately 600-km. The area studied has a variety of surface characteristics consisting of both flat area and highly complex surfaces. The coordinates of the target area at the upper left is 98.83040E, 18.7702N and at the lower right is 99.02550E, 18.5918N. The interested area covers approximately is 406 square kilometers of land. Surface complexity observed from DEM shows diversity of surface type. High complex area (mountainous terrain) covers around 30% of the land in the north-west zone and the remaining 70% in the eastern and southern zones of the image is low complex areas (urban). The image in Figure 1 showing the landscape of the area was acquired from worldview-1 on February 23, 2008. Worldview-1 image satellite is operating at an altitude of 496 kilometers with very high resolution 50 cm panchromatic at nadir. Geolocation accuracy specification of the instrument is 6.5 m CE90 at nadir, with actual accuracy in the range of 4.0 – 5.5 m CE90 at nadir, excluding terrain and off-nadir effects.

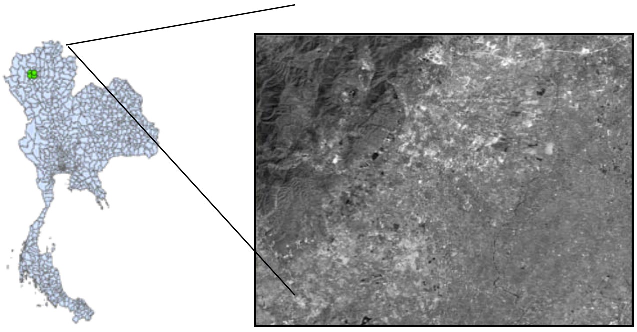

Figure 1: Study area in Chiangmai and Lampoon, Thailand.

There are 78 points GCPs and Independent Check Points (ICPs) for the image provided by Land Develop Department of Thailand (LDD) with an accuracy of 0.2-m. Acquisition method the position of GCPs and ICPs by using static and kinematic GPS survey.

3. 3D POLYNOMIAL MODEL

Polynomial Model is the equation used to represent the existing data. A polynomial equation can be created by determining the coefficient of the control point, which depends on the nature and complexity of surface data. In general, the polynomial equations used for modifying the images are often found in the 2nd order or 3rd order. Independents variables used to create an equation consists of variables X, Y and Z where X and Y are the coordinates of the plane and Z is the level of control points. Dependent variables are the position of the pixels r_p and c_p where r_p is the position of the image on the horizontal axis, the c_p is the position of the image on the vertical axis. Polynomial modeling is used as a tool to create new surface model with enhanced accuracy both in the shape and position of the image by using control points to determine the coefficients of the model. The coordinates' functions are as shown below.

$$r_p = p(X_n, Y_n, Z_n) \quad (1)$$
$$c_p = p(X_n, Y_n, Z_n) \quad (2)$$

where;
r_n = row of pixel in image
c_n = column of pixel in image
X_n, Y_n, Z_n = ground coordinate values

Function $p(X_n, Y_n, Z_n)$ for second order polynomial can be created is as follows;
2nd order Polynomial

$$r_p = a_0 + a_1X + a_2Y + a_3Z + a_4XY + a_5XZ + a_6YZ + a_7X^2 + a_8Y^2 + a_9Z^2 \quad (3)$$
$$c_p = a_0 + a_1X + a_2Y + a_3Z + a_4XY + a_5XZ + a_6YZ + a_7X^2 + a_8Y^2 + a_9Z^2 \quad (4)$$

In general, polynomial transformations with terms up to the first order can model a rotation, a scale, and a translation and are computationally economical. As additional terms are added, more complex warping can be achieved.

The a_j, j = *0, 1, ...* , 9 is the coefficient that is unknown. Coefficient a_j can be calculated using the least square method for the error E of all data n deviated from the function $p(X_n, Y_n, Z_n)$ as follow;

$$E = \sum_{i=1}^{n}\left[r_p - \left(a_0 + a_1 X + a_2 Y + \cdots + a_9 Z^2\right)\right]^2 \tag{5}$$

Then associate the minimal errors with E by differentiation and assign the equation to equal to zero, causing the equation to include the following sub-10 equations.

$$\frac{\partial E}{\partial a_0} = 0,\ \frac{\partial E}{\partial a_1} = 0, \frac{\partial E}{\partial a_2} = 0, \ldots, \frac{\partial E}{\partial a_9} = 0 \tag{6}$$

Results of the equations will be as shown in the matrix which includes the following sub-10 equations.

$$\begin{bmatrix} n & \sum_{i=1}^{n} X_i & \sum_{i=1}^{n} Y_i & \cdots & \sum_{i=1}^{n} Z_i^2 \\ \sum_{i=1}^{n} X_i & \sum_{i=1}^{n} X_i^2 & \sum_{i=1}^{n} X_i Y_i & \cdots & \sum_{i=1}^{n} X_i Z_i^2 \\ \sum_{i=1}^{n} Y_i & \sum_{i=1}^{n} X_i Y_i & \sum_{i=1}^{n} Y_i^2 & \cdots & \sum_{i=1}^{n} Y_i Z_i^2 \\ \vdots & \vdots & \vdots & \cdots & \vdots \\ \sum_{i=1}^{n} Z_i^2 & \sum_{i=1}^{n} X_i Z_i^2 & \sum_{i=1}^{n} Y_i Z_i^2 & \ddots & \sum_{i=1}^{n} Z_i^4 \end{bmatrix} \begin{Bmatrix} a_0 \\ a_1 \\ a_2 \\ \vdots \\ a_9 \end{Bmatrix} = \begin{matrix} \sum_{i=1}^{n} r_p \\ \sum_{i=1}^{n} X_i r_p \\ \sum_{i=1}^{n} Y_i r_p \\ \vdots \\ \sum_{i=1}^{n} Z_i^2 r_p \end{matrix} \tag{7}$$

The square matrix size (10x10) on the left side of this equation is a symmetric matrix with known value along with the vector size (10x1) on the right side of this equation. The value coefficients a*0*, a*1*, a*2*, ..., a9 can be calculated by using the methods of solving equations by Invert Matrix.

4. GCPs SELECTION AND DISTRIBUTION BY EVEN DISTRIBUTION METHOD

GCPs should be evenly distributed throughout the whole image (Jingtao, 2009). Selection of control points in order to generate geometric corrections is usually done by evenly distributing GCPs throughout the area used in the square grid. The advantage of even distribution is that it makes it easy to calculate and allocate the position of GCPs. The disadvantage is the limited accuracy and is not considering the topography that makes the accuracy of the model unreliable.

The location of GCPs for each point of that method may be located at inaccessible locations such as water bodies or mountain peaks. Therefore this method makes it easy to locate positions on the image but difficult to actualize on the field.

5. SURFACE COMPLEXITY CLASSIFICATION

Complexity of surface is shown the different surface or terrain characteristic at any selected point compared with the around that point. Generally, the complexity of a surface area is classified by the intensity of the variety of high and low lands. In some cases, at any high areas may have low complexity and at any low areas maybe more complex. The key factors identifying terrain complexity consist of height and the Standard Deviation (STDEV) of the heights in the interested area.

In the conventional GCPs distribution is there is only one area/zone, not classify the surface characteristic on the images, some area consists of different types of surface characteristic/complexity. Consequently, the area that is used to determine the distribution of GCPs should be split into two zones. Each zone is to be classified by its height and standard deviation (STDEV).

Many histogram-based threshold approaches (Boukharouba, 1985) regard finding a threshold in the histogram for binarizing an image as approximating the histogram with two distribution functions. Quen-Zong (2005) proposed the procedures to find the Change-point detection from cumulative histograms as threshold selection by determine maximum distant from line L to cumulative histogram, line L is connected between first points to last point on cumulative histogram.

5.1. Changing Point Detection by Using Height Distribution

Zoning height can be identified using data collected from each grid point of DEM data. This data is then used to create a graph of frequency distribution. According to Quen-Zong (2005), the changing point can be determined using the percentage of cumulative data from the cumulative curve.

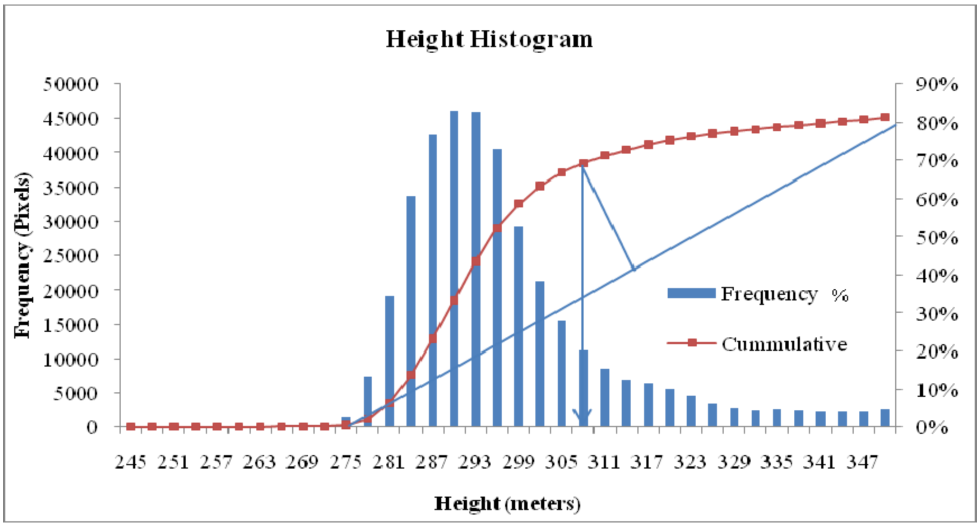

Figure 2: Histogram of Height and Cumulative Distribution

Figure 2 shows the distribution on the X-axis as height in meters, the left side of the Y-axis is the frequency of each height interval and right side of the Y-axis is the cumulative percentage of each height interval. Information from Figure 3 identifies the changing height point as 308 meters.

5.2 Changing Point Detection Using Standard Deviation (STDEV) Distribution

STDEV is achieved as the result of the calculation process using a 3x3 matrix for each height pixel. The STDEV result represents and locates the center of the matrix and the same calculation is used to determine the STDEV for the entire image. To create a standard deviation histogram the proposed method by Quen-Zong (2005) is also used in the determination of the changing point.

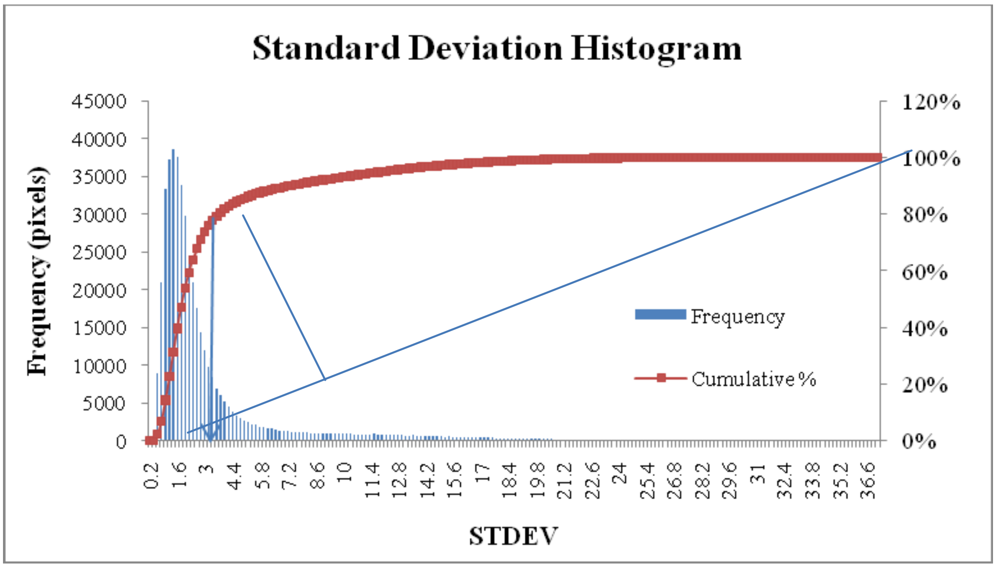

Figure 3: Histogram of Standard Deviation Distribution

Figure 3 shows the distribution of STDEV value on the X-axis is with the left side of the Y-axis being the frequency of each STDEV interval and right side of the Y-axis being the cumulative percentage of each STDEV interval. The changing STDEV point in this figure is 3.

6. CLASSIFICATION/ZONING

After the changing points are found, both height frequency distribution and STDEV frequency distribution information will be available for use to classify the surface into zones. The classification is done by choosing a height of greater than 308 meters and the STDEV of more than 3 as a high complexity zone and those areas with the height of less than 308 m and the STDEV value of below 3 are to be classified as the low complexity zone.

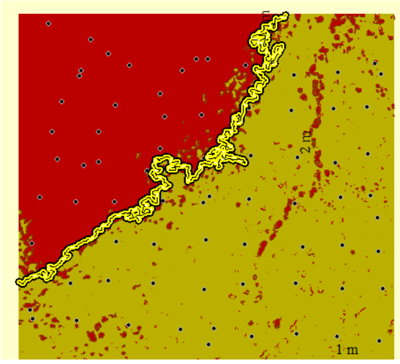

Figure 4: Two zones are separated by complexity classification

Zoning via Global Mapper software is shown in the Figure 4. Here the area is divided into 2 zones; high complexity at the north-east area and low complexity at the south-west area. The zones in the image are separated by the yellow line.

7. NUMBER OF GCPS FOR EACH ZONE

The model used in the geometric correction for identifying the number and positions of GCPs in this study is the 2^{nd} order of 3D polynomial. There are ten variables used in the form of coefficients of the polynomial consisting of a_0 to a_9. The required amount of GCPs for 2^{nd} order is fixed ten points for an image. Imagery is classified into two zones using the zoning method and the ten points are distributed to those two zones. The number of GCPs to be distributed for each zone is determined through consideration of both the area size and the level of complexity.

The proportion of the area size (measured from the image) between the high and low complexity zones without considering the level of complexity are at the rationed as 0.35 and 0.65 parts respectively. The trial weights for level of complexity are assigned to 0.55 - 0.80. This study proposes the method of calculation for the number of GCPs in each zone as;

$$rGCP_i = \frac{A_i W_i}{\sum_{i=1}^{n} A_i W_i} \; x \; tGCP \qquad (8)$$

where;
$rGCP_i$ = GCPs Requirement of Zone i
tGCP = Total GCPs Requirement (10 points in this study)
A_i = Proportional Area Size of Zone i
W_i = Trial Designed Weight for Zone i

Table 1: Trial weighting the complexity and amount of GCPs for each zone

Cases	High Complex					Low Complex					Total
	Area (%)	**Weight**	**Area x Wt.**	**% Influence**	**GCPs - N**	**Area (%)**	**Weight**	**Area x Wt.**	**% Influence**	**GCPs - N**	**GCPs Required**
Event. Distr.	10 GCPs										
I	35	**0.55**	19.3	39.7	**4**	65	**0.45**	29.3	60.3	**6**	10
II	35	**0.65**	22.8	50.0	**5**	65	**0.35**	22.8	50.0	**5**	10
III	35	**0.74**	25.9	60.5	**6**	65	**0.26**	16.9	39.5	**4**	10
IV	35	**0.81**	28.4	69.7	**7**	65	**0.19**	12.4	30.3	**3**	10

Table 1 shows five scenarios for the case being studied. In the first scenario, GCPs is evenly and proportionally distributed throughout the area based on the fundamental principles of the using ten GCPs points over the entire image on a regular basis. For all cases, the area sizes are the same in proportion. As an example, the calculation for case 1 is processed under the information criteria of the high complexity area having the influence weight of 0.55 and an area proportion of 0.35 (fixed) and the low complexity area having an influence weight is 0.45 and an area proportion of 0.65 (also fixed). Based on the information, the amounts of GCPs distributed in each zone are calculated to be 4 and 6 in the low and high complexity zones respectively. Results of the other scenarios are calculated as shown in the Table 1.

8. ALLOCATION OF GCPS LOCATION USING TRIANGULATION

Positioning of GCPs in each zone should be distributed suitably. This is to make sure that the error can be distributed equally to each zone, which in this study selection of GCPs is selected by using a triangle shape, because triangle is more stability shape. Number of GCPs from the previous section was selected from the existed GCPs provided by Land Development Department Thailand (LDD). Triangles created should be similar in size. Selected locations of GCPs are shown in the images below.

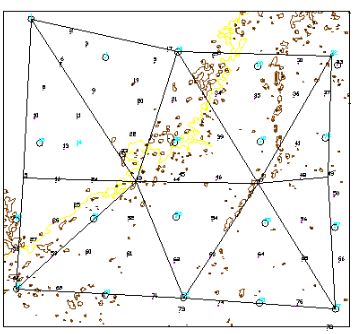

(a) Evenly Distributed

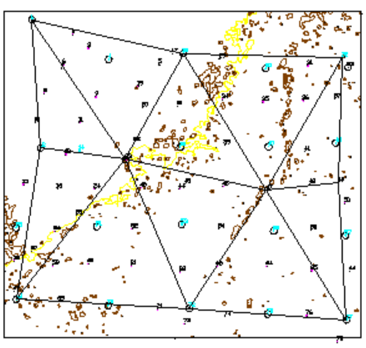

(b) Case I 4 – 6

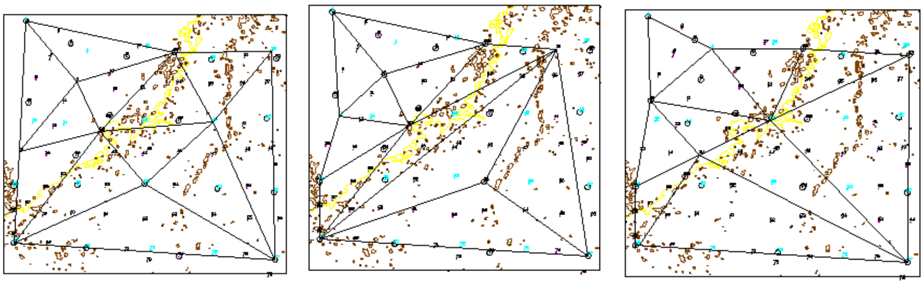

(c) Case II 5 – 5 (d) Case III 6 – 4 (e) Case IV 7 - 3

Figure 5: GCPS allocation for each trial cases
(a) Evenly Distributed (b) Trial Case I (c) Trial Case II (d) Trial Case III (e) Trial Case IV

The first is the case scenario where GCPs is evenly distributed throughout the area. Latter scenarios in cases 1 to 4 represent proportional distribution of GCPs. For example, the interpretation of in the case scenario III, is that the number 6 – 4 means there are 6 GCPs distributed in the high complexity zone and 4 GCPs are distributed in low complexity zone.

9. RESULTS AND ACCURACY ASSESSMENT

Evaluation of the accuracy of the methods selected for determining the distribution of GCPs is a measure of errors that occurred after the transformed pixel is compared between position on the image after transformation and the same position on the ground points. Accuracy of the transformation can be measured using the Root Mean Square Error (RMSE) with all 68 Independent Check Points (ICPs) scattered throughout the image. The equation used in the calculation is;

$$Average\ RMSE = \sqrt{\left(\sum_{i=1}^{n}(x_{act}-x_{est})^2\right) + \left(\sum_{i=1}^{n}(y_{act}-y_{est})^2\right)} \quad (9)$$

where;

n = the number of control points
x_{act} and y_{act} = actual location of control point x and y
x_{est} and y_{est} = estimated location of control point x and y

Table 2: RMSE result of the check points

Case No.	**RMSE Result**								
	ICP – X, Pixels			**ICP – Y, Pixels**			**Average X-Y, Pixels**		
	Total	**High**	**Low**	**Total**	**High**	**Low**	**Total**	**High**	**Low**
Event.Distr.	2.28	3.57	0.70	1.94	3.02	0.62	2.11	3.30	0.66
Case 1	1.21	1.81	0.58	0.65	0.74	0.59	0.93	1.27	0.59
Case 2	1.77	2.68	0.76	0.66	0.78	0.58	1.22	1.73	0.67
Case 3	0.74	0.87	0.65	1.17	1.42	0.99	0.96	1.15	0.82
Case 4	4.47	6.01	3.14	6.37	8.43	4.64	5.42	7.22	3.89

Table 2 shows the errors that occurred when GCPs distribution are selected from different complexity weighting. Even distribution is a popular method for selecting GCPs amount and location. This is done by applying the same weight to every zone. In this case, the 2 zones weighting are %50 each and the complexity of surface is ignored. Result shows RMSE average value of 2.1pixels. The last case allocated a weighting value at the maximum value of %80, as a result, yielding the RMSE value at the high average of 5.42pixels. RMSE value is low in two cases, 1 and 3, where the weighting proportions are 55and %75with the resulting RMSE average of 0.93and 0.96 respectively.

10. CONCLUSION

The study on the importance of the level of complexity or nature of the surface height in relations to the selection of GCPs and its location in each area using the 2nd order 3D polynomial confirms that there are affects to the accuracy of the transformation, especially in the high land or mountain area. Proportional increase in the number of GCPs at the high area or high complexity area will reduce errors. The study results show that the average error is reduced to 55% and for high area decreased by 87% when the proportion of high complexity to low complexity is 55: 45.

To transform object space to image space with a set of GCPs, especially when the image does not have physical sensor model the complexity of the image should be considered. Other factors that should be taken into account are the height distribution and the standard deviation distribution by using DEM. In addition, this study can be applied to aerial photographs or satellite imaging especially as guidance in identifying the number and location of GCPs for each complexity area, especially in the study area that have a variety of surface types.

This study is helpful to the researcher in reducing the time for trial and error used for the selection of the GCPs location. It can also be applied to the different images by assigning trial weighting and classifying/zoning of surface complexity using load free DEM site and distributing suitable numbers of GCPs for high and low complexity zones.

11. FURTHER STUDY

In this study, analysis and distribution of GCPs location was used only on a satellite image from woldview1. For higher reliability, further studies should be done using other satellite imagery tools such as ALOS and THEOS etc and confirm precisions through using comparative results.

REFERENCES

Arif, F.; Akbar, M.; An-Ming Wu., 2006. *Geometric Correction of High Resolution Satellite Imagery and its Residual Analysis*, Advances in Space Technologies, International Conference on Digital Object Identifier, pp. 162 – 166.

Ayoub, F.; Leprince, S.; Binet, R.; Lewis, K.W.; Aharonson, O.; Avouac, J.-P., 2008. *Influence of camera distortions on satellite image registration and change detection applications*, Geoscience and Remote Sensing Symposium 2008, IGARSS 2008, IEEE International, Volume 2, pp.II-1072-II-1075.

Boukharouba, S.; Rebordao, J.M; Wendel. P.L., 1985. *An amplitude segmentation method based on the distribution function of an image*. Graphical Models Image Process.29, pp. 47–59.

Chang Kang-tsung., 2006. *Introduction to Geographic Information Systems*, 3rd ed.; McGraw-Hill, United States, pp. 128.

Jaebin Lee; Changno Lee and Kiyun Yu., 2011. *Autoregistration of High-Resolution Satellite Imagery Using LIDAR Intensity Data*. *KSCE Journal of Civil Engineering*, 15, 375-384.

Jingtao Zhang and Bo Cheng., 2009. *Distribution optimization of ground control points in remote sensing image geometric rectification based on cluster analysis*, conference on Medical Imaging, Parallel Processing of Images, and Optimization Techniques, Proc. SPIE 7497, 749707, doi:10.1117/12.833671.

Quen-Zong Wu; Hsu-Yung Cheng; Bor-ShennJeng., 2005. *Motion detection via change-point detection for cumulative histograms of ratio images*, Pattern Recognition Letters, Volume 26, Issue 5, pp. 555-563.

Sezan, M.I., 1985. *A peak detection algorithm and its application to histogram-based image data reduction*. Graphical Models Image Process. pp. 47–59.

Toutin, T.; Briand, P.; Chénier, R., 2004. *GCPS requirement for high-resolution satellite mapping*, Proc. XX Congress ISPRS, Istanbul, Turkey

Tsai, D.M., 1995. *A fast thresholding selection procedure for multimodal and unimodal histograms*. Pattern Recognition Lett. 16 (6), 653–666.

Zhang Wangfei; GaoJianguo; XuTianshu; Huang Yanru., 2009. *The Selection of Ground Control Points in a Remote Sensing Image Correction Based on Weighted Voronoi Diagram*, Information Technology and Computer Science, ITCS 2009. International Conference on, Volume 2, pp. 326-329

A PRELIMINARY FEASIBILITY STUDY OF RAILWAY CONSTRUCTION IN KOREA

Yongtaek LIM[1], Juhye KIM[2], Cheol PARK[2]
[1] Professor, Chonnam National University, Korea
limyt@chonnam.ac.kr
[2] Msc Student, Graduate School of Chonnam National University, Korea

ABSTRACT

Recently a significant interest for railway, environmental-friendly transportation mode, has been increased due to reducing green house gas of CO2, and Korean government has focused on rail-oriented public transportation policies. Under this environment, several economic evaluations of the railway construction have been performed. For this purpose, conventional travel demand forecasting steps, such trip generation, trip distribution, mode choice and trip assignment, has been used. Through this process and economic evaluation method, economic verification has been performed. In this study we review economic feasibility of railway construction for Indeogwon-Suwon railway construction project in Korea.

Keywords*: railway, traffic demand, preliminary feasibility study, economical analysis*

1. INTRODUCTION

A preliminary feasibility study for railway investment can analyze through comparing costs, spent in constructing railroads, and benefits, which occurred as a result of it, and traffic demand is one of the factors, that has significance impact on estimation of cost and benefits when evaluating validity. Through estimation of traffic demand, it evaluates whether that business would be promoted or not and investment priorities and it is utilized in calculation of proper supply scale and impact analysis of areas, constructing railway has impact on.

These traffic demands could be estimated in various ways, but in case of our country, 4 stages model is the most utilized. The reason of it is phased consistency of traffic demand's estimation process, which model implies, could be understood easily even to amateurs. 4 stages traffic demand estimation method is a method that estimates traffic demand based on traffic zone successively by dividing it into 4 stages: trip generation, trip distribution, mode choice and trip assignment.

2. METHOD

2.1 Set analysis range

Base year in this estimation of traffic demand is 2010 and public launch year is 2020 and analysis target year is 2059, which is a 40 years after opening. But due to capital area's network of capital area's transportation head office is to 2021 and O/D will be provided to 2036, set the final analysis year as 40 years after the opening but suppose that benefits are constant after 2036, middle analysis year of this business. Influence of traffic business is a spatial range, that should be concerned when analyzing feasibility of the business because of occurrence of "distinguishable changes in traffic pattern' by project implementation and setting a influence as a region, included in evaluating economic feasibility of business, could have impact directly on economical analysis so it should be carefully set. Sphere of influence is separated into two: sphere of direct influence and sphere of indirect influence and explanations of each are as follows.

Sphere of direct influence is a spatial range, which needs specific O/D and construction of network to analyze minutely effect of project implementation as a adjacent land geographically and it should include all enforced section of that business, which changes of traffic pattern occurred directly according to project implementation. Sphere of Indirect influence is a region, except sphere of direct influence area among geographical range, which should be included in calculation's scope of benefits due to occurrence of traffic pattern's changes and it includes sphere of direct influence and its range is greater than or equal to sphere of direct influence's.

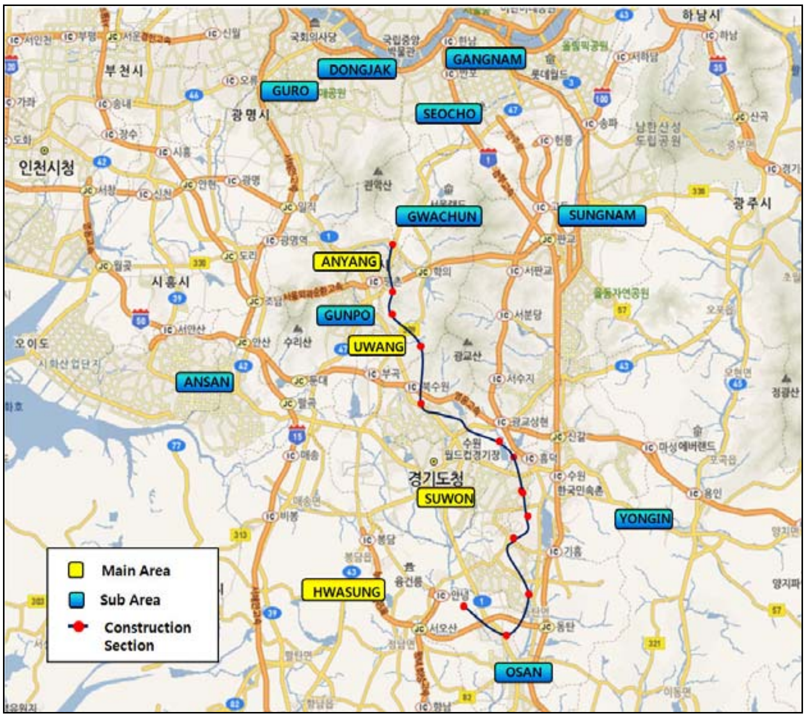

Figure 1: Choosing sphere of influence of this business

2.2 Selection basic data and revision

First we should set a basic data for demand analysis considering administrative district of business area. Basic data examples, this study's demand analysis uses, is a O/D and network data, provided by 『2010 Renewal data of capital area's transportation head office(2010. 5)』 of capital area's transportation head office but it carried out an analysis by reflecting additionally revision of network error, which was in influence sphere and future network of roads and developmental projects. For trip generation and trip distribution, it used O/D, which has public confidence and was suggested professional research institute, vicariously.

It reflected additionally for business, which project implementation was allowed among future developmental plan, not included in capital area transportation head office's O/D, selected as a basic data, and revised population planning, which was incorrectly reflected, among developmental plan, included already.

Also it is judged that there is a high possibility of excessive or depopulation estimation of people, getting into and out at each station in estimating of prospective demand of business route, so it departmentalized zones targeting influence sphere, where business would be enforced.

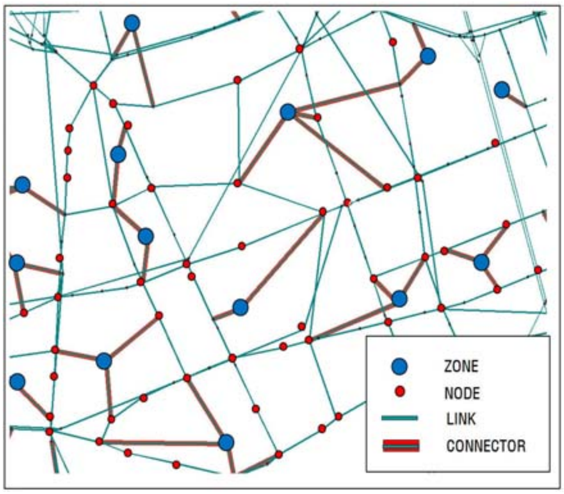

Figure 2: Network configuration

2.3 Setting base year of railway trip assignment model

For railroad, it judged whether model properly reflects reality by comparing observed getting into and out population, counted according to route and stations by the railroad central operation body.

Observed getting into and out population at that time is a people, who get into and out through certain station's gate through AFC (Automatic Fare Collection) and transit passengers, who get into and out at other stations, are excluded. Because each railroad central operating body couldn't get a data about transit passengers of each station, who doesn't pass the gate. Adding the number of passengers, who get into and out at the certain station, and the number of transit passengers, who transfer from other routes, is a total getting into and out population. Because getting on and off population, estimated at each station, in model is a total population, so pure population, except transit passengers among them, should be compared with observed population.

Table 1: Observed getting into and out population and assignments getting into and out population of base year's station

(unit : person/day, %)

Station	Boarding passengers			Alighting passengers		
	Observation	Estimation	Error rate	Observation	Estimation	Error rate
Gunpo	7,567	8,132	7.47	7,032	7,798	10.89
Uiwang	7,783	7,420	-4.66	7,387	6,961	-5.77
Sungkyunkwan University	16,161	18,415	13.95	15,070	19,823	31.54
Hwaseo	8,700	10,533	21.07	8,726	9,551	9.45
Suwon	43,971	48,702	10.76	44,686	50,201	12.34
Seryu	4,764	4,956	4.03	4,390	4,992	13.71
Byeongjeom	15,376	17,757	15.49	15,243	15,191	-0.34
Sema	1,841	1,615	-12.28	1,705	1,465	-14.08
Osan University	1,562	1,422	-8.96	1,520	1,394	-8.29
Osan	9,285	9,450	1.78	9,095	10,119	11.26
Seonbawi	4,822	4,507	-6.53	4,032	3,999	-0.82
Seoul Racecourse	6,312	7,641	21.06	6,606	6,537	-1.04
Seoul Grand	7,559	7,854	3.90	8,028	7,408	-7.72
Gwacheon	5,297	5,292	-0.09	4,673	4,862	4.04
Indeokwon	17,882	18,957	6.01	18,009	16,074	-10.74
Pyeongchon	12,766	15,128	18.50	12,640	14,016	10.89
Beomgye	28,334	25,571	-9.75	28,651	31,112	8.59

2.4 Mode choice

Share of means about project implementation should be recalculated because there is a demand, transferred from plane when estimating demand of railroad unlike general street network business. Mode choice model among traditional traffic demand 4 stages model could become various forms of models like trip distribution. means sharing or means sharing. route assignment according to estimation phase and aim. In preparatory feasibility survey, integrated model of means sharing and route assignment is usually utilized to calculate rates of switching means according to changed network at implementing project.

This paper used Incremental Logit model, which can draw consistency by grasping characteristic of passenger's passing behavior, as a basic model. But in the case of occurring Zero cell to solve Zero cell problem, which would occur when new means are introduced, Additive Logit model could be utilized restrictively.

Incremental Logit calculates probability of selection of each alternatives using variation of utility by changes of explanatory variables. That is, it calculates usefulness of when project implemented and not and computes new means sharing rate, which considers changes of usefulness. This model is a transformed way from K factor Logit and revision pile, applied to fit observation sharing rates and sharing rates of model, no need to applied because observation sharing rates is considered together with changes in utility.

This methodology is usually used in United States and Europe and it has advantage that it excludes effect by heap constant and in could more properly reflect effect of project implementation.

$$P_i^* = \frac{P_i \exp \triangle V_i}{\sum P_i \exp \triangle V_i}$$

P_i^* i: Selection probability of means for project implementation
P_i i: Sharing observation rates of means for not implementing project
$\triangle V_i$ i: Changes in utility of means before and after project implementation

Table 2: Changes in volume of trip and means sharing rates as a result of means sharing in 2020

Classification		Car	Bus	Taxi	Subway	KTX
trip	not implementing	23,365,648	16,924,836	3,303,544	9,955,379	24,436
	implementing	23,353,533	16,911,582	3,303,247	9,981,414	24,067
Means sharing rates	not implementing	43.61%	31.59%	6.17%	18.58%	0.05%
	implementing	43.59%	31.57%	6.17%	18.63%	0.04%

2.5 Trip assignment

Railways passing is generally composed of access pass, from starting point to railroad means, railway pass and access pass, to destination. When separating it by time, it could be distinguished into time of outside(access passing time, waiting time and boarding time) and time of inside. Also for the passing case, transit between rails, occurred, transit time(included in time of outside) could be added. Railway does not consider capacity restriction in trip assignment process and it basically choose line and route based on optimal strategy.

2.6 Estimating prospective traffic demand

After estimating volume of traffic and traffic characteristics for project not implementing and implementing by assigning O/D of each means, obtained through calculation process of base year, it suggests changes in volume of traffic of major roads and railway following project implementation.

Following graph shows maximum thru passenger from 106 station to 108 station as a result of predicting passenger demand of each station in 2020 and 2036.

Table 3: Result of predicting passenger demand of each station in 2020

(unit: person/day)

station	down (Suwon districts)			up (Indeogwon districts)		
	Boarding	Alighting	Thru passenger	Boarding	Alighting	Thru passenger
101	29,352	0	29,352	0	33,736	0
102	5,845	2,030	33,166	2,520	5,480	33,736
103	1,983	1,452	33,698	1,502	2,158	36,694
104	1,255	926	34,027	1,106	1,240	37,350
105	6,592	7,648	32,970	7,612	6,912	37,482
106	11,771	4,503	40,238	4,400	10,335	36,782
107	4,436	9,958	34,716	12,080	5,791	42,717
108	17,638	10,010	42,343	9,522	19,726	36,431
109	3,108	7,534	37,917	8,666	4,085	46,633
110	623	6,448	32,092	7,116	590	42,054
111	291	29,756	2,627	32,996	191	35,528
112	141	1,747	1,021	1,976	226	2,723
113	0	1,021	0	973	0	973
Total	83,035	83,033		90,469	90,470	

It is a picture, that shows changes in getting on again population of around route for double track subway project implementation between Indeogwon and Suwon in 2020. Getting on again population of construction line and line number 4(Gwacheon districts) has been increased and that of shinbundang line, line number 1, section between Indeogwon and Kumjung of line number 4 has been decreased.

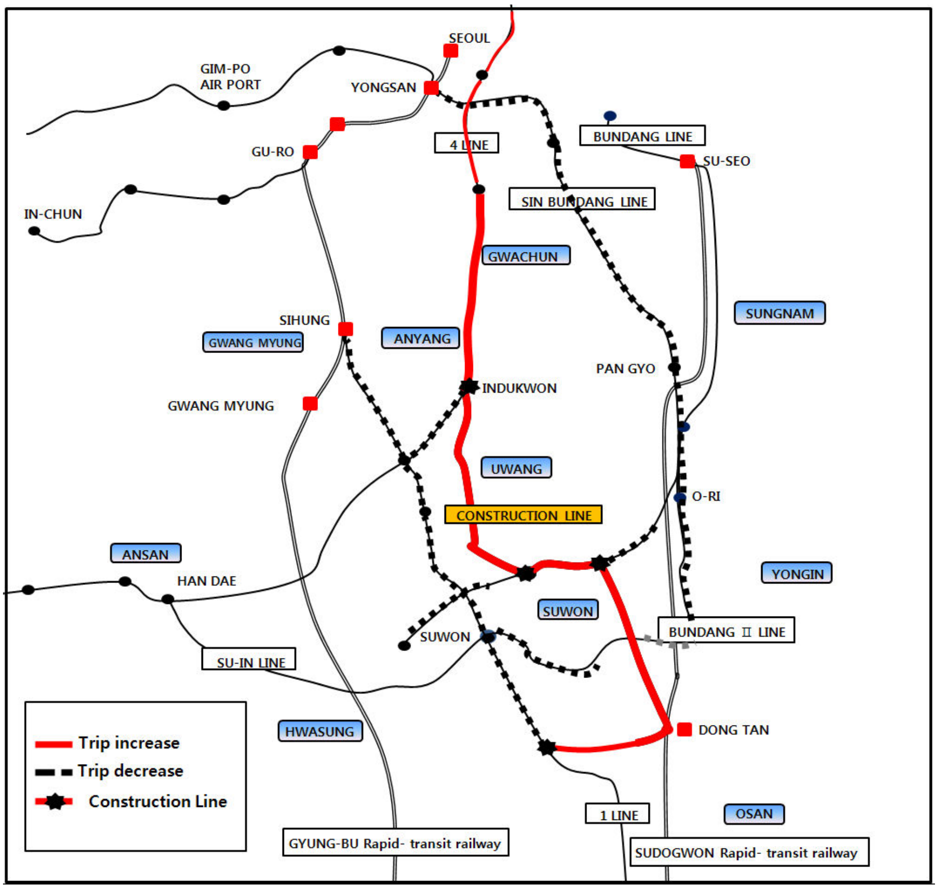

Figure 3: Thru passenger change of surrounding line in 2020

2.7 Computation benefits

Benefits, which occur by implementation of transportation investment, are divided into two: direct benefits, transportation aspects and indirect benefits, social benefits due to transportation improvement. Direct benefits, which happen to users for transportation utilities when transportation business like road and railroad implementing, are reduction of vehicle operating costs, reduction of travel time, decrease in car accident, increase in comfort, improvement of punctuality and improvement of stability. Among these, making reduction of vehicle operating costs, reduction of travel time and decrease in car accident as a monetary value is a relatively easy but making increase in comfort, improvement of punctuality and stability as a currency value is difficult because their effect could be varied according to satisfaction of individual. Meanwhile, for the case of railroad business, there is a need to reflect benefits by transit demand of flight and shipping and decrease benefit of accident/delay according to improvement of crosswalk but measuring them is not easy.

Indirect benefits are ripple effects, that occur to every people regardless of using traffic facilities when enforcing transportation business and are reduction of environmental costs, effect of regional development, expansion of market area and reforming effect of industrial structure. For the case of railroad business, benefits of wealth by reduction of maintenance and administrative expense of highway, due to transit demand, and retrenchment of parking space's opportunity cost, owing to reduced parking demand and cut of traffic congestion and road space during construction would be additionally considered.

Table 4: Results of calculating benefits

(unit: one million won)

year	Benefits of reduction in trip time			Benefits of reduction in operating costs	Benefits of reduce in car accidents	Benefits of reduce in environmental costs	Benefits of reduction in parking costs	Total
	Road	Railroad	Total					
2020	110,137	-13,654	96,482	19,423	1,788	2,500	5,041	125,234
2026	125,650	-10,113	115,537	20,580	1,972	2,836	8,112	148,964
2031	144,622	-8,413	136,209	21,334	2,010	2,922	9,121	171,523
2036	148,321	-8,126	140,195	22,219	2,030	2,972	9,054	176,470

Table 5: Summary of economical analysis results

(unit: one hundred million won)

Classification	The task
Current value of benefits	16,024
Current value of costs	20,817
B/C	0.77
NPV	-4,793

3. CONCLUSION

Analysis about economic feasibility helps accurate understanding about business making us grasp how much economic values this business has. Furthermore, information about economic feasibility of the business is utilized as a data, the most basic and essential in analysis at policy-level.

Economic evaluation is a process, that apprehends economic feasibility and finance of the business through calculation like B/C ratio, NPV and IRR and to supplement error of various estimation, used in economic analysis, it fulfills sensitivity analysis about impact that changes in major variables has on economic feasibility. Especially, economic analysis judges economic feasibility of that targeting business by comparing benefits that make changes in traffic pattern as a monetary value, which occurred at traffic network in influence sphere due to project implementation and size of costs, which occurred for the entire period of analysis due to project implementation

REFERENCES

Deasik YUN, 2001. travel demand forecasting 4 steps, *Transportation* *demand analysis*, Korea. 33-217

Kangsu KIM, 2008. Mode choice, *Preliminary feasibility study standard guide correction repletion research of road and railroad part business (the 5th editions)*. The Korea Development Institute. Korea. 265-276.

THE USE OF FLY ASH CONCRETE WITH EXPANSIVE AGENT ON CONCRETE REPAIR

Michael COO[1] and Thanakorn PHEERAPHAN[2]
[1]Graduate Student, Structural Engineering Department,
Asian Institute of Technology, Thailand
mikecoo@gmail.com
[2]Professor, Structural Engineering Department, Asian Institute of Technology, Thailand
thanakorn@ait.ac.th

ABSTRACT

This study was performed to develop a low-cost concrete repair material with the use of an industrial waste material with pozzolanic properties such as fly ash by replacing 20% to 50% of the designed binder proportion, and to test the mechanical as well as semilong term hardened properties of this mixture which includes compressive strength, splitting tensile strength, slant shear strength and flexural strength of repaired concrete prisms. To evaluate the field performance of this developed repair material in actual service, a full-scale beam repair procedure was also simulated. Results have shown that the replacement of 50% fly ash and the addition of 7% expansive agent is the optimum mix proportion for use in the target applications with both normally compacted and selfcompacting grade. The developed concrete attains 7 day compressive strength, splitting tensile strength and slant shear strength of 42 MPa, 3 MPa, and 7 MPa respectively and a free shrinkage of <100 microns in 120 days with a low-cracking tendency classification from ASTM C1581 test. The full-scale beam testing showed that the performance of the repair material is adequate for use on repairing of the member and to restore the original load capacity of the member. Costing only 20% more (1,480 vs.1,200 THB for a m3 of repair concrete to ASTM Type 1 cement only binder), significant improvements in many (or all) areas are achieved, e.g., 40% increase in splitting tensile strength, low cracking tendency and <100 microns shrinkage in 120 days. Therefore achieving a concrete repair material with similar properties as those currently available in the market at a fraction of the cost (2050 THB vs. 34,000 THB)

***Keywords**: concrete; repair; fly ash; expansive agent; ring Test; dimensional stability; cracking Tendency; Restrained Shrinkage; Free Shrinkage; Beam Repair;*

1. INTRODUCTION

During service, concrete structures are expected to provide safety against failure as well as appropriate serviceability for the expected loads. Overloading, exposure to weather and other deteriorating substances may cause concrete structures to lose their intended service requirements. Appropriate action needs to be taken in order to restore service requirements of these structures. Concrete structures may have a lower initial cost of construction, but without proper maintenance and adherence to loading limits, these structures tend to deteriorate and lose their initial design intent. Repair and structural strengthening are two major approaches undertaken to restore the design intent of these structures.

In the past 25 years, repair and rehabilitation of concrete structures in western countries have been a major industry due to the deterioration of structures built during their construction boom 4 decades ago. Annual spending averaging at $21 Billion is spent on concrete repair in the United States alone (Emmons & Sordyl, 2004). This explosive growth of the repair and rehabilitation industry results in the need for more improvement and understanding of concrete repair materials. Asia is also fast approaching this structural deterioration phenomenon due to the construction boom in the continent during the past decade. Rapid building of structures and the lack of comprehensive concrete durability data during that time led buildings to deteriorate at an unexpected and rapid rate, making repair and strengthening a growing industry in the Asian region. It should be noted that Thailand also has not been secluded from the durability and early cracking of concrete structures; survey shows that deterioration started even just after a decade of construction.

The concrete repair industry is growing in Asia, and the demand for concrete repair materials is also on the rise, but until now, proprietary and expensive repair materials are used, making repairs costly and forcing structure owners to delay repair jobs, which will eventually become a concern on safety and serviceability of the structure. Effective, durable and convenient-to-use concrete repair material, especially at an economical cost that can be adopted to be used on high-volume repair applications is therefore developed.

Cracking has been a major concern in the use of conventional concrete as a repair material in deteriorated structures, as not only unsightly surface repairs are a concern but also the performance of the repaired portion of the structure. Repairing repairs is a common encountered problem when normal concrete is used; this is due to the restrained condition that the existing concrete is imposing on the fresh repair material, which will eventually affect the serviceability and long-term performance of repair (Kovler & Bentur, 2009). To mitigate and reduce cracking, suggested solutions from ACI Committee 223 includes the use of expansive cement. However, expansive cement is not produced by local cement manufacturers, which makes attaining the material uneconomical and impractical for low-cost repair works. Expansive additive is instead made use of in this research since it is a more cost-effective alternative, as well as being available locally. Expansive additives, although mitigates cracking on repair materials, can incur additional cost to the final production of repair concrete, thus; it is proposed in this research to add fly ash, an industrial waste material which is collected in the magnitude of 3 million metric tons per year in Thailand alone (Tangtermsirikul, 2005).

With the replacement of fly ash on the total binder of the repair concrete, an economical blend of binder can be attained as well as durability, shrinkage, fresh mechanical ability and strength characteristic improvement from binders based on Ordinary Portland Cement (Siddique, 2003) (Ghosh, 1981) (Bilodeau & Malhotra, 1992) (Naik, Singh, & Hossain, 1994) (Shafiq & Cabrera, 2004).

2. EXPERIMENTAL PROGRAM

The program is divided into 3 parts: (1) Development of a repair concrete for general purpose repair applications, with sub parts as checking the fresh and hardened properties of the proposed mix proportions until target requirements (Table 1) are met and (2) this blend of binder is designed with a modified coarse and fine aggregate content and the addition of limestone powder to pass a self-compacting grade concrete according to slump flow, L-box and V-funnel target requirements (Table 2) are met. (3) Repair beam mock-up test, which will be carried upon after final mix proportion has been decided according to the target requirements and comparing the total material cost as illustrated in Figure 1.

Figure 1: General Overview of Repair Concrete Development

Table 1: Repair Concrete Target Requirements

TEST	Target
Splitting Tensile Strength (ASTM C496)	2.8-3.8 MPa (7 days curing)
Free Shrinkage (ASTM C403)	<100 microns
Cracking Tendency Ring Test (ASTM C1581)	28 day no crack
Compressive Strength (ASTM C39)	>40 MPa (7 days curing)
Slant Shear (ASTM C882)	7.5-10 MPa (7 days curing)

Table 2: Self Compacting Concrete Fresh Properties Target Requirements

Test Method	Target Requirement
Slump Flow	>700 mm
T-50	2-5 seconds
L-Box	h2/h1 > 0.8
V-funnel	<8 seconds

A total of 5 beams with the following properties is tested (a) Control beam without repair (b) Normal concrete repaired beam at 7 days curing (c) Same beam as b but repair is allowed to stay for 28 days (d) SCC Concrete repaired beam at 5 days curing (e) same as beam number 4 but repair is allowed to stay for 28 days.

3. MATERIALS

3.1 Cement

A locally produced Ordinary Portland Cement (OPC) conforming to ASTM classification TYPE 1 is used throughout the experiment.

3.2 Aggregate

Coarse aggregate used is crushed limestone, laboratory sieved to a maximum size of 13mm and fine aggregate of limestone sand which passed sieve opening No. 4 and retained on sieve opening No. 100, as per requirement from ASTM C33 with Fineness Modulus of 2.74. All aggregates are locally quarried, washed with laboratory water and air dried before use.

3.3 Fly ash

Pulverized fly ash obtained from Mae Moh Power Plant in Lampang Province of Thailand, which meets the general requirements of ASTM as Type-F.

3.4 Expansive Additive

Commercially available expansive additive classified as Type-K expansive cement when added to portland cement.

3.5 High Range Water Reducing Admixture (HRWR)

The super-plasticizer used for the production of Self Compacting Concrete (SCC) is a commercially available High Range Water Reducing Admixture which is polycarboxylic based liquid admixture that complies with ASTM C494 Type A & Type F, High Range water reducing admixture.

3.6 Mid-Range Water Reducing and Retarding Admixture (MRWR)

Chemical admixture used for normally compacted concrete (NCC) in this study to improve fresh properties while maintaining a fairly low w/c ratio is a commercially available liquid admixture that complies with ASTM C494 Type-A (Water-Reducing).

4. CONCRETE SPECIMEN PREPARATION

Aggregates are washed and air dried, weighed using digital laboratory scale along with the cement, fly ash, water and MRWRA/HRWR. Specimens are prepared on a laboratory temperature of 25-32°C and a relative humidity of 50-55% and cured at the same curing temperature and humidity. All specimens prepared are left in the mould for 24 hours, de-moulded, water cured for 7 days and air dried until time of testing.

4.1 Concrete Mixing and Fresh Properties Evaluation

Concrete is mixed using a laboratory mixer then slump according to ASTM C143 checked and recorded as T0 which is the time right after mixing, slump is then continuously monitored for 120 minutes at 30 minute intervals. Initial and final setting time of fresh concrete is also tested using ASTM C403 method where coarse aggregate is seived out of the mixture and penetration resistance is checked until 3.5 MPa and 27.6 MPa as initial and final setting time of the mixture.

4.2 Test on Hardened Concrete

Tests on hardened concrete include Compressive strength which complies with ASTM C33 for mixing, curing and specimen sampling. Splitting tensile strength using 100 mm x 200 mm cylinder specimens, tested at 1, 7, and 28 days. Free shrinkage measurement from all the samples are also monitored using ASTM C157 method up to 120 days of curing. All samples tested on hardened concrete are water cured for 7 days and then air dried thereafter, maintaining a laboratory curing condition of 50 ± 5% RH and 25 ± 5°C Temperature throughout the curing period.

5 CONCRETE PROPERTIES EVALUATION

5.1 Compressive Strength

Compressive Strength testing is made in accordance with BS 1881 Part 116 using 150 mm x 150 mm x 150 mm cubic specimens. The compressive testing machine used is a “Shimadzu” Universal Testing Machine of type UMH 200A set at a maximum loading of 200 Tons. Loading rate is limited to 0.15 to 0.35 MPa/s or 0.35 to 0.8 Ton/s in this specimen.

5.2 Splitting Tensile Strength

Tensile strength of specimens was tested in accordance with ASTM C 496 splitting tensile strength method. Concrete cylinders with the dimension of 100 mm x 200 mm are casted and tested horizontally. The same load testing equipment from the compressive strength testing but is set to have a load limit of 100 Tons.

5.3 Slant Shear Strength

Concrete being used as a repair material should bond to a certain degree with the substrate concrete, in this study, the use of a slant shear test in compliance with ASTM C882 is used due to the simple and effective approach in determining the bond strength between two materials, which in this case the substrate concrete and the repair concrete.

This method of testing is chosen because of the practicality and suitability to our application since this method subjects the bond surface between the two different materials into shear and compressive stresses which are also happening on the actual concrete structures being repaired.This method is done by first cutting of the substrate concrete into 30° angles and placed at 100mm x 200mm cylinder molds then repair concrete is casted on top.

5.4 Free Shrinkage Test

Free or unrestrained shrinkage of specimens are taken in accordance with ASTM C157. A prismatic specimen is casted, cured and measured, using a digital length comparator with measurement reading capability up to 1x10-6 m/m. Relative length of samples is taken as the difference between the starting readings of the samples at 1 day and the consequent days reading divided by the gague length of the sample which is the distance between the head of two stainless steel bolts which in this case is set to 240mm. Length comparator equipment is set to zero at every test of the sample.

5.5 Restrained Ring Test

Completely restrained specimens are casted on a steel ring that completely restrains dimensional shrinkage of the concrete by the ring. This test is done in accordance with the specifications and suggestions of ASTM C1581. The objective of this testing procedure is to capture the real time strain of the concrete during hydration, drying, curing and finally determine the cracking strain of the sample under a completely restrained condition. Ring specimens are prepared by casting the concrete on a steel ring with attached strain gages and connected to a data logger to monitor strains. Strain measurement is done on the steel ring assuming that the casted concrete is completely transferring strain on the restraining steel ring and therefore, strains on concrete while on the fresh and hardening state is monitored until the time of cracking.

6. RESULTS AND DISCUSSION

6.1 Fresh Concrete Properties

All mixtures exhibit excellent workability even with a low w/c ratio due to the addition of a plasticizing admixture and even better after replacement of fly ash from the binder. Mix proportions are shown on Table 3 and Table 4. Minimum initial slump after mixing and after 2 hours of the samples are 22 cm and 6 cm respectively, samples with the replacement of fly ash exhibit a higher initial slump but with a similar final slump after 2 hours except that of 50% fly ash exhibits an even higher final slump when compared to the control mix. Fresh properties of concrete containing fly ash are also observed to be more workable when compared to the control concrete based upon the ease of sampling, casting on moulds and vibration time until consolidation. This can be explained by the generally accepted characteristic of fly ash which in addition or replacement to concrete binders, reduces water demand for a given workability compared to pure Portland cement concrete due to the spherical and smaller size of fly ash particles, therefore making mixes with fly ash more workable. In this research, Slump of fly ash concrete are investigated and shown in Table 5 and graphed values in Figure 2 to Figure 3.

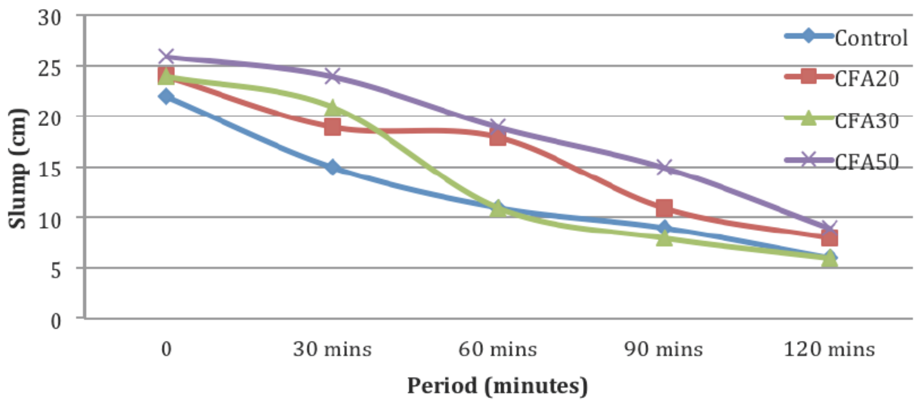

Figure 2: Effect of Fly ash replacement on Slump of concrete

Table 3: Selected Mix Proportions of Normally Compacted Concrete Specimens

Aggregate type	Crushed Limestone (12mm) / Limestone Sand (FM2.7)							
Mixture ID	**Control**	**CFA20**	**CFA30**	**CFA50**	**CFA20E7**	**CFA30E7**	**CFA40E7**	**CFA50E7**
Cement (kg/m^3)	485	388	339.5	242.5	388	339.5	291	242.5
Fly ash(kg/m^3)	0	97	145.5	242.5	97	145.5	194	242.5
Limestone Powder(kg/m^3)								
Expansive Additive (kg/m^3)	-----	-----	-----	-----	34			
Coarse Aggregate(kg/m^3)	1075							
Fine Aggregate(kg/m^3)	755							
Water (kg/m^3)	180							
Retarder/MRWRA (L/m^3)	1.2							
HRWR (L/m^3)								
Proportion Characteristics								
w/c	0.37							
expansive/c	-------------				0.07			
Vw/Vp								

Table 4: Slump and Setting Time

	Slump (cm)						Setting Time (minutes)	
Time	0	30 mins	60 mins	90 mins	120 mins		Initial (3.5 Mpa)	Final (27.6 Mpa)
Control	22	15	11	9	6		140	175
CFA20	24	19	18	11	8		180	220
CFA30	24	21	11	8	6		165	210
CFA50	26	24	19	15	9		210	285
CFA20E7	26	21	15	12	9		185	225
CFA30E7	26	23	18	12	9		195	260
CFA40E7	26	23	18	15	12		230	270
CFA50E7	28	21	17	15	12		240	290

Table 5: Mix Proportions of Self Compacting Concrete Specimens

Aggregate type	Crushed Limestone (6mm)
Mixture ID	SFA50E7
Cement (kg/m^3)	242.5
Fly ash(kg/m^3)	242.5
Limestone Powder(kg/m^3)	84
Expansive Additive (kg/m^3)	34
Coarse Aggregate(kg/m^3)	784
Fine Aggregate(kg/m^3)	759
Water (kg/m^3)	180
Retarder/MRWRA (L/m^3)	
HRWR (L/m^3)	4
Proportion Characteristics	
w/c	0.37
expansive/c	0.07
Vw/Vp	0.8

6.2 Influence of Fly ash Replacement and Expansive Additive on Fresh Properties of Concrete

Since workability is one of the important factors in the development of concrete mix designs especially on repair applications since placement concerns and work done on concrete is more complicated than the placement of normal concrete which is important to assess its performance and ease of application while on the fresh state in the field. Figure 2 shows the effect of fly ash on slump loss of fresh concrete. It can be observed that as fly ash replacement increases, a slight increase in initial slump occurs, but with the replacement level of 30% a sharp decrease in slump loss is observed at the time interval between 30 minutes and 60 minutes. The increase in workability of concrete mixtures containing fly ash has also been studied by Hobbs and Brown and concluded that as replacement levels of fly ash in cementitious materials increase by 10%, the compacting factor and overall workability increased as the same order as it would by increasing water by 3%, which is essential in high strength concrete and repair applications where a low water content is needed for early strength and durability requirements while lowering the required dosage of plasticizing admixtures in order to achieve a desired workability for the intended application.

6.3 Effect of Expansive Additive on Slump loss of Concrete with Fly ash replacement

The addition of expansive agent on binders of concrete with fly ash replacement increased the initial and final slump of the concrete mixture up to 6 cm with the 50% fly ash replacement and 4 cm for the lowest replacement level of 20% fly ash mixture as shown on Figure 3. These results have validated the question whether the addition of more fines or cementitious material in our mixture, specifically expansive additive in powder form, will affect the fresh properties of the mixture and whether the additional dosage of super plasticizer is needed. Although with an addition of expansive agent on the concrete mixture, the addition of fly ash in magnitudes of 10% from other researchers (Hobbs, 1983) is still effective in reducing water demand and therefore increasing the slump of the mixture without adversely requiring an additional water demand or the addition of super plasticizers to meet the required fresh properties of this mixture. Figure 3 shows the similarity of slump loss on different fly ash replacement with expansive additive.

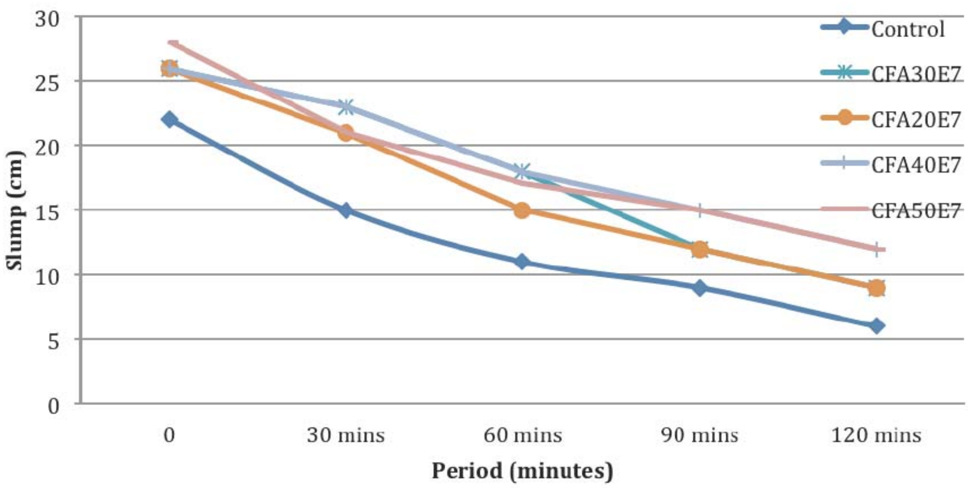

Figure 3: Effect of Fly ash with Expansive agent on slump

6.4 Setting Time

The rate of stiffening of the concrete mixture is expressed in setting time, codes on the application and placing of concrete allows the cement to be worked upon and placed until initial setting of the mixture is reached. In this repair concrete developed, a minimum setting time of 2 hours is set as a target in order to allow time for delivery and compensate for the delay and complications of actual site work. As seen on Figure 4, all setting times including the control concrete is more than the set target, but with the replacement of fly ash in 10% intervals, initial setting time is delayed for about 20 minutes for the 20% and another 20 minutes for the 30% mixture, but when replacement level reached 50%, a steep increase of greater than 1 hour is achieved from control. These findings have also correlated with the results by several researchers (Joshi, 1993) which concluded that fly ash when replaced in binders of concrete mixtures produces a retarding effect.

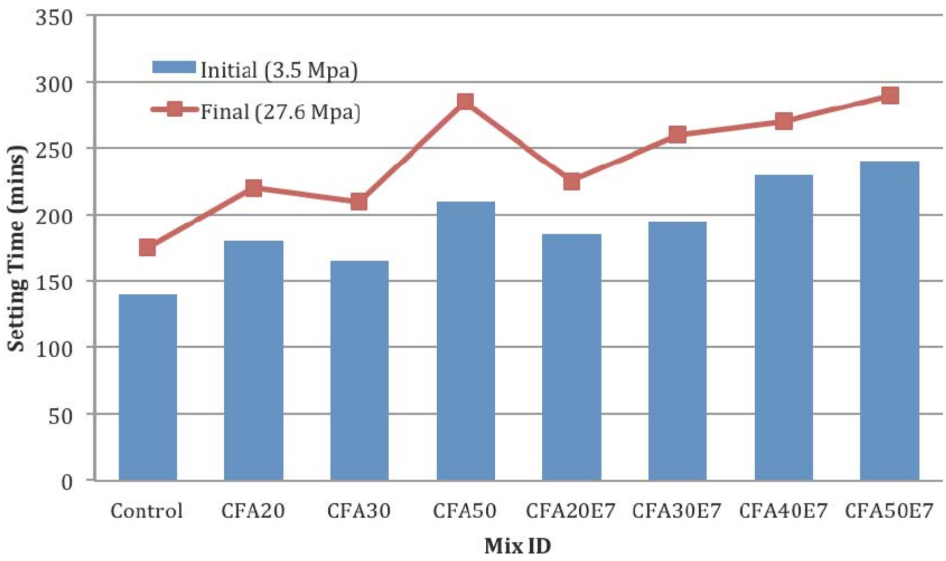

Figure 4: Setting Time Comparison between mixtures

6.5 Self Compacting Concrete Fresh properties

Properties of the Self-compacting Concrete developed are in Table 5. These target requirements meets the specification of ACI 237 and the more stringent requirement suggested by researchers (Hwang, Khayat, & Bonneau, 2006).

Table 5: Results of Developed SCC concrete

Test Method	Target	Result
Slump Flow	>700 mm	810 mm
Slump Flow T-50	2-5 Seconds	4 Seconds
L-Box	h2/h1 > 0.8	1.0
V-funnel	< 8 seconds	6 Seconds

HARDENED PROPERTIES

6.6 Compressive Strength of Concrete with Fly ash Replacement

Compressive strength of different fly ash addition is compared as a function of curing time is plotted in Figure 5. This graph shows the mixtures where fly ash is replaced as part of the binder as a step in finding the proper mix proportion for the repair concrete being developed. As seen from the graph, a higher 7 days early strength than the control concrete can be achieved by using a 30% fly ash replacement.

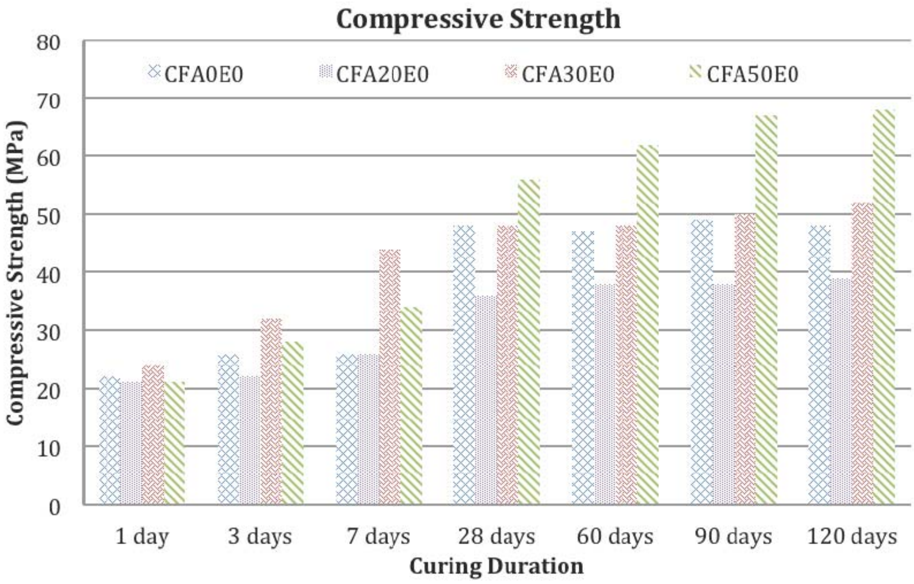

Figure 5: Concrete Compressive Strength

6.7 Compressive strength of concrete with fly ash replacement with the addition of expansive agent

For the improvement of early compressive strength of repair concrete, the addition of an expansive additive is chosen since the concrete mix proportion is already employing a low water to binder ratio and it is essential to maintain this for early strength. This addition of expansive agent improves early strength of the concrete as well as bond strength ,which will be presented in the following sections, due to the formation of ettringite crystals, this evolution is discussed further in other researchers (Hu & Li, 1999), which also concludes that the addition of powder form expansive agents improve the compressive strength of mixture.

Figure 6 illustrates the compressive strength between samples with and without addition of expansive additive and the control concrete. This graph shows that in this case, compressive strength decreased for the 30% fly ash mixture after the addition of the expansive additive while the 50% fly ash mixture gained more strength after the addition of expansive agent. This phenomenon exhibited by the mixture may be due to the early pozzolanic reaction of the 30% fly ash replacement in which without an expansive agent, gains early strength but otherwise, a different reaction is observed, due to the ettringite crystal formation which occurs at roughly the same time as the mixture gains strength, and one hypothesis is that these two reactions occuring together can cause a reduction in the concrete strength.

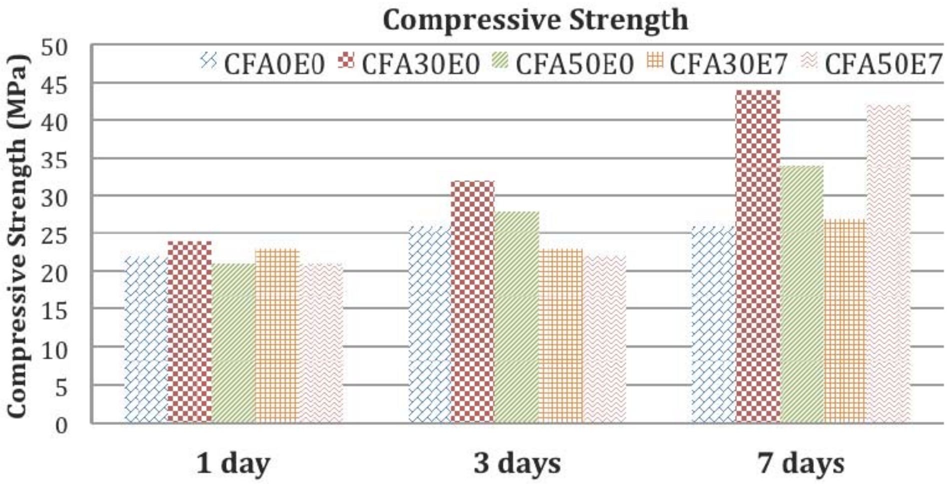

Figure 6: Concrete Compressive Strength with Expansive Additive

6.8 Compressive Strength of Self Compacting Concrete with 50% fly ash replacement and the addition of expansive agent

Based on the results until this point, we can see the advantages on the early compressive strength gain produced by the addition of an expansive agent while the fly ash replacement gains strength on the long term while lowering the total cost of the mixture. In this section, this same binder proportion is modified in order to comply with the SCC grade concrete specifications (Hwang, Khayat, & Bonneau, 2006). Final SCC mix proportion is shown in Table 4. The modification of this binder content to be made into SCC broadens the application range of this mixture being developed. Moreover, it is also essential to check the properties of the SCC mixture, and in this section, the compressive strength is compared with the control mixture and the normally compacted concrete. Results are shown in Figure 7 and it can be observed that by changing the aggregate content and adding more fines such as limestone powder in the mixture, similar 3 day strength can be achieved but a slightly delayed strength gain thereafter.

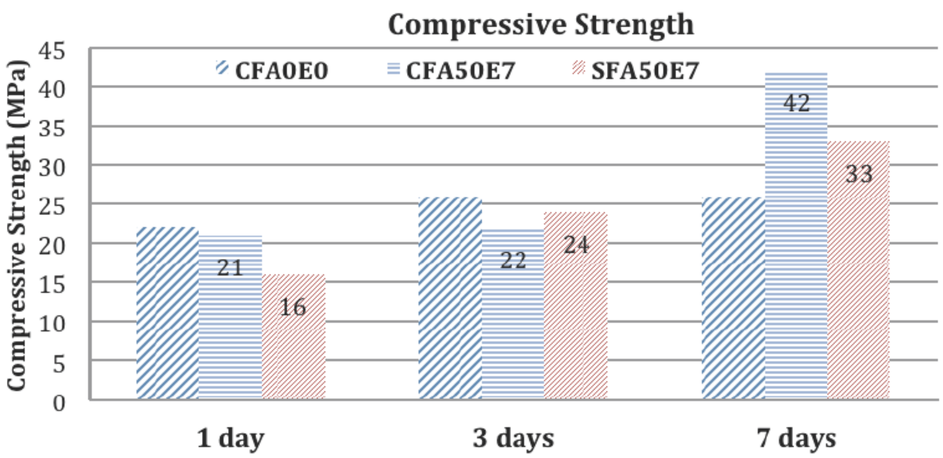

Figure 7: Effect of mixture modification from NCC to SCC concrete of 50% Fly ashreplacement and expansive agent addition

6.9 Free Shrinkage of concrete with fly ash replacement

With the compressive strength results presented in the previous section, it is also essential to determine the dimensional stability of the concrete material since one of the most crucial performance of the repair material according to several researchers is the tendency of the material to crack due to drying shrinkage and incompatibility to the substrate concrete. Concrete mixtures with fly ash replacement at different magnitudes are compared with their free shrinkage to determine whether a type of mixture is suitable for the repair of structures, in this study, a shrinkage limit of less than 300 microns is set, noting that this limit is set above the 400 microns minimum of USACE/ICRI manuals of concrete repair practice, this limit however, does not ensure that the repair material does not crack, only that this concrete proportion will generally be applicable to concrete repair. A free shrinkage plot of the concrete being studied in this research which has replacements of different levels of fly ash is presented in Figure 8. Free shrinkage of the concrete mixtures with 20% and 30% fly ash replacements exhibits a high free shrinkage, even greater than the control concrete, but it s observed that the 50% fly ash replacement has exhibited a free shrinkage train similar to that of control concrete.

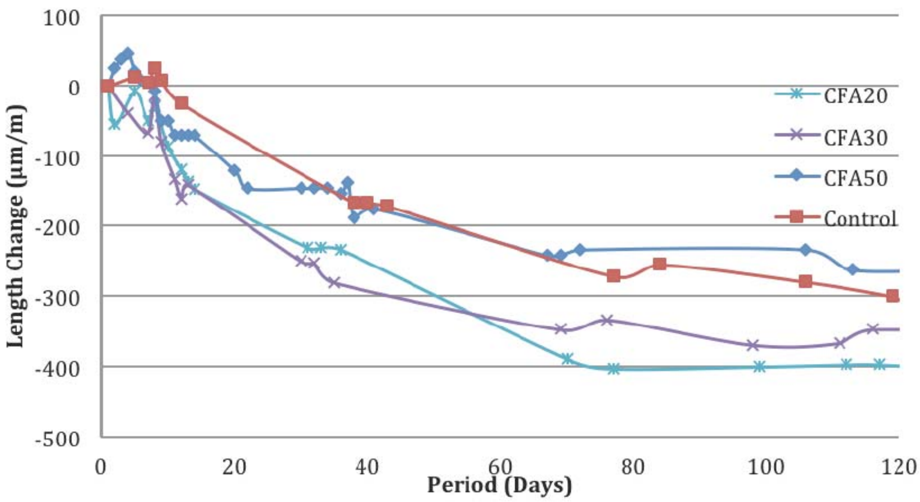

Figure 8: Free shrinkage of samples with fly ash replacement

6.10 Free shrinkage of concrete with fly ash replacement and expansive agent addition

Free shrinkage of the following mixtures with fly ash replacements and expansive agent addition is presented in this section; these mixtures are compared to the control concrete and the 50% fly ash concrete since shrinkage of the 20% fly ash samples have already exceeded limiting shrinkage strain of 300 microns. Figure 9 shows that the expansive agent addition to the fly ash concrete has been effective in drying shrinkage reduction of the mixture to 92 microns in 120 days of curing comparing to the 262 microns for the 50% fly ash admixture alone; from this mixture a 65% decrease in shrinkage of the concrete is observed. The SCC mixture noting that it has the same binder proportion as the NCC counterpart mixture, has an identical free shrinkage strain as the NCC mixture. These two mixtures has shown good dimensional stability when compared to other mixes in this study, therefore more trials are done in this mix to determine if other properties meet the requirements.

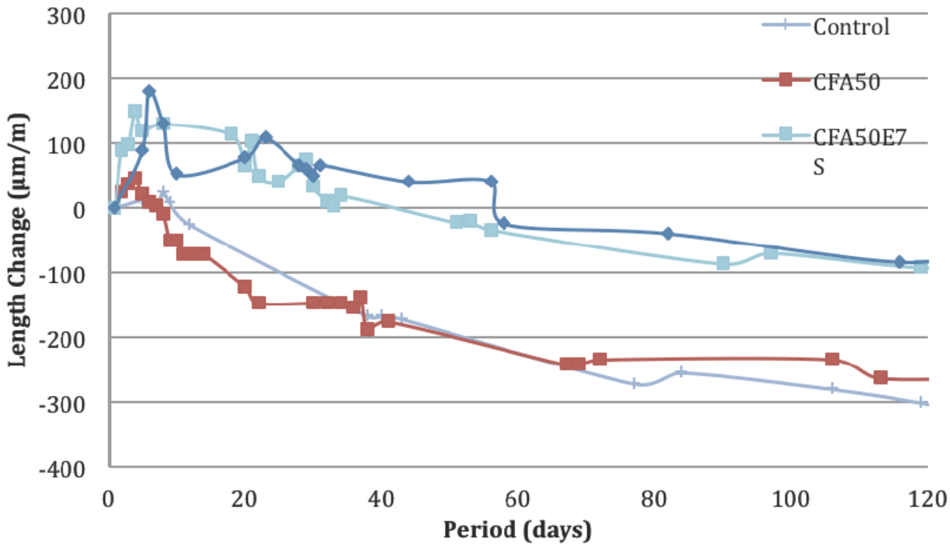

Figure 9: Free shrinkage of samples with 50% fly ash replacement and expansive addition

6.11 Splitting Tensile Strength

The splitting tensile strength is tested in accordance with ASTM C496 to evaluate the tensile strength in the concrete developed under load. Results are shown in Figure 10, 1 day, 7 days, and 28 days cured sample is taken from the prepared specimens to evaluate the tensile strength of the mixtures. Results shows that the replacement of fly ash without expansive additives in mixtures based on Figure 9 resulted in a decrease of tensile strength of 19% during early age but with the exception of the 50% replacement (CFA50) which gained a significant 50% addition during the 7 days of curing, this results only verifies that concrete with low levels of fly ash can reduce the tensile strength of mixtures while high volume fly ash due to more fines by volume in the mixture can increase the tensile strength capacity of the concrete which also correlates with the compressive strength of the concrete that has followed the same trend. Comparing these results with the addition of expansive additive, a similar trend is also observed where early age tensile properties of the concrete with 20% and 30% fly ash replacements even with the addition of expansive additive tensile strength decreases, but with the replacement of 50% fly ash to the binder, an increase in tensile strength is observed even at early ages which is nearly the same magnitude as the one without expansive additive. Therefore, based on these test results, a conclusion that expansive additive to fly ash concrete may help increase the tensile strength but at a very minimal level and a later age of the concrete. Self-compacting concrete however has exhibited a 41% for the 28 day cured specimen. This good reaction may be an indication that the addition on limestone powder on fly ash concrete improves ettringite growth on the hydration of cement and therefore promotes a higher tensile strength on concrete; this chemical hydration reaction is elaborated further in the referenced research (Weerdt, Kjellsen, Sellevoid, & Justnes, 2011.

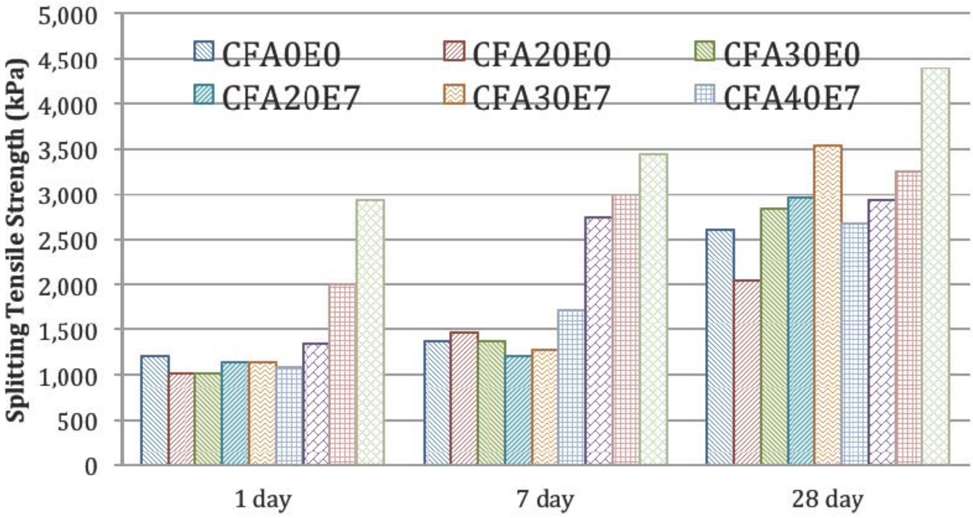

Figure 10: Splitting Tensile Strength

6.12 Slant Shear Strength

Slant shear test results of selected mixture are shown in Figure 10, comparing the control mixture coded as CFA0E0 with the 50% fly ash replacement (CFA50), a 60% decrease in early bonding strength and 100% decrease after 28 days curing, this can be justified due to the delayed strength gain of the concrete found on the compressive strength of the same sample. This however is not the same trend when an expansive agent is added to the mixture, even with 50% fly ash replacement of the mixture, the 1 day bonding strength of the mixture is similar to the control concrete, which is mostly due to the addition of an expansive agent which improves bond strength as also observed by other researchers (Halicka, 2009). This same binder content when modified into SCC has decreased bonding strength when compared to the NCC counterpart, but still 9% and 7% greater than the control mixture in terms of bonding. This property of the SCC mixture may be due to the high fines on the SCC mixture.

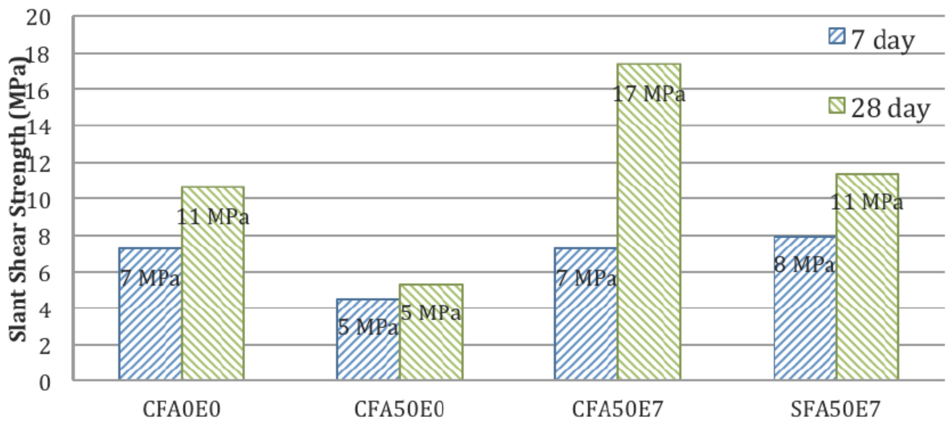

Figure 11: Slant shear strength of selected specimens

6.13 Ring Test (Cracking Tendency)

In order to determine the sensitivity to cracking of the developed mixture, a cracking tendency test is performed as per ASTM C1581 specification. This test consists of casting a concrete ring around a steel ring. The top and bottom surfaces are sealed so that drying will only be initiated on the outer circumferential surface. This ring specimen restraint configuration is chosen to be performed in this study due to certain advantages over other test methods, one of the main advantage is that when concrete is casted as a ring specimen, no stress concentrations are imposed on the concrete specimen unlike the linearly restrained specimens, therefore allows the concrete to undergo internal volumetric change, stress development, creep and creep relaxation evenly throughout the element, and with the circumferential surface exposed to drying and the top and bottom portion of the ring sealed, cracks are readily visible, which indicates that the maximum tensile strain capacity of the concrete has been reached. The recording of the strains transferred by the concrete on the internal steel ring, compressive strain can be captured and taken as the internal tensile stress of the concrete specimen. This tensile strain capacity of the specimen can be taken as a general value and specific to the concrete mixture at a given curing condition since this maximum tensile strain comes from the internal hydration, deformation and relaxations of the concrete specimen alone, therefore through this setup, concrete can be partially isolated from other factors that may interfere with the internal strain mechanisms of the sample. There are 3 separate samples evaluated for cracking tendency in this study, with each representing each steps in the development of the repair concrete in this research. The first concrete specimen tested is the control concrete (CFA0E0), this mix proportion has high cement content (485 kg/m3) and a low water-cementitious material ratio. This proportion is tested to know the tensile strain propagation of plain concrete without any binder modification; cracking of the concrete specimen is shown in Figure 11.

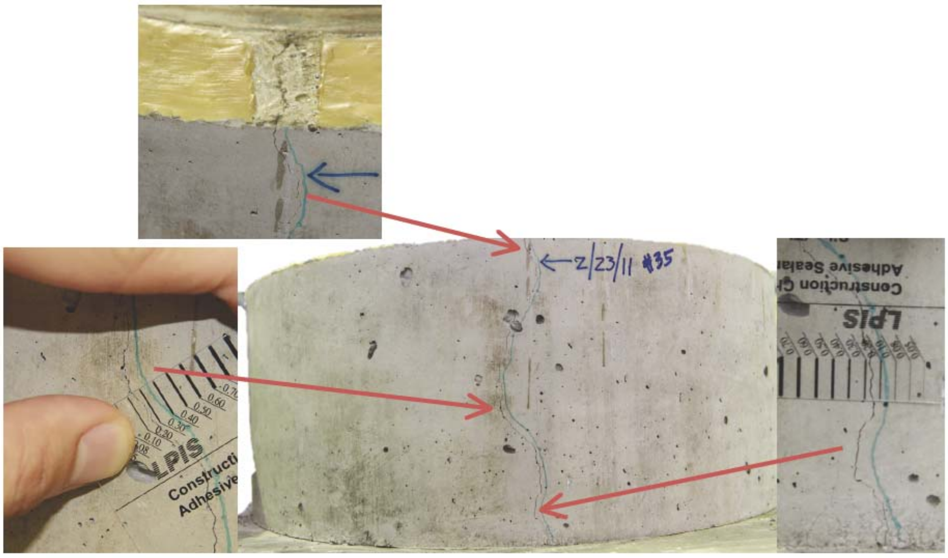

Figure 11: Typical cracking of Restrained Ring specimen

6.14 Control Ring specimen

Two ring specimens of the control sample is casted and monitored for strain development then calculated for the stress rate with respect to the ring dimensions, results and testing data are presented in Table 6, detailed explanation on how to determine these testing data and linear regression results are found in ASTM C1581 standard. Calculating the stress rate and comparing to the cracking tendency classification from ASTM C1581, results suggests that the control mix has a high potential for cracking, and based on the graph shown on Fig. 12, the strain of the specimen increased rapidly and reaching the tensile strain capacity at a little less than 3 days, this shows that by using plain concrete as a repair material, especially when restrained by an old concrete, this material will crack when the strain of the material will reach 150 microns.

Table 6: Stress Rate of Control Concrete Specimen

Control Ring				ASTM C1581-04	
time:	2.831 days				
slope:	77.461	0.000077461		**Average Stress Rate, S**	**Potential for cracking**
alfa:	4.603E-05			S≥0.34 (MPa/day)	High
G	72200	MPa		0.17≤S<0.34 (MPa/day)	Moderate-High
stress rate:	0.9875332	MPa/day		0.10≤S<0.17 (MPa/day)	Moderate-low
				S<0.1 (MPa/day)	Low

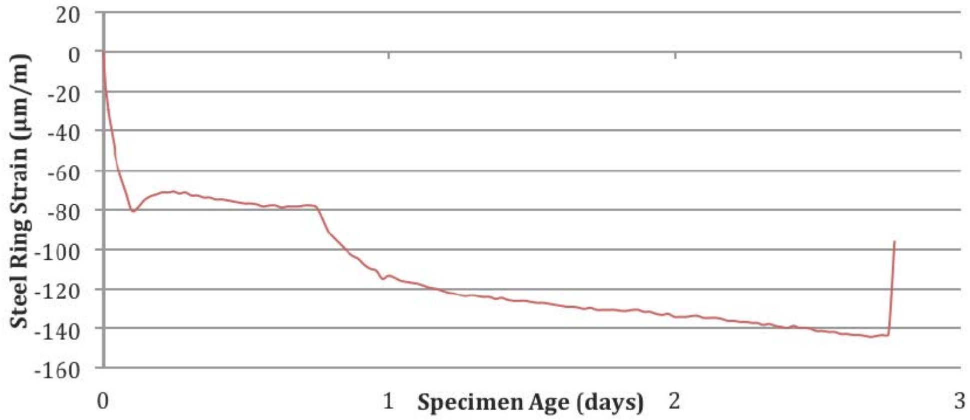

Figure 12: Control Specimen Ring Strain Plot

50% Fly ash replaced Ring specimen

Through finding out the stress rate of the control specimen which is very high, a 50% fly ash mixture is tested, to verify that a delayed reaction through pozzolanic activity of the fly ash can minimize the strain propagation of the concrete element allowing more time for the concrete to relieve stresses through stress relaxation or creep, as researchers (Hossain & Weiss, 2004) who have studied the stress propagation on concrete ring specimens have observed. Tabulation of the data is shown in Table 7, as shown, the stress rate of the mixture has decreased significantly, but it is observed that the value is just 3% lower than the low-cracking potential limit set by ASTM. Moreover, a cracking time of 33 days exceeds the limitations of USACE for concrete materials used in repair, the plotted figure with strain against curing duration is plotted in Figure 13, it shows that the strain propagation of the 50% fly ash replaced mixture is indeed more slowly than the control mixture, and through this delayed strain propagation, stress relaxation of the sample takes place.

Table 7: Stress Rate of 50% fly ash replaced Concrete Specimen

CFA50				ASTM C1581-04	
time:	33.625 days				
slope:	90.941	9.09E-05		**Average Stress Rate, S**	**Potential for cracking**
alfa:	1.57E-05			S≥0.34 (Mpa/day)	High
G	72200	Mpa		0.17≤S<0.34 (Mpa/day)	Moderate-High
stress rate:	0.097635	Mpa/day		0.10≤S<0.17 (Mpa/day)	Moderate-low
				S<0.1 (Mpa/day)	Low

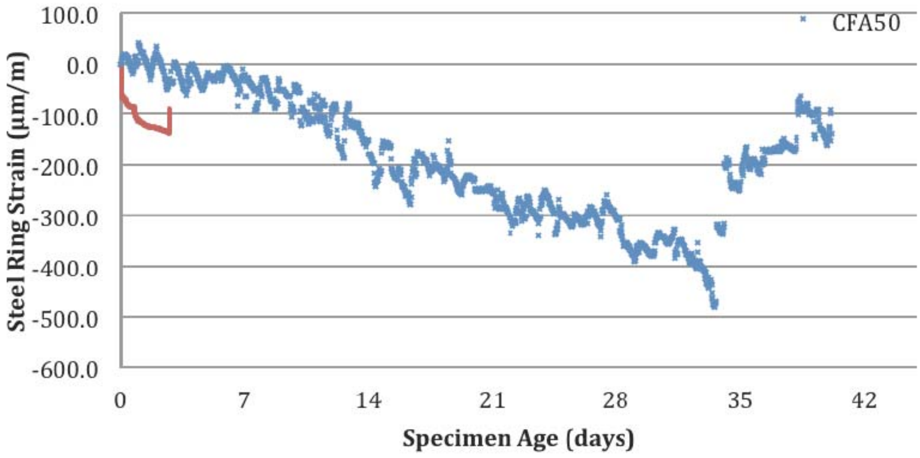

Figure 13: Strain propagation of 50% fly ash replaced concrete and control concrete

50% Fly ash replaced with Expansive Admixture addition Ring specimen

Strain measurements of 50% fly ash addition concrete, with and without expansive agent is presented in Figure 14 and the stress rate calculations are presented in Table 8. Results as seen from the graph that with the addition of expansive agent to the 50% fly ash concrete, a very minimal (<50 microns) deformation of the concrete specimen can be achieved, moreover the maximum strain from this specimen read -110 microns on the negative end and 60 microns on the positive end, which from observation of cracking at the surface of the concrete, this is still not deleterious since the concrete have not shown any cracking during the test duration. It is also noticed in the graph that expansion of the concrete started at around 5 days of curing then a gradual decrease in shrinkage occurred until around 28 days of curing, and beyond this period a minimal deformation is recorded. As for the results of the calculation of stress rate, a very low stress rate is occurring from the specimen, but it should also be noted that these stress rate calculations are based on the linear regression of the graph, which is considering the median of the values and assuming a linear relationship from the casting of the specimen until continuous curing.

Table 8: Stress Rate of SCC 50% fly replaced Concrete Specimen with expansive addition

SFA50E7				ASTM C1581-04	
time:	36 days				
slope:	7.6969	7.7E-06		**Average Stress Rate, S**	**Potential for cracking**
alfa:	1.3E-06			S≥0.34 (Mpa/day)	High
G	72200	Mpa		0.17≤S<0.34 (Mpa/day)	Moderate-High
stress rate:	0.00772	Mpa/day		0.10≤S<0.17 (Mpa/day)	Moderate-low
				S<0.1 (Mpa/day)	Low

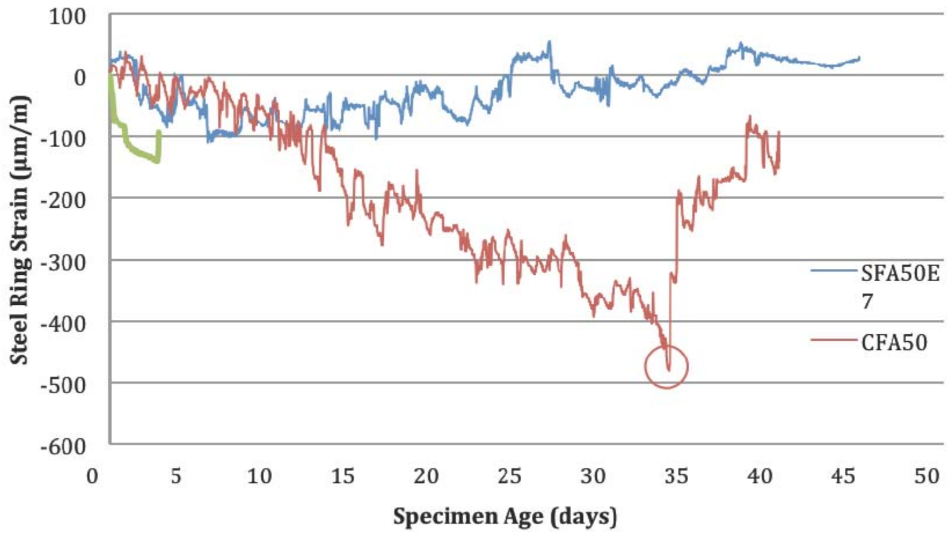

Figure 14: Strain propagation of 50% fly ash replaced concrete, with and without expansive agent addition

6.15 Full Scale reinforced concrete beam repair

In this section, results of load against mid-span deflection of the repaired beams attained from third-point loading of full scale beam specimens. Control beams are cured for 90 days before repair material is casted, no surface preparation or bonding agent is used in the beam surface. This testing is to evaluate the inherent performance of the repair material under actual service.

Normally Compacted Concrete beam repaired on compression zone

The normally compacted concrete repair material developed is performance tested on a simulated beam repair procedure. This repair is casted on the compressive zone of the substrate beam that is cured for 60 days and tested after 7 days curing of the repair material. Results from the test as shown in Fig. 15 suggest that at 7 days of curing, the repaired beam can already sustain a load similar to that of the control beam without repair. An increase of 50% of the elastic range of the specimen and an increase of 6% on the ultimate load capacity of the beam is also observed after 7 days curing of the repair material. These results represent that the repaired members can be open to service 7 days after repair casting.

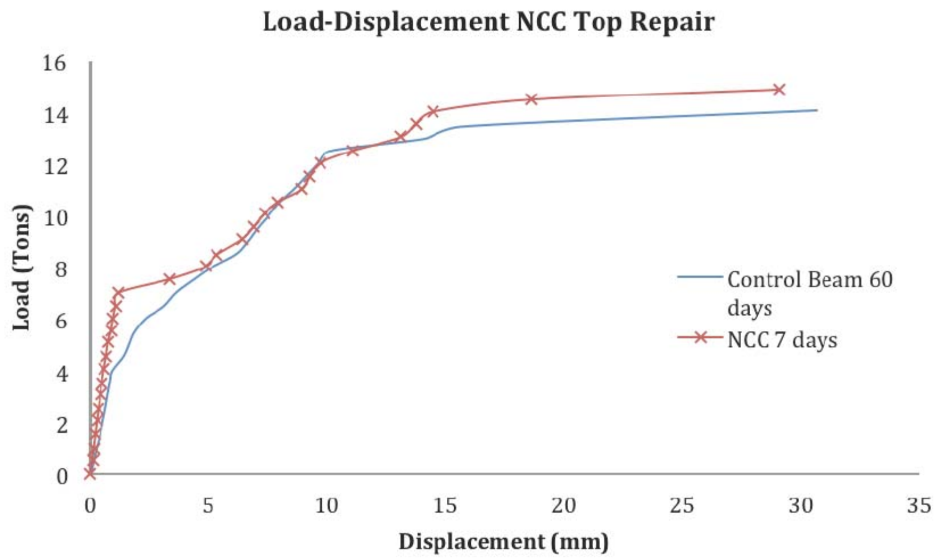

Figure 15: Load against mid-span deflection of control and NCC repaired beam

Self Compacting Concrete repair on tensile zone

Results of the SCC repaired beam from the tensile zone compared to the control beam without repair is presented in Figure 16. Casting of the SCC material at the bottom of the beam is done without consolidation. Load-testing is done after 5 days curing of the repair material, results have shown that a similar elastic deflection with the control beam is observed during the elastic stage of the graph, but an elastic limit of 9 tons is achieved with the repaired SCC beam while the control beam 4 tons, a 225% increase in elastic load capacity of the beam. Moreover, a similar ultimate strength of the beam is observed during failure of the specimen.

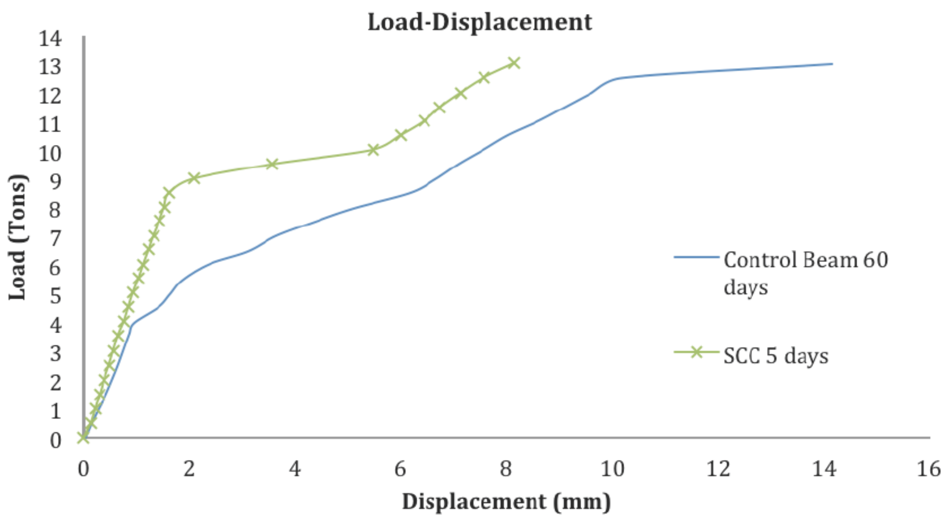

Figure 16: Load against mid-span deflection of control and SCC repaired beam

Long term behaviour of NCC and SCC concrete repair

Beam where the repair material is casted and left to cure for 28 days is discussed in this section. Curing of the specimens is 7 days moist curing and air dried thereafter, beams after casting the repair material is left outdoors and exposed to weather. Cracking or the delamination of the repair material is visually monitored during this time, but none has occurred after 28 days of curing. Load testing of long term specimens are also presented in Figure 17 to present the long term performance of the members, which as the results suggest, the original performance of the control beam has been restored after repair.

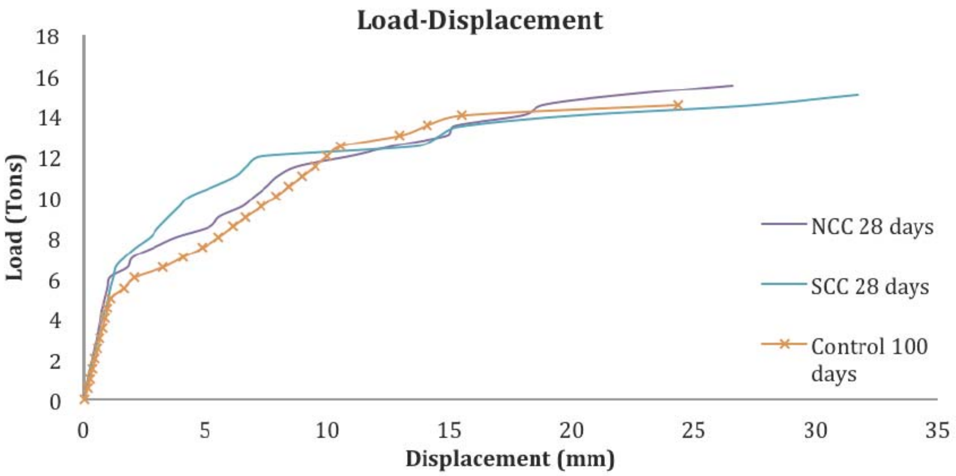

Figure 17: Load against mid-span deflection of control and SCC long term repaired beam

6.16 Cost

This section compares the properties of the developed repair concrete to that of similar commercial repair concrete products currently offered in the market. Performance from data sheets of three commercial products supplied in mortar bags and extended with coarse aggregate are used for the comparison of performance. Cost of commercial product for a yield of one cubic meter of repair concrete is calculated based on the manufacturers' specified proportion of packed material to coarse aggregate ratio for a yield of one cubic meter. While the cost of the developed concrete is calculated based on the raw cost of each material and therefore, noting that additional cost aside from the base materials such as development, testing and marketing are not considered in the cost. Tabulated values of the performance of three commercial products and the developed concrete are shown in Table 9.

Table 9: Tabulated properties of commercial products vs. developed repair concrete

TEST	Brand ES66	Brand ZC	Brand SC	CFA50E7 Repair Concrete
Cost	45,000 THB/ cu m	55,000 THB/ cu m	37,500 THB/cu m	2,050 THB/ cu m
Split Tensile (ASTM C496)	3.8 MPa (7d)	2.7 MPa (7d)	2.1 MPa (7d)	3 MPa (7d)
Free Shrinkage (ASTM C157)	600 microns (28d)	<500 microns (28d)	143 microns (28d)	66 microns (28d)
RING TEST (ASTM C1581)	60 day no crack	60 day no crack	Not Tested	60 day no crack
Compressive (ASTM C39)	41.4 MPa (7d)	27.6 MPa (7d)	36.5 MPa (7d)	42 MPa (7d)
Slant Shear (ASTM C882)	14.8 MPa (7d)	10.3 MPa (7d)	7.5 MPa (7d)	7.2 MPa (7d)

Cost Comparison with commercial product of similar properties and applications

Based on the data shown in Table 9, a repair concrete of similar performance to highly priced commercial products is developed at the fraction of the cost (94.5% lower cost than the cheapest product considered). The price of the developed repair concrete binder considered should be noted that it is calculated based on the cost of raw materials and based on the current market price as of research period, unit prices of these materials are shown in Table 10 and binder costs of different fly ash replacements with expansive agent brand S in appendix D.

Table 10: Unit Cost of Binder Materials

Cement (ASTM Type 1)	THB 2,500 / Ton
Expansive Agent S	THB 20,000 / Ton
Fly ash	THB 800 / Ton

CONCLUSIONS

Based on the results obtained from the experimental study, the following conclusions can be drawn:

1. The normally compacted repair concrete type with a total binder of 485 kg/m3 with 50% fly ash replacement and 7% expansive agent addition can be effectively used as a low-cost, low-cracking tendency, dimensionally stable(>100 microns), and high early strength (42 Mpa in 7 days) concrete repair material.

2. A self-compacting repair concrete with the same binder proportion can achieve a high slump flow (810 mm), good passing ability, non-segregating, high early strength(33MPa in 7 days), low shrinkage (>100 microns) and low cracking tendency material (>60 days no crack).

3. Full-scale reinforced concrete beams repaired with the developed material exhibited enhancement of performance in terms of higher load

before first cracking and an increased elastic limit of the repaired beam in comparison to the original beam without repair.

4. A low-cost (2,050 THB/cu m) concrete repair material is developed with a performance similar to those of expensive concrete repair materials.

REFERENCES

Emmons, P., & Sordyl, D. (2004). *Vision 2020: A vision for the concrete repair protection and strengthening industry*.

Kovler, K., & Bentur, A. (2009). Cracking sensitivity of normal and high-strength Concretes. *ACI Materials Journal*, V. 106,No. 6.

Siddique, R. (2003). Effect of fine aggregate replacement with class F fly ash on the mechanical properties of concrete. *Cement and Concrete Research 33* , 539-547.

Ghosh, R. (1981). Creep of fly ash Concrete. *ACI Journal 78* , 351-387.

Bilodeau, A., & Malhotra, V. (1992). Concrete incorporating high volumes of ASTM Class F flyashes: mechanical properties and resistance to deicing salt scaling and to chloride-ion penetration. . *ACI Special Publication*, 319-349.

Naik, T., Singh, S., & Hossain, M. (1994). Permeability of concrete containing large amounts of fly ash. *Cement and Concrete Research 24* , 913-922.

Shafiq, N., & Cabrera, J. (2004). Effects of initial curing condition on the fluid transport properties in. *Cement & Concrete Composites 26* , 381–387.

Joshi, L. S. (1993). High strength concrete with high volumes of Canadian subbituminous coal ash. *Third International Symposium on Utilization of High Strength Concrete*.

Hwang, S., Khayat, K., & Bonneau, O. (2006). Performance-based specifications of self-consolidating concrete used in structural applications. *ACI Materials Journal*, V. 103 No. 2.

Hu, S., & Li, Y. (1999). Research on the hydration, hardening mechanism, and microstructure of high performance expansive concrete. *29*.

Weerdt, K., Kjellsen, K., Sellevoid, E., & Justnes, H. (2011). Synergy between fly ash and limestone powder in ternary cements. *Cement and Concrete Composites* , 30-38.

Halicka, A. (2009). Active repairs of structures with materials based on expansive cement. *Archives of Civil Engineering*.

Hossain, A. B., & Weiss, J. (2004). Assessing residual stress development and stress relaxation in restrained concrete ring specimens. *Cement and Concrete Composites*, 531-540.

ANALYSIS OF MID RISE STRUCTURE MADE BY TIMBER AND STEEL -SIMULATION OF SHAKING TABLE TESTS BY TIME HISTORY RESPONSE ANALYSIS

Kazuki TACHIBANA[1], Mikio KOSHIHARA[2]
[1] M.Eng., Graduate Student School of Eng.The University of Tokyo, Japan
ktachi@iis.u-tokyo.ac.jp
[2] Associate Professor, IIS, The University of Tokyo, Japan
Kos@iis.u-tokyo.ac.jp

ABSTRACT

Recently, environmental issues such as global warming have gained international attention with worldwide focus on ways to reduce human impacts. The efficient use of wood materials is one of the effective methods of reducing environmental load from the standpoint of "carbon fix" and "suppression of carbon-dioxide emissions". Based on this, the development of mid-to-high-rise wooden buildings in a safe and effective manner has attracted attention world wide. Mid-rise and high-rise wooden structures are gaining popularity in many countries including Japan. The paper discussed about seismic ability of Mid-rise and high-rise wooden structures on the shaking table test. The shaking table test is NEESWood 2009, US and Japanese researcher did. The specimen is 6 stories timber and first story is steel structure. I simulated P- δ curve by using the test results. For them we could simulate specimen story period, displacement and shear force.

Keywords*: shake table testing, seismic response, mid-rise building, light-frame wood, earthquake.*

1. INTRODUCTION

Recently, environmental issues such as global warming have gained international attention with worldwide focus on ways to reduce human impacts. The efficient use of wood materials is one of the effective methods of reducing environmental load from the standpoint of "carbon fix" and "suppression of carbon-dioxide emissions". Based on this, the development of mid-to-high-rise timber buildings in a safe and effective manner has attracted attention world wide. Mid-rise and high-rise timber structures are gaining popularity in many countries including Japan. Some companies have begun to go as high as four stories in wood and the Japanese. Government has mandated that a certain percentage of public structures be made of wood. This increasing interest and government mandate serve as the motivation for this paper.

In July 2009 a full-scale mid-rise light-frame apartment building was subjected to a series of earthquakes at the world's largest shake table in Miki, Japan. On NEESWood project, US and Japanese researchers worked jointly to test the building. We already considered about the structural design of the building in relation to Japanese Building Codes. The purpose of this study is simulation of shaking table tests by time history response analysis on the result of the test.

2. SHAKING TABLE TEST

2.1 Specimen

This specimen consisted of a single story of steel with six stories of wood on top. Figure 1 shows a panoramic view of the specimen. The timber building was approximately 18.14m x 12.14m (60ft x 39ft) in plan view and about 16.82m (56ft) tall. The design details of the building were quite extensive and only a basic description of the structural configuration is provided here for brevity. The floor plan, layout plan and the direction are shown by Figure 2. Shear walls in Capstone building used mostly 2x6 framing and 12mm (15/32 inch) T&G Oriented Strand Board (OSB) on either one or both sides. The nail which we used is "10d common" (length: 7.6mm, diameter: 3.8mm). The nail schedule was mostly 2"/12" or 3"/12" in the lower floors. Incorporation of a new wall type was also investigated in the project. A double mid-ply wall (mid-ply wall) system designed to handle high shear demand that exceeds the capacity of traditional shear walls was included. Also because of the high shear capacity of shear walls, high strength shear screws were used at the top and sill plates of the shear walls instead of bolts. These SDS screws had a tested ultimate capacity of approximately 1 kip per-connector in shear. Studs are D.fir from 2nd to 4th story and S-P-F from 5th to 7th story. Gypsum wall board (GWB) was installed on all inside walls except mid-ply wall and ceilings with tape and putty on all joints except the wall-to-ceiling joints and corners. Each shear wall stack included glulam beams as shear collectors in between stories. The glulams were fully supported by shear walls except in one line between the elevator shaft and stairwell where they acted as beams since no bearing and/or shear wall was present. Finishing as many joints as possible was desirable in order to provide realistic damage inspection results. For reference, the origin is the left corner, and the short dimension of the building is designated as the X direction and the long dimension as the Y direction. (Following Figure 2) Wood shear walls were designed as stacked wall systems with a combination of steel rod hold-downs (ATS) with mechanical shrinkage compensating devices at each end to prevent overturning, reduce uplift, and remove slack from the tie-down system that would otherwise develop from in-situ reductions in wood moisture content and natural settling of the structure.

Figure 1: The panoramic view of specimen

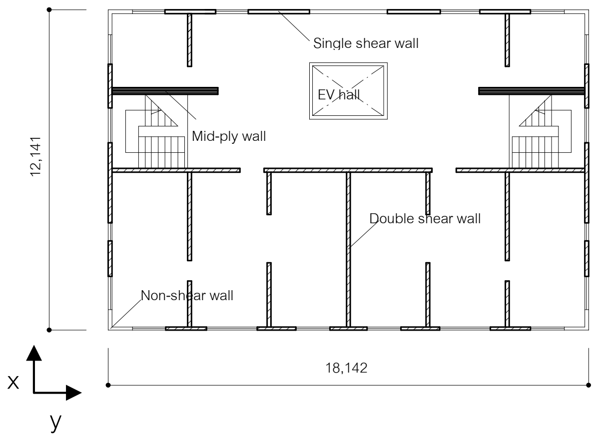

Figure 2: The floor plan and layout plan

2.2 Test plan

We used Nothridge CanogaPark wave by changing times. The time is decided by Hazard level on return period. In Seismic test (ST) 1and 2, the tension of Steel brace was loosed. The brace in ST3~5 was tied. Table 1 shows more detail information.

Table 1: Seismic test schedule

Seismic test	Test date	Brace situation	Hazard level	Scaling factor	PGA (g)		
					X	Y	Z
1	6/30/2009	Loose brace	50%/50 yr	0.53	0.19	0.22	0.26
2			7%/50 yr	1.40	0.50	0.58	0.69
3	7/6/2009	Tied braced	50%/50 yr	0.53	0.19	0.22	0.26
4			10%/50 yr	1.20	0.43	0.50	0.59
5	7/14/2009		2%/50 yr	1.80	0.65	0.75	0.88

2.3 damage inspection

After shaking table test, we did damage inspection. The damage was only the clack of gypsum board and the place was mainly corner of opening. Figure 3 shows the example. By the damage inspection, it was clarified that there are much damage especially at 4th and 5th story. It shows a similar result in story drift at 3rd ~ 5th story.

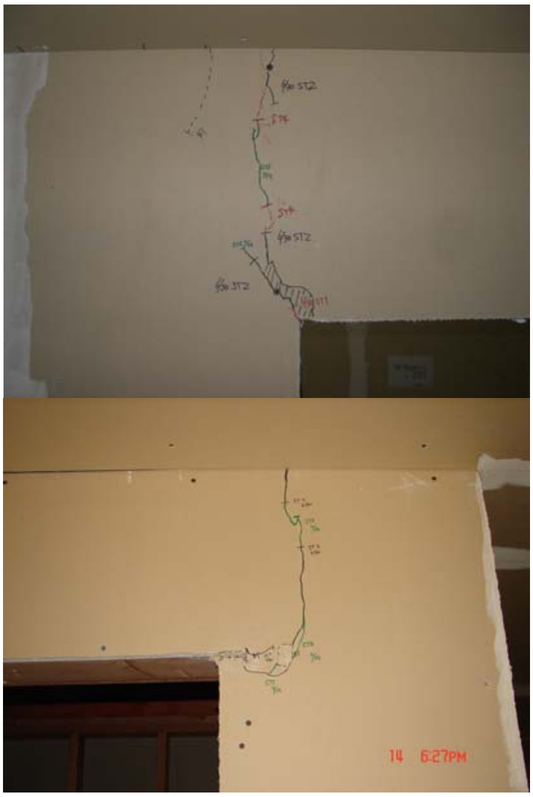

Figure 3: Damage inspection
(L:5th story south center wall R:4th story EV hall)

3. MODELING

3.1 Test result

Displacement measured by image processing. The measuring points exist 7 points per story. The circle and square points in Figure 4 show the place setting sensors. The circle one is the sensor measuring displacement. The square one is the sensor measuring acceleration.

Test result is a spatial model actually. We averaged all measured points per stories for changing mass model from spatial model. Story drift is the value taking Shaking table data or averaged data at lower story from averaged displacement at one story. The average about acceleration follows that (center x 2 + 4 corner)/6. Shear force can calculate that the acceleration multiply mass.

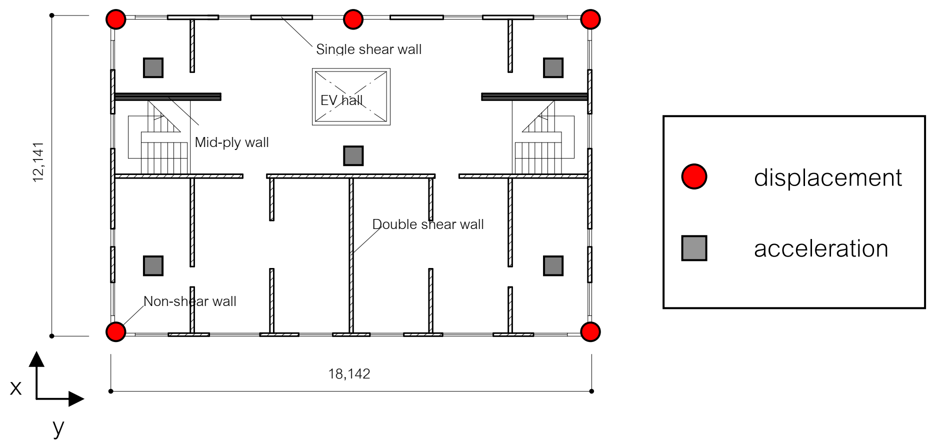

Figure 4: Position of measuring sensor

3.1 Specimen

We made a specimen model for analysis. The model was based on test results. Because we can see it didn't achieve *Pmax*, We expressed tri-linear before *Pmax*. Figure 5 shows an example to make Skelton curve. SC in the figure means Skelton curve.

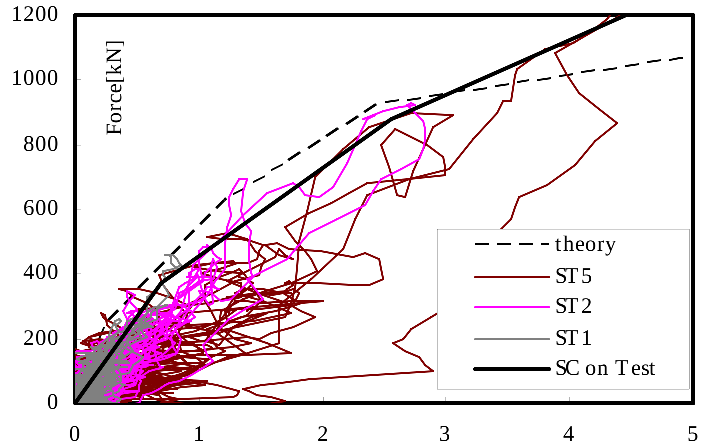

Figure 5: Skelton curve from test result

4. ANALYSIS

4.1 Time historical analysis

We analysis by non-linear, time historical analysis is "increment displacement express" based on *Wilson θ*. Formula 2 show "increment displacement express". Formula 2 consist Formula 1 in Figure 6. The Damping matrix is the following formula 3 and 4.

$$-[M]\{\ddot{y}_0\}=[M]\{\ddot{x}\}+[C]\{\dot{x}\}+[K]\{x\} \tag{1}$$

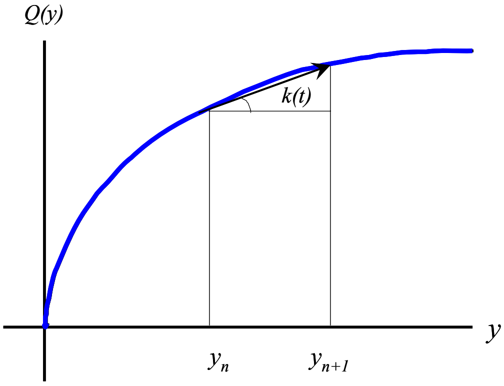

Figure 6: increment displacement express

$$
\begin{aligned}
&-m\Delta\ddot{y}_0 = m\Delta\ddot{x} + c\Delta\dot{x} + k(t)\Delta x \\
&\Delta x = x_{n+1} - x_n, \Delta\dot{x} = \dot{x}_{n+1} - \dot{x}_n \\
&\Delta\ddot{x} = \ddot{x}_{n+1} - \ddot{x}_n, \Delta\ddot{y}_0 = \ddot{y}_{0n+1} - \ddot{y}_{0n}
\end{aligned}
\tag{2}
$$

[M]: mass matrix, [C]: damping matrix, [K]: stiffness matrix

$$
\begin{aligned}
&c_{ij} = c_{ij}^{*} / \omega^{(j)} \\
&h_{ij}^{(j)} = c_{ij}^{*} / \left(2k_{ij}\right) \\
&c_{ij} = 2h_{ij}^{(j)} k_{ij} / \omega^{(j)}
\end{aligned}
\tag{3}
$$

$$
[C] = \begin{bmatrix} c_{11} & \cdots & c_{1j} \\ \vdots & \ddots & \vdots \\ c_{i1} & \cdots & c_{ij} \end{bmatrix} \quad [K] = \begin{bmatrix} k_{11} & \cdots & k_{1j} \\ \vdots & \ddots & \vdots \\ k_{i1} & \cdots & k_{ij} \end{bmatrix} \tag{4}
$$

4.2 Analysis model

We used *magara* model for timber light frame and normal model for steel as historical models. Figure 7 shows each historical model. The parameters of *magara* model are based on the study for light frame at past. Table 2 shows the parameters. I didn’t consider historical after *Pmax* on normal model here because even ST5 didn’t achieve *Pmax*.

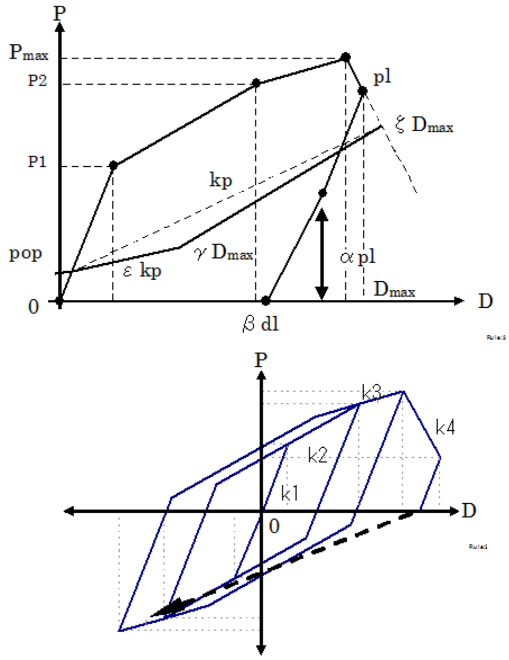

i) magara model ii) normal model

Figure 7: analysis model

Table 2 magara model parameters for light frame

α	β	γ	ε	ζ	Pop
0.25	0.75	0.5	0.6	1.04	P_{max} x 0.125

4.3 EARTHQUAKE WAVE

We used measured earthquake wave on shaking table for loosing time lag. Figure 8 shows Nothridge CanogaPark 180% wave, Y direction. On next term, we compare analysis to test result for using this wave.

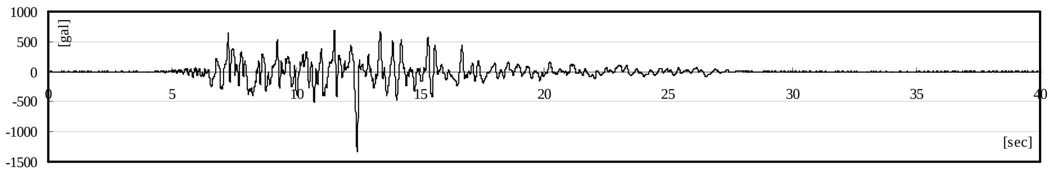

Figure 8: Nothridge CanogaPark 180% Y direction (measured wave)

5. RESULT

Figure 9 shows the analysis result on ST5 Y direction because the displacement of Y direction is bigger than X direction. The result shows analysis result of 2nd story is bigger than the test result. But it is safety value. We can see not fit on 1st story. (Figure 10) Figure 11 shows time history shear force comparing analysis to test. The result shows period is mainly fitting and safety value. Safety vale means analysis result is bigger than test result.

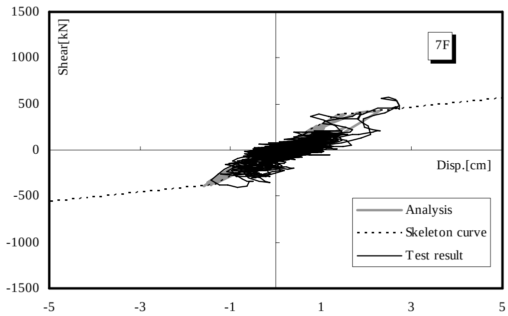
7F
Shear[kN]
Disp.[cm]
Analysis
Skeleton curve
Test result
1500
1000
500
0
-500
-1000
-1500
-5
-3
-1
1
3
5

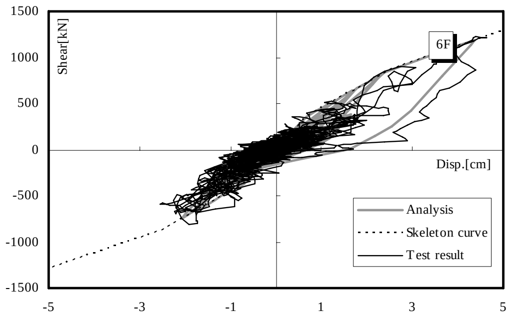
6F
Shear[kN]
Disp.[cm]
Analysis
Skeleton curve
Test result
1500
1000
500
0
-500
-1000
-1500
-5
-3
-1
1
3
5

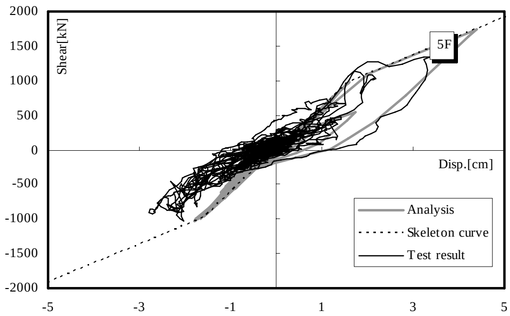
5F
Shear[kN]
Disp.[cm]
Analysis
Skeleton curve
Test result
2000
1500
1000
500
0
-500
-1000
-1500
-2000
-5
-3
-1
1
3
5

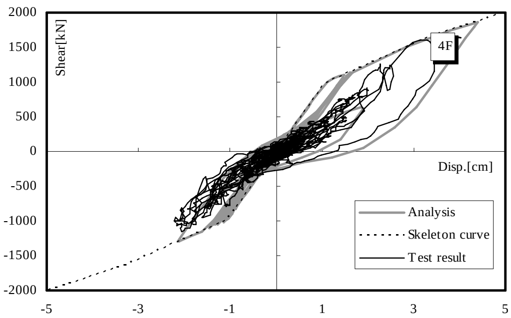
4F
Shear[kN]
Disp.[cm]
Analysis
Skeleton curve
Test result
2000
1500
1000
500
0
-500
-1000
-1500
-2000
-5
-3
-1
1
3
5

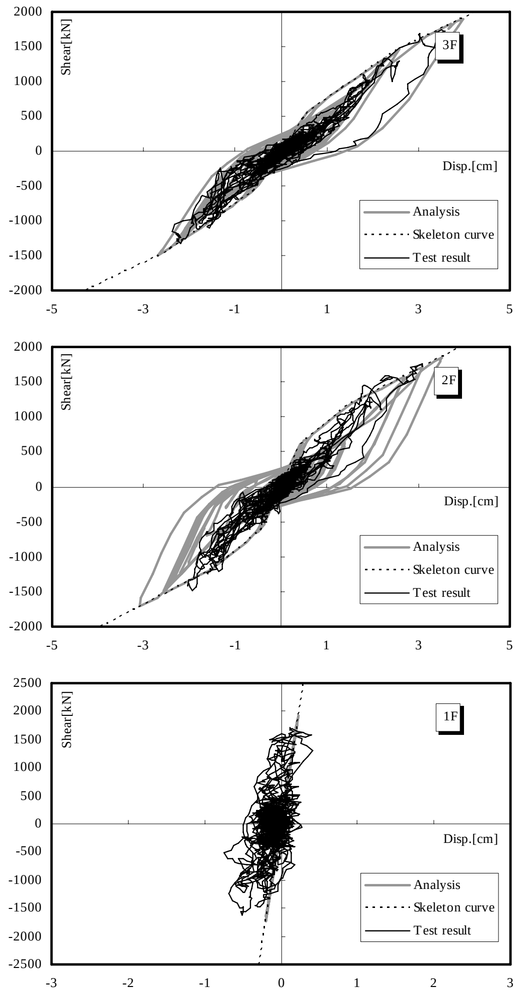

Figure 9: Shear force- story displacement comparing Test result to Analysis on ST5

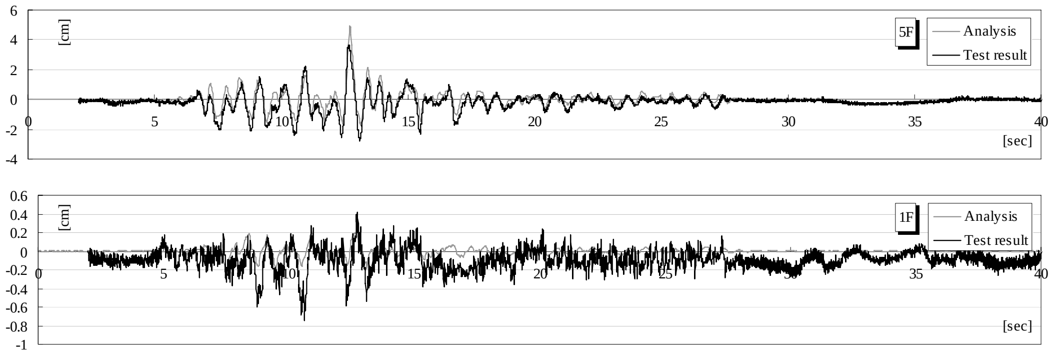

Figure 10: Time history response (story displacement)

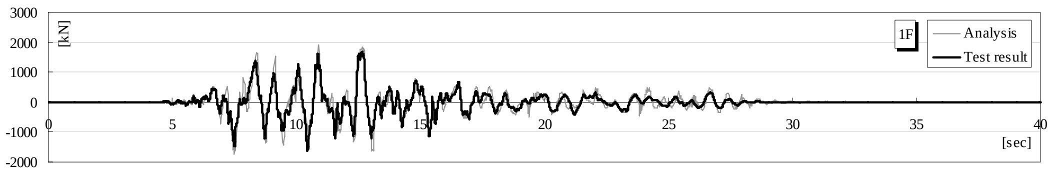

Figure 11: Time history response (story shear force)

6. CONCLUSION AND RECOMMENDATIONS

We simulated P- δ carve by time history analysis using Skelton carve on Test result. The simulation result shows the following methods:

- ・The result show 4th and 5th story displacement is bigger than the other stories as the test result. This is a characteristic change happened actually,
- ・Period almost fit the test result.
- ・On 1st story, analysis displacement didn't fit the test result. But shear force by analysis show safe for test.

This is not theory model such as simply summing each Skelton curves on each story. Therefore we will consider the way to make Skelton curve.

REFERENCES

Japan 2x4 home builders association: Structural calculation guidelines for light frame wooden structure. 2007

Kazuki TACHIBANA, Hiroshi ISODA, Tomoya OKAZAKI, Mikio KOSHIHARA, Evaluation of the NEESWOOD Capstone Test Specimen using Japanese Building Codes, WCTE2010

Architecture vibration theory, Yorihiko OSAKI, syoukoku-sya, 1996

NEESWood Project: Structural and Environmental Engineering, University at Buffalo, State University of New York, Buffalo, available on-line at http://www.nsf.gov/news/newsmedia/neeswood/

The Building Center of Japan: The Building Standard Law of Japan. June 2004

Takuya MAGARA, Tatsuya MIYAKE, Hiroshi ISODA, Shinichiro TAMORI, Akira SASAGAWA, A STUDY ON THE MAXIMUM SEISMIC RESPONSE DISPLACEMENT OF WOOD FRAME CONSTRUCTIONS : Prediction of the maximum seismic response displacement of single-mass system based on energy input ratio, Journal of structural and construction engineering. Transactions of AIJ (506), 75-82, 1998-04-30.

AN EMPIRICAL ANALYSIS OF SUCCESS AND FAILURE FACTORS FOR PUBLIC-PRIVATE PARTNERSHIPS IN TOLL ROAD INVESTMENTS

Sathita TAOTHONG[1], Piyapong JIWATTANAKULPAISARN[2] and Kunnawee KANITPONG[3]
[1]Research Associate, Asian Institute of Technology, Thailand
sathita_taothong@hotmail.com
[2]Transportation Engineer, Bureau of Planning, Department of Highways, Thailand
[3]Assistant Professor, Transportation Engineering Program, Asian Institute of Technology, Thailand

ABSTRACT

As the infrastructures and public services require a high investment cost and the government has a limited of budget, a new approach called Public-Private Partnerships (PPPs) is introduced to overcome this problem. This PPPs scheme allows the private sectors to participate and finance in public infrastructures and public services projects. Toll road and highway is one of the infrastructures that popular used PPPs scheme as a solution to that problem. The objective of this study is to empirically examine the success and failure factors of the PPPs toll road and highway projects using the logistic regression technique. Five main success and failure factors: project's country attributes, past experiences with PPPs toll road and highway project, government support, project characteristics and the private sector's attributes are proposed for the analysis. The estimation results draw conclusions that all of the sub-factors in the project's country attributes factor such as project's region, corruption level, democratic level, income level, GDP growth and political stability take an important role to the outcome of the project. The past experiences with PPPs toll road and highway project also with the private sector's attributes factor and the type of Private Participation in Infrastructure (PPI) seem to have effects to the project as well. One interesting point from the results is that the project route appeared to be significant to the success of PPPs toll road and highway project, especially if considering with the existing of competing route factor

Keywords*: Public-Private Partnerships, toll road and highway, Logistic regression model, success factors, failure factors.*

1. INTRODUCTION

1.1 Background

In every country, fundamental infrastructures and public services such as electricity, telecommunications, water services, waste management, public transportation, health care, fire service and social services are the principle facilities for their citizen's living life. In the past, the public sector solely owned and provided the capital for implementing these fundamental infrastructures and public services. But because of theses infrastructures and public services require a high investment cost and the government has a limited of budget, a new approach namely Public-Private Partnerships (PPPs) is introduced to overcome the problems. This approach named Public-Private Partnerships (PPPs) is a scheme that allows the private sectors to participate and finance in public infrastructures and public services projects by entering into a certain period of contractual agreement.

1.2 Objective

This study aims to examine the success and failure factors for PPPs toll road and highway projects as to enhance our understanding of the influences of each factor, which could in turn lead to a better direction for implementing PPPs toll road and highway projects in the future.

2. PREVIOUS STUDIES RELATED PPPS TRANSPORT PROJECTS

2.1 Previous study topic in PPPs transport projects

Among the previous studies related PPPs transport project, toll road and highway is the most attention sector with various topics chosen. Financing is one of the general topics which are focused by many researchers. The detail of the investment program together with the value of money and the project's return were analyzed in order to consider the worthiness of the projects (e.g. Reeves, 2005; Mayer, 2007). Moreover, revenue sharing risk, risk transfer and bidding process were sometimes included in these financial studies (e.g. Mayer, 2007; Kalidindi, 2009; A.B. Alonso-Conde et al., 2007). According to the PPPs framework studies, not just only the steps and the process of launching PPPs projects were identified (e.g. Sussman and Ward, 2006; Queiroz, 2007; De Jong and Rui et al., 2010), but the policy, regulations and agreements were also the main contents of these studies' topic neither (e.g. Chan and Subprasom, 2007; Goodliffe, 2002). However, risk allocation is another title that was widely concerned and can be combined with other topic studies as well. In the risk allocation studies, several types of risk that related to the PPPs projects were classified (e.g. Ogunlana and Abednego 2006), and the risk transfer strategies were discussed (e.g. Singh and Kalidind, 2006; Medda, 2007; Phang, 2007). In addition, other topics such as success and failure factors in transport PPPs and concession contract had also been in the list of transport PPPs studies either. These studies identified and analyzed the factors that have an influence to the success of the project (e.g. Galilea and Medda, 2009; Renato E.Reside, Jr., 2009; Tam, 1999; Bagchi and Paik, 2001). It is observed that most of the studies in this success and failure factors used the case studies in many countries to be the key answers.

2.2 Success and failure factors in PPPs transport project

From the previous studies, many researchers have proposed and describe numerous factors in terms of descriptive context which related to the success of the PPPs projects. These factors can be concluded and classified into six aspects: Public sector, Private sector, The public or users, Financial, Risk and Contractual arrangement (e.g. Chen and Subprasom, 2007; Jacobson and Choi, 2008; Mahalingam, 2010; Ogunlana and Abednego, 2006; Queiroz, 2007; Sussman and Ward, 2006; Tam, 1999; Tang et al., 2009; Zhang, 2005).

However, there are some studies that focused only on success and failure factors in terms of empirical analysis (Galilea and Medda, 2009; ADBI , 2009). The research by Galilea and Medda (2009) focuses on the factors that have the effects to the success and failure of PPPs transport projects in all four sectors: toll road and highway, seaport, airport and railroad and mass public transit. Its objective is to investigate the role of three main factors in the success of the transport PPPs: national experience, the presence of private investors, and the influence of multilateral lenders, by logistic regression model. Meanwhile, the working paper by ADBI (2009) focused on the factors which stress the failure of PPPs projects in all infrastructures sectors: Energy, Telecom, Transport and Water. The objective of this empirical research is to estimate the factors that account for the greatest level of stress in infrastructure projects; Regulation, Tariff/Political, Legal and Institutional framework, Macroeconomic-economic conditions during the operations phase, Economic conditions during project design phase, structure of transaction, Multilateral and bilateral support, Contract, Nationality, Country's fiscal capacity and Sectoral dummies, by probit regression model.

3. METHODOLOGY

3.1 Proposed success and failure factors

This study is the extension of Galilea and Medda's work in the topic of "Analyzing the influence of national political and economical factors on the success of public-private partnerships in transport" which focusing on the success and failure factor in PPPs transport projects that cover in all sectors. To specify only in toll road and highway project, five main success and failure factors have been modified and added from Galilea and Medda (2009) for their influence's analysis which are the project's country attributes, past experiences with PPPs toll road and highway project, government support, project characteristics and private sector's attributes as shown in the Table 3.1.

Table 3.1: Comparison between Galilea and Medda's success and failure factors and this study

Factors	Galilea and Medda (2009)	This study
Project's country attributes		
Region	✓	✓
Corruption level	✓	✓
Democratic level	✓	✓
Income level	✓	✓
GDP growth	✓	✓
Political stability	×	✓
Past experiences with PPPs toll road and highway project		
Government's past experiences	✓	✓
Private sector's past experiences	×	✓
Government support		
Government support	×	✓
Project characteristics		
Project route	×	✓
Existence of competing route	×	✓
Route length	×	✓
Type of Private Participation in Infrastructure (PPI)	×	✓
Private sector's attributes		
Number of private investors	✓	✓
Percentage of private sector ownership	✓	✓

3.2 Data and variables

The data used in this study is mainly taken from the Private Participation in Infrastructure Projects. This study also utilizes other sources of the data such as the index values from the Transparency International, The Economist, the World Development Indicators (WDI) by The World Bank and the World Bank Governance Indicators. Online Google map is also used for examining the characteristics of the PPPs toll road projects.

3.3 Model

In this analysis, binary logistic regression model is used which represents two possible values: success or fail. The formula using in the model is as followed

$$P(Y) = \frac{1}{1+e^{-Y}} \tag{1}$$

Where $Y = \beta_0 + \beta_1 X_1 + \beta_2 X_2 + \beta_3 X_3 + \ldots + \beta_k X_k$

And P = probability of the success

Y = dependent variable

X_i = independent variables
β = vector of parameter

To estimate the unknown parameters (β), Maximum Likelihood Method is used which selects values of the model parameters (β) that maximize the log-likelihood function which shown below

$$l = \log L(\beta) = \sum_{i=1}^{N} Y_i \log\left(P_i\right) + (N - \sum_{i=1}^{N} Y_i) \log\left(1 - P_i\right) \qquad (2)$$

Where P = probability of the success
Y = dependent variable
N = number of observation project

Dependent Variable (Y)

The dependent variable (Y) is equal to 1 if the project is successful which is in the status of Concluded, and Operational (more than 50, 60 and 70% of the concession period). On the other hand, the dependent variable (Y) is equal to 0 if the project is failed which is in the status of Cancelled and Distressed.

Independent Variable (X)

Many independent variables are created in this study in order to analyze their influence and significant to the success of the PPPs toll road and highway project. The name of the created variables and the definitions are shown in the Table 3.2.

Table 3.2: The variable's names and definitions

Variable	Definition
Region1EAP	1 = The project is located in East Asia and Pacific region, 0 = otherwise
Region3LAC	1 = The project is located in Latin America and the Caribbean region, 0 = otherwise
Corruption	Corruption index of the project's country during the concession period provided by the Transparency International which ranges between 0-10 points (minimum point shows the most corruption of the country)
Democratic	Democratic index of the project's country during the concession period provided by The Economist which ranges between 0-10 points (maximum point shows the most democratic governance of the country)
PoliticalStab	Political Stability index of the project's country during the concession period provided by The World Bank Governance Indicators which ranges between -2.5 to 2.5 (maximum point shows the most stable governance of the country)
GDPavg	The average of the annual Gross Domestic Product growth of the project's country during the concession period
IncomeLM	1= The project is in the Low or Lower Middle Income

	level country classified by The World Bank, 0 = otherwise
SuccessGovExp	Number of past successful project (concluded and operational) done in the country at the moment of the PPPs project's financial closure
FailGovExp	Number of past failed project (cancelled and distressed) done in the country at the moment of the PPPs project's financial closure
SuccessPrivExp	Number of past successful project (concluded and operational) done by the same private companies at the moment of the PPPs project's financial closure
FailPrivExp	Number of past failed project (cancelled and distressed) done by the same private companies at the moment of the PPPs project's financial closure
GovSupport	1 = Hosting governments provide financial support in terms of fixed government payment to the private sectors to reduce the financial risk of a project, 0 = otherwise
Urban	1 = The project is located within the same urban area, 0 = otherwise
Parallel	1 = There is a parallel road far from the road project in the range of 0-5 km 2 = There is a parallel road far from the road project in the range of 6-10 km 3 = There is a parallel road far from the road project in the range of 11-20 km 4 = There is a parallel road far from the road project more than 20 km / no parallel road
UrbanParal	The multiple between *Urban* variable and *Parallel* variable which means there is another existing road project which runs parallel to the road project located within the same urban area
RouteLength	The length of the road project in kilometer unit
PPIGreenfield	1 = The project which a private entity or a public-private joint venture builds and operates a new facility for the period specified in the project contract, 0 = otherwise
NumberPrivate	Number of private companies involved in the project
PrivatePercentage	The percentage of the project company that is owned by private sectors

4. EMPIRICAL RESULTS

4.1 Estimation results

Estimation results from total of 218 PPPs toll road projects in the status of Concluded, Cancelled, Distressed and Operational can be divided into three project operating duration; more than 50, 60 and 70% of the concession period as shown in Table 4.1.

Table 4.1: Estimation results

Variable	Operating Duration of the project								
	≥ 50% of the concession period			≥ 60% of the concession period			≥ 70% of the concession period		
	model 1	model 2	model 3	model 1	model 2	model 3	model 1	model 2	model 3
Corruption	0.3374**	0.1862	-0.066	0.2992	1.5507*	0.2915	0.1318	1.9960*	0.5297
GDPavg	0.4293*	0.7211*	0.7287	0.4767**	0.8803	0.8194	0.4334	0.8493	0.6039
PrivatePercentage	0.0358*	0.1587**	0.1605*	0.0271	0.1938**	0.1953**	0.0301*	0.1763***	0.1589**
Region1EAP	-3.8623*	-10.2126**	-8.4436	-3.3564**	-18.3319**	-11.9498**	-3.7328*	-20.7526***	-11.3798**
Region3LAC	-1.9333	-5.0776**	-3.9146	-1.2236	-7.4163**	-6.0599**	-1.9198***	-8.9994***	-4.4572**
Democratic		-0.7193	-0.9811		-3.0850***	-2.4438***		-3.294	-2.5846
IncomeLM	1.6663*	5.4427**	4.1081*	1.3924	3.1200*	2.1626*	1.6038**	3.7644	3.1888**
SuccessGovExp	0.0176	0.1007**	0.0578	-0.0176	0.0668	-0.0806	-0.0112**	0.1054	0.0145
FailGovExp	-0.048	0.0214	0.012	-0.0081	0.0942	0.1915	0.0065	0.1969	0.2382
NumberPrivate	0.0484	0.0905	0.0905	0.0454	0.2016	0.2176	0.0816	0.2519	0.2126
PoliticalStab		2.4880***	2.6349***		2.9142***	2.5859***		2.7181***	2.5716**
SuccessPrivExp		-0.3295**	-0.2269		-0.4053*	-0.2936		-0.4468	-0.3727
FailPrivExp		-0.5580*	-0.6370*		-0.6547	-0.8358*		-0.5041	-0.5802
GovSupport		-1.2993	-0.7165		2.0373	0.4532		3.5118	2.1217
Urban		-3.6959**	-3.9565**		-5.2954*	-5.6990**		-5.3519*	-5.2266
Parallel		-0.0694	-0.2485		-0.0346	-0.4527		-0.0455	-0.4016
UrbanParal		1.6423*	2.0301*		2.5646*	3.1595**		2.1268	2.9051
RouteLength		-0.0017	-0.0036		-0.0004	-0.0018		0.0037	0.0011
PPIGreenfield			-2.2170***			-3.5497**			-3.9270*
constant	-3.1447	-6.4552	-3.2345	-3.2142	3.0524	4.6	-2.7789	4.0403	4.9654
Log-likelihood	-75.1673	-47.27	-42.8439	-65.128	-33.5104	-29.2457	-53.4871	-21.588	-18.4984
observation	197	158	153	141	109	104	105	76	71

*** means the coefficient of the variable is significant at the 1% level
** means the coefficient of the variable is significant at the 5% level
* means the coefficient of the variable is significant at the 10% level

4.2 Success and Failure factors

Based on the empirical analysis, there are a number of factors that could explain the success and failure of PPPs toll road projects. These include

• *Region*. The project located in East Asia and Pacific region or Latin America and the Caribbean region is more likely to be distressed or cancelled, compared to those located in other regions (e.g. Europe and Central Asia, Middle East and North Africa, South Asia and Sub-Saharan Africa regions).

• *Corruption level.* The results show that PPPs toll road projects in countries with high levels of corruption are more likely to be cancelled or stressed as the private sectors may confront with the excessive cost due to the influence from the politics such as they have to pay for the special authorization or permission or pay for the bribe in order to win the project bidding.

• *Democratic level*. The higher democratic level of the project's country can be implied that the government do not have the full power in every decisions which can cause the delay and tend to encourage the failure of the project.

• *Income level*. It is possible that the project located in the Low or Lower Middle Income level country would meet with the successful, compared to those projects in Upper Middle Income level country.

• *GDP growth***.** The higher GDP growth rate of the project's country would support the successful as it represents the less probability of being failed by the economic crisis which encourages the initiation of the investment by the private sector. Moreover, the demand to travel in the country with strong economic growth is higher than in the country with low GDP growth rate.

• *Political stability*. In case the project located in the country with high level of government stability, the outcome would be successful. In case the government is changed too frequent, it will affect the continuation of the project's progress. The new government may not support the project as it is the previous government's work.

• *Past experience with PPPs toll road and highway project*. The results reveal that the project located in the country with higher number of past successful projects and the project invested by the private companies which have lower number of past failed project is likely to be successful. It is convinced that the government that had been achieved in arranging PPPs agreement in the past will attract the private sectors to invest in more new projects and the private sector who has had good experiences in construction, operating, financing and managing the PPPs toll road and highway projects, would better understand the strengths and weaknesses of the PPPs project.

• *Project route*. The results confirm that the project located within urban area tends to be cancelled or distressed due to the cost overrun from land acquisition process, demolishing existing buildings and facilities or traffic management payment during the construction phase. Moreover, project in the urban area may have to compete with another parallel route or other modes of transport as well.

• *Potential competing roads when combining with the location of the project route*. The project located within urban area with farther distance from the parallel roads is more likely to successful, compared to those located nearby the parallel road, with the reason that the demand is less shared between these two road projects.

- *Type of Private Participation in Infrastructure (PPI).* The Greenfield project has a higher tendency to achieve the successful than the Brownfield project. Since the project in this type of private participation is a new built infrastructure, the private companies who would like to participate in this project may also have to do and take the risk in the construction section, apart from the operation part. Besides, the demand of the new toll road and highway project is difficult to forecast as there has never been a statistic data of the road user existed. Consequently, the inaccurate demand forecast could occur.
- *Percentage of private sector ownership*. The success of the project corresponds with the higher percentage of the private sector ownership. The private sector can get the high rate of returns or incentives from higher private's percentage owned. This caused the project to be monitored and managed in the best efficient processes.

However, some factors appear to be insignificant in this study included the past failed experiences of the government, government support, competing route, the route length and number of private investors.

5. CONCLUSION

5.1 Summary

This empirical analysis reveals evidence on the success and failure factors of the PPPs toll road projects as follows:

- The project in the East Asia and Pacific region and Latin America and the Caribbean region have a probability to face with the failure
- The project located in the low corruption level and low democratic level country or Low or Lower Middle Income level country tends to be successful
- The project located in the country with higher political stability and high GDP growth rate is likely to meet with the success
- The higher number of past successful projects that have been done in the country and the lower number of past failed project that have been done by the same private companies encourages the project to be successful
- The road project which located within urban area is likely to meet with the failure
- In case the project is located within urban area, the farther of the distance between the road project and another competing route has less effects the failure of the project
- The Greenfield project tends to be successful easier than the Brownfield project
- The higher percentage of the project company that is owned by private sectors is corresponded with the success of the project

5.2 Implications

From the estimation results about the project's country attributes, they are useful for the private investors who want to participate in the PPPs toll road projects. In this regard, they could use this information as an indicator for making investment decisions. In case the project is not located in the country with these potentially successful factors, it is necessary to more carefully examine the risks associated the project and the project's contract agreement as well as to prepare themselves in tackling issues that are likely to occur.

The finding of the significant of the past experience on PPPs toll road is useful implications for both public and private sectors. The public sector can decide whether or not private firms with unsatisfactory records on the previous PPPs toll road project(s) should be allowed to join in the bidding process. On the other hand, there could be probably less risk of the project failure for private firms if they decide to participate in the project in a country with more experience on successful PPPs toll road projects.

For the project characteristic factors, the type of the project route and the type of Private Participation in Infrastructure seem to be significant and have explicit effects on the success of the PPPs toll road projects. These findings could help both the public and private sectors to consider the location of the project and be aware of the construction risks that could emerge from the project. Essentially, solutions to address the issues of excessive time and costs need to be prepared if the construction of toll road projects is designed to take place within urban areas.

The presence of competing routes could lead the PPPs toll road projects in urban areas to be failed. While these suggest that planning and design of toll road projects in urban areas should consider alternative route alignments as far as possible from any major parallel roads. Thus, possible mechanisms to mitigate the demand risks need to be seriously taken into account in designing PPPs structures and allocating risks associated with the project.

With respect to the type of Private Participation, it is found that Greenfield PPPs toll road projects are more risky than Brownfield projects. It is confirm the need to more explicitly take into account a higher degree of risks inherent to the Greenfield investment as a result of several factors. The design of well-defined contractual structures and the provision of availability payment could reduce risk and increase the chance of the project being successful.

REFERENCES

ADBI (Asian Development Bank Institute), 2009. *Global Determinants of Stress and Risk in Public-Private Partnerships (PPP) in*

Infrastructure in ABDI Working Paper Series, No. 133, 2009, Edited by Renato E. Reside, Jr.

Chen, A., Subprasom, K., 2007. *Analysis of regulation and policy of private toll roads in a build-operate-transfer scheme under demand uncertainty.* Transportation Research Part A 41 (6), 537-558.

Galilea, P., Medda, F.,2009. *Analyzing the Influence of National Political and Economic Factors on the Success of Public-Private Partnerships in Transport.* Transportation Research Board Compendium of Papers 09 (3854), 01-16

Khanom, N.A., 2010. *Conceptual Issues in Defining Public Private Partnerships (PPPs).* International Review of Business Research Papers 6 (2), July 2010, 150 -163.

Tam, C.M., 1999. *Build-operate-transfer model for infrastructure development in Asia: reasons for successes and failures*. International Journal of Project Management 17 (6), 377-382.

Zhang, X., 2005. *Critical Success Factors for Public-Private Partnerships in Infrastructure Development*. Journal of Construction and Management 131 (1), 3-14.

EFFECT OF GAS AND OIL PIPELINES IN SENSITIVE AREAS TO ENVIRONMENTAL CHANGE

Yushi NAKAO[1] and Haruo SAWADA[2]
[1]Graduate Student, Graduate School of Engineering, University of Tokyo, Japan
nakao@iis.u-tokyo.ac.jp
[2]Professor, Institute of Industrial Science, University of Tokyo, Japan

ABSTRACT

This paper aims to assess the impact of pipeline on the surrounding environment focusing on the Trans-Alaska Pipeline System as a heat source. Based on the Landsat-7 thermal band, surface temperatures are compared among the pipeline, the service road for the pipeline, and the surrounding fields. Both the pipeline and the road tend to show lower surface temperatures than the surroundings in winter, and higher surface temperatures in summer.

Keywords*: Landsat, surface temperature, thermal band.*

1. INTRODUCTION

1.1 Background

The 1,287.961 km long Trans-Alaska Pipeline System delivers crude oil from the Prudhoe Bay oil field (70.2846°N 148.6796°W) to an oil port in Valdez (61.130833°N, -146.348333°W), the most northern ice-free port in North America. Its construction began in 1975 and opened for service in 1977. Nearly 700 km of the pipeline is equipped with heat-pipes and is elevated above ground to prevent thermal interactions between the warm oil which can reach 63°C at maximum and the continuous and discontinuous permafrost that it passes over (U.S. Department of the Interior Bureau of Land Management, 2004). Still, vegetation clearance upon construction and maintenance along with global warming continue to affect the ground thermal conditions (Smith *et al.*, 2010).

Research has concentrated on the effect that the harsh and vulnerable environment has on the pipelines (Seligman, 2000), rather than the effect that the pipeline brings to the surrounding environment. Satellite based remote sensing, which observe vast areas with the same sensor system, will have the potential to find out the impact of the pipeline to the surrounding environment.

It is also a very important ability of satellite remote sensing to chase or trace the effects and land cover change over many years.

1.2 Objective

This study aims to assess the pipeline's effects on the surrounding environment, focusing on the impact of its heat.

2. METHODOLOGY

2.1 Framework

Figure 1 shows the flow how the surface temperatures on and near the pipelines are acquired.

The geological information of the pipeline and the service road running parallel to the pipeline is derived manually by the interpretation of Landsat image, and the surface temperatures alongside the facilities are calculated and placed in order. The temperature difference between the pixel containing the pipeline/road and the adjacent pixel is calculated throughout the image.

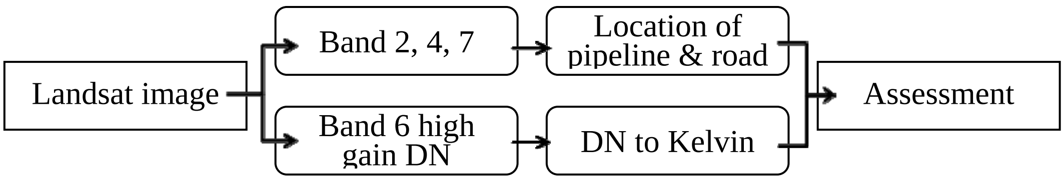

Figure 1: Assessment of surface temperatures around the pipeline and service road

2.2 Data Used in This Study

The satellite data used are shown in table 1. Both represent the same area, one in August and the other in April. The area subjected contains the north-end, or the beginning of the pipeline to about 130km ahead through mostly continuous permafrost plain and some hilly areas toward the end of the scene. There is a gravel road (the Dalton Highway, Alaska Route 11) along the pipeline built as a supply road for constructing and servicing the pipeline and oil facilities. The location of the pipeline and the roadis shown on the entire Landsat image of Figure 2 (left, from point A to point B), which were acquired on August 31, 2000. The location of the image in Alaska is shown on the map of Figure 2 (right).

Table 1: Satellite data used for evaluation of ground surface temperature

Path / Row	Date	Local time	Sun elevation	Sun azimuth	Cloud cover
72 / 11	2000/8/31	13:20:52	28.88°	172.40°	0.05 %
72 / 11	2001/4/27	12:20:03	34.32°	172.71°	23.30 %

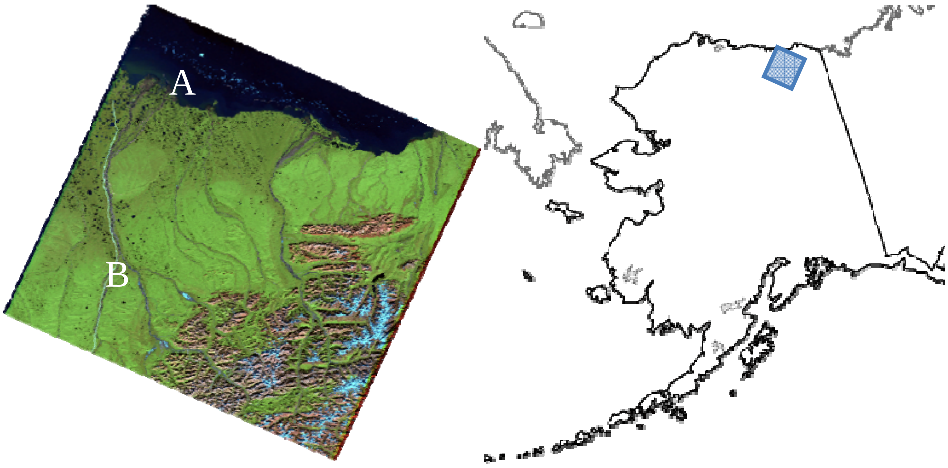

Figure 2: Landsat image on August 31, 2000 (left) and its cover area (right)

2.3 Converting the Digital Number of the Landsat Thermal Band to Temperature

Estimation of ground surface temperature is carried out using the thermal band data of the Landsat-7 Enhanced Thematic Mapper Plus (ETM+). In this study, the high gain of band 6 was used. The digital numbers (DN) of band 6 with a range between 0 and 255 is converted to radiance values using the following values specific to the individual scene as shown in the equation below.

$$R = \frac{L\max - L\min}{QCAL\max - QCAL\min} \times \left(QCAL - QCAL\min\right) + L\min \quad (1)$$

In this case QCAL(Quantized calibrated pixel value)max=255, QCALmin=1, QCAL=DN, Lmax=12.650, and Lmin=3.200.
The radiance data is then converted to degrees in Kelvin using the following equation.

$$K = \frac{1282.71}{\ln\left(\frac{666.09}{R} + 1\right)} \quad (2)$$

3. RESULTS AND DISCUSSIONS

3.1 The Pipeline

Figure 3 shows the temperature difference between the pixel including the pipeline and the pixel right next to it in August and figure 4 shows the temperature difference in April. The temperature difference between the pixel including the pipeline and two pixels next to it is on figure 5 for August and figure 6 for April.

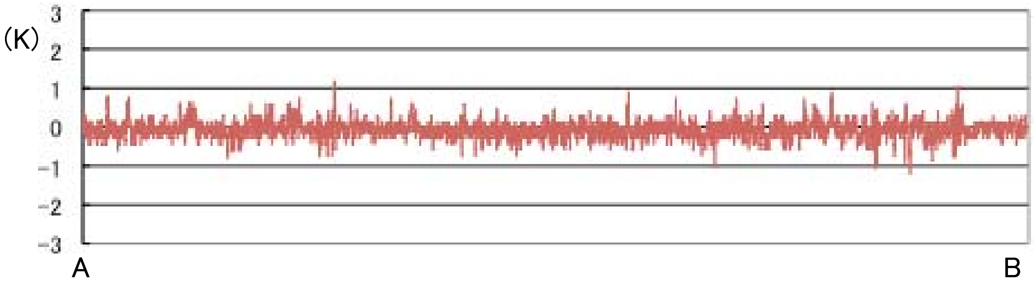

Figure 3: Temperature difference of the pipeline and the adjacent pixel in August

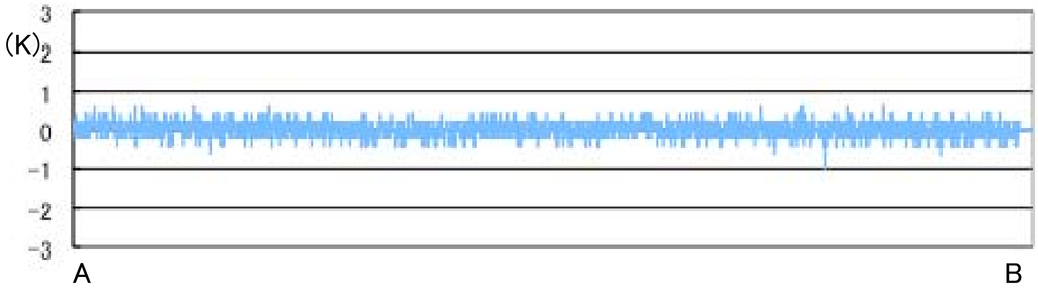

Figure 4: Temperature difference of the pipeline and the adjacent pixel in April

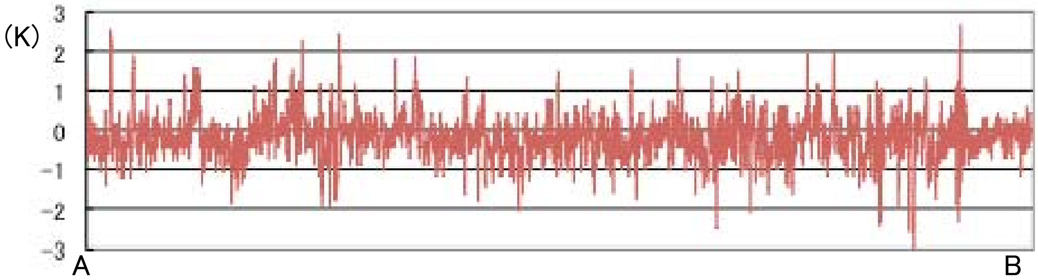

Figure 5: Temperature difference of the pipeline and the second next pixel in August

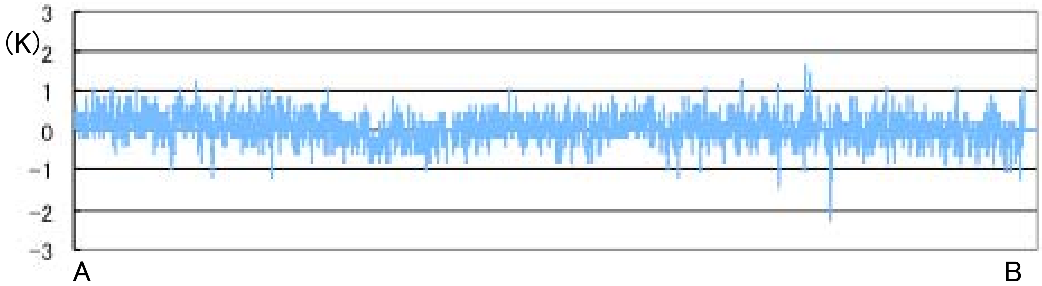

Figure 6: Temperature difference of the pipeline and the second next pixel in April

Spatial resolution of thermal pixel is 60m by 60m and table 2 shows the number of pipeline pixels with values higher than, equal to, or lower than the adjacent pixels. The pixels with the pipeline tend to show lower surface temperatures in summer and higher temperatures in winter.

Table 2: Number of pixel with temperature higher, equal to, or lower compared to the neighboring pixel

	Neighboring pixel	# of pixels with value higher than the neighboring pixel	# of pixels with value equal to the neighboring pixel	# of pixels with value lower than the neighboring pixel
August	next pixel	1865	447	2178
	second next	1673	125	2692
April	next pixel	1742	1536	1117
	second next	2211	794	1390

3.2 The Road

Figure 7 shows the temperature difference between the pixel including the road and the pixel right next to it in August and figure 8 shows the values in April. The temperature difference between the pixel including the road and two pixels next to it is on figure 9 for August and figure 10 for April.

Table 3 shows the number of pipeline pixels with values higher than, equal to, or lower than the adjacent pixels. The impact of the road results in lower temperature compared to the surroundings in summer and higher temperature in winter.

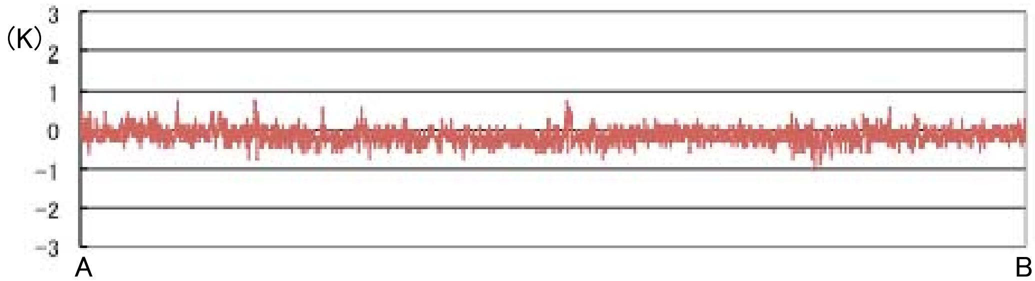

Figure 7: Temperature difference of the road and the adjacent pixel in August

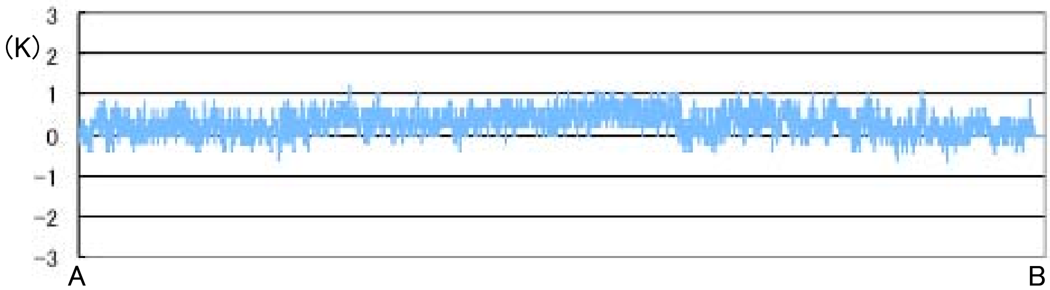

Figure 8: Temperature difference of the road and the adjacent pixel in April

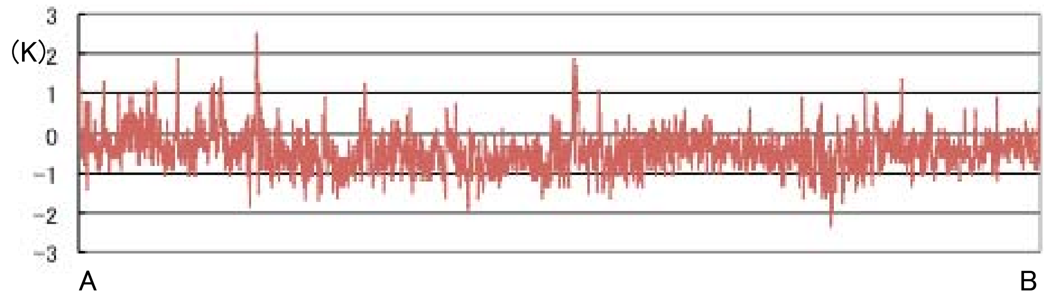

Figure 9: Temperature difference of the road and the second next pixel in August

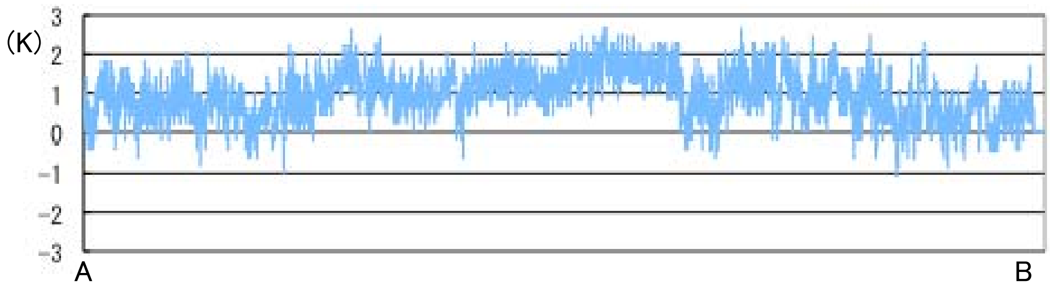

Figure 10: Temperature difference of the road and the second next pixel in April

Table 3: Number of pixel with temperature higher, equal to, or lower compared to the neighboring pixel

	Neighboring pixel	# of pixels with value higher than the neighboring pixel	# of pixels with value equal to the neighboring pixel	# of pixels with value lower than the neighboring pixel
August	next pixel	1237	316	2750
	second next	736	69	3498
April	next pixel	3828	195	280
	second next	4074	68	161

4. CONCLUSIONS AND FUTURE WORKS

The thermal effect of the pipeline and its service road on the environment was discussed. Both the pipeline and the service road show the same trend that the surface temperature is lower than the surroundings in summer and higher in winter. However, the thermal trend is not evident for the pipeline. This is most probably because the road is wider and represents a larger portion in a 30m pixel compared to the pipeline, which consists of a 1.2m pipe with a narrow access trail. This is to say that by surveying environmental change around roads in a similar environment of a pipeline, environmental change around pipelines may be estimated.

Additional study must be done on scenes in different months and locations. Because the geological information of the pipeline and the road is acquired manually, its accuracy must be ensured for proper assessment. The actual temperature measured at the site may also become necessary to support the results.

REFERENCE

Barsi A., Hook S., Palluconi F., Schott J., Raqueno N., 2003. Landsat TM and ETM+ thermal band calibration. *Canadian Journal of Remote Sensing*, vol. 29, no. 2, 141-153.

Khrenov N. N., 2010. Reliability of chilled gas pipelines in permafrost. *Soil Mechanics and Foundation Engineering*, vol. 47, no. 1. 26-31.

U.S. Department of the Interior Bureau of Land Management, 2004. Environmental Assessment of the Proposed Reconfiguration of the Trans-Alaska Pipeline System, EA-03-009 BLM Serial Nos. AA-5847 and FF-12505

Seligman B. J., 2000. Long-Term Variability of Pipeline±Permafrost Interactions in North-West Siberia. *Permafrost and Periglacial Processes*, vol. 11 no. 1, 5-22

Smith S L. and Riseborough D W., 2010. Modelling the thermal response of permafrost terrain to right-of-way disturbance and climate warming. *Cold Regions Science and Technology* vol. 60, 92–103

EFFECTS OF ENVIRONMENTAL CONDITION ON CORROSION OF STRUCTURAL STEEL IN MARINE ENVIRONMENT OF THAILAND

Prasong Permsuwan [1], Pakawat Sancharoen [2], Somnuk Tangtermsirikul[3]
Paiboon Sreearunothai[4], Ekkarut Viyanit[5] and Wanida Pongsaksawad [5]

[1] Graduate student, School of Civil Engineering and Technology, Sirindhorn International Institute of Technology, Thammasat University, Thailand
Prasong_civilnu@hotmail.com
[2] Researcher, Construction and Maintenance Technology Research Center, Sirindhorn International Institute of Technology, Thammasat University, Thailand
[3] Professor, School of Civil Engineering and Technology, Sirindhorn International Institute of Technology, Thammasat University, Thailand
[4] Lecturer, School of Bio-Chemical Engineering and Technology (BCET), Sirindhorn International Institute of Technology, Thammasat University, Thailand
[5]Researcher, National Metal and Materials Technology Center (MTEC), 114 Thailand Science Park, Thailand

ABSTRACT

Structural steels which are hot-rolled steel grade SS400 according to JIS G3101, hot-rolled steel grade SM490YA according to JIS G3106 and hot-rolled atmospheric corrosion resisting steel grade SMA490A according to JIS G3114 were exposed from January 2010 until January 2011 to marine and industrial environment at Maptaphut industrial estate, Rayong, Thailand. The specimens were exposed in two conditions that were atmospheric and tidal zone. The corrosion behaviors of specimens were studied by means of weight loss measurement according to ISO8407, compositions of rust layers by XRD analysis and characteristic of rust layer by SEM analysis. Also, environmental conditions such as temperature, relative humidity, and deposition rate of chloride were monitored monthly. The corrosion rates of specimens were also measured by potentiodynamic polarization in laboratory. The results showed that corrosion rate at 12 months of carbon steel was higher than that of weathering steel.Furthermore, specimen in tidal zone showed higher corrosion rate than atmospheric zone obviouslydue to effects of biofouling and wet-dry condition. The result can be used for material selection and designing service life of steel structure in Thailand.

***Keyword**: corrosion, marine, atmospheric, tidal, carbon steel, weathering steel, chloride.*

1. INTRODUCTION

Structural design of both reinforced concrete and steel structures consider mainly the strength of members. But durability design or service life design, which also affects the safety of structure, is rarely concerned. Particularly, the steel can be deteriorated rapidly when it is subjected to corrosive environmental condition.Carbon steel and weathering steel are used in steel structure including high-rise building, bridge, offshore platform, sheet piling, steel pile and coastal facilities. Normally, steel structures in marine environment are deteriorated by atmospheric corrosion. Also, some part of those steel structures such as steel piles or sheet piles are immersed in the sea water. So the area between the lowest sea level and the highest sea level is influenced by tidal zone corrosion.

Atmospheric corrosion is an electrochemical reaction occurring on metal surface in a presence of thin film electrolyte. In case of atmospheric corrosion, structural steel in marine environment deteriorates primarily by climatic factors such as temperature, relative humidity, and the presence of chloride and SO_2. Normally, rust formed on surface of carbon steel is porous with poor adherent, and cracked at the outer part (Castano et al., 2010). This phenomena causes oxygen, water, Cl^- and SO_2 from outside to penetrate to the steel substrate easily (Yuantai et al, 2009). For corrosion resisting steel, at the early stage, the rust is formed similarly to the carbon steel. But as the exposure time increased, the rust layer becomes more compact, denser, and tighter (Renato, et al., 2003). For this reason, the rust layer acts as the barrier to inhibit corrosive species and then the rate of corrosion is decreased.

The compositions of rust layer have been observed by several researchers.Mainly, the compositions of rust found in marine environment are composed of lepidocrocite (γ-FeOOH), goethite (α-FeOOH), akaganeite (β-FeOOH) and magnetite (Fe_3O_4). The γ-FeOOH is usually formed in the early stage and transformed to α-FeOOH and Fe_3O_4. This α-FeOOH is important key to reduce corrosion becauseits compact and dense structure prevent penetration of water, oxygen and corrosive species from the environment. However, area with presence of chloride is often observed β-FeOOH which has porous and loose structure.

In Thailand, environmental conditions are different from other countries. There is no sufficient data of atmospheric corrosion to model or predict steel corrosion in order to design service life of steel structures in Thailand. Also, there is limit information on atmospheric and tidal corrosion. In addition, the standard currently used to design steel structures in Thailand was adopted from other countries. It is essential to study the corrosion behavior of structural steel in Thailand. The aim of this paper was to investigate the corrosion behavior of SS400, SM490YA and SMA490A steels in the marine environment of Thailand.

2. EXPERIMENTAL PROGRAM

2.1 Specimen preparation

The materials tested in this study are three kinds of structural steel; 1) hot-rolled steels for general structure grade SS400 according to JIS G3101, 2) hot-rolled steels for welded structure grade SM490YA according to JIS G3106, and 3) hot-rolled atmospheric corrosion resisting steels for welded structure grade SMA490A according to JIS G3114. Their chemical compositions determined by spark emission spectrometer are shown in Table 1 together with the specified values in the standard. ISO 8565 standard specification suggests the following procedures for specimen preparation before exposure test. Specimens were cut from the steel plate to the size of 150×70×3 mm for SS400 and SM490YA steels, and 150×70×5 mm for SMA490A steel. The mill scale on the surface of the specimens was mechanically removed by sand blasting and then wet-polished by 600 grade sand paper on all surfaces. Finally, the specimens were rinsed with distilled water and ethyl alcohol, dried by blower, weighted and immediately placed in desiccators before the test.

Table 1: Chemical compositions of different types of steel

Steel types	Chemical composition (% by wt)									
	C	Si	Mn	P	S	Cr	Ni	Cu	Al	Mo
Standard JIS G3106	≤ 0.20	≤ 0.55	≤ 1.65	≤ 0.035	≤ 0.035	-	-	-	-	-
SM490YA	0.070	0.218	0.352	0.009	0.016	0.031	0.073	0.154	0.013	0.015
Standard JIS G3101	-	-	-	≤ 0.05	≤ 0.05	-	-	-	-	-
SS400	0.047	0.174	1.039	0.010	0.006	0.026	-	-	-	-
Standard JIS G3114	≤ 0.18	0.15-0.65	≤ 1.4	≤ 0.035	≤ 0.035	0.45-0.75	0.05-0.30	0.30-0.50	-	-
SMA490A	0.115	0.396	0.368	0.076	0.005	0.681	0.16	0.368	0.021	0.003

2.2 Exposure test

Exposure site is located at Maptaphut industrial estate, Rayong, Thailand as shown in Figure 1. The position coordinates of this location is 12° 39’ northern latitude and 101° 10’ eastern longitude. Even though, environment of exposure site is marine environment but this area is also an industrial estate with coal- power plant, oil refinery, chemical industry, etc. The experiment was conducted from January 2010 to January 2011. The exposure test was conducted in two conditions which were atmospheric and tidal zone exposure.

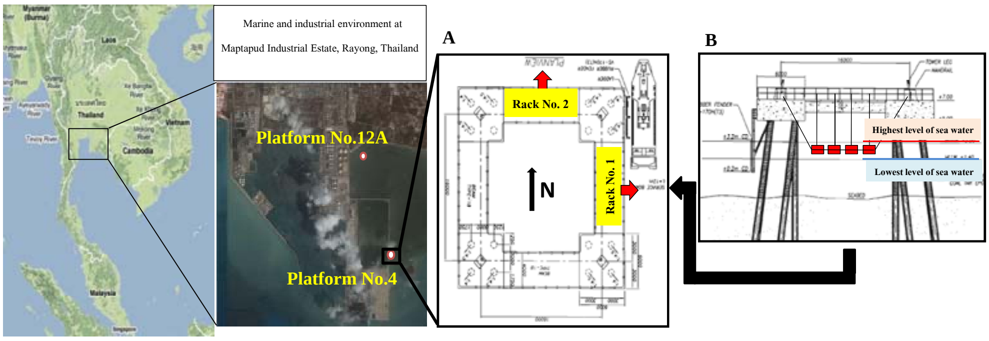

Figure 1: Details of the exposure site:(A)atmospheric exposure and(B)tidal exposure

For atmospheric exposure, two exposure racks according to ISO 8565 were set on the high voltage transmission tower platform No. 4 only. Rack No.1 faced to the East and rack No.2 faced to the North directions with the rack slope of 45° to the horizontal as shown in Figures 1 and 2.

For tidal exposure, sample was placed in the plastic box and installed under the transmission tower platform number 4 and 12A of which water quality are different. The position of the boxes was set in the middle between the highest and the lowest sea water level in order to simulate wet-dry condition as shown in Figures 1 and 2. Environmental conditions such as temperature and relative humidity were monitored monthly by sensors connected to a data logger near the rack No.1. The results are shown in Table 2.

Figure 2: The exposure rack of atmospheric zone (left) and tidal zone (right)

Chloride deposition rate was measured monthly by using the wet candle method according to ISO 9225, and surface of wet candle exposed to atmosphere is 100 cm^2. Also, the wet plate modified from standard wet candle method was installed in 4 directions in order to measure effect of wind directions on chloride deposition rate. The results are shown in Table 2.The sea water properties, mainly chloride and sulfate concentration, were measured by Ion-chromatography. The results are shown in Table 2.

The compositions of corrosion products were characterized by X-ray diffraction (XRD) method using X-ray diffractometer (Rigaku TTRAX III 50 kV 300mA) with Cu target. The scan is performed at a speed of 10°/min, a scan step of 0.02 at 2θ and range from 10° to 70° at 2θ. The characteristic of rust layer was observed by SEM analysis using JEOL model JSM-6301F.

After 1, 3, 6 and 12 months, exposed specimens and monitored data were collected for analysis. Corrosion products were removed chemically by HCl acid etching according to ISO 8407. After corrosion products had been removed completely, the specimens were rinsed with ethanol, dried with blower and weighted to measure weight loss.

Table 2: Atmospheric conditions and sea water properties

Atmospheric conditions			Sea water properties			
Monthly average temperature (°C)	Monthly average relative humidity (%)	Monthly average Cl^- deposition (mg/(m^2.day))	Chloride (ppm)		Sulfate (ppm)	
			Tower4	Tower12A	Tower4	Tower12A
30.6	61.3	22.5	19586	18821	3147	3041

Table 3:Chloride deposition rate of each direction

Wet-plate Direction faced to	East	North	West	South
Chloride deposition rate (mg/(m^2.day))	27.75	27.39	27.94	39.43

3. RESULTS AND DISCUSSION

3.1 Environmental characteristics at exposure site

The environmental characteristics measured at the exposure sites are shown in Table 2. According to ISO 9223, environmental conditions are classified in term of chloride deposition rate (class S) and sulfur dioxide deposition rate (class P). Also, Time of wetness (TOW) (classτ), the period of time when relative humidity is greater than 80% and temperature is greater than 0ºC, is also used for the classification. Environmental condition of exposure site is classified as S1 because chloride deposition rate is 22.47 mg/m^2.day which is between 3-60 mg/m^2.day. Environmental condition is classified as class τ3 because TOW is 9.1% which is between $3 < \tau \leq 30$ %. Also, the corrosive categories of the exposure site can be classified as C2 (low) to C4 (high) class by S1 and τ3 depending on classification of sulfur dioxide. As shown in Table 3, the result of the wet plate shows that chloride deposition of rack No. 2facing north is higher than that of rack No. 1facing east because of the wind direction.

3.2 Thickness loss

Figure 4 shows examples of the surface appearance of SS400 steel after 12 months exposure at atmospheric and tidal zone. In atmospheric zone, dark-brown rust product uniformly covered the entire surface while uneven surface was observed in specimens exposed to tidal zone and were covered with tightly attached biofouling. Other types of steel showed similar appearance after 12 months exposure.

Generally, the corrosion rate of steel exposed to real environment was calculated in term of thickness loss. The equation used to calculate thickness loss is shown in Eq.1

$$C = \frac{W}{\rho A} \times 10^4 \qquad (1)$$

where C is the thickness loss (μm), w is the weight loss (g) of specimen after being exposed, ρ is the density of the steel (7.86 g/cm^3) and A is the exposed surface area of the specimen (both sides) (cm^2).

Figures 5a and 5b show thickness loss of SS400, SM490YA and SMA490A steels exposed to atmospheric zone for 12 months on rack No.1 andrack No.2, respectively. In both exposure racks, the thickness loss of SS400, SM490YA and SMA490A steels continuously increasedfrom the beginning to 12 months but the rate of corrosion decreased with increasing time. Especially, corrosion rate of SMA490A steel obviously decreased at the long term because rust layer was more compact and denser.

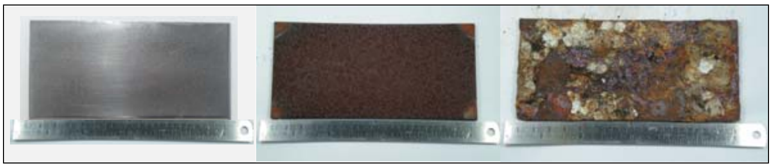

(a) **(b)** **(c)**

Figure 4: Appearance of SS400 steel: (a) before exposure, (b) after 12 months of exposure in atmospheric condition and (c) after 12 months of exposure in tidal condition

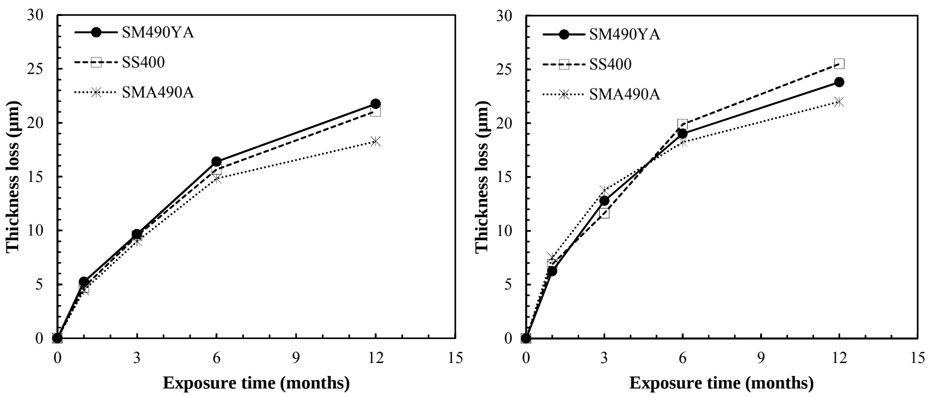

(a) **(b)**

Figure 5: Thickness loss of specimens versus exposure time at atmospheric zone on; (a) rack No.1 and (b) rack No. 2

The thickness loss of SS400, SM490YA and SMA490A steels exposed to tidal zone after 12 months under platform No.4 and 12A are shown in Figures 6a and6b. In tidal zone, the thickness loss of specimens is very high (greater than-200 μm) after 12 months of exposure.Both platforms, thickness loss of SMA490A was the lowest because of its alloying composition. Particularly, rate of corrosion of specimens under platform No.4 shows almost constant increasing without effect of protective rust layer. As the results, the thickness loss of specimens under platform No.4 is significantly higher than those under platform No.12A. This is because different water quality such as higher $O_2$and higher Cl^- concentration content which causes fast growing of biofouling as well as accelerates steel corrosion was observed under platform No.4.

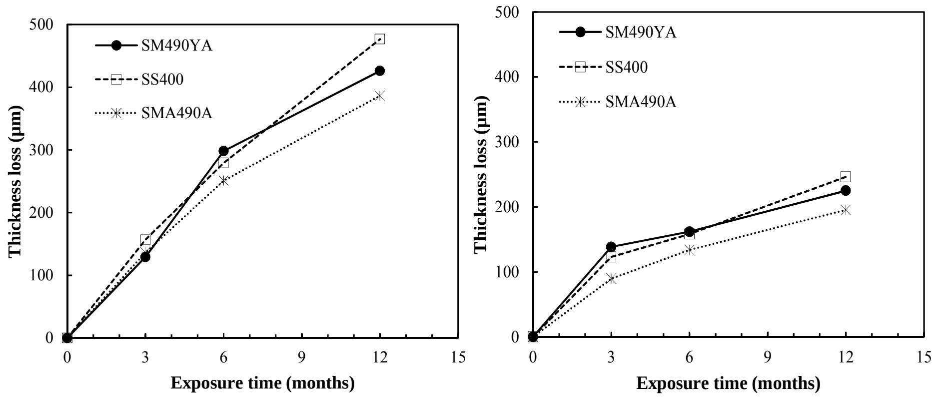

(a) **(b)**

Figure 6 :Thickness loss of specimens versus exposure time at tidal zone under; (a) platform No.4 and (b) platform No.12A

3.3 Corrosion product analysis

3.3.1 Cross section of rust layer

The cross section analysis of steel exposed to atmospheric zone for 12 months showed irregular layer of corrosion product with thickness about 25-70 µm. And rust layers were less compact as shown in Figure 7a. This layer showed some sites with localized corrosion, which probably act as anodes in the first steps of atmospheric corrosion (Castano et al., 2010). In tidal zone, the cross section showed thicker layer of corrosion products than that found in atmospheric zone as well as some site with deep localized corrosion as shown in Figure 7b. The thickness of the layer of corrosion products was approximately 25–200 µm. The deeper localized corrosion may be contributed by biofouling. It attached on part of steel surface and caused severe local corrosion. This can be the weak point of structures.

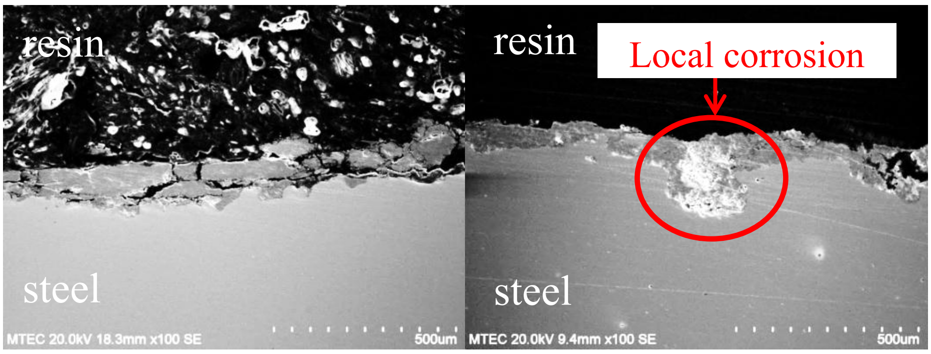

(a) **(b)**

Figure 7: Rust layers on the SM490YA steel exposed for 12 months as; (a) atmospheric zone and (b) tidal zone

3.3.2 Composition of rust layer

The main phases of the rust layers formed on the steels exposed to atmospheric zone for 12 months were γ-FeOOH, followed by β-FeOOH and α-FeOOH as shown in Figure 8a. It can be seen that the main phase observed on SM490YA, SS400 and SMA490A was γ-FeOOH. It normally occurred at the beginning of corrosion. Then with the interaction of oxygen and water, γ-FeOOH partly or entirely transformed to more stable α-FeOOH (Zise et al., 2007). As the result, there was low amount of α-FeOOH that recently formed on the steels. Generally, β-FeOOH was only found in high chloride containing environment. As many researchers, investigated the effect of chloride ion on the transformation of rust formed on the carbon steel and observed that the content of β-FeOOH increased with the concentration of Cl ions in the environment. Kamimura et al. (2006) also reported that β-FeOOH was electrochemically active and the existence of β-FeOOH influenced the corrosion behavior of weathering steel exposed at marine site.

For tidal zone, the phases of rust layer formed on the steel exposed for 12 months in both locations was mainly Fe_3O_4 followed by γ-FeOOH, α-FeOOH and β-FeOOH, respectively as shown in Figure 8b. Peaks of Fe_3O_4 phases had high intensity with a small intensity of other phases. For occurring of Fe_3O_4, many researchers reported that γ-FeOOH formed on the steel surface did not only reacts with the oxygen and water and become α-FeOOH, but also reacts with Fe^{2+} dissolved from the iron and forms Fe_3O_4. As the results, there was Fe_3O_4 in rust layers only in tidal zone. There were many phases with high intensity because in severely corrosive sea water, rust layers formed very fast and rapidly transform to another phases. Anyway, rust layers in tidal zone did not act as efficiently protective rust layers like that of atmospheric zone because rust layers formed in this zone cannot inhibit corrosive species penetrated to surface of steel. For calcite phase, it was composition of biofouling shell attaching on the corrosion products.

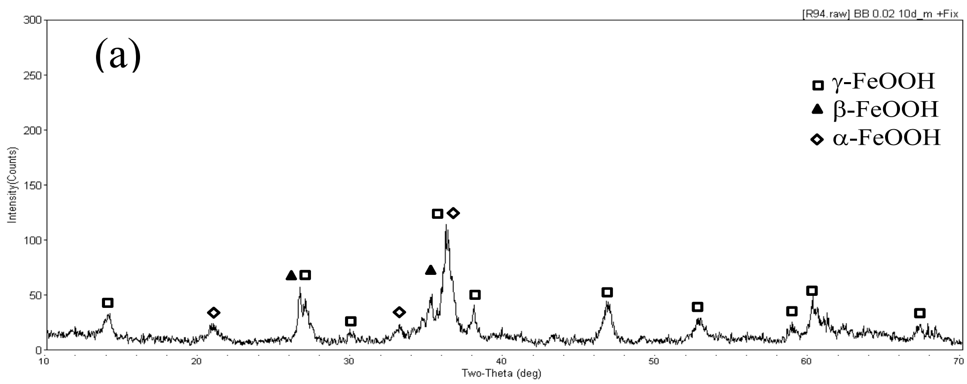

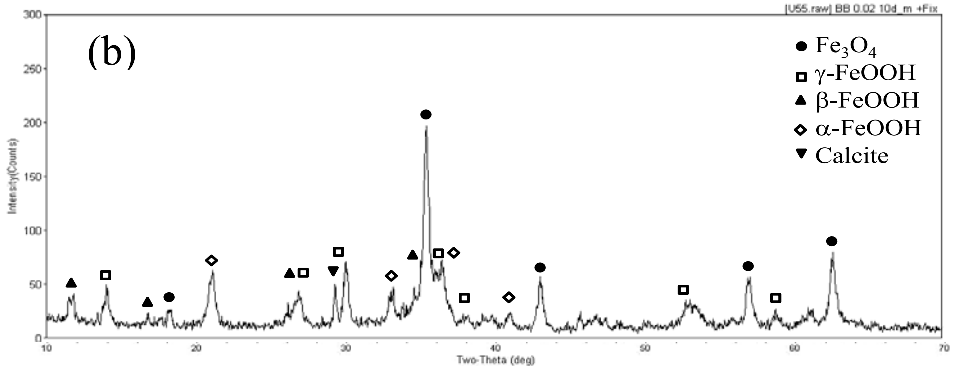

Figure 8: XRD spectra of corrosion products obtained from SM490YA for 12 months as; (a) atmospheric zone and (b) tidal zone

3.4 Corrosion rate

The prediction of corrosion rate of steel exposed to atmospheric condition was proposed by several researchers as a bi-logarithmic equation as shown in Eq.2. This equation usually fits well with corrosion behavior over time.

$$C = At^{B} \quad (2)$$

where C is the thickness loss (μm), t is the exposure time (month), and A, B are constants. The constants A and B can be determined by plot in log-log coordinate between steel thickness loss and exposure time. The regression analysis was conducted in log-log coordinate to determine values of constants A and B value.

For corrosion rate prediction equation, several researchers considered the B value as the growth law of corrosion product: parabolic or linear.If the B value is in the range of 0.5 to 1, the corrosion products do not significantly protect the steel surface from corrosion and is called a linear growth. On the other hand, if the B value is lower than 0.5, it indicates a parabolic growth by formation of protective rust layers to reduce rate of corrosion in the long term.

The corrosion rates per year and the values of A and B constant in all exposure zones of SS400, SM490YA and SMA490A steels were calculated from the bilogarithimic equation and shown in Table 4.

For atmospheric zone, the corrosion rate of rolled steel (SS400 and SM490YA) is higher than corrosion resisting steel (SMA490A) in both racks because B value of SS400 and SM490YA are higher than 0.5 which indicate high rate of corrosion. The key factor causing the difference of corrosion rate is the chemical composition of the steel. The corrosion rate of SMA490Ais the lowest because the corrosion resisting steel contains some alloy elements such as Cu, Cr, and Ni that improve the corrosion resistance as shown in Table 1. Q.C. Zhang et alhave studied the distribution of alloying elements during formation of rust layers. They reported that the presence of Cu restrains the supply of oxygen, retards the anodic dissolution and reduces the electronic conductivity of rust layers. For this reason, the corrosion rate of SMA490A steel is reduced. The corrosion rate of rack No.2 is higher than that of rack No.1 for all types of steel because rack No.2 is affected by the wind direction making higher Cl^- deposition rate on the specimen surface from the results of wet-plate. This shows the importance of the effect of local environmental conditions on steel corrosion. From the result, the corrosive category of environment at exposure site can be defined as class C3 (medium) based on ISO 9223.

In case of tidal zone corrosion, the corrosion rate of tidal zone is significantly more aggressive than atmospheric zone. The corrosion rates of tidal zone and atmospheric zone show the difference of more than 10 times. The high Cl^- concentration and wetting in tidal exposure accelerated corrosion process byformation of β-FeOOH. Although the α-FeOOH phase was formed on both carbon steel and weathering steel but the rust layers were not act as the protective barrier causing the high B value. Because, the α-FeOOH phase was not uniformly formed on the surface of steel and then rust layers cannot sufficiently protect the Cl^- penetration. Also, the effect ofbiofouling increased corrosion rate significantly. Biofouling is considered a major factor to control the corrosion behavior since the biofouling attached to the surface of steel tightly. Biofouling consumes oxygen, while supplies acid due to its excretion. As a result, steel subjects to extra corrosion due to acid (Coetser, 2005).Eventually, the corrosion affecting from biofouling is local corrosion which is more severe and difficult for predicting the rate. In term of location, corrosion of specimens under platform No.4 is more severe than that of the specimens under platform No.12A because the differences in Cl^-, sulfate and oxygen concentration. Moreover, specimens under platform No.12A is located in calm sea water and low water quality that has low oxygen concentration causing slow activity and slow growing of biofouling.

Table 4: Corrosion rate and constant values of steels

Steel type	Condition	Location	Corrosion rate (μm/year)	A	B
SM490YA	Atmospheric	Rack 1	**22.68**	5.25	0.59
		Rack 2	**25.86**	6.59	0.55
	Tidal	Under 4	**461.42**	54.45	0.86
		Under 12A	**218.63**	91.62	0.35
SS400	Atmospheric	Rack 1	**22.21**	4.83	0.61
		Rack 2	**26.50**	6.81	0.55
	Tidal	Under 4	**480.29**	65.46	0.80
		Under 12A	**238.60**	68.71	0.50
SMA490A	Atmospheric	Rack 1	**19.93**	4.63	0.59
		Rack 2	**23.53**	7.93	0.44
	Tidal	Under 4	**398.53**	61.66	0.75
		Under 12A	**196.18**	48.31	0.56

The typical rates of corrosion for structural steel suggested by BS 6349-1 standard are shown in Table 5. BS 6349-1 standard recommends the corrosion rate for steel structure design in various exposure zones. The results of this study show that average corrosion rate of the steels in atmospheric zone areapproximately 23.45 μm/year. So the standard is acceptable to be used to design steel structures in atmospheric zone in Thailand. On the other hands, the results of average corrosion rates of the steels in tidal zone in this study are approximately 332.27 μm/year. The standard recommends maximum limit of 100 μm/year. Therefore, the standard is not suitable for steel structure design in tidal zone in Thailand.

Table 5: Typical rates of corrosion for structural steels temperate climates (BS 6349-1)

Exposure zone	Corrosion rate μm/year		Results of the study μm/year		
	Mean	Upper limit*	SM490YA	SS400	SMA490A
Atmospheric zone	**40**	**100**	**25**	**26**	**23**
Splah zone	80	170	-	-	-
Tidal zone	**40**	**100**	**461**	**480**	**398**
Seawater immersion zone	40	130	-	-	-

**The upper limit is the 95% probability values*

4. CONCLUSIONS

1. Corrosion resistance of SMA490A steel is the highest in all conditions because itschemical compositions improve the characteristic of protective rust layers.
2. Corrosivity of sea water in tidal zone is significantly higher than atmospheric environment. This phenomenon is contributed by the effects of biofouling and high chloride concentration. Corroding mechanism of biofouling must be concerned in tidal zone corrosion and studied in the future.
3. Calculation of corrosion rate specified in the BS 6349-1 standard might not be suitable for structural steels exposed to Thailand environments especially for tidal zone corrosion.

ACKNOWLEDGEMENT

The research was funded by the Electricity Generating Authority of Thailand (EGAT).

REFERENCES

Castano J.G., et al, 2010, "*Atmospheric corrosion of carbon steel in Colombia*", Corrosion science, 52, pp. 216-223.

Coetser S. E. and Cloete T. E., "*Biofouling and bio corrosion in industrial water systems*", Critical reviews in microbiology, 31, 2005, pp. 213-232.

Kamimura, T. et al., 2006."*Composition and protective ability of rust layer formed on weathering steel exposed to various environments*". Corrosion Science, 48(9), pp.2799-2812.

Renato A.A., et al, 2003, "*Characterization of corrosion products formed on steels in the first months of atmospheric exposure*", Materials research, 6, pp. 403-408.

Yuantai M., et al, 2009, "*Corrosion of low carbon steel in atmospheric environments of different chloride content*", Corrosion science, 51, pp. 997-1006.

Zhang Q.C., et al, 2002, "*Corrosion behavior of weathering steel in marine atmosphere*", Materials Chemistry and physics, 77, pp. 603-608.

Zise W. et al., 2007. "*The Morphology, Phase Composition and Effect of Corrosion ProductonSimulated Archaeological Iron*". Chin. J. Chrm. Eng, 15(3),pp.433-438

APPLICATION OF ELASTIC WAVE MEASUREMENT TO MODEL TESTS USING BENDER ELEMENTS

Sho OH[1] and Reiko KUWANO[2]
[1] Graduate Student, School of Eng., The University of Tokyo, Japan
soh@ iis.u-tokyo.ac.jp
[2] Associate Professor, ICUS, IIS, The University of Tokyo, Japan
kuwano@iis.u-tokyo.ac.jp

ABSTRACT

Elastic wave measurement using Bender Elements have been developed as a dynamic measurement method for element test in geotechnical field. Now this method is expected to apply also for model tests in order to obtain the pressure distribution inside soil chamber. This research aims to obtain the basic performance information of bender elements in model tests. First, in order to detect the wave arrival clearer, signal analysis is conducted. Low frequency noise is reduced by polynomial approximation, and high frequency noise is dealt with FFT filter. Next, the effect of attaching aluminum block to bender element is discussed. Some change in the received wave form is found, but wave velocity was almost same. Also, property of wave propagation is checked using plural receiver for one transmitter. Finally, shear modulus is calculated for obtained data for validation. Results showed good agreement with those of element test.

Keywords*: elastic wave measurement, bender elements, model test, aluminum block, increment of earth pressure*.

1. INTRODUCTION

Box culvers are structures buried inside high embankment as tunnels for water, electric line, communicate line and so on. In designing of these box culverts, increase in vertical earth pressure must be considered, since differential settlement often occurs around a buried structure, as schematically shown in Figure 1. However, in practice, the increment of vertical earth pressures on underground structures is estimated in the empirical manner, mainly based on the information of past earth pressure measurements in limited of sites (General guidelines for road earthworks, 1999). In this method, degree of settlement and mechanical properties of backfill materials are not considered. Some researches have been conducted to solve this problem. However, due to the limited performance of earth pressure transducers used in experiment, details of the earth pressure distribution were not clearly understood.

Recently, a sophisticated trap door apparatus is developed by Ebizuka and Kuwano (2010), in order to improve the problems in previous studies. A soil chamber for trap door testing is constructed, the inside of which is shown in Figure 2. It can accommodate model ground of 700mm wide, 294mm long and 555mm high. The base of the chamber consists of five separated movable blocks whose size is 99.8mm wide, 293.6mm long and 105mm high, and fixed parts in both sides, in order to create uneven settlement in the model ground, as schematically shown in Figure 3.

The final goal of this research is to obtain pressure distribution inside model test using this soil chamber to quantitatively evaluate the vertical earth pressure acting on buried structures. For the method of measurement, elastic wave measurement using bender element is chosen.

Elastic wave measurement using bender elements have been developed as a dynamic measurement method for element test. Measuring propagation time of S wave inside soil gives shear modulus of soil. And by conducting shear wave tomography, distribution of pressure can be obtained. Although this is a useful method, no application for model test is conducted before. In this paper, basic performance information of bender elements is studied for model tests.

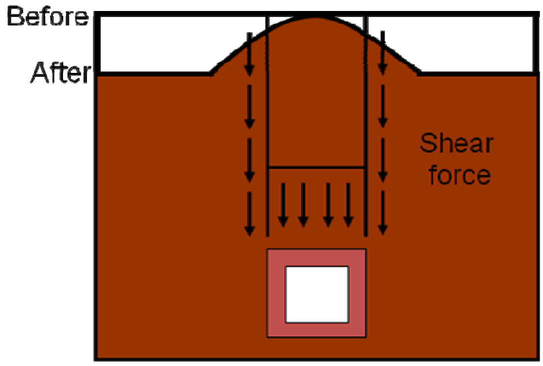

Figure 1: Increment of the earth pressure due to the uneven settlement

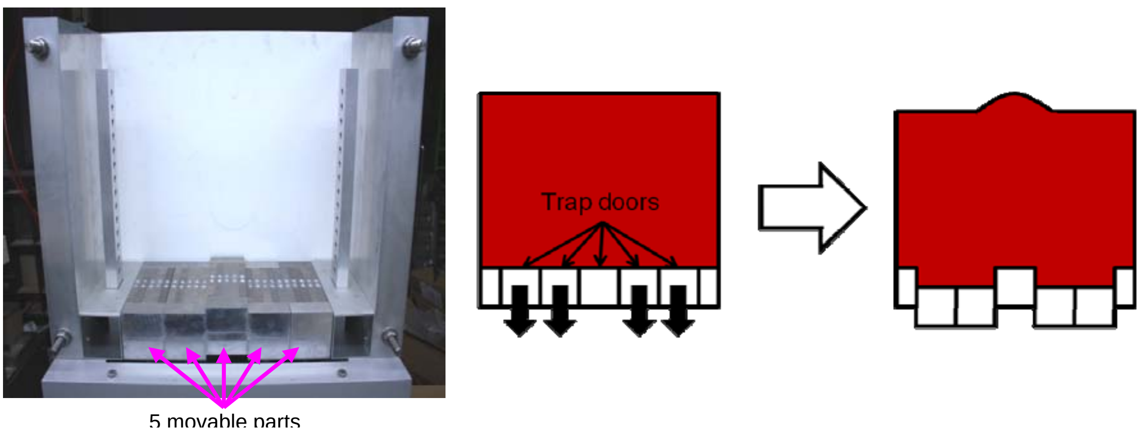

Figure 2: Detail of soil chamber

2. ELASTIC WAVE MEASUREMENT

2.1 Bender Elements

Bender elements are small measurement devise that transfer electric voltage to physical deformation and vice versa. There are two types of elements as shown in Figure3. Series type is more suitable for receiver and parallel type is better used as transmitter. Measurement is done by burying these two types of bender elements in soil.

(a) (b)

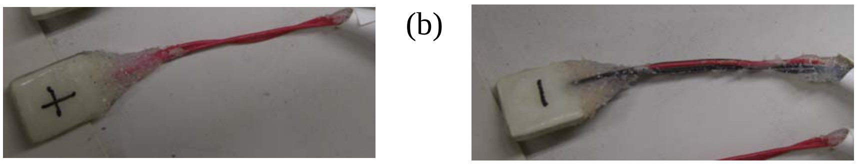

Figure 3: Bender Elements of (a) Series and (b) Parallel type

2.2 Measurement Apparatus

Measurement apparatus used in this study is shown in Figure4, and the details of setting are shown in Table 1.

Table 1: Setting of Aparatus

Output Voltage of Function Generator	8Vpp
Trigger Interval	1s
Wave form	Sin wave
Amplifier rate	100 time
Averaging times by Oscilloscope	20

(a) (b)

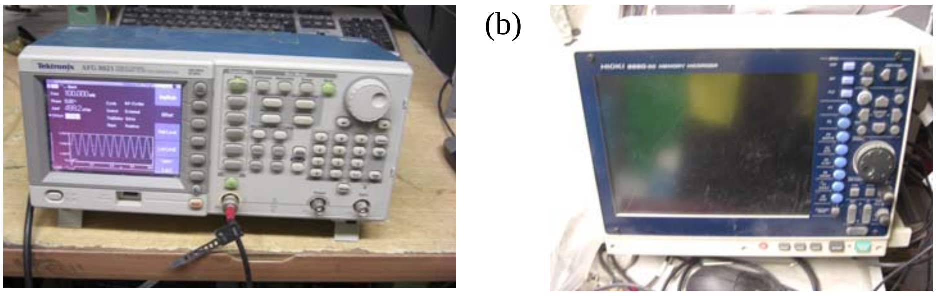

Figure 4: Aparatus used in this study
(a) Function Generator (b) Oscilloscope

3. DETECTION OF WAVE ARRIVAL

The biggest problem of bender element application in model test so far is the difficulty of detection of wave arrival. In order to make the detection more accurate, two methods are taken. One is signal analysis and another is attaching an aluminum block on the top of bender element. The effect of each method is discussed in this chapter.

3.1 Signal Analysis

Figure 5 (a) shows original obtained wave signal. To reduce the large low noise in this signal, polynomial approximation using quadratic curve is conducted for 2000 points out of 5000. Subtracting the fitted curve from the original signal gives more clear view of response but still some high frequency noise as shown in Figure 5 (b).

(a)

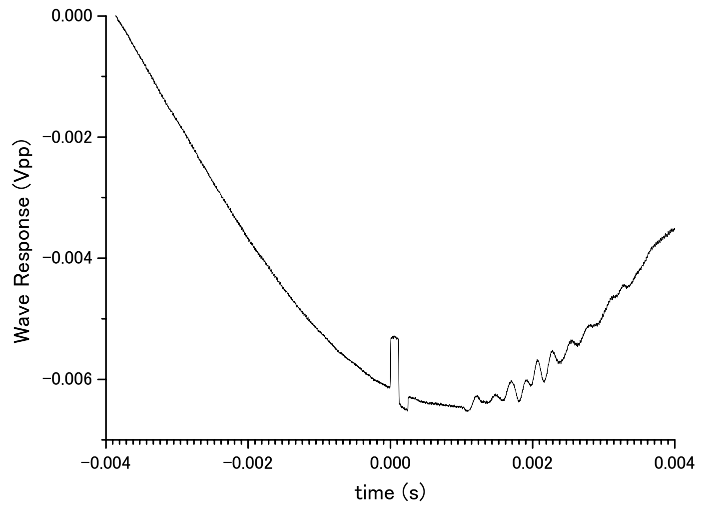

(b)

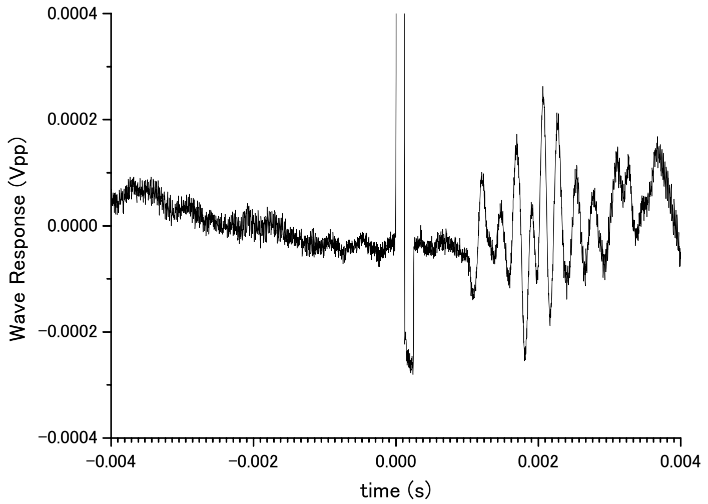

Figure 5: (a)Original obtained signal and (b) Low noise reduced signal

In order to reduce the high frequency noise, the spectrum intensity of signal at -0.003 to -0.001s (before wave arrival) and 0.001 to 0.002 (after wave arrival) is compared and shown in Figure 6. Three strong peaks seen before wave arrival (a) are reduced after wave arrival (b), therefore these frequency can be regarded as noise.

(a)

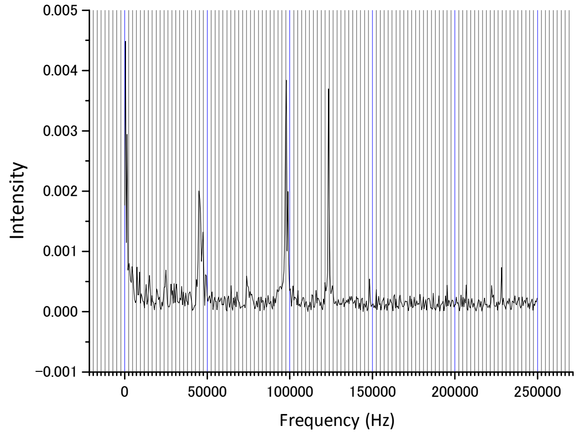

(b)

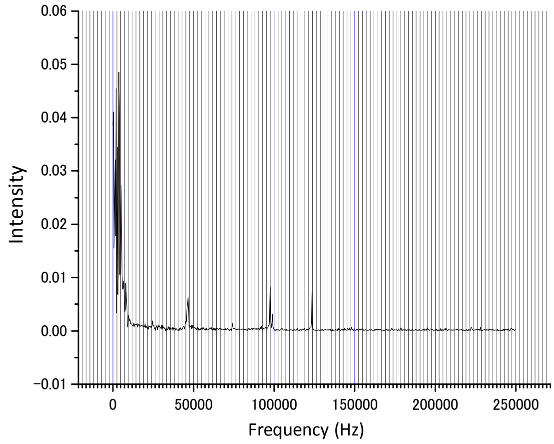

Figure 6: Spectrum intensity (a) before wave arrival and (b) after wave arrival

Removing high frequency noise by FFT filter gives final version of wave signal as shown in Figure 7. Method of wave detection is shown in Figure 8.

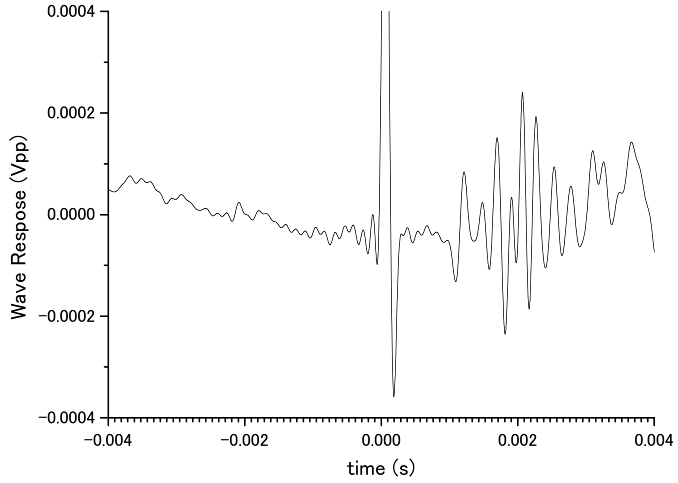

Figure 7: Wave signal after noise cutting

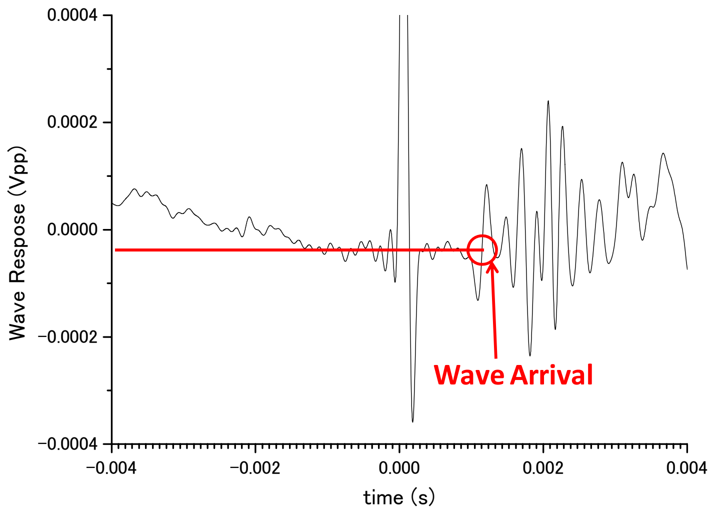

Figure 8: Wave arrival point

3.1.1 Effect of Aluminum Blocks

In element tests, attaching aluminum blocks on top of a bender element reduced much noise and gave clear wave. This method is applied also for model tests. Size of aluminum blocks used in this study is 5mm/5mm/10mm.

There are several ways of attaching. Results are shown in Table 2.

Table 2: Results of aluminum block

Transmitter	**Receiver**	**Obtained Signal**
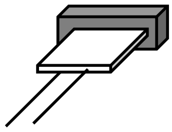	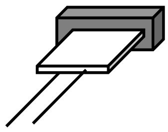	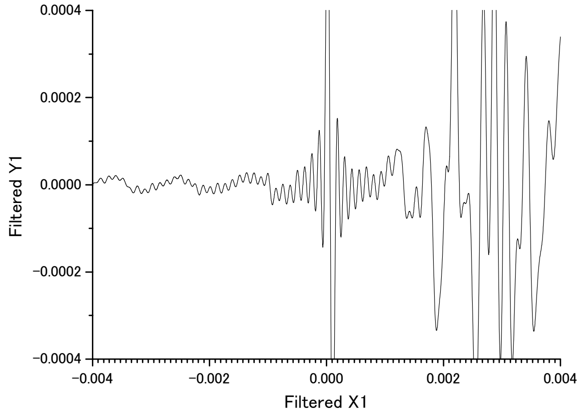
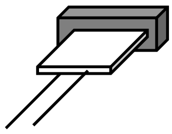	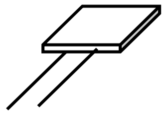	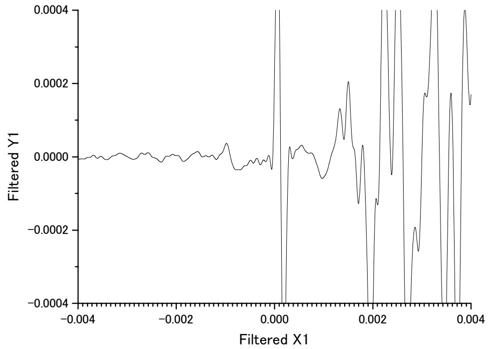
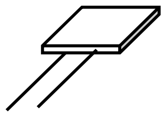	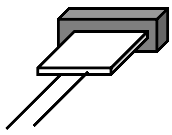	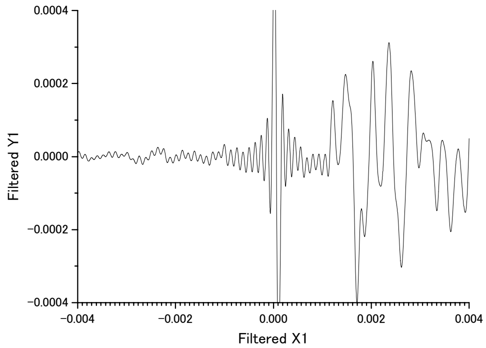
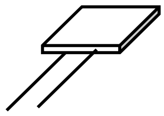	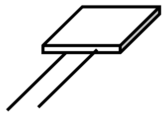	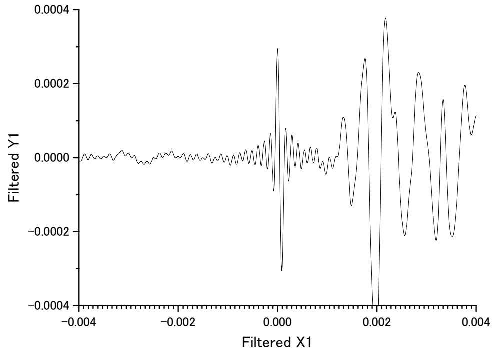

Following facts can be said from this result. Attaching aluminum block to both transmitter and receiver make arrival of wave small. Transmitter with aluminum block cause different shape of arrival wave, but travel time is almost same as non-aluminum block. Attaching aluminum block to receiver gives almost same wave shape and arrival time with non-aluminum blocks. As a result, attaching aluminum blocks does not have effect to clear arrival wave in model test.

4. VALIDATION OF OBTAINED DATA

4.1 Simitenous Receiving

Property of shear wave propagation should be checked. Three receivers are set for one transmitter to see if wave is propagating in straight way as shown in Figure 9.

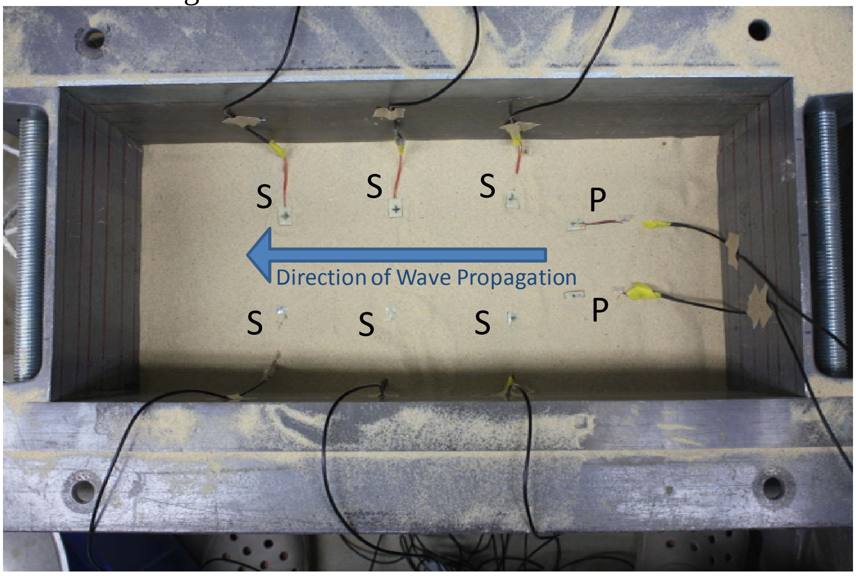

Figure 9: Experiment for wave propagation checking

Results are shown in Figure 9. Divergence of result for last receiver is rather large because of the long distance between bender elements. Wave velocities are almost same, which suggest wave is propagating in straight way.

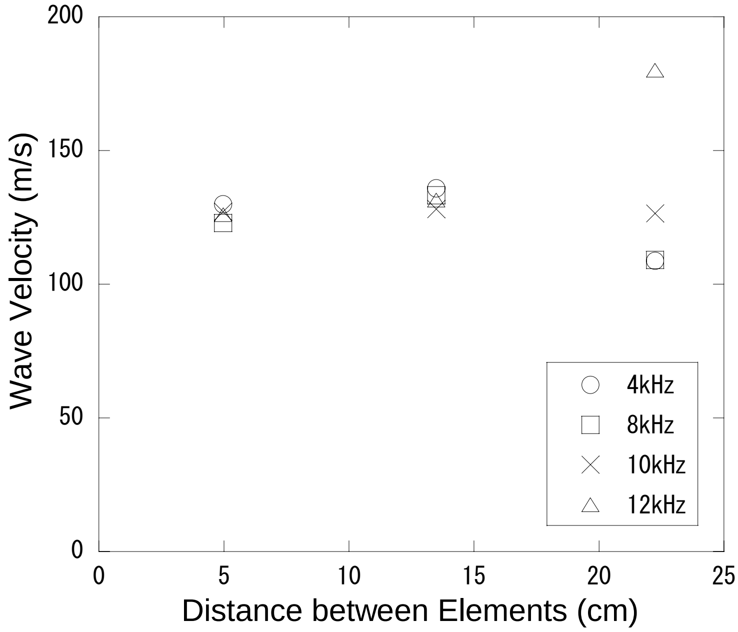

Figure 9: Results for wave propagation checking

4.2 Shear modulus

Shear modulus is calculated for obtained data using following formulas.

$$G = \rho V_s^{\,2} \tag{1}$$

$$f(e) = \frac{(2.17-e)^2}{1+e} \tag{2}$$

where G is shear modulus, e is density, Vs is shear wave velocity and e is void ratio. Since model test is conducted under nearly uniform condition, next relationship is approximated for calculation. Results agreed favorably with element test as shown in Figure 10.

$$\sigma_h = \frac{1}{2}\sigma_v \tag{3}$$

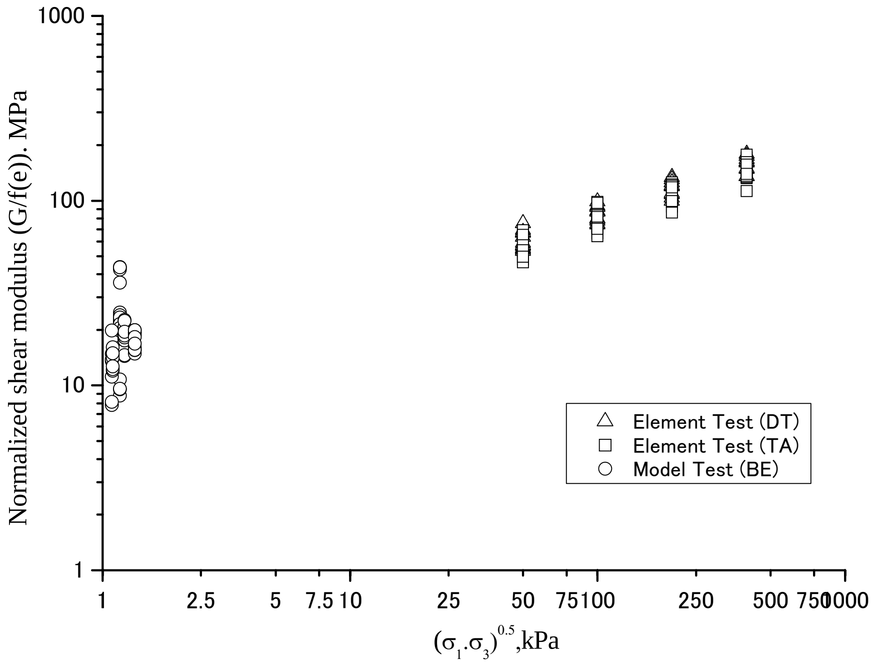

Figure 10: Normalized shear modulus versus earth pressure

5. CONCLUSION

1. In order to detect the wave arrival clearer, signal analysis is conducted. Low frequency noise is reduced by polynomial approximation, and high frequency noise is dealt with FFT filter.
2. Effect of attaching aluminum block to bender element is discussed. Some change in the received wave form is found, but wave velocity was almost same.
3. Property of wave propagation is checked using plural receiver for one transmitter and found to be in straight way.
4. Shear modulus is calculated for obtained data for validation. Results showed good agreement with those of element test.

REFERENCES

General guidelines for road earthworks - culvert work -, 1999. Japan road association, ISBN 978-4889504101, Maruzen Print Co. Ltd. (in Japanese).

Kuwano, R., Horii, T. and Kohashi, H., 2007, Increment of Earth Pressure Acting on a Buried Box Structure due to Differential Settlements, *New Frontiers in Chinese and Japanese Geotechniques, Proceedings of the Third Sino-Japan Geotechnical Symposium,* 2007, 309-314.

Suwal, L., Kuwano, R., Small strain stiffness measurement of sand and gravel using disk shaped piezo-electric transducer, 5th International Conference on Earthquake Geotechnical Engineering, 2011.

WATER RESOURCES DEVELOPMENT IN KONTO BASIN, INDONESIA: IS THAT ENVIRONMENTALLY SOUND?

Md. Reaz Akter MULLICK[1] and Mukand S BABEL[1]
[1]Water Engineering and Management,
Asian Institute of Technology, Thailand
reazmullick@gmail.com

ABSTRACT

Multiple uses of water are inevitable to produce more with less water. A sequential multiple use water systems in the Konto River, Indonesia is examined to understand the existing operation of the system where water is sequentially used in three hydropower plants and then in an irrigation project from a upstream reservoir named Selorejo. Environmental flow requirements for the river are estimated. It is found that the current operation policy does not ensure environmental flow requirements downstream to Selorejo reservoir which might cause environmental degradation and loss of ecosystem goods and services for the basin. The system is simulated for three different levels of environmental flow provisioning at the downstream of Selorejo. Ensuring environmental flow causes reduction in power production and higher level of environmental flow provisioning results higher reduction in power production. Changes in power production due to different environmental flow levels are examined and presented, which will help the basin managers to decide and ensure certain environmental flow level for the Konto basin.

Keywords*: multiple use of water; water-use benefit; environmental flow; tradeoff; Konto River, Indonesia.*

1. INTRODUCTION

Growing water demands and limits over supply augmentation often entail competition and conflicts among the water users. Situation aggravates when environmental flow (EF) is considered for the rivers. Environmental flow is the provision of certain amount of flow to maintain the river health. While encountering such challenges, society constantly seeks to maximize the value that the limited resources provide and efforts are therefore committed to utilize the available water resources efficiently and effectively. Along this line, multiple uses of water i.e. using the available water for more than one uses or in production systems is inevitable to produce more with less water (Khan, 2010). However, intensification of multiple use of water in the catchment may affect downstream flow both in terms of quality and quantity. Hence, there is a need to revisit the multiple use water management activities and environmental sustainability at a system or catchment level (Bakker and Matsuno, 2001).

Multiple use of water exists at different levels, namely: homestead level (lowest level, where people use water for different uses around or near the homestead); water system level (the level of much communal water infrastructure, e.g. irrigation canal, domestic distribution network); and catchment or river basin level (multiple uses of water occur from upper catchments down to estuaries) (Van Koppen et al., 2006). Furthermore multiple use of water can be classified into several types, namely: MPR (multipurpose reservoir), MPN (multipurpose network), MU+ (multiple use domestic plus or productive plus, often productive plus is found as irrigation plus), MU-seq (sequential system), and MF (multi function, e.g. paddy field system) (Smits et al., 2008). MUS systems are usually found *de facto*, meaning that systems were developed with a single use in mind, but are *de facto* used for multiple purposes by users themselves or in a planned manner by later-adopting specific management measures or infrastructural add-ons to facilitate some other small-scale uses. This is probably still the most common type of system (Van Koppen et al., 2006).

This paper aims to demonstrate an 'MU-seq' type of multiple use at the Konto River, Indonesia, where water from an upstream reservoir is sequentially used in three hydropower plants and then in an irrigation project. The schematic of the system is presented in Figure 1. The used water is not redirected back to Konto main course. The paper further widens the analysis by checking whether the system provides enough water as EF downstream to reservoir and in case when EF demand is not satisfied scenarios are run with EF provision and loss in power production is examined.

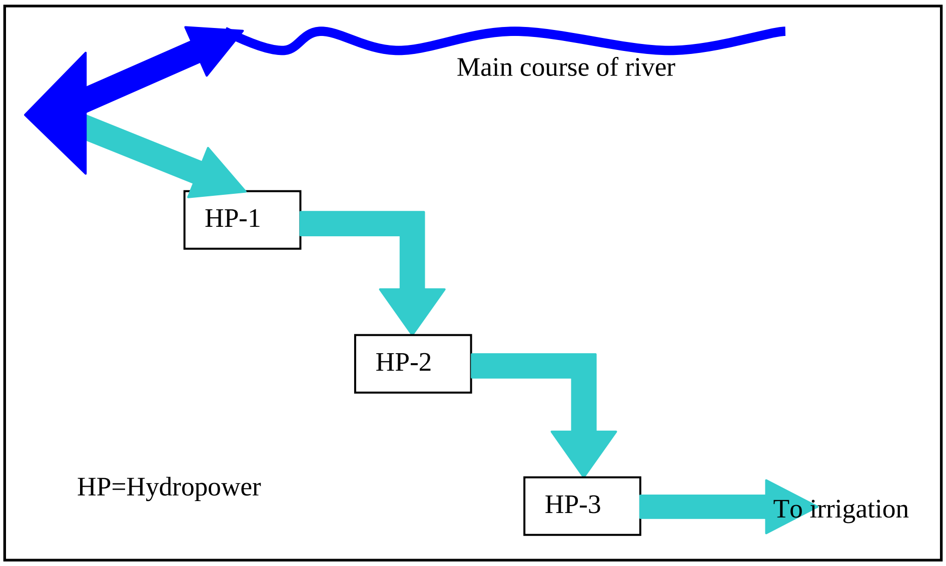

Figure 1: Schematic diagram of the sequential multiple use water at Konto

2. STUDY SITE

The Konto River basin in east Java, Indonesia is actually a sub-basin of the Brantas river basin. Selorejo reservoir is at the upstream of the Konto river. The Konto at the downstream of Selorejo flows towards north-west and finally drains to the Brantas. The total basin area of the Konto is 687 km^2 which can be divided into two parts, upper (above Selorejo reservoir) and lower (downstream of Selorejo). Catchment area for the upper part is about 236 km^2 that comprises Konto river 148 km^2, Kwayangan river 12.5 km^2, Pinjal river 44.3 km^2 and Selorejo reservoir 31.3 km^2 (Solihah, 2011). Lower part of Konto basin has an area of 451 km^2. Three small tributaries are found meeting the Konto in this lower part, namely: Sambong (catchment area 3.13 km^2), Nogo (catchment area 1.35 km^2) and Nambaan (catchment area 3.69 km^2) (Solihah, 2011). Average annual rainfall in the basin is about 2,700 mm whereas annual average evaporation is about 1,470 mm. Two season are mainly observed, wet (November -April) and dry (May-October) in the region. Roughly 80% of the rainfall occurs in the wet season. The plains and delta consist of alluvial soils (silt, clay loams) well suited to paddy cultivation. The annual average temperature is 23.5^0C, with maximum monthly temperature of 24.5^0C in January, and a minimum temperature of 22.7^0C in July. Annual average relative humidity is 79.9%, with a minimum humidity of 75% in January, and maximum of 83% in September (Solihah, 2011).

Selorejo reservoir commissioned on 1970 is situated at the upper part of Konto and is equipped with a hydropower plant, namely Selorejo power plant. In addition to Konto river, the reservoir is feed by Pinjal and Kwayangan river. The capacity of the reservoir is about 40 MCM with a water surface area of 4 km^2. The Selorejo hydropower started running since 1972 has capacity of 4.5 MW and the design discharge of 14.8 m^3/s. The release from Selorejo hydropower plant was redirected to the Konto before the construction of Mendalan and Siman hydropower plants in 2003. However, currently the release from Selorejo hydropower is subsequently being used by another two power plants Mendalan and Siman respectively and then in Konto irrigation project. Figure 2 shows the schematic of the lower part of the Konto River (the study site) including the water uses.

The topography of the region resonates well in terms of getting considerable heads in building these two other hydropower plants, namely: Mendalan and Siman after the Selorejo plant. The plants are run-off-river type. The tail water elevation of the Selorejo power plant is 582.00 m a.m.s.l. Part of the release from Selorejo plant is taken using a 3.25 km long tunnel to Sekuli daily retention pond which stabilizes the discharge from Selorejo and supplies water to Mendalan hydropower plant having an installed capacity of 7.0 MW and design discharge of 8.5 m^3/s. The tunnel capacity that feeds Sekuli retention pond is 9.25 m^3/s. A 5.55 m^3/s capacity pipe sends back the extra discharge from Selorejo plant to Konto main stream. Water Elevation of the Sekuli pondage is 573.17 m a.m.s.l. and the tail-water elevation of Mendalan power plant is 422.90 m a.m.s.l. that creates an effective head of 150.27 m for Mendalan power plant (PJT-I, 2007).

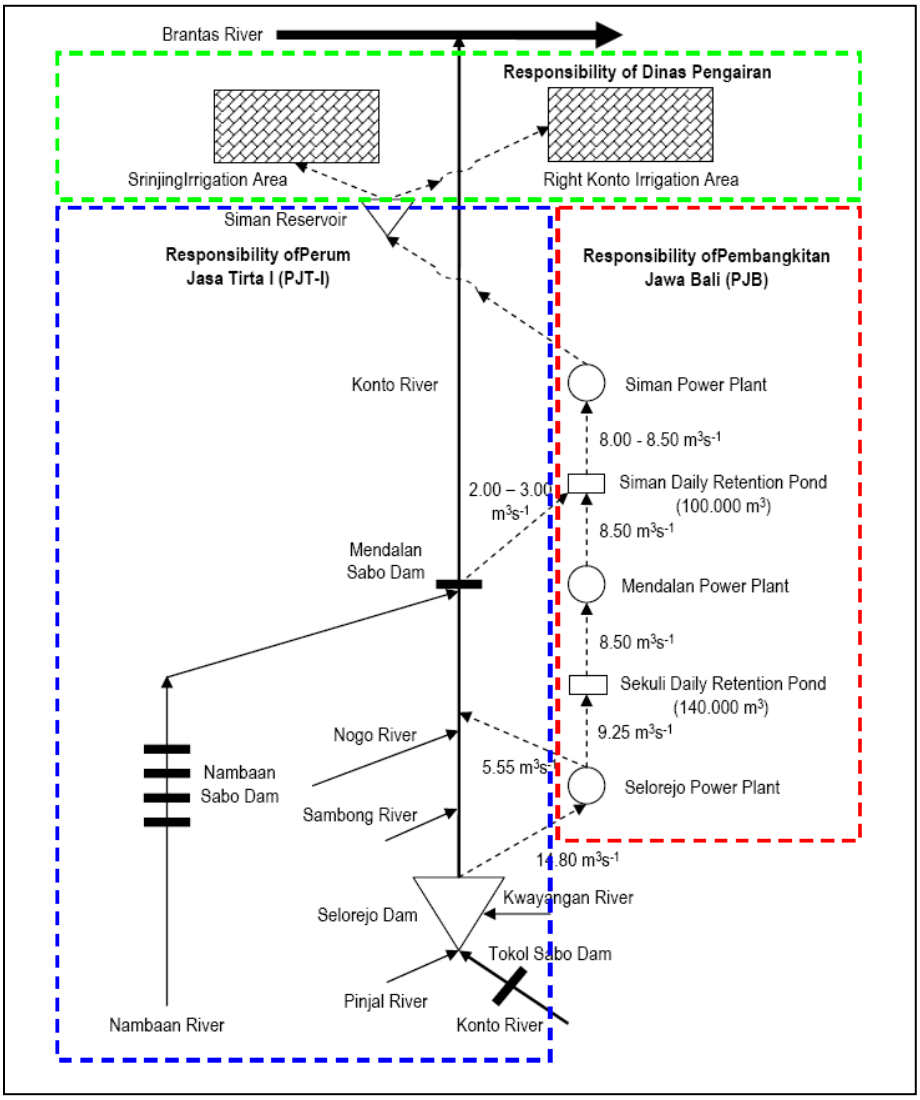

Figure 2: Schematic of the Konto river study site

Note: Discharge values mentioned in the figure are the capacities of tunnel/pipes

The release from Mendalan power plant is carried by a 3.2 km long tunnel and sent to Siman retention pond where Siman Hydropower plant is installed with the capacity of 9.0 MW and with design discharge of 8.5 m^3/s. The effective head of Siman hydropower plant is 106.4 m (PJT-I, 2007). At the point of Mendalan sabo-dam (Sabo-dam is a kind of silt arresting dam); facility to divert 2 – 3 m^3/s flow to Siman pond is available to stabilize the power production from Siman plant. Effective head for Siman power plant is 106.4 m (Solihah, 2011). The water used in Siman power plant goes to Siman reservoir from where the Left- and Right-Konto irrigation projects get supply of irrigation water. The entire water resources is managed by the public company named PJT-I.

3. METHODS AND DATA

The system is simulated for the current operation policy using a spread sheet model and power production from each power plant is calculated. Based on communication with PJT-I, it is understood that the system is currently running with the aim of maximizing power generation. PJT-I provided all the required data for the analysis. The obtained data includes monthly inflow to and release from Selorejo reservoir, monthly power production from three power plants, monthly flow for the three tributaries of the Konto, namely: Sambong, Nogo and Nambaan for last ten years (1999 - 2008). Power production from Mendalan and Siman plants were available for last six years (2003 – 2008) since both of the plants came into operation on 2003. Storage-area-elevation for the Selorejo reservoir was also collected from PJT-I database.

Environmental flow requirements are estimated for the Mendalan Sabo dam point and checked whether EF demands are meeting at this point in the current operation. In case EF is not ensured at Mendalan sabo dam point, the system is simulated with three different level of EF. For each simulation with different level of EF, power production is calculated.

Estimation of EF at Mendalan sabo-dam point of Konto

Information related to flow in the Konto at natural condition i.e. the flow before commissioning Selorejo reservoir on 1970 is not available. However, inflow to Selorejo is recorded and obtained from PJT-I. This flow can be used as proxy to the natural flow in the Konto if the Selorejo reservoir would not been there. At the downstream of Selorejo dam, three very small (in terms of discharge) tributaries met with the Konto (Figure 2). Up to the point of Mendalan sabo-dam, the length of the reach is about 8 km and after this point there is no major water abstraction from the Konto. Environmental flow is considered immediately downstream of this point after the diversion to Siman pond. Environmental flow is estimated based on the inflow to Selorejo with the addition of Sambong, Nogo and Nambaan flow. Only ten years monthly discharge data is in hand, hence Tennant method (Tennant, 1976) is adopted, which deals with only mean annual flow (MAF). Environmental flow requirements for wet and dry season are certain percentages of MAF for different environmental status according to Tennant.

4. RESULTS

4.1 Simulation of the system for existing operation

Inflow to Selorejo reservoir is known and acts as the upper boundary of the model. Reservoir operation is constrained by minimum and maximum storage i.e. 8.09 MCM and 39.6 MCM respectively. Hydropower generations are constrained as maximum discharge limit of the penstock. Based on this boundary and constraints, the simulation model is set up in a spread sheet and run with six years (2003 - 2008) mean monthly dataset, which represents the existing scenario. Downstream of Selorejo, only observed information is the Selorejo release, which is compared with the model output. The model output fits with the observed data with a correlation coefficient (*r*) of 0.88, root mean square error (RMSE) of 1.18 m^3/s and overall volume error (OVE) of 0.08 m^3/s.

In this simulation of existing operation, release from Selorejo first meets Selorejo power plant's demand. In case of higher release from the dam than the penstock capacity of Selorejo power plant, the extra flow spills to Konto main stream. Outflow from Selorejo plant is then going to Mendalan and Siman power plant subsequently. If it is necessary, small amount of flow is diverted to Siman plant from Mendalan sabo dam point. The observed and simulated power productions are compared for this existing operation and it shows a considerable well agreement. Performance of the simulation is measured using two parameters; namely: RMSE and OVE and reported in Table 1. Figure 3 shows the simulated and observed power for the Selorejo power plant. The simulated power productions from Selorejo, Mendalan and Siman power plants are 25,951, 78,844 and 57,611 MWh respectively. The total power production is obtained to be 162,407 MWh from the simulation model.

Table 1: Simulation model performance in terms of energy generation for existing condition

Power plant	RMSE (MWh)	OVE (MWh)
Selorejo	167.61	29.13
Mendalan	474.64	48.78
Siman	557.09	35.15

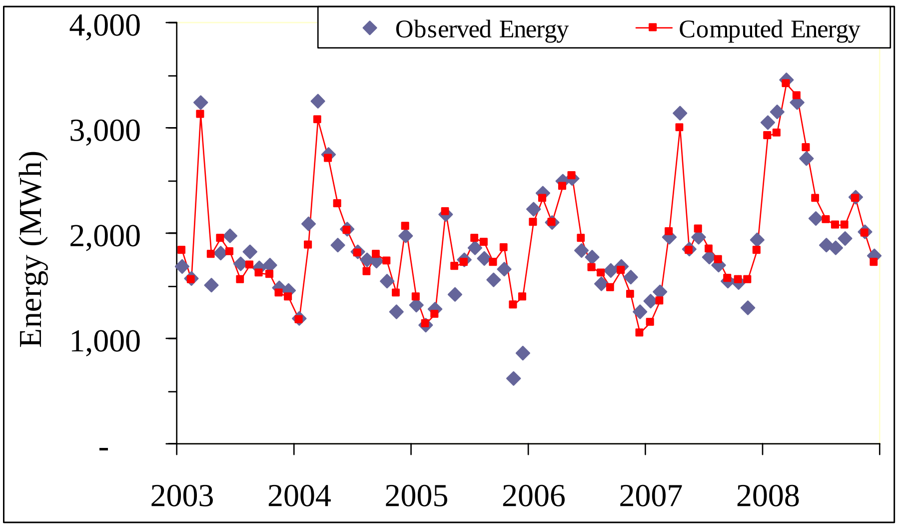

Figure 3: Observed and simulated monthly power production from Selorejo Power plant

4.2 EF requirements at Mendalan sabo-dam point of Konto

Based on ten years mean monthly inflow to Selorejo reservoir in addition to the flow of Nogo, Sambong and Nambaan river, MAF of Konto at Mendalan sabo dam point is estimated to be 10.74 m^3/s. Two seasons are considered, namely: high flow season (November – April) and Low flow season (May – October). Environmental flow requirements for both the seasons and for different environmental (habitat) status are calculated as prescribed by Tennant and reported in Table 2. Keeping in mind of maximization of overall benefit from offstream water uses 'fair or degrading' environmental condition is considered to be maintained which is 30% and 10% of MAF i.e. 3.22 and 1.07 m^3/s for the high and low flow season respectively.

Table 2: EF requirements for the Konto based on Tennant method

Environmental status as defined by Tennant	**EF requirement (m^3/s)**	
	High flow season (November - April)	**Low flow season (May - October)**
Flushing flow	20.48 (200%)	20.48 (20%)
Optimum range	6.44 – 10.74 (60 – 100%)	6.44 – 10.74 (60 – 100%)
Outstanding	6.44 (60%)	4.30 (40%)
Excellent	5.37 (50%)	3.22 (30%)
Good	4.30 (40%)	2.15 (20%)
Fair or degrading	3.22 (30%)	1.07 (10%)
Poor	1.07 (10%)	1.07 (10%)
Severe degradation	<1.07 (<10%)	<1.07 (<10%)

High flow season = November to April; Low flow season = May to October;
EF= environmental flow; MAF= mean annual flow

4.3 Checking EF at Mendalan Sabo dam for existing operation

The monthly flow at Mendalan sabo dam is estimated from the simulation model for the existing operation system and compared with the EF requirements for 'Fair or degrading' level as estimated and presented in Table 2. It is observed that in dry season the actual flow does not meet the EF requirements. Comparison of the actual flow and EF requirements are plotted in Figure 4.

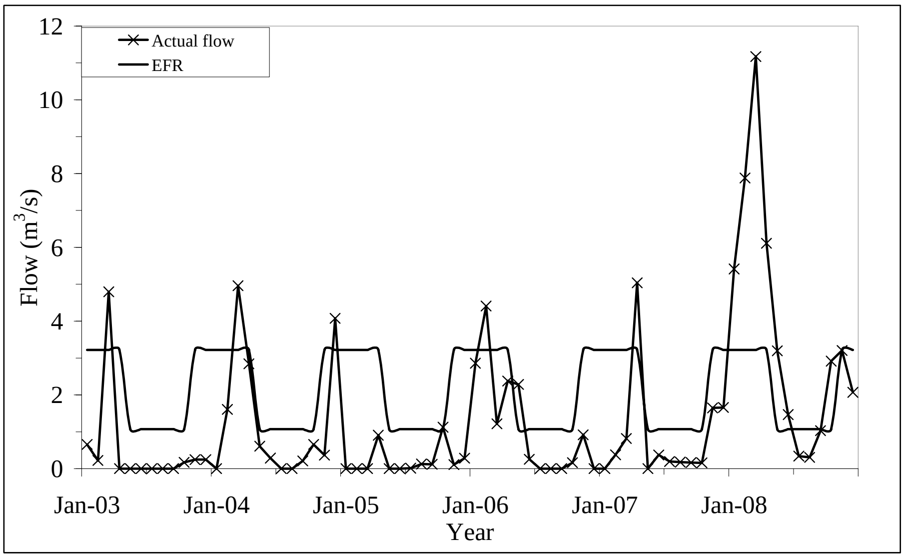

Figure 4: Existing estimated flow and required environmental flow at Mendalan sabo dam, Konto

4.4 Power production after ensuring EF

Environmental flows can be regarded as not exactly empirically determined figures, but they are more value judgments depending on the aim of river management. Specific physical situation and the expected state of the ecosystem should control the EF decision making. Without limiting the economic growth, achieving environmental sustainability is the main challenge along this line and that can be achieved within the context of wider EF assessment framework incorporating in the river basin planning. Considering such critical issues, three different values of EF are used and power production in each case is estimated.

Three different level of EF is tested, namely: (1) ‘Poor’ condition for the high flow season with a flow of 1.07 m^3/s and ‘Severe degradation’ for the low flow season with a flow of 0.75 m^3/s labeled as ‘Low’ level of EF, (2) ‘Fair or degrading’ for both the season with a flow of 3.22 m^3/s for the high flow season and 1.07 m^3/s for the low flow season labeled as ‘Medium’ level of EF, (3) ‘Good’ status for both high and low flow season is considered with the flow of 4.3 and 2.15 m^3/s respectively labeled as ‘High’ level of EF. All these ‘poor’, ‘fair’ and ‘good’ environmental status is as defined by Tennant.

Power production in the three levels of EF provisioning is estimated using the simulation model. The power production values are presented in Table 3. Figure 5 shows the power production relative to existing condition for various EF levels.

Table 3: Power production while ensuring EF at Mendalan Sabo dam

EF level	Power production (MWh)			
	Selorejo	Mendalan	Siman	Total
No EF	25,951	78,844	57,611	162,407
Low	23,556	73,354	53,723	150,633 (7%)
Medium	20,344	66,987	49,511	136,843 (16%)
High	17,492	59,615	44,854	121,962 (25%)

Note: value in parenthesis indicates % change with respect to no EF condition

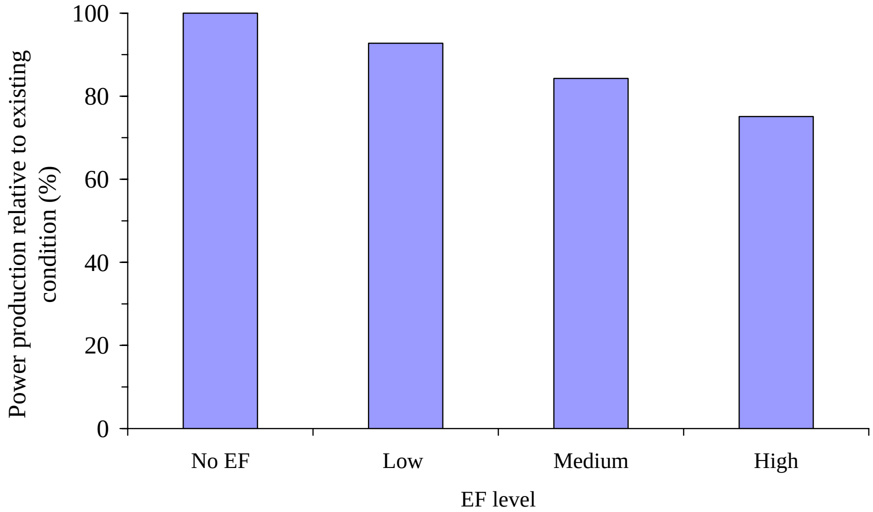

Figure 5: Power production relative to existing operation while EF is ensured

It is observed from Table 3 that higher the level of EF provisioning results higher reduction in power production. Higher reduction is observed in Selorejo plant. Total power production is reduces by 7, 16 and 25% from the existing condition for ensuring low, medium and high level of EF respectively.

6. CONCLUSION

In the present study, the sequential multiple water use system in the Konto river basin in Indonesia is thoroughly analyzed. The system is simulated for the existing operation policy which does not ensure EF downstream to Selorejo reservoir. Such operation of the reservoir might cause environmental degradation to the downstream part of Konto. Environmental flow is therefore necessary to maintain, however, provisioning EF results reduction in power production. The system is then simulated for three different levels of EF namely, low, medium and high. Ensuring EF with high level results higher reduction in power production from the system. Nevertheless, at least low level of EF is strongly suggested to be ensured.

The results from this analysis will help authorities to realize the cost of EF provisioning for the Konto river basin.

ACKNOWLEDGEMENT

This research is part of the doctoral study by the first author at Water Engineering and Management (WEM), Asian Institute of Technology (AIT) which has been supported by the scholarship provided under the AIT-Norwegian Ministry of Foreign Affairs (AIT-NMFA) Cooperation Program. Authors also acknowledge DUPC, UPaRF and its donors (DGIS, UNESCO-IHE and AIT) for partially funding the research. Thanks are also extended to PJT-I and UNPAR for providing data and information related to the research reported here.

REFERENCES

Bakker M. and Matsuno Y. (2001). A framework for valuing ecological services of irrigation water. *Irrigation and Drainage Systems*, vol. 15, pp. 99-115.

Khan, M. A. (2010). *Enhancing water productivity through multiple uses of water in Indo-Gangetic basin*. Paper presented ISDA (Innovation and sustainable development) 2010, Montpellier, June 28-30, 2010. Available online http://www.isda2010.net/var/isda2010/storage/original/application/9dc633a9f77b8f381062d94ffdfb43a0.pdf accessed on 05/06/2011

Perum Jasa Tirta (PJT) – I. (2007). *Manual Operasi Dan Pemeliharaan Bendungan Selorejo* (Dam Operation and Maintenance Manual Selorejo). PJT - I, Malang.

Smits, S., Renwick, M., Renault, D., Butterworth, J. and Van koppen, B. (2008). *From practice to policy: background paper for the symposium on multiple-use services*. International Symposium on Multiple-Use Water Services Addis Ababa, Ethiopia, 4-6 November 2008.

Solihah, R. (2011). *Analisis pemanfaatan potensi air waduk Selorejo* (Analysis of the potential use of water from reservoir Selorejo) B.Sc. Thesis at Universitas Katolik Parahyangan (UNPAR), Indonesia.

Tennant, D. L. (1976). Instream flow regimes for fish, Wildlife, Recreation and Related Environment Resource, *Fisheries*, vol. 1, 1976, pp. 6-10.

Van Koppen, B.; Moriarty, P.; Boelee, E. (2006). *Multiple-use water services to advance the millennium development goals*. Research Report 98. International Water Management Institute, Colombo, Sri Lanka.

A STUDY ON LONG-DISTANCE EVACUATION MEASURE TO LARGE-SCALE FLOOD DISASTERS IN JAPANESE THREE MAJOR METROPOLITAN AREAS

Hiroyuki NAKAI[1] and Takaaki KATO[2]
[1]Graduate Student School of Eng., The University of Tokyo, Japan
h-nakai@iis.u-tokyo.ac.jp
[2] Associate Professor, ICUS, IIS, The University of Tokyo, Japan

ABSTRACT

The purpose of this study is to examine what should be of evacuation measures by the municipality which is exposed to the danger of a large-scale flood disaster through the analysis of the flood hazard map. The plains of Japanese three major metropolitan areas holds an extensive risk to the flood disaster such as broadness of flooded area, flooded length and accumulation of population. In this study, contents of the flood hazard map which is distributed to the citizens were analyzed to understand the current state of evacuation measures at a large-scale flood disaster in each municipality. Most of municipalities assign facilities where the flood was assumed to the refuge. It is necessary to take evacuation measures in consideration of characteristics of the region such as broadness of flooded area and flooded length. Moreover, when long distance evacuation is prescribed, it becomes very important to use the transportation such as public traffic and bicycles and how to evacuate the senior citizen and the handicapped person in priority. The assessment model is to be established at two points; the time to complete evacuation by behavioral traits like use of transportation, and the scale and the arrangement of the refuge.

Keywords*: flood, evacuation, hazard map, contents, below sea level area*

1. INTRODUCTION

1.1 Background of this study

Recently, an increase in the flood damage risk originating in the climatic change is pointed out. Global warming progresses because of increase of a heat-trapping gas such as anthropogenic carbon dioxide, and the normal temperature rise of 0.74℃ every 100 years is confirmed according to the fourth evaluation report issued by Intergovernmental Panel on Climate Change (IPCC). A further normal temperature rise is expected, and the rise of the sea level, an increase of the downpour frequency and enlargement of typhoons are assumed. About 50% of the population and about 75% of the property have concentrated on the flood assumption district in the waste plain where it accounts only for about 10% of the area of the country in Japan. The incidence of a large-scale flood damage by the flood and the climax can be said that it decreases in recent years as the maintenance of the flood control facilities such as the embankment advances, and consciousness of crisis to the flood damage is weakening at the same time as people's reliance and relief to the flood control business rise. However, danger over the maintenance target such as the flood control facilities rises by a great climatic variation, and the possibility of the occurrence of a large-scale flood damage due to the flooding and the climax flood cannot be disregarded in the metropolitan area located in the littoral region and the low-lying area in Japan. It is thought that not only a lot of lives and the properties are lost as confirmed by the climax disaster caused by Hurricane Katrina in New Orleans, but huge damage and confusion are caused socially and economically if a large-scale flood damage occurs by any chance.

1.2 Flood disaster risk in the large-scale below sea level areas

The district below the average flood tide level is called a below-sea-level area. Tokyo metropolitan district, Chukyo metropolitan district and Kinki metropolitan district are generically called three major metropolitan areas, and the population, undertaking activities and the educational institution concentrate there. The more than half of the total population of Japan concentrates on three major metropolitan areas at the end of March in 2007, and it can be said that it forms the center part of the country.

In three major metropolitan areas, wide plains exist, and especially on gulf coast, there are regions below the average flood tide level called the below-sea-level area. The below-sea-level area in Japan is assumed to be chiefly formed by the subsidence by an excessive drawing up underground water. The total size of the below-sea-level area is about 580 km^2 in January, 2006; 116 km^2 in Tokyo metropolitan district, 336 km^2 in Chukyo metropolitan district and 124 km^2 in Osaka metropolitan district. Moreover, over four million people reside there in total; 1.76 million people in Tokyo metropolitan district, 900,000 people in Chukyo metropolitan district and 1.38 million people in Osaka metropolitan district.

The ground level is low in the below-sea-level area, and it exists on gulf coast, it is located in the lower part of large rivers. Therefore, it is assumed that various flood damage such as inundation inside the levee, the flood and the climax occurs. Large area is continuously flooded once the flood damage occurs. It is expected that the flood continues for a long term of two weeks or more because natural drain is not done if the drain facilities are not used in the below-sea-level area.

Therefore, the victims are pressed long-term refuge life. A large difficulty is attended to the rescue supply to people who are isolated in the flooded district assumed to reach several hundred thousand people in the metropolitan area. The efficiency improvement of the goods delivery is attempted by bringing the evacuee together in the refuge. Furthermore, it is preferable to move outside the flooded district and to make them do a long-term relocation. However, it is thought that a large difficulty is attended also by the safe inducement of the evacuee outside the flooded district. It is thought that the seriousness of the flood damage risk is exposed in the large-scale below-sea-level area when a large-scale flood damage.

2. CONTENTS ANALYSIS OF FLOOD HAZARD MAPS

2.1 Meaning of flood hazard maps to take measures to large-scale flood disasters

It is necessary to provide the measures for smooth, prompt evacuation such as the means of information transmission and the refuge areas for the damage reduction at a large-scale flood damage. The flood hazard map is located as a well-known means to the resident of these measures. The local government was obligated to make public of the flood hazard map in Japan along with the flood control law revision in June, 2001. As a result, the rate of information disclosure that was 23.1% at the end of 2003 rose up to 85.2% in January, 2011. Therefore, it is thought that the current state of a large-scale flood damage measures in each municipality can be evaluated by analyzing the flood hazard map.

2.2 Objective and item of analysis

In this chapter, contents of the flood hazard map were analyzed for the local government where the flood district extended to the width of about 1km or more in the municipality including the flood assumption district in the river that flowed to the below-sea-level area in Japan's three major megalopolises. It is because of the idea it is expected that it takes some time to evacuate in such a place, and giving information about disaster prevention to the resident by the flood hazard map becomes important for smooth, prompt evacuation in the idea of evacuation measures.

Municipalities for the analysis were the following 116 municipalities, and 105 municipalities to which the flood hazard map was open to the public on the Internet were analyzed among these. (Table 1)

Table 1: Municipalities for flood hazard map analysis

Major metropolitan areas	Prefecture	Municipality
Tokyo metropolitan district (48 municipalities)	Tokyo	Edogawa, Katsushika, Adachi, Koto, Sumida, Taito, Arakawa, Kita, Itabashi (9 municipalities)
	Saitama	Wako, Asaka, Shiki, Fujimi, Kawagoe, Kawashima, Yoshimi, Kawaguchi, Hatogaya, Toda, Saitama, Ageo, Okegawa, Konosu, Gyoda, Kumagaya, Kazo, Ina, Kuki, Hasuda, Shiraoka, Miyashiro, Sakado, Higashimatsuyama, Soka, Misato, Yashio, Yoshikawa, Koshigaya, Matsubushi, Kasukabe, Sugito, Satte (33 municipalities)
	Chiba	Urayasu, Ichikawa, Matsudo, Nagareyama, Noda (5 municipalities)
	Ibaraki	Goka (1 municipality)
Chukyo metropolitan district (34 municipalities)	Aichi	Nagoya, Ama, Oharu, Kiyosu, Kitanagoya, Toyoyama, Ksugai, Yatomi, Aisai, Tsushima, Inazawa, Ichinomiya, Kanie, Tobishima (14 municipalities)
	Gifu	Gifu, Hashima, Kakamigahara, Kasamatsu, Ginan, Kaizu, Wanouchi, Anpachi, Mizuho, Kitagata, Ogaki, Yoro, Godo, Ono, Ibigawa (15 municipalities)
	Mie	Kuwana, Kisosaki, Kawagoe, Asahi, Toin (5 municipalities)
Osaka metropolitan district (34 municipalities)	Osaka	Osaka, Moriguchi, Neyagawa, Hirakata, Kadoma, Daito, Higashiosaka, Settsu, Suita, Ibaraki, Takatsuki, Toyonaka, Ikeda, Yao, Sakai, Matsubara, Fujiidera, Kashiwara (18 municipalities)
	Kyoto	Oyamazaki, Nagaokakyo, Muko, Kyoto, Uji, Kuiyama, Joyo, Ide, Yawata, Kyotanabe, Seika, Kizugawa (12 municipalities)
	Hyogo	Itami, Kawanishi, Amagasaki, Nishinomiya (4 municipalities)

I arranged the analysis item based on the description item provided in "Guidance of flood hazard map edit" (Table 2). The description item can be classified into three; "Contents of the map" including information that is the necessity of the description on the map, "Information about evacuation" which is necessary to evacuate, and "Shelter use information" which enlighten the disaster awareness in daily life. "Contents of the map" and "Information about evacuation" are thought to be more important were totaled and analyzed in the present study.

Table 2: Items for flood hazard map analysis

Contents of the map		Information about evacuation	
Flood-assumed area		Getting information	Where to get information
Refuge area			How to get information
Designation to evacuate from flood-assumed area			Contact information of government
District	Zone-by-zone refuge areas		Contact information of disaster-related facilities
	The number of districted areas	A series of evacuation	Acquaintanceship at normal times
Refuge	Refuges for who need help on evacuation		Acquaintanceship on evacuation
	Avairable floors of refuges		Taking out list
	Contact information of refuges		Information about refuge life
	Type of refuges	When to start evacuation	Action on evacuation order
Route	Danger area on evacuation		Earlier evacuation order to who need help
	Underground facility and flooded road		Distinction of evacuation order by floor of home
	Designation of evacuation route		Note about time change
Facilities	Hospital	Transportation	Designation of transportation device
	Public institution		Special note about using cars
Note about flow rate		Difficulty and speed of walking at flooded condition	
		Note about those who need help	
		Figure about depth of flood	

2.3 Result of analysis

When the description rate to the flood hazard map was arranged, it became the following. (Figures 1 and 2) Especially important items for thinking about the evacuation activity were shown in red. The item described by all the hazard maps is only "Position of the refuge area". The difference of the description rate of “contents of the map” by the item is large, and “information about evacuation” has understood the description rate is generally high compared with “contents of the map”. It is thought that characteristics of the region are reflected on “contents of the map” better than “information about evacuation. Moreover, there is a municipality where necessary information of escape route is insufficient when the residents evacuate, and the improvement is hoped for.

Next, the flood hazard map of each item was arranged. (Figure 3) As a result, the item with an especially remarkable difference by the area is "Designation of long-distance evacuation", "Notification of evacuation route", and "Available floors of refuges".

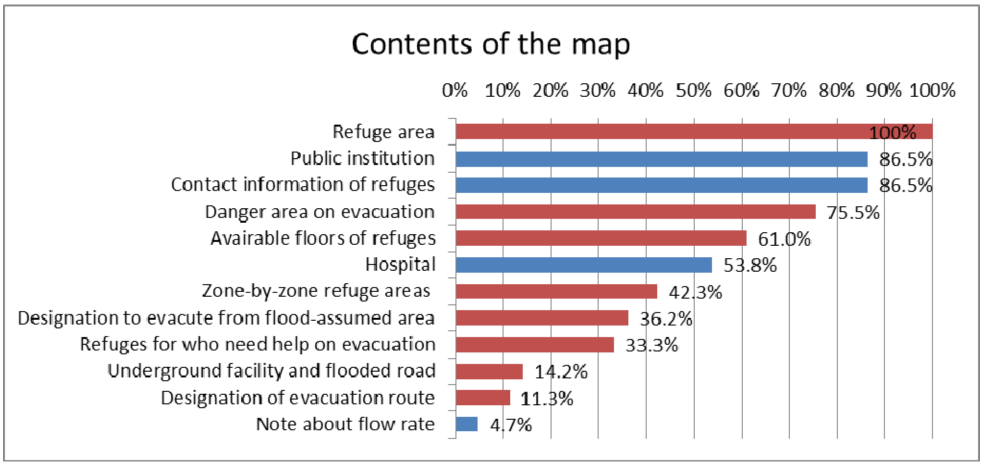

Figure 1: Contents of the map

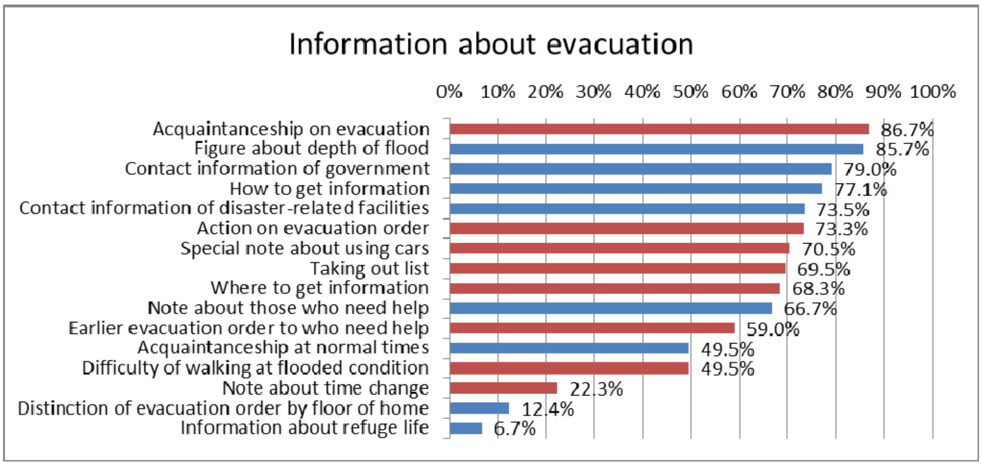

Figure 2: Information about evacuation

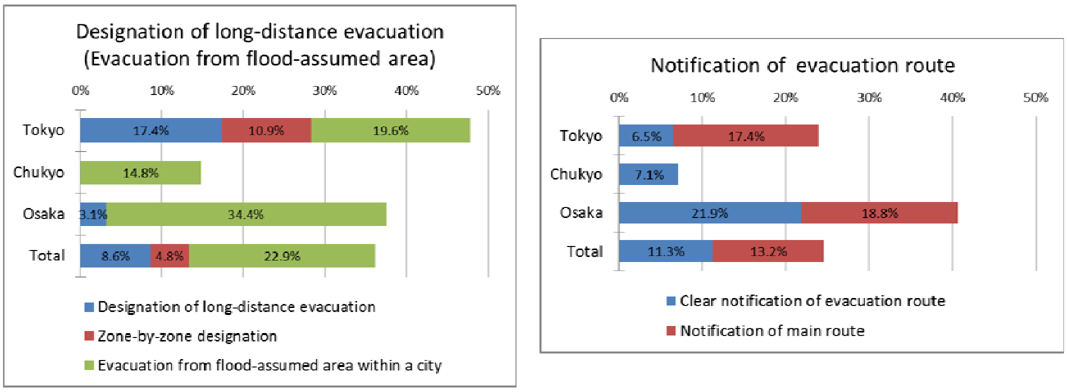

Figure3: Item with remarkable difference by municipality

2.4 Sort flood hazard maps by type

It has been understood to be able to classify evacuation measures of each municipality at a large-scale flood damage into the following three types by the character in the specified refuge area through the contents analysis of the flood hazard map.

(1) Municipality where description exists for long-distance evacuation outside municipality (13 municipalities) In the municipality whose flood area is wide and whose whole area is almost flood assumption area, it is thought that long-distance evacuation (Evacuate over the municipality field) is necessary, and the municipality enumerated in this item has included long-distance evacuation in some shape in the flood hazard map.

(2) Municipality where design refuge out of the flood-assumed area in the municipality or refuge at less flood-assumed area (23 municipalities) When the district by the height's there in the municipality it that is not flooded in the region exists in the municipality, the necessity of large area shelter can evade the few isolation of the refuge at the ponding.

(3) Municipality that specifies refuge to the nearest refuge in flood assumption district (70 municipalities) In the other than the above-mentioned two types, it is specified to evacuate to the nearest refuge in the flood district, and 66.0% of the whole (70 municipalities) is the hazard maps of this type.

3. CONSIDERATION ABOUT EVACUATION MEASURES TO LARGE-SCALE FLOOD DISASTERS

In this chapter, the indicator of the matter that should be going to advance the examination to the problem exposed by the hazard map contents analysis in Chapter 2 is shown.

The first point is improvement of flood hazard maps corresponding to characteristics of the region. The refuge that conforms by the struck situation can be set, and the flood hazard map be improved for evacuation measures chiefly provided based on spatial characteristics by understanding regional characteristics in two axes (the time axis and the space axis).

The second point is making and giving public notice of the flood assumption district map including a change with the lapse of time. In including "Time axis" in evacuation measures, there is a part not ameliorable in each municipality. About this, it is necessary to make public in the form of that each municipality can use "Flood water arrival time map" and "Distribution map of the ponding time" besides the flood assumption district map in the flood hazard map as an output of the flood simulation done in each river office.

The third point is a review of the refuge capacity. It is necessary to review the refuge capacity from the viewpoint of depth of flood and ponding time and availability of the stockpile. Whether capacity of specified refuges is enough is considered, if it is assumed to evacuate to the refuge in the flood district at a large-scale flood damage. If it is not enough, it is necessary to review the specification of the refuge considering the possibility of long-distance evacuation.

The fourth point is an examination about the transportation method on long-distance evacuation. Though long-distance evacuation on foot is basically specified, it is not easy to think that this policy is the best when thinking about prompt and adequate evacuation. It is necessary for groping for the possibility of evacuation using the public transportation facility and the bicycle. In addition, it is necessary to decide a main route and the direction of evacuation to achieve the prompt evacuation conduct, because an indefinite part is a lot about route of evacuation.

Finally, there are problems of who need help on evacuation. First of all, it is important to list who need help on evacuation. And then, it is important to secure cooperators, rapid transportation to refuges, and refuges for those who need help.

In considering of evacuation measures at a large-scale flood damage, it had turned out not to be examined enough, so the measures ideas about the above-mentioned five items was presented with the importance of the problem. It is necessary to improve in evacuation measures at a large-scale flood damage, and to be held off to the minimum of damage for the assumed risk in each municipality.

4. CONCLUSION

4.1 Conclusion of this study

The rate of making public of the flood hazard map went up greatly by revising the flood prevention law in 10 years. "Guidance of flood hazard map edit" is made public along with the flood control law revision, and the flood hazard map is made as a part that takes measures against the flood of the river in each municipality including the flood assumption district based on the guidance. However, it was clearly shown that there was a big difference between a municipality thought for the examination situation of evacuation measures to be examined enough and municipality not so in the current state. Moreover, becoming what suits a more actual water disaster condition has understood evacuation measures from introducing "Time axis" when thinking about the flood assumption. It is thought that the present study is meaningful each municipality examines a large-scale flood damage measures in these two points.

4.2 Agenda and next vision

The study on the public assistance in evacuation measures at a large-scale flood damage was advanced in this thesis. However, there is a limit within the range where the public assistance can be done. Therefore, the role of the self-help and the mutual assistance is very important. The self-help is to think about and provide for the disaster routinely. And, the mutual assistance is the activity of the voluntary organization for disaster prevention. Therefore, it is necessary to hold an enough conference between each subject routinely so that the self-help, the mutual assistance, and the public assistance are interlocked and synchronized well.

Moreover, it is necessary to improve not only such soft measures but also continuous hard ones such as the reliabilities of the safeguard facility, construction of the piloti, and the maintenance of the pedestrian deck connected with the station. However, because the memories of a past flood damage are weakened by maintenance in hard respect, and resident's disaster awareness is decreasing, it is necessary to continue to hold a warning for the danger of a large-scale flood damage, to maintain and improve resident's disaster awareness and self-reliant efforts.

I want to keep on studying about improvement of the evacuation completion rate and achievement of rapid evacuation by comparative study using valuation modeling of evacuation method, and edit of real-time hazard map which express in the shape of fixed to one by one risk and make it public through the web.

REFERENCES

Kazuya, S., and Osamu, M., 2007. Comparison of Contents of Japanese Hazard Map to the Earthquake Flood. *Digest of Academic Lecture 2007* F-1, Japanese Architecture Academy, 643-644

Fumio, N., 2006. Public Presentation of the Hazard Map using the Internet. *Collection of Lecture Papers 2006,* Japan Society of Geoinfomatics, 91-92

MLIT Japan, Portal Site of Hazard Map: *http://disapotal.gsi.go.jp/index.html*

MLIT Japan, Manual to Create Flood Hazard Map:
http://www.mlit.go.jp/river/basic_info/jigyo_keikaku/saigai/tisiki/hazardmap/index.html

MLIT Japan, Approach to the Climate Shift by River Bureau:
http://www.mlit.go.jp/river/basic_info/jigyo_keikaku/gaiyou/kikouhendou/index.html

MLIT Japan, Review Meeting of Storm Surge on Below Sea Level Area:
http://www.mlit.go.jp/river/shinngikai_blog/past_shinngikai/shinngikai/takashio/index.html

Cabinet Office, Government of Japan, Expert Study Meeting about Countermeasure against the Mass Flood Disaster:
http://www.bousai.go.jp/jishin/chubou/suigai/index.html.

INTERNATIONAL CENTER FOR URBAN SAFETY ENGINEERING
Institute of Industrial Science, The Universiy of Tokyo
4-6-1 Komaba, Meguro-ku,
Tokyo 153-8505, Japan
http://icus.iis.u-tokyo.ac.jp
E-mail: icus@iis.u-tokyo.ac.jp

Tel: (+81-3)5452-6472
Fax: (+81-3)5452-6476